Large-scale Simulation of Cross Effect Dynamic Nuclear Polarisation Dynamics and Relaxation of a Tempol-doped Water/Glycerol Sample Below 30K

by

Federica C. Raimondi

Thesis submitted to the University of Nottingham for the degree of Doctor of Philosophy

January 2020

Supervisors:
Dr. Walter Köckenberger
Prof. Igor Lesanovsky

Abstract

Dynamic nuclear polarisation (DNP) provides significant signal enhancement compared to conventional thermal polarisation techniques used in typical nuclear magnetic resonance applications. Of the possible DNP mechanisms, the cross effect (CE), involving triple spin flips between two interacting electrons and a nucleus upon irradiation with a microwave field, is the most efficient at low temperatures and microwave irradiation amplitudes. In silico optimisation of parameters affecting CE enhancement, such as radical concentration and design, require simulation of large spin systems. However, the computational expense of solving the full Liouville-von Neumann equation for such systems makes this approach intractable after only a few spins. In the first part of this thesis, it is shown that the non-equilibrium nuclear polarisation buildup in the static CE case is effectively driven by incoherent 3-spin Markovian dissipative processes. These processes can be modelled using a classical kinetic Monte Carlo simulation algorithm, whose computation time scales favourably with system size. With this theoretical approach, it has been shown that it is possible to simulate systems consisting of over 120 spins in a timely fashion, allowing the study of many-body effects such as spin diffusion. It has also enabled predictive simulations that examine the effect of certain parameters on the CE DNP enhancement.

Simulations on cubic grids of 125 nuclear spins with varying degrees of linear randomisation on the spins' positions show that optimal enhancement is achieved for randomisations of 5% to 10%. The addition of glassing agents to the solvent to ensure even distribution of radical in the sample therefore also affects the polarisation enhancement by altering the dipolar matrix in the bulk. The same 125-spin cubic

grid (with 0% randomisation) is used to verify that the removal of protons with high secular interactions has a positive impact on the polarisation enhancement, while the removal of protons with high pseudo-secular interactions has a negative impact. Knowledge of how protons in the immediate vicinity of electrons affect the polarisation dynamics can aid in the design of radical molecules.

In many cases, the experimentally more relevant CE DNP mechanism is magic angle spinning (MAS) DNP, where the sample is spun at frequencies up to ∼100kHz. While the Hamiltonians of the CE under static and MAS conditions are almost identical, save for the time dependence acquired by some of the terms under MAS, the mechanisms leading to CE DNP have little in common. The kinetic Monte Carlo algorithm developed previously can therefore no longer be used. Furthermore, because the MAS dynamics are periodic with the rotor period, the problem of prohibitively long simulation times is exacerbated by the need to track dynamics within a rotor period as well as stroboscopically. In the fast simulation algorithm presented here, the polarisation-exchanging dynamics within a rotor period are modelled using a highly efficient Landau-Zener formalism. These dynamics are calculated only once to determine the average propagator in a period, which is then used in conjunction with a correction term accounting for the slow nuclear buildup over many periods to calculate the long-time stroboscopic dynamics.

To illustrate the versatility of the fast simulation algorithm, sweeps of the microwave frequency, static field strength & MAS spinning frequency were performed for the 52 structural protons of bTbk. Parameter sweeps such as these are a key building block in the development of an optimised CE DNP experiment. In another simulation, 100 solvent protons are added to the structural protons of bTbk to examine how the bTbk-solvent dynamics depend on the proton concentration in the solvent. It is shown that if the proton relaxation rate is relatively high, the radical and solvent evolve independently. This could pave the way to even faster simulation algorithms that replace the radical with a single representative nucleus and focus on the solvent

dynamics. This is useful because experimentally, it is generally the solvent protons that are observed, since the radical protons are too strongly hyperfine shifted for the receiver coil to pick them up.

Though not involved in the CE mechanism per se, relaxation plays a pivotal role in the efficacy of CE DNP, and is the focus of the last part of this thesis. The nuclear longitudinal relaxation time (T_{1n}) is studied for a range of temperatures, radical concentrations and proton concentrations in a Tempol monoradical-doped water/glycerol matrix. Temperature and proton & radical concentrations can be tuned in DNP experiments, and having a good understanding of how their variation affects nuclear relaxation is crucial to finding a parameter regime that optimises DNP enhancement. The temperature range spans from 2.6K to 30K and thus sheds light on nuclear relaxation behaviour below 10K, which is not often found in literature. Furthermore, a new formalism is developed that attempts to relate the observed longitudinal relaxation time to the electron relaxation in the radical and spin diffusion.

For all concentrations of Tempol, T_{1n} increases drastically below 15K, in some cases almost doubling as the temperature goes from 5K to 3K. Interestingly however, the T_{1n}s of 10mM and 20mM samples are longer than those of a 0mM sample at low temperatures. This contradicts the common assumption that the addition of *any* quantity of radical should act to decrease the relaxation time. It is suggested that this could be because the Tempol pushes out oxygen in solution, which may be more effective at relaxing protons, thereby initially increasing the relaxation time until enough Tempol is added to offset the loss of oxygen. The new formalism is demonstrated to fit well for temperatures above 10K, but it does not capture well the low-temperature behaviour.

In summary, the work presented in this thesis demonstrates the benefit of large-scale simulations of DNP systems. It provides novel approaches to modelling the effect of critical parameters of static and MAS DNP that can be extended to increasingly large and complex spin systems. A detailed study of the low-temperature T_{1n} relaxation

of Tempol contributes to the burgeoning literature on relaxation below 10K, and gives a more accurate picture of how relaxation should be taken into account in DNP simulations.

Acknowledgements

I dedicate this thesis to Mr. Tappe and Mr. Rawlings, whose unwavering support and encouragement in high school ultimately led to this point: the completion of a PhD in physics. It is funny to think back to 10th grade, when I took physics to avoid taking it as an IB course, and when I feared and loved maths in equal measure. And yet here I am, 11 years later, having devoted 7 of my 8 years of higher education to physics, and specialising in a highly mathematical branch. Few students can boast having had such fantastic teachers, and I will forever be grateful to both for what they taught me about myself, and about life.

Of course, this thesis would not exist were it not for the help and guidance of my supervisor Walter Köckenberger and our resident mathematician Alexander Karabanov, so a huge thank you goes to them. I also thank Alexey Potapov & Roman Shakhovy for their help with all things experimental, and Igor Lesanovsky for stimulating discussions in group meetings. This experience would not have been the same without the lovely people of the SPMIC, and I will particularly miss the K-Team – Adam, Ed, SP, Tommy, & Anto (+ Mark) – who have teased, comforted, helped and brought joy on so many occasions. Finally, I thank my parents for always putting me and my sister first, for teaching us how to survive in this unforgiving world, and for giving us the best childhood anyone could ask for.

List of Common Symbols

Symbol	Meaning	Equation
A_{jk}	Secular hyperfine interaction strength	2.14
$\hat{a}(t)$	Difference in secular coupling	5.10
B_0	Static magnetic field	-
$B_1(t)$	RF-field	-
B_{jk}	Pseudo-secular hyperfine interaction strength	2.15
$D,\ d_{kk'}$	Dipolar interaction strength / electron / nuclear	2.13
$\hat{\hat{\mathcal{D}}}$	Dissipator	2.10
$e_1,\ e_2$	Electron 1 / electron 2	
$\hat{H}.$	Hamiltonian	-
$\hbar$	Reduced Planck constant	-
$\hat{I}.$	Nuclear spin operator	-
$I(t)$	Integral of spectrum	7.1
$\hat{J}_{1z},\ \hat{J}_{2z}$	Nitrogen spin operator	-
$\hat{\hat{K}}(t)$	Memory kernel	2.24
k_B	Boltzmann constant	-
$\hat{\hat{\mathcal{L}}}$	Liouville superoperator	2.11
N	Number of spins / time steps	-
n	number of spinning periods	-
$n_\mathrm{b},\ n_\mathrm{c}$	Nuclei core / bulk	-
$n_k,\ n$	k^{th} nucleus	-
$p,\ p_\mathrm{th}$	Thermal polarisation	1.7
$p_\mathrm{e},\ p_\mathrm{n}$	Polarisation / electron / nuclear	p.28
PAS	Principal Axis System	-
r	Separation between spins	-
$R_{0,1\mathrm{n}}$	Matrix relaxation	-
$R_1,\ R_{1\mathrm{e}},\ R_{1\mathrm{n}}$	Longitudinal relaxation rate / electron / nuclear	-
$R_2,\ R_{2\mathrm{e}},\ R_{2\mathrm{n}}$	Transverse relaxation rate / electron / nuclear	-
$R_\mathrm{inh},\ R_\mathrm{PM},\ R_\mathrm{SD}$	Inherent / paramagnetic / spin diffusion nuclear longitudinal relaxation	-
$\hat{S}.$	Electron spin operator	-
T_0	Activation temperature	-
$T_1,\ T_{1\mathrm{e}},\ T_{1\mathrm{n}}$	Longitudinal relaxation time / electron / nuclear	-
$\bar{T}_1,\ \bar{T}_{1\mathrm{n}}$	Average nuclear longitudinal relaxation time	-
$T_2,\ T_{2\mathrm{e}},\ T_{2\mathrm{n}}$	Transverse relaxation time / electron / nuclear	-
T	Temperature	-
T_r	MAS period	-
t_0	Instance of avoided level crossing	-

List of Common Symbols

Symbol	Meaning	Equation
$\dot{\Gamma}$	Effective rates (kinetic Monte Carlo)	3.12 & 3.13
$\gamma,\ \gamma_{\mathrm{S}},\ \gamma_{\mathrm{I}}$	Gyromagnetic ratio / electron / nuclear	-
$\Delta,\ \Delta_1,\ \Delta_2$	Microwave offset / electron 1 / electron 2	-
$\Delta(t)$	Difference between electron microwave offsets	p. 123
Δ_0	Microwave offset (MAS)	-
$\Delta_j^{(g)}(t)$	Time-dependent microwave offset (MAS)	-
$\hat{\Delta}_{1,\mathrm{Z}_1},\ \hat{\Delta}_{2,\mathrm{Z}_2}$	Total detuning / electron 1 / electron 2	-
$\delta(t)$	Detuning (Landau Zener)	2.42
$\delta R_{1\mathrm{n}}$	Non-inherent nuclear relaxation	8.4
$\delta\bar{T}_1$	Error average nuclear longitudinal relaxation	7.3
ϵ_{DNP}	DNP enhancement	-
$\eta,\ \hat{\eta}_1,\ \hat{\eta}_2$	Adiabaticity conditions / electron 1 / electron 2	3.9
θ	Angle between B_0 and vector joining two spins	-
θ_{flip}	RF-field flip angle	p. 176
θ_{M}	Magic angle	-
μ_0	Vacuum permeability	-
ν_{MAS}	MAS spinning frequency	-
$\hat{\rho},\ \hat{\rho}_{\mathrm{S}},\ \hat{\rho}_{\mathrm{E}}$	Density operator / system / environment	2.2 & 2.16
$\hat{\rho}_{\mathrm{th}}$	Thermal equilibrium density matrix	2.3
τ_0	High temperature correlation time	-
$\tau_{90\%}$	Time to reach 90% buildup	-
τ, τ_{c}	Correlation time	2.46 & 8.2
τ_{d}	Delay time	-
τ_{DNP}	DNP buildup time	-
τ_{r}	Recovery time	-
$\Omega(t)$	Mixing rate (Landau Zener)	2.43
ω_1	Microwave irradiation strength	-
$\omega_{\mathrm{L}},\ \omega_{\mathrm{S}},\ \omega_{\mathrm{I}}$	Larmor frequency / electron / nuclear	1.2
$\omega_{\mu\mathrm{w}}$	Microwave irradiation frequency	-

Contents

1 Introduction **1**

1.1 Dynamic Nuclear Polarisation 2

1.1.1 DNP Simulation 3

1.1.2 Simulating Large Spin Systems 4

1.2 Concepts of Nuclear Magnetic Resonance 4

1.2.1 Introducing Spin and its Behaviour in a Magnetic Field 4

1.2.2 The Rotating Frame & the RF-field 7

1.2.3 Relaxation 9

1.3 Relaxation in DNP 10

1.4 Enhancement and Polarisation 11

1.5 Outline of Thesis Structure 12

2 Theory Toolbox **15**

2.1 Basic Quantum Mechanics 15

2.1.1 The Density Operator 16

2.1.2 Thermal Equilibrium Density Matrix 17

2.1.3 Superoperators 18

2.1.4 Markovian Evolution 19

2.1.5 The Markovian Master Equation in Lindblad Form 20

2.1.6 Lindblad Propagator 22

2.2 The Cross Effect Hamiltonian 23

2.2.1 Lab and Rotating Frame Hamiltonians 23

2.2.2 Interaction Parameters 27

2.2.3 Polarisation 28
2.3 Adiabatic Elimination 28
2.3.1 Coherence Subspaces 29
2.3.2 Nakajima-Zwanzig Projection Operators 30
2.3.3 Steady State Solution for the Environment 32
2.3.4 Solution for the System 34
2.4 Krylov-Bogolyubov Method of Averaging 37
2.5 Classical Kinetic Monte Carlo Algorithm 39
2.5.1 Implementation of Variable Time-step Classical kMC 39
2.6 Landau-Zener Theory 44
2.6.1 Avoided Level Crossing 44
2.6.2 Landau-Zener Formula 44
2.7 Nuclear Longitudinal Relaxation 46
2.7.1 Inherent Nuclear Longitudinal Relaxation 47
2.7.2 Paramagnetic Relaxation 49
2.8 Electron Longitudinal Relaxation 51
2.8.1 Direct Process 52
2.8.2 Raman Process 52
2.8.3 Orbach Process 53
2.8.4 Local Mode Process 53
2.8.5 Thermal Process 54

3 Static Cross Effect DNP **55**
3.1 Introduction 55
3.2 Static Cross Effect 55
3.3 Energy Level Diagram 57
3.4 Efficient Cross Effect DNP and Incoherent Dynamics 58
3.4.1 Efficient CE DNP 59
3.4.2 Single Spin with Microwave-driven Dynamics 59
3.4.3 Efficient Simulation of the Cross Effect 62

3.5 Adiabatic Elimination . . . 63
3.5.1 Rotating Frame Energy Level Diagram . . . 64
3.5.2 Zero Quantum Coherence Projection . . . 65
3.5.3 Zeeman Projection . . . 68
3.6 Interpretation of the Effective Rates . . . 70
3.7 kMC Algorithm Implementation . . . 73

4 Application of the kinetic Monte Carlo Algorithm 75
4.1 Cross Effect DNP Efficiency . . . 75
4.1.1 Electron Dipolar and Pseudo-secular Hyperfine Interactions . 76
4.1.2 Microwave Irradiation Amplitude . . . 78
4.1.3 Effect of Temperature . . . 79
4.1.4 Effect of Electron Transverse Relaxation . . . 81
4.1.5 Discussion . . . 82
4.2 Error Testing the Zeeman Projection . . . 82
4.2.1 Discussion . . . 86
4.3 Steady State Polarisation and Buildup Time . . . 87
4.3.1 Discussion . . . 90
4.4 Many-body kMC Simulation . . . 92
4.4.1 Geometry for Large-scale Simulation . . . 92
4.4.2 Large-scale Simulation Results . . . 93
4.4.3 Time Saving with kMC Algorithm . . . 97
4.5 Effect of Solution Geometry on Nuclear Polarisation . . . 99
4.5.1 Creation of Grid Geometry . . . 100
4.5.2 Randomisation Simulations . . . 103
4.5.3 Discussion . . . 105
4.6 Effect of Radical Geometry on Nuclear Polarisation . . . 110
4.6.1 Removing Spins . . . 111
4.6.2 Discussion . . . 115

5 Magic Angle Spinning DNP **117**

5.1 Introduction . . . 117

5.2 MAS Cross Effect Hamiltonian & Simulation . . . 119

5.2.1 Polarisation Events . . . 122

5.3 Energy Level Diagram . . . 126

5.4 Approximations to the Master Equation . . . 128

5.4.1 Non-adiabaticity and Coherent Decay of Electron Events . . . 128

5.4.2 Non-adiabaticity and Coherent Decay of CE Events . . . 130

5.4.3 Hyperfine and Nuclear Dipolar Interactions . . . 134

5.5 Incoherent Decay in Landau-Zener Theory . . . 140

5.5.1 Application of the Incoherence Conditions . . . 141

5.5.2 Dynamics in One Rotor Period . . . 141

5.6 Fast Simulation Algorithm . . . 144

5.7 Comparison to Other Groups . . . 146

6 Application of MAS Fast Simulation Algorithm **149**

6.1 bTbk Geometry . . . 150

6.2 Error Testing of the Fast Algorithm . . . 151

6.2.1 Integration Time Step . . . 152

6.2.2 Powder Averaging Protocol . . . 153

6.2.3 Electron Relaxation Rate Scan . . . 155

6.2.4 MAS Frequency Scan . . . 156

6.3 Nuclear Exchange Dynamics . . . 157

6.3.1 Geometry . . . 158

6.3.2 Simulations . . . 158

6.3.3 Discussion . . . 159

6.4 bTbk Core Simulations . . . 161

6.4.1 Static Field Sweep . . . 161

6.4.2 Discussion . . . 162

6.4.3 MAS Frequency Sweep . . . 164

6.4.4 Discussion . . . 165
6.5 Simulations of bTbk in Solvent . . . 166
6.5.1 Geometry . . . 166
6.5.2 Simulations . . . 167
6.5.3 Discussion . . . 168

7 Experiment Toolbox **171**
7.1 Hardware & Software . . . 171
7.2 NMR measurement . . . 175
7.3 Error Analysis and Uncertainty . . . 179
7.4 Electron Paramagnetic Resonance . . . 182

8 NMR Experiments **185**
8.1 Paramagnetic Centres . . . 186
8.1.1 Tempol . . . 186
8.1.2 Dissolved Oxygen . . . 187
8.2 Tempol Experiments . . . 187
8.2.1 Sample Preparation . . . 188
8.2.2 Experiment Procedure . . . 188
8.2.3 Results . . . 190
8.2.4 Discussion . . . 193
8.3 Degassed Samples . . . 195
8.3.1 Sample Preparation . . . 195
8.3.2 Experiment Procedure . . . 196
8.3.3 Results . . . 196
8.3.4 Discussion . . . 197
8.3.5 Non-monotonicity of Tempol Concentration Dependence . . . 198
8.4 Deuterated Experiments . . . 200
8.4.1 Sample Preparation . . . 200
8.4.2 Experiment Procedure . . . 201
8.4.3 Results . . . 202

8.4.4 Discussion 204
8.5 Fitting the Proton Relaxation Rate 206
8.5.1 Electron Relaxation Rate 208
8.5.2 Nuclear Relaxation Rate 208
8.5.3 Discussion 210

9 Conclusion **213**
9.1 Static Cross Effect DNP 213
9.2 MAS Cross Effect DNP 214
9.3 Tempol Experiments 215

A Theory Toolbox Appendix **219**

B Acquisition Parameters **221**
B.1 Delay Times & Other Parameters 221
B.2 Saturation Recovery Pulse Sequence 222

Chapter 1

Introduction

The theories of dynamic nuclear polarisation (DNP) and nuclear magnetic resonance (NMR) relaxation were developed at similar times in the mid-20^{th} century. This is when Overhauser first predicted the possibility of DNP [1], and Heitler and co. first started developing a theory of relaxation for polarised spins [2]. In both fields, experimental advancements initially far surpassed the development of an accurate theory. DNP for example was routinely used before a robust theoretical framework was developed. Such frameworks however, are crucial for understanding the underlying physics and, in the age of computing, for writing simulations. With the immense computational power of modern computers, it is possible to push the boundaries of our knowledge to ever more complex systems. Predictive simulations can be used to maximise DNP performance by finding appropriate parameter regimes, while sophisticated fitting algorithms can determine what relaxation pathways are present in a system, and to what extent. In the chapters that follow, both techniques will be employed.

This thesis can be divided roughly into three sections: the first two are theoretical, and focus on developing fast, accurate simulation algorithms for DNP under static and magic angle spinning (MAS) conditions. The last on the other hand is experimental, and sheds light on the relaxation mechanisms active in DNP systems. At first glance, the theoretical and experimental parts may appear to be rather disjointed. However,

once one takes into consideration the pivotal role of relaxation in DNP, the need for a detailed study of its behaviour seems obvious. All three parts address gaps in the theory or knowledge at the time of writing. While predictive simulations of static and MAS DNP existed before the writing of this thesis, they were restricted to smaller spin systems and faced different parameter limitations. Similarly, there have been many studies of electron and nuclear relaxation in DNP systems; the novelty added here is the low temperatures (2.6K to 30K) at which experiments were performed and the level of detail in the analysis of Tempol relaxation.

1.1 Dynamic Nuclear Polarisation

The DNP mechanism was first proposed by Overhauser [1] in 1953, and was verified experimentally shortly after by Carver & Slichter [3]. Further work throughout the next two decades demonstrated DNP in both liquids [4, 5] and solids [6, 7], with pioneerig work by Griffin's group in the 1990's demonstrating efficient solid state DNP at high magnetic fields [8]. The essence of DNP is a transfer of electron polarisation to surrounding nuclei upon irradiation of a sample with microwaves. Because electrons are much more responsive to an applied static magnetic field than nuclei, they become much more polarised in a given field. Transferring their polarisation to the nuclear ensemble therefore greatly enhances its polarisation with respect to the thermal state.

There are four known DNP mechanisms. The Overhauser effect [1] enhances nuclear polarisation via cross-relaxation between electrons and nuclei. The spin flips causing enhancement arise from rotational and translational modulation of the electron-nuclear hyperfine coupling terms. Carver & Slichter demonstrated the Overhauser effect in solids with high electron mobility [3]. Shortly after it was also demonstrated in liquids [4, 5], where it is in fact the *only* known DNP mechanism. In the last decade, the Overhauser effect has additionally been shown to be active in solid dielectrics under MAS [9, 10]. The remaining three DNP mechanisms are all active in the solid state and are distinguishable by the number of electrons and type of

transition participating in the DNP process. The solid effect (SE) involves a single electron that transfers its polarisation via forbidden zero-quantum or double-quantum transitions [11, 12]. In the cross effect (CE), the polarisation difference between two dipolar-coupled electrons is transferred to nuclei via the pseudo-secular hyperfine interaction. The CE was first described by Kessenikh et al. in 1963 [13, 14] and further developed by Hwang & Hill in 1967 [15, 16]. The predictive algorithms developed throughout this thesis are for the CE mechanism. Finally, in the thermal mixing (TM) mechanism, many coupled electrons act together to transfer their polarisation to the nuclear ensemble.

1.1.1 DNP Simulation

Historically, theoretical models of the DNP process have been based on thermodynamic phenomenological rate equations in which the system is split into several heat reservoirs brought into contact by microwave irradiation [17]. Though such an approach can to some extent describe the nuclear polarisation enhancement, it cannot be used to model how radical properties or system geometries affect the polarisation dynamics [18]. For this, a quantum mechanical description is needed [19].

Quantum mechanical descriptions of static DNP appeared in the late 1990's, with Jeschke deriving the first three-spin Hamiltonian in 1998. His Hamiltonian was capable of describing the DNP process via transient electron polarisation [20], but, like other early formalisms, lacked detailed treatment of relaxation and was derived for systems in low magnetic fields. The largest CE DNP signal enhancements however, are generally observed for magnetic fields above 5T [21]. The work of Vega's group [22, 23, 24, 25, 26], the Köckenberger group [19, 27, 28, 29] and Hu [30] in more recent years has lead to more accurate and larger scale simulations of DNP. In these simulations, relaxation is meticulously accounted for, and appropriate approximations have been made to allow the simulation of larger systems.

1.1.2 Simulating Large Spin Systems

The principal concern when it comes to simulating large and complex spin systems is the reduction of state space, which scales as 2^N in Hilbert space and 4^N in Liouville space, N being the number of spins in the system. Although the DNP Hamiltonian lies in Hilbert space, calculations are generally performed in Liouville space, to allow easier incorporation of dissipative effects. The size of the matrices that store the state of the system therefore quickly becomes prohibitively large, even for small N. There are many techniques to circumvent the exponential scaling problem, from approximations that keep the calculations in Hilbert space [23], to ones that eliminate un-informative states [28, 29, 31]. However, no matter how good a given formalism may seem, it is nonetheless merely an approximation to the true dynamics, and is therefore subject to limitations.

1.2 Concepts of Nuclear Magnetic Resonance

This section introduces the basic concepts of nuclear NMR and is based on books by Cowan [32] and Breuer & Petruccione [33].

1.2.1 Introducing Spin and its Behaviour in a Magnetic Field

Spin is an intrinsic property of elementary particles, hadrons, and atomic nuclei. It is a form of angular momentum, and as such has both a magnitude and direction, and can be represented by a vector. However, in contrast to classical angular momentum, the quantum mechanical property of spin is quantised [34]. The spin vector can therefore only point in discrete directions, determined by the spin quantum number. This thesis looks exclusively at systems consisting of protons and electrons, both of which have a spin quantum number of $1/2$. For spin-$1/2$ particles, the z-component of the spin vector can point in only two directions: up (spin-up, $|\uparrow\rangle$), or down (spin-down, $|\downarrow\rangle$).

The magnetic moment ($\vec{\mu}$) of a quantum particle is proportional to its spin and interacts with an applied magnetic field. For spin-1/2 particles, this interaction leads to a splitting of degenerate (equal) energy levels into two non-degenerate levels when the spin is placed in a magnetic field. The lower energy level corresponds to the z-component of the spin vector being aligned with the magnetic field, and the higher to the z-component being anti-parallel. This splitting of energy levels in a magnetic field is known as the Zeeman effect, and the energy gap between the levels is directly proportional to the strength of the magnetic field (FIG. 1-1) [35].

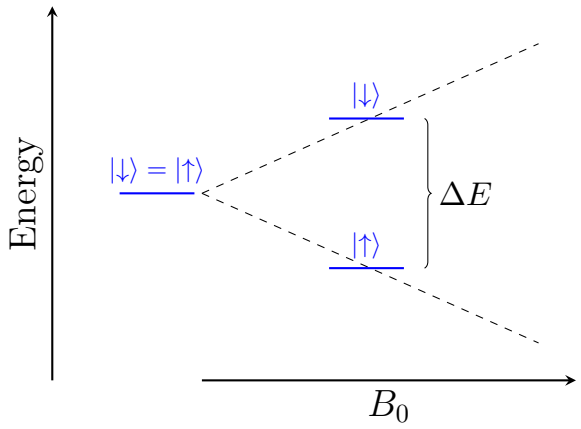


Figure 1-1: Zeeman splitting of an energy level (blue) when a spin-1/2 particle is placed in a magnetic field. The energy gap ΔE is the Zeeman energy.

The energy splitting is given by

$$\Delta E = -\hbar\gamma B_0, \tag{1.1}$$

where $\hbar$ is the reduced Planck constant, γ is the gyromagnetic ratio and B_0 is the applied static field. The Planck-Einstein relation dictates that a transition between the two energy levels will take place only if the applied frequency is on resonance with the energy gap. This leads directly to a very important quantity in magnetic resonance, the Larmor frequency

$$\omega_{\mathrm{L}} = -\gamma B_0. \tag{1.2}$$

When a microscopic particle is placed in a magnetic field, it experiences a torque due

to its magnetic moment $\vec{\mu}$. However, generally of more interest is the macroscopic magnetisation $\vec{M}$, which is the total magnetic moment per unit volume. The equation of motion of the magnetisation vector is found by summing over the equations of motion for each magnetic moment (of a given type), and is given by

$$\dot{\vec{M}} = \gamma \vec{M} \times B_0. \tag{1.3}$$

Conventionally, the static field B_0 is applied along the z-axis. Therefore, assuming that $M_y(0) = 0$ (this is arbitrary but simplifies calculations), the solution to EQ. 1.3 is

$$\begin{aligned} M_x(t) &= M_x(0)\cos(\gamma B_0 t) \\ M_y(t) &= -M_x(0)\sin(\gamma B_0 t) \\ M_z(t) &= M_z(0). \end{aligned} \tag{1.4}$$

EQ. 1.4 describes the collective, macroscopic dynamics of a spin ensemble after it has been disturbed from thermal equilibrium (M_{eq}), where $M_x(0) = 0$ and there are no transverse dynamics. The component $M_z(t)$ parallel to the magnetic field is fixed, whereas in the transverse xy-plane the magnetisation rotates about z with a fixed magnitude $M_x(0)$. Spins with $\gamma > 0$, such as protons, rotate anti-clockwise, whereas spins with $\gamma < 0$, such as electrons, rotate clockwise. The angular velocity of rotation is precisely ω_{L}.

NMR and its cousin electron paramagnetic resonance (EPR) measure the dynamics of the polarisation p, which is the net magnetisation along B_0. In EPR the polarisation tends to be large and easy to see over the noise. In NMR on the other hand, the signal is generally small and difficult to detect. This is due to the large difference in gyromagnetic ratios, which affect how responsive a spin is to an applied magnetic field, between nuclei and electrons. The proton gyromagnetic ratio (γ_{I}) is approximately 660 times smaller than that of electrons (γ_{S}), while for other nuclear species it is even smaller. Nuclei are therefore much less responsive to an applied magnetic

field than electrons, and more difficult to polarise.

An ensemble of spins obeys the laws of thermodynamics. The probability P_i of finding the system in any one of its energy eigenstates is thus given by the Boltzmann distribution

$$P_i \propto \exp\big(-\frac{E_i}{k_{\mathrm{B}}T}\big), \tag{1.5}$$

where i denotes the i^{th} state of the system, k_{B} is the Boltzmann constant, T is the absolute temperature, and $k_{\mathrm{B}}T$ is the thermal energy. The ratio of two probabilities is known as the Boltzmann factor, and depends on the energy difference between two states i and j:

$$P_i/P_j = \exp\big(-\frac{E_j - E_i}{k_{\mathrm{B}}T}\big) = \exp\big(-\frac{\hbar\omega_{\mathrm{L}}}{k_{\mathrm{B}}T}\big).$$

If N is the total number of spins (of a given type) in a system, then the number of spins in each energy level is

$$\begin{aligned} N_\uparrow &= N\frac{\exp\big(-\frac{\hbar\omega_{\mathrm{L}}}{k_{\mathrm{B}}T}\big)}{\exp\big(-\frac{\hbar\omega_{\mathrm{L}}}{k_{\mathrm{B}}T}\big)+\exp\big(\frac{\hbar\omega_{\mathrm{L}}}{k_{\mathrm{B}}T}\big)} \\ N_\downarrow &= N\frac{\exp\big(\frac{\hbar\omega_{\mathrm{L}}}{k_{\mathrm{B}}T}\big)}{\exp\big(-\frac{\hbar\omega_{\mathrm{L}}}{k_{\mathrm{B}}T}\big)+\exp\big(\frac{\hbar\omega_{\mathrm{L}}}{k_{\mathrm{B}}T}\big)}. \end{aligned} \tag{1.6}$$

Since the polarisation is just a measure of the net magnetisation along B_0, it is given by the simple relation

$$p = \frac{N_\uparrow - N_\downarrow}{N} = \tanh\big(\frac{\hbar\omega_{\mathrm{L}}}{2k_{\mathrm{B}}T}\big). \tag{1.7}$$

1.2.2 The Rotating Frame & the RF-field

So far, a spin ensemble placed in a static magnetic field with B_0 pointing along the positive z-axis and subject to no perturbations has been considered. In practice however, perturbations are necessary to measure the magnetisation experimentally. At

equilibrium (in the presence of B_0), the system has some equilibrium magnetisation M_{eq} along the z-axis. To measure this magnetisation, it must be tipped into the transverse plane by an oscillating field $B_1(t)$, where it can induce a signal in the receiver by creating a non-zero transverse component $M_x(t)$. $B_1(t)$ is conventionally applied along the x-axis and oscillates at the Larmor frequency. This typically corresponds to the radio-frequency (RF) range of the spectrum, which is why $B_1(t)$ fields are often referred to as RF-fields. For electrons, $B_1(t)$ generally lies in the upper end of the RF spectrum in the microwave region. RF-fields are not applied continuously, but in "pulses" that are just long enough to tip the magnetisation by the desired angle. Types of pulses and pulse sequences will be discussed in relation to the experiments performed in Section 7.2.

Though necessary, the addition of $B_1(t)$ complicates treatment of the problem in the lab frame, so it is customary to proceed into the rotating frame of reference. The rotating frame is ubiquitous in many areas of physics as it simplifies the description of dynamics. In the lab frame (refer to FIG. 1-2), spins precess about B_0 (orange) at a frequency of ω_{L}. When $B_1(t)$ (red) is applied, it rotates in the xy-plane at a frequency ω_{RF}, and causes the magnetisation (blue) to tilt away from its equilibrium (purple). How far the magnetisation is tipped depends on how long $B_1(t)$ is applied for. The lab frame dynamics have many time-dependent, oscillating parts that make treatment more complex. Many of these can however be eliminated by moving into a frame rotating at the Larmor frequency. This eliminates the precession of the spins, and, since in general $\omega_{\text{RF}} = \omega_{\text{L}}$, also the time dependence of $B_1(t)$. Therefore, in the rotating frame, the effect of B_1 is simply to tilt the magnetisation $M_z(0)$ away from z. It is now easier to consider the effect of fields other than B_0, such as $B_1(t)$, or changes in the phase or magnitude of $\vec{M}(t)$.

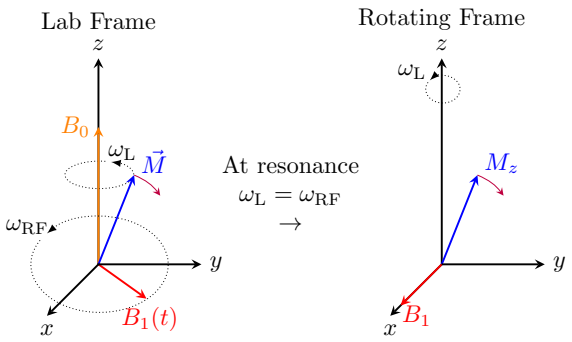


Figure 1-2: Precession of the magnetisation vector in the lab and rotating frames of reference.

1.2.3 Relaxation

Relaxation processes take place when the system is perturbed from equilibrium, by $B_1(t)$ for example. EQ. 1.4 suggests that if $M_z(t)$ is tipped in the rotating frame by $B_1(t)$, it will simply remain in its new position, even after the removal of $B_1(t)$. Experimentally however, this is known not to be the case: the transverse components of $M(t)$ decay to zero (transverse, T_2, or spin-spin relaxation), and the longitudinal component recovers to equilibrium M_{eq} (longitudinal, T_1, or spin-lattice relaxation).

EQ. 1.4 assumes that each spin experiences *exactly* the same magnetic field. This is however not the case. Each spin itself creates a minute magnetic field seen by its neighbours, and B_0 & $B_1(t)$ are never fully homogeneous. Each spin therefore precesses at a slightly different rate (refer to EQ. 1.2). The motional incoherence of the spins due to their interactions with each other and the lattice leads to relaxation.

T_1 involves energy exchange between a spin's magnetic energy and other degrees of freedom in the system, referred to as the "lattice". Because it requires matching energy conditions, it is generally slower than T_2, which is a form of destructive interference between spins as they dephase. The phenomenological equations of motion of $\vec{M}(t)$ taking into account relaxation are known as the Bloch equations, and are given by [36]

$$\dot{M}_x(t) = \gamma\big[\vec{M}(t) \times B_0\big]_x - M_x(t)/T_2$$
$$\dot{M}_y(t) = \gamma\big[\vec{M}(t) \times B_0\big]_y - M_y(t)/T_2$$
$$\dot{M}_z(t) = \gamma\big[\vec{M}(t) \times B_0\big]_z - (M_z(t) - M_{\mathrm{eq}})/T_1.$$

The magnetisation components in the longitudinal and transverse plane now include an exponential term that accounts for an exponential decay (in the case of the transverse magnetisation) or increase (in the case of the longitudinal magnetisation) of the magnetisation:

$$M_x(t) = M_x(0)\cos(\omega_{\mathrm{L}}t)\exp(-t/T_2)$$
$$M_y(t) = M_x(0)\sin(\omega_{\mathrm{L}}t)\exp(-t/T_2)$$
$$M_z(t) = M_{\mathrm{eq}} - (M_{\mathrm{eq}} - M_z(0))\exp(-t/T_1).$$

This phenomenological description often applies, but not always. Especially in the case of EPR, relaxation is not always exponential and adaptations have to be made. It is also important to keep in mind that relaxation is a macroscopic phenomenon, describing the process by which an *ensemble* of spins returns to the equilibrium determined by the Boltzmann factor. It makes little sense to speak of a single spin returning to equilibrium [37].

1.3 Relaxation in DNP

The third part of this thesis focuses on relaxation pathways in DNP systems. In DNP, the microwave irradiation drives particular electron-nuclear flip-flips ($|\uparrow_{\mathrm{e}}\rangle|\uparrow_{\mathrm{n}}\rangle \rightleftarrows |\downarrow_{\mathrm{e}}\rangle|\downarrow_{\mathrm{n}}\rangle$) or flip-flops ($|\uparrow_{\mathrm{e}}\rangle|\downarrow_{\mathrm{n}}\rangle \rightleftarrows |\downarrow_{\mathrm{e}}\rangle|\uparrow_{\mathrm{n}}\rangle$), depending on the resonance condition of the microwave field. For efficient DNP, these transitions must be properly balanced with transitions due to electron and nuclear relaxation mechanisms. To understand better why, consider a system comprising a fully polarised electron ensemble (a reasonable assumption at low temperatures), and an unpolarised nuclear ensemble. The system is irradiated with a microwave field resonant with electron-nuclear flip-flop transitions, such that the nuclear spin-up state is favourably populated. Furthermore,

the microwave field strength (ω_1) is high enough that the rate of driving is much larger than the nuclear longitudinal relaxation rate ($1/T_{1\mathrm{n}}$). Initially, all electrons are in the spin-up state. A nuclear spin that is in the spin-up state can therefore not participate in a driven electron-nuclear transition because the only transition available to it is a flip-flip, which is off resonance with the microwave irradiation. A nuclear spin in the spin-down state on the other hand can flip-flop with an electron, putting the electron in the down state and the nucleus in the up state. The down state electron now poses a risk to nuclear spins that are already in the up state, since it can take one of them back into the down state through a flip-flop. However, in most cases the powerful electron relaxation mechanism acts before the driving force, and takes the spin-down electron back into the thermal equilibrium up state, allowing the cycle to begin again. For this process to be effective, the electron (which for small electron concentrations must service a large number of spins) must always return to thermal equilibrium before nuclear relaxation has time to flip *any* of the nuclear spins. The above is true as long as the nuclear relaxation has no origin other than the coupling of the nucleus to the electron. If other, purely nuclear, relaxation mechanisms are present, the nuclear polarisation will never become equal to the electron polarisation, $p_{\mathrm{n}} < p_{\mathrm{e}}$ [38].

1.4 Enhancement and Polarisation

The definition of enhancement is a point of some contention in the DNP community, with different groups having different definitions for different cases. In the static case it is sometimes defined as the ratio of polarisations with and without microwave irradiation. In the MAS case things are more complex because in addition to the microwave irradiation, sample spinning leads to a phenomenon known as depolarisation [39], which decreases the polarisation from thermal polarisation. Throughout this thesis it is always assumed that the thermal nuclear polarisation is negligible. The nuclear enhancement is then simply the DNP-induced polarisation. Furthermore, the electron and nuclear polarisations are always normalised to the electron thermal

polarisation.

1.5 Outline of Thesis Structure

The remaining eight chapters of this thesis are as follows:

2. **Theory Toolbox**: Introduces the basic quantum mechanics of DNP and the mathematical tools used in Chapters 3 & 5 to derive fast simulation algorithms. Towards the end, the electron and nuclear relaxation mechanisms are described in more detail.

3. **Static Cross Effect DNP**: Describes the static CE mechanism and outlines the kinetic Monte Carlo (kMC) algorithm able to simulate large spin systems.

4. **Application of the kMC Algorithm**: Uses a combination of the full master equation and the kMC algorithm to study in more detail the static CE polarisation dynamics. This includes the effect of radical and solvent geometries.

5. **Magic Angle Spinning DNP**: Describes the MAS CE mechanism and outlines the fast simulation algorithm able to simulate large spin systems.

6. **Application of MAS Fast Simulation Algorithm**: Uses a combination of the full master equation and the fast simulation algorithm to study in more detail the validity of the fast simulation algorithm and the MAS CE polarisation dynamics. This includes the effect of solvent geometries.

7. **Experiment Toolbox**: Introduces the concept of NMR measurement and describes the experimental setup in detail.

8. **NMR Experiments**: Shows and discusses the results of NMR experiments at low temperatures. The effects of radical concentration, temperature, and proton concentration on nuclear relaxation are examined. In the last section, the effect of paramagnetic relaxation is modelled.

9. **Conclusion**: Concludes the thesis with some final remarks and suggestions for future work.

Chapter 2

Theory Toolbox

In the first part of this chapter the key mathematical concepts that will be used throughout the theory part of this thesis are introduced. The quantum mechanical framework is first developed and initial approximations that hold in the context of NMR are made. Next, general cases of the adiabatic elimination procedure and kinetic Monte Carlo algorithm are described. These both pertain to the simulation algorithm developed for the static CE. This is followed by a short description of Krylov-Bogolyubov averaging, which is used in the derivation of both the static CE and the MAS CE simulation algorithms. Finally, the Landau-Zener approximation used for the MAS CE simulation algorithm is outlined.

From Section 2.7 onward, focus is on the theory of relaxation, which is used in the experimental part of this thesis. Nuclear longitudinal relaxation mechanisms in solids are introduced first, starting with inherent nuclear longitudinal relaxation and ending with paramagnetic relaxation. In the final section of this chapter, electron longitudinal relaxation mechanisms in the solid state are described.

2.1 Basic Quantum Mechanics

While the classical picture of NMR presented in the Introduction is useful for gaining an intuitive understanding of the macroscopic dynamics and how these produce a

signal in a spectrometer, it fails to give an accurate description of the microscopic dynamics that enable DNP. For this, a quantum mechanical picture is required. Furthermore, since the interaction between a CE system and its environment is a crucial element of the DNP process, this necessarily leads to an open quantum system treatment of the dynamics. In this and the next section the reader is taken step-by-step through the quantum mechanics required to understand the form of the CE master equation and Hamiltonian. More detail can be found in REFs. [33, 40].

2.1.1 The Density Operator

The evolution of an isolated quantum system is described by the Schrödinger equation

$$i\frac{\partial |\psi\rangle}{\partial t} = \hat{H} |\psi\rangle , \tag{2.1}$$

where $|\psi\rangle$ is the state of the system at time t (a vector) and $\hat{H}$ is the Hamiltonian operator describing its dynamics (a matrix) [40]. The CE quantum system however is not isolated, but tends to exchange with its environment, and while it is not impossible to solve EQ. 2.1 for the system as well as the entire environment, it is not practical. Instead, the density operator formalism is used to describe the dynamics [i].

When a system exchanges with its environment, it is no longer possible to factorise the combined state into its constituent pure-state vectors. The total state is therefore no longer given in the form of a vector $|\psi\rangle$ as it is in EQ. 2.1, but rather by a density matrix $\hat{\rho}$. For a system with a basis $|\phi_i\rangle$, a general density operator is given by

$$\hat{\rho} = \sum_{ij} \rho_{ij} |\phi_i\rangle \langle\phi_j| , \tag{2.2}$$

where the elements ρ_{ij} of the density matrix are given by $\langle\phi_i| \hat{\rho} |\phi_j\rangle$ [40]. In general, the density matrix has both diagonal elements (eigenvalues or populations) and off-diagonal elements (coherences). The eigenvalues describe the classical probability of

[i] Note that the terms density operator and density matrix will be used interchangeably.

a particular measurement outcome (i.e. the probability of a particular state being occupied) [41]. Measurements on the system therefore collapse the density matrix into a diagonal state. Coherences on the other hand are a quantum phenomenon describing the coherent evolution of superpositions of states [42]. For a system interacting with an environment, coherences tend to decay with time, taking the system to a diagonal state [43].

If the ensemble of spins has independent states, each spin can exist in any of its possible states, irrespective of what state other spins in the ensemble are in. The total density operator is then given by the tensor product of the density matrices for each spin

$$\hat{\rho} = \hat{\rho}_1 \otimes \hat{\rho}_2 \otimes ... \otimes \hat{\rho}_N.$$

For spin-1/2 particles $\hat{\rho}_i$ has dimension 2×2, so an N-particle system will have dimension $2^N \times 2^N$.

2.1.2 Thermal Equilibrium Density Matrix

A ubiquitous assumption in the field of NMR is the "high field approximation", which posits that interactions with external magnetic fields are much stronger than any internal NMR interactions such as dipolar or hyperfine interactions. The thermal equilibrium density operator ($\hat{\rho}_{\mathrm{th}}$) is therefore well approximated by the Zeeman terms of the Hamiltonian (describing the magnetic interaction of the spins with B_0) only, as all other terms are negligible in comparison. Two additional assumptions can be made: the first is that the nuclear Zeeman terms can also be neglected since the nuclear polarisation is low compared to that of electrons, and the second is that all electrons achieve the same polarisation p_{e}. This last statement is not trivial, as it is essential that the electrons have a large g-anisotropy for CE DNP to take place. It is therefore not obvious that they should be equally polarised. However,

the g-anisotropy necessary for effective CE DNP is much smaller than the average electron Larmor frequency, such that the thermal equilibrium density matrix is well approximated by

$$\hat{\rho}_{\mathrm{th}} = Z_0^{-1} \mathrm{e}^{-\beta \hat{H}_{\mathrm{Z}}} = \frac{1}{2^N} \Pi_j (1 - 2p_{\mathrm{e}} \hat{S}_{jz}), \tag{2.3}$$

where Z_0 is the partition function, $\hat{H}_{\mathrm{Z}}$ is the electron Zeeman Hamiltonian, $\hat{S}_{jz}$ is the z-component of the electron spin operator, j is the electron index and ω_{S} is the electron Larmor frequency [44]. $\hat{\rho}_{\mathrm{th}}$ is diagonal in the Zeeman frame and is therefore invariant under rotation by the microwave term (this will be discussed shortly).

2.1.3 Superoperators

Superoperators act on an operator $\hat{X}$ and transform it into a new operator. $\hat{X}$ can be the density matrix or any other operator, such as the electron spin operator $\hat{S}$ or the nuclear spin operator $\hat{I}$. All linear superoperators can be written in the form

$$\hat{\hat{O}}[\hat{X}] = \sum_j \hat{K}_j \hat{X} \hat{K}_j^{\dagger}, \tag{2.4}$$

where the Kraus operators $\hat{K}_j$ are linear operators that satisfy

$$\sum_j \hat{K}_j^{\dagger} \hat{K}_j = \mathbb{1}. \tag{2.5}$$

EQ. 2.4 is the Kraus decomposition of a superoperator, and can be applied to any superoperator that preserves the physicality of a density operator. A physical density operator is one that is Hermitian, has trace 1, and has no negative eigenvalues. Combined, these three properties ensure that when a measurement is made on a system, the eigenvalues are real, and the probabilities for all possible measurement outcomes sum to one with no negative probabilities.

It is convenient now to make some notes on notation. Superoperators are denoted by a double hat ($\hat{\hat{\ }}$), and once defined will be referred to by their symbol. For example,

after defining $\hat{\hat{O}}[\hat{X}]$ in EQ. 2.4, it would be referred to simply as $\hat{\hat{O}}$. The dagger (†) is used to denote a Hermitian conjugate. The Hermitian conjugate of an operator is simply its complex conjugate transpose. The dash ($'$) is used to show that an operator or state has changed from some state $\hat{X}$ to some new state $\hat{X}'$. When applied to spin indices, the prime denotes different spins of the same type. Finally, it is implied that the dimensions of operators always match. In EQ. 2.5 for example, this means that the identity matrix $\mathbb{1}$ has the same dimensions as the Kraus operators $\hat{K}_j$. The spin operators $\hat{S}$ and $\hat{I}$ must too have the dimensions of the system and are formed by taking the tensor products of the spin-1/2 Pauli matrices with the identity matrix. For example, in a 3-spin system, if σ_z is the 2×2 Pauli matrix, then

$$\hat{S}_{1z} = \sigma_z \otimes \mathbb{1} \otimes \mathbb{1}, \quad \hat{S}_{2z} = \mathbb{1} \otimes \sigma_z \otimes \mathbb{1}, \quad \hat{S}_{3z} = \mathbb{1} \otimes \mathbb{1} \otimes \sigma_z.$$

2.1.4 Markovian Evolution

The density matrix equivalent of the Schrödinger equation is the Liouville-von Neumann (LvN) equation [33]

$$\frac{\partial}{\partial t}\hat{\rho} = -i[\hat{H}, \hat{\rho}]. \tag{2.6}$$

For the evolution of EQ. 2.6 to take a form analogous to the Schrödinger equation, the state $\hat{\rho}(t+\delta t)$, where δt is a short time interval, must depend on the state of the system no earlier than immediately before ($\hat{\rho}(t)$), and its evolution must be independent of the state of the environment. When these conditions are met, evolution is Markovian [40]. There are several aspects of Markovian evolution that are useful when studying complex systems. One such aspect is that information flow is unidirectional, namely from the system to the environment. This means that the evolution of the system depends on *its* reduced state only [ii]. Another is that in many cases, if unidirectionality is to hold, there must be a clear separation of time scales between the system and the

[ii] The reduced state of the system is the state for which it is possible to calculate the value of observables acting on the system only, i.e. the properties of the system that can be measured ignoring the environment.

environment. If τ_S and τ_E are the evolution time scales of the system and environment respectively, and τ_D is the time scale of dissipation in the system due to its interaction with the environment, then if

$$\tau_D \gg \tau_S \gg \tau_E, \tag{2.7}$$

Markovian evolution applies [33]. The latter half of EQ. 2.7 states that if the environment evolves much faster than the system, it quickly 'forgets' any information acquired from it and is therefore unlikely to feed it back (one-way flow of information). This is the "Markovian approximation" and is effectively a coarse-graining of the dynamics – terms in the Hamiltonian oscillating at $\omega > 1/\tau_S$ are filtered out. Such coarse-graining becomes useful when the dynamics of interest (τ_D in this case) are slow compared to the dynamics of the system.

EQ. 2.6 forms the basis of the "master equation" that will be used to describe the DNP dynamics. However, in its current form it describes the unitary (reversible) evolution of a closed quantum system, whereas the DNP master equation requires an open quantum system description that can account for the irreversible dynamics caused by the system-environment coupling. This is achieved by adding a dissipative part to the LvN equation.

2.1.5 The Markovian Master Equation in Lindblad Form

If the evolution of the system is Markovian (does not depend on the state of the environment or any state but the present state) and can therefore be expressed in the form of EQ. 2.6, and if there exists a physical operator (which can therefore be represented by a Kraus decomposition) that transforms $\hat{\rho}(t)$ into $\hat{\rho}(t + \delta t)$, then the evolution is described by EQ. 2.8:

$$\dot{\hat{\rho}} = -i[\hat{H}, \hat{\rho}] + \hat{\hat{\mathcal{D}}}_{TOT}\hat{\rho}, \tag{2.8}$$

where $\hat{H}$ is the Hamiltonian of the system only and does not take into account the

environment or interactions with it, and $\hat{\hat{\mathcal{D}}}_{\mathrm{TOT}}$ is the dissipative term accounting for irreversible dynamics such as relaxation.

The simplest thermal relaxation model is based on random field fluctuations that disturb a spin's immediate environment. In this simple model only single-spin jump operators are used that either drive the system back to thermal equilibrium (longitudinal relaxation) or cause decoherence of the spins (transverse relaxation). In this model, the dissipative part of EQ. 2.8 takes the form [29]

$$\begin{aligned}\hat{\hat{\mathcal{D}}}_{\mathrm{TOT}} = &\sum_j \left[\frac{R_{1\mathrm{e}}}{2}\left((1-p_{\mathrm{th}})\hat{\hat{\mathcal{D}}}[\hat{S}_{j+}] + (1+p_{\mathrm{th}})\hat{\hat{\mathcal{D}}}[\hat{S}_{j-}]\right) + 2R_{2\mathrm{e}}\hat{\hat{\mathcal{D}}}[\hat{S}_{jz}]\right]... \\ &+ \sum_k \left[\frac{R_{1\mathrm{n}}}{2}\left(\hat{\hat{\mathcal{D}}}[\hat{I}_{k+}] + \hat{\hat{\mathcal{D}}}[\hat{I}_{k-}]\right) + 2R_{2\mathrm{n}}\hat{\hat{\mathcal{D}}}[\hat{I}_{kz}]\right],\end{aligned} \tag{2.9}$$

where [33]

$$\hat{\hat{\mathcal{D}}}[\hat{L}_k]\hat{\rho} = \hat{L}_k\hat{\rho}\hat{L}_k^\dagger - \frac{1}{2}(\hat{L}_k^\dagger\hat{L}_k\hat{\rho} + \hat{\rho}\hat{L}_k^\dagger\hat{L}_k). \tag{2.10}$$

p_{th} is the electrons' thermal polarisation, $R_{1\mathrm{e}}$ & $R_{1\mathrm{n}}$ are the electron and nuclear longitudinal relaxation rates respectively, and $R_{2\mathrm{e}}$ & $R_{2\mathrm{n}}$ their transverse rates respectively. $\hat{L}_k$ are the Lindblad jump operators causing instantaneous jumps between eigenstates of the system. By inspection, it is evident that it is these jump operators that give rise to the irreversible dynamics absent in EQ. 2.6. $\hat{L}_k$ have the form $\hat{L}_k = \sqrt{\Gamma_k}\hat{X}$, where Γ_k is the flip rate for each $\hat{L}_k$ and $\hat{X}$ is some operator. In the context of DNP, $\hat{L}_k$ describe jumps caused by relaxation mechanisms, and their associated rates are accordingly dependent on the electron and nuclear relaxation rates. The superoperator $\hat{\hat{\mathcal{D}}}_{\mathrm{TOT}}$ will frequently be referred to as the dissipator.

A lot can be learned from EQ. 2.9 about the relaxation dynamics of the system. The longitudinal rates for example are seen to be associated with the spin operators $\hat{S}_\pm$ and $\hat{I}_\pm$, which cause transitions between the eigenstates of the system, thereby engendering longitudinal relaxation. Furthermore, the electron longitudinal flip rate

is weighted by the electron thermal polarisation. This creates an imbalance in the flip up and flip down rates that is crucial for the DNP mechanism, as it ensures that the electrons relax to their thermal state, and are thus able to polarise multiple nuclei. The transverse rates on the other hand are associated with Zeeman operators $\hat{S}_z$ and $\hat{I}_z$, which shift energy levels in the system. This causes decoherence of the spins in the transverse plane as they no longer all precess at the same Larmor frequency. In its current form, EQ. 2.9 simply describes relaxation of the system back to a thermal equilibrium where the nuclear polarisation is negligible.

2.1.6 Lindblad Propagator

The most robust method for evaluating the evolution of the density operator under the action of relaxation is to take the entire system from Hilbert space into Liouville space. However, in doing so the exponential scaling problem of the matrix dimensions is exacerbated, and treatment of large spin systems becomes impossible unless approximations can be made to reduce the Liouville state space. Kuprov et al. showed in 2007 that such a Liouville state space restriction is viable [45]. Others [22, 23, 30] have opted to perform calculations in Hilbert space.

EQ. 2.8 is difficult to analyse as the density operator is both left- and right- multiplied by operators. However, in Liouville space the master equation can be reformulated such that a single superoperator acts on the density matrix from the left [46]. For reasons that will become clear shortly, this process is sometimes referred to as vec-ing [47]:

$$\frac{\partial}{\partial t}\hat{\vec{\rho}} = \hat{\hat{\mathcal{L}}}_{\mathrm{H+D}}\hat{\vec{\rho}}, \tag{2.11}$$

where $\hat{\hat{\mathcal{L}}}_{\mathrm{H+D}} = \hat{\hat{\mathcal{L}}}_{\mathrm{H}} + \hat{\hat{\mathcal{L}}}_{\mathrm{D}}$ and $\hat{\hat{\mathcal{L}}}_{\mathrm{H}}$ & $\hat{\hat{\mathcal{L}}}_{\mathrm{D}}$ are given by

$$\begin{aligned}
\hat{\hat{\mathcal{L}}}_{\mathrm{H}} &= -i(\mathbb{1} \otimes \hat{H} - \hat{H}^{\mathrm{T}} \otimes \mathbb{1}) \\
\hat{\hat{\mathcal{L}}}_{\mathrm{D}} &= \sum_k \gamma_k \big((\hat{L}_k^{\dagger})^{\mathrm{T}} \otimes \hat{L}_k - \frac{1}{2}\mathbb{1} \otimes \hat{L}_k^{\dagger}\hat{L}_k - \frac{1}{2}(\hat{L}_k^{\dagger}\hat{L}_k)^{\mathrm{T}} \otimes \mathbb{1} \big).
\end{aligned}$$

$\hat{\hat{\mathcal{L}}}_{\mathrm{H}}$, sometimes referred to as the Liouville superoperator, describes the unitary dynamics engendered by the Hamiltonian, while $\hat{\hat{\mathcal{L}}}_{\mathrm{D}}$ describes the non-unitary dynamics caused by dissipation. The rates γ_k are positive and are the coefficients of the dissipators in EQ. 2.9.

In the form of EQ. 2.11, solving for the density matrix becomes trivial:

$$\hat{\vec{\rho}}(t) = \mathrm{e}^{-i\hat{\hat{\mathcal{L}}}_{\mathrm{H+D}}t}\hat{\vec{\rho}}(0).$$

It is important to note that the density matrices are now column-stacked vectors (akin to state vectors in the Schrödinger equation) and have dimension $4^N \times 1$. Thus, while the dimension of the state space remains $2^N \times 2^N$, the size of the matrices acting on the density operator increases to $4^N \times 4^N$.

2.2 The Cross Effect Hamiltonian

In this section the CE Hamiltonian is discussed in some detail. Although the discussion only explicitly addresses the static case, it is understood that it applies for the MAS case as well, the only difference being that the interaction terms acquire a time dependence. However, it is erroneous to believe that simply because the Hamiltonians are the same, the mechanisms leading to DNP are the same. The static and MAS DNP cases are in fact very different, as will become apparent in later chapters.

2.2.1 Lab and Rotating Frame Hamiltonians

The general form of the lab frame CE Hamiltonian is [29]

$$\hat{H} = \hat{H}_{\mathrm{Z}} + \hat{H}_{\mathrm{SS}} + \hat{H}_{\mathrm{II}} + \hat{H}_{\mathrm{IS}} + \hat{H}_{\mu\mathrm{w}},$$

where $\hat{H}_{\mathrm{Z}}$ is the Zeeman Hamiltonian, $\hat{H}_{\mathrm{SS}}$ is the electron dipolar interaction Hamiltonian, $\hat{H}_{\mathrm{II}}$ is the nuclear dipolar interaction Hamiltonian, $\hat{H}_{\mathrm{IS}}$ is the hyperfine in-

teraction (hfi) Hamiltonian describing interactions between electrons and nuclei, and finally $\hat{H}_{\mu\mathrm{w}}$ is the microwave irradiation Hamiltonian.

Zeeman Hamiltonian

The Zeeman Hamiltonian is given by

$$\hat{H}_{\mathrm{Z}} = \omega_{\mathrm{S}_1}\hat{S}_{1z} + \omega_{\mathrm{S}_2}\hat{S}_{2z} + \omega_{\mathrm{I}}\sum_k \hat{I}_{kz},$$

where ω_{I} is the nuclear Larmor frequency. It represents the coupling between the spins and B_0 and is by far the strongest interaction in the DNP Hamiltonian. This large disparity between the Zeeman term and the remaining terms in $\hat{H}$ has the useful consequence that many interactions can be neglected in comparison to $\hat{H}_{\mathrm{Z}}$, or viewed simply as perturbations to it. An immediate application of this is to the dipolar interaction Hamiltonians $\hat{H}_{\mathrm{SS}}$ and $\hat{H}_{\mathrm{II}}$, which are greatly simplified.

Dipolar Interaction Hamiltonians

The dipolar interaction Hamiltonians describe the interaction between spins of the same type. In the lab frame, their full form is given by the "dipolar alphabet" [48], shown here in terms of the nuclear spins (for the electrons, the nuclear spin operators are replaced with the electron spin operators and the nuclear gyromagnetic ratio with that for electrons)

$$\hat{H}_{\mathrm{II}} = \sum_{k<k'} \frac{\mu_0}{4\pi}\frac{\hbar^2\gamma_{\mathrm{I}}^2}{r^3}\big(\hat{A}+\hat{B}+\hat{C}+\hat{D}+\hat{E}+\hat{F}\big),$$

where μ_0 is the permeability of free space and r is the separation between the interacting spins. The terms $\hat{A}$ to $\hat{F}$ are given by:

- $\hat{A} = (1-3\cos^2\theta)\hat{I}_{kz}\hat{I}_{k'z}$,
- $\hat{B} = -\frac{1}{4}(1-3\cos^2\theta)(\hat{I}_{k+}\hat{I}_{k'-} + \hat{I}_{k-}\hat{I}_{k'+})$,
- $\hat{C} = \hat{D}^* = -\frac{3}{2}\sin\theta\cos\theta\mathrm{e}^{-i\phi}(\hat{I}_{kz}\hat{I}_{k'+} + \hat{I}_{k+}\hat{I}_{k'z})$,

- $\hat{E} = -\frac{3}{4}\sin^2\theta \mathrm{e}^{-i2\phi}\hat{I}_{k+}\hat{I}_{k'+}$,
- $\hat{F} = -\frac{3}{4}\sin^2\theta \mathrm{e}^{i2\phi}\hat{I}_{k-}\hat{I}_{k'-}$,

where θ is the angle between an external magnetic field and the vector joining the interacting spins, and ϕ is its azimuthal angle. In its entirety, the dipolar alphabet encodes the mutual orientation of the two spins, and all terms must be taken into account in the absence of a strong magnetic field. However, since in NMR B_0 is generally strong and therefore the Zeeman interaction large compared to all other interactions, it is possible to truncate the dipolar alphabet and instead use the "secular approximation". For homonuclear spins, $\hat{A}$ and $\hat{B}$ commute with the Zeeman Hamiltonian. $\hat{C}$ to $\hat{F}$ on the other hand do not commute and can therefore be assumed to make a negligible contribution to the dipolar Hamiltonian. In the secular approximation the dipolar Hamiltonian is

$$\hat{H}_{\mathrm{II}} = \sum_{k<k'} \frac{\mu_0}{4\pi}\frac{\hbar^2\gamma_{\mathrm{I}}^2}{2r^3}\big(2\hat{I}_{kz}\hat{I}_{k'z} - \frac{1}{2}\hat{I}_{k+}\hat{I}_{k-} - \frac{1}{2}\hat{I}_{k-}\hat{I}_{k+}\big).$$

Microwave Hamiltonian

In practice, the additional rotation introduced by the Zeeman Hamiltonian complicates treatment of the CE system in the lab frame. It is therefore customary to proceed into the microwave rotating frame to remove the time-dependent dynamics introduced by $\hat{H}_{\mu\mathrm{w}}$.

For a microwave field applied along the x-direction, proceeding into the microwave rotating frame is equivalent to a rotation about the z-axis of the form: $R_z(t) = \mathrm{e}^{-i\omega_{\mu\mathrm{w}}t\hat{S}_z}$, where $\omega_{\mu\mathrm{w}}$ is the microwave *frequency* (not to be confused with the microwave *strength* (or amplitude) ω_1) [44]. The irradiation frequency $\omega_{\mu\mathrm{w}}$ determines the detuning of the energy levels from resonance, whilst the strength determines how strongly a transition is driven. $\omega_{\mu\mathrm{w}}$ is far off-resonance from the nuclear Larmor frequency; its effect on the nuclear Zeeman interaction is therefore negligible. It is however near-resonance for the electron spins, and as a consequence detunes them. It is therefore necessary

to adjust ω_{S} in the Zeeman Hamiltonian to $\Delta = |\omega_{\mathrm{S}} - \omega_{\mu\mathrm{w}}|$.

In the rotating frame the microwave Hamiltonian goes from being time-dependent: $\hat{H}_{\mu\mathrm{w}}(t) = \frac{\omega_1}{2}\mathrm{e}^{-i\omega_{\mu\mathrm{w}}\hat{S}_z}(\hat{S}_+ + \hat{S}_-)\mathrm{e}^{i\omega_{\mu\mathrm{w}}\hat{S}_z}$, to being time-independent: $\hat{H}_{\mu\mathrm{w}} = \frac{\omega_1}{2}(\hat{S}_+ + \hat{S}_-)$, where the factor 1/2 appears if linearly polarised microwave radiation is used [29]. Terms commuting with the Zeeman Hamiltonian, such as the secular dipolar Hamiltonians, are unaffected by a transition into the microwave rotating frame. The hfi Hamiltonian on the other hand is truncated.

Hyperfine Interaction Hamiltonian

The hfi consists of the Fermi contact term, which describes the magnetic interaction between an electron and nucleus when their wave-functions overlap, and the tensor interaction $\overleftrightarrow{A}$. In general, it can be assumed that the separation between spins is large enough that the Fermi contact term can be neglected [iii]. The dipolar term on the other hand plays an integral part in the dynamics.

In the lab frame, the hfi Hamiltonian is given by

$$\hat{H}_{\mathrm{IS}} = \sum_{jk} \hat{S}_j \cdot \overleftrightarrow{A} \cdot \hat{I}_k,$$

where $\overleftrightarrow{A}$ is the hfi tensor. In the microwave rotating frame, terms in the tensor product that that do not commute with $\hat{S}_z$ acquire an oscillatory $\omega_{\mu\mathrm{w}}$ time dependence that causes them to average out. $\hat{H}_{\mathrm{IS}}$ therefore becomes

$$\hat{H}_{\mathrm{IS}} = \sum_{jk}(A_{jk}\hat{I}_{kz} + B_{jk+}\hat{I}_{k+} + B_{jk-}\hat{I}_{k-})\hat{S}_{jz},$$

where $j = 1, 2$ is the electron index, k is the nuclear index, and A_{jk} & $B_{jk\pm}$ are the secular and pseudo-secular hfi strengths respectively.

[iii] An important exception to this is the delocalisation of an electron over the oxygen-nitrogen bond in nitroxide radicals. This is a specific case and will be discussed later in the thesis.

Rotating Frame Hamiltonian

The complete Hamiltonian in the microwave rotating frame is thus given by [29]

$$\begin{aligned}\hat{H} = &\Delta_1\hat{S}_{1z} + \Delta_2\hat{S}_{2z} + \omega_{\mathrm{I}}\sum_k \hat{I}_{kz}... \\ &+ D(2\hat{S}_{1z}\hat{S}_{2z} - \frac{1}{2}\hat{S}_{1+}\hat{S}_{2-} - \frac{1}{2}\hat{S}_{1-}\hat{S}_{2+})... \\ &+ \sum_{k<k'} d_{kk'}(2\hat{I}_{kz}\hat{I}_{k'z} - \frac{1}{2}\hat{I}_{k+}\hat{I}_{k'-} - \frac{1}{2}I_{k-}I_{k'+})... \\ &+ \sum_{jk}(A_{jk}\hat{I}_{kz} + \frac{B_{jk+}}{2}\hat{I}_{k+} + \frac{B_{jk-}}{2}\hat{I}_{k-})\hat{S}_{jz}... \\ &+ \sum_j \frac{\omega_1}{2}(\hat{S}_{j+} + \hat{S}_{j-}),\end{aligned} \tag{2.12}$$

where $\Delta_{1,2}$ are offsets of the electron Larmor frequency from the microwave irradiation, and D & $d_{kk'}$ are the electron and nuclear dipolar interaction strengths. Note that the x and y spin operators have been replaced by the relevant raising and lowering ($\pm$) operators to give a more intuitive picture of the flip-flop dynamics. For the static case in the Zeeman eigenbasis, the pseudo-secular hfi and flip-flop terms of the electron dipolar interaction are off-diagonal and responsible for mediating polarisation transfer from electrons to nuclei.

2.2.2 Interaction Parameters

It is instructive to know the specific forms of the interaction parameters, as these will be used recurrently throughout the next few chapters. In all cases the angle θ is the angle between the static field vector (conventionally along z) and the vector joining the two interacting spins, and r is the magnitude of this vector. The point-dipole approximation has been used since it is assumed that the separation between spins is much larger than the size of the spins themselves.

The dipolar interaction terms D for electrons and $d_{kk'}$ for nuclei are

$$D = \frac{\mu_0}{4\pi}\frac{\hbar^2\gamma_{\mathrm{S}}^2}{2r^3}(1 - 3\cos^2\theta), \tag{2.13}$$

where μ_0 is the permeability of free space, and for $d_{kk'}$ the nuclear gyromagnetic ratio γ_{I} is used instead of the electron gyromagnetic ratio γ_{S}.

The secular hfi A_{jk} has a similar form

$$A_{jk} = \frac{\mu_0}{4\pi}\frac{\hbar^2\gamma_j\gamma_k}{2r^3}(1 - 3\cos^2\theta), \tag{2.14}$$

but with heterogeneous gyromagnetic ratios.

Finally, the pseudo-secular hfi is given by

$$B_{jk+} = \frac{\mu_0}{4\pi}\frac{\hbar^2\gamma_j\gamma_k}{2r^3}(3\sin\theta\cos\theta\mathrm{e}^{-i\phi}), \tag{2.15}$$

where ϕ is the azimuthal angle to the magnetic field. In general only the magnitude of B_{jk} is of interest however, which is independent of ϕ. Therefore, $B_{jk\pm}$ can be replaced with B_{jk}.

2.2.3 Polarisation

The polarisation p of the system is calculated by taking the trace of the density operator $\hat{\rho}$ with the Zeeman operators $\hat{I}_{kz}$ or $\hat{S}_{jz}$ at each point in time [44]:

$$p_{\mathrm{S}_j} = \mathrm{Tr}(\hat{\rho}\hat{S}_{jz}), \qquad p_{\mathrm{I}_k} = \mathrm{Tr}(\hat{\rho}\hat{I}_{kz}).$$

2.3 Adiabatic Elimination

Adiabatic elimination is a standard and powerful tool used in many areas of quantum physics [49]. It is of use when interactions with an environment or an external driving

field are such that off-resonance dynamics do not affect the dynamics of the system. As with other techniques, such as the derivation of the master equation in Section 2.1.4, adiabatic elimination relies on a clear separation of time scales between the slow-evolving subspace of interest and much faster-evolving subspaces. This enables the derivation of an effective Hamiltonian closed in the low-energy subspace, which is often more likely to be accessible and controllable experimentally [49]. This effective Hamiltonian incorporates only the *effect* of the coupling to states with much higher energy. Any excess of information is eliminated adiabatically, or in other words, without affecting the system. The elimination procedure follows from the adiabatic theorem posited by Born and Fock in 1928 which states that, if the perturbation on a system prepared in a particular eigenstate acts slowly enough, and if there is a clear gap between the eigenvalue of that state and the rest of the Hamiltonian spectrum, the system will remain in this instantaneous eigenstate [50]. Thus, if the change caused by the perturbation is slow, the change in shape of the eigenfunctions is slow and does not trigger quantum jumps. The populations of eigenstates therefore remain constant, even though the eigenstates themselves have changed.

Adiabatic elimination plays an important role in the derivation of the static CE kinetic Monte Carlo algorithm, playing the dual role of reducing the state space significantly and producing effective dynamics that can be modelled using a classical approach. It will be shown in a later section that the classical approach has enormous computational gain. In this section the adiabatic elimination procedure is outlined in general terms, with some comments on the specifics of the static CE case.

2.3.1 Coherence Subspaces

For a system of N spins, there are $2N+1$ coherence subspaces ranging from $-N$ to N: $\mathfrak{L} = \{\mathfrak{L}_{-N}, \mathfrak{L}_{-N+1}, ...\mathfrak{L}_0, ..., \mathfrak{L}_{N-1}, \mathfrak{L}_N\}$. These individual subspaces are composed of the spin operators and correspond to combinations of up and down spin flips. Each coherence order subspace can additionally be separated into spin orders as shown in TAB. 2.1. The coherence order is determined by the net flips or flops and the spin

order by the number of spins involved.

Coherence / **Spin**	0	1	2
0	$\mathbb{1}$	-	-
1	$\hat{I}_{kz}$ & $\hat{S}_{jz}$	$\hat{I}_{k\pm}$ & $\hat{S}_{j\pm}$	-
2	$\hat{I}_{kz}\hat{S}_{jz}$, $\hat{S}_{jz}\hat{I}_{kz}$	$\hat{S}_{j\pm}\hat{I}_{kz}$, $\hat{I}_{kz}\hat{S}_{j\pm}$	$\hat{S}_{j\pm}\hat{I}_{k\pm}$, $\hat{S}_{j\pm}\hat{I}_{k\pm}$
	$\hat{S}_{j\pm}\hat{I}_{k\mp}$, $\hat{I}_{k\pm}\hat{S}_{j\mp}$	$\hat{S}_{jz}\hat{I}_{k\pm}$, $\hat{I}_{k\pm}\hat{S}_{jz}$	$\hat{S}_{j\pm}\hat{S}_{j'\pm}$
	$\hat{I}_{k\pm}\hat{I}_{k'\mp}$	$\hat{S}_{j\pm}\hat{S}_{j'z}$	$\hat{I}_{k\pm}\hat{I}_{k'\pm}$
	$\hat{S}_{j\pm}\hat{S}_{j'\mp}$	$\hat{I}_{k\pm}\hat{I}_{k'z}$	

Table 2.1: First three coherence and spin orders.

In this thesis, the goal of the adiabatic elimination is to produce an effective Hamiltonian closed in the zero coherence subspace. This subspace can itself be truncated at the fourth spin order [27].

2.3.2 Nakajima-Zwanzig Projection Operators

Projections onto the relevant subspace are performed using the Nakajima-Zwanzig [51, 52] projection operators $\hat{\mathcal{P}}$ and $\hat{\mathcal{Q}}$, where $\hat{\mathcal{P}}$ projects onto the subspace of interest, and $\hat{\mathcal{Q}}$ projects onto the complementary subspace. By definition, the sum of the two projection operators must encompass the entire state space, i.e. $\hat{\mathcal{P}} + \hat{\mathcal{Q}} = \mathbb{1}$.

When two systems are in an entangled state, it is no longer possible to separate state vectors for each system. It is therefore no longer possible to predict the expectation values of observables of just one of the systems, just of the combined system. By tracing over the environment (i.e. the complementary subspace), it is possible to 'remove' it from the compound system. This enables the measurement of observables acting solely on the system of interest, ignoring the environment. The expectation value of any observable $\hat{O}$ in the system is then given by the trace of the reduced state of the system: $\langle\hat{O}\rangle = \mathrm{Tr}(\hat{O}\hat{\rho}_{\mathrm{S}})$. In the Nakajima-Zwanzig procedure, the operation of

tracing over the environment is viewed as a formal projection $\hat{\rho} \mapsto \hat{\mathcal{P}}\hat{\rho}$, where $\hat{\mathcal{P}}\hat{\rho}$ is the relevant part of the density matrix.

Separation of State Spaces

Consider a slow-evolving system ($\hat{\rho}_{\mathrm{S}} = \hat{\mathcal{P}}\hat{\rho}$) entangled with a rapidly fluctuating environment ($\hat{\rho}_{\mathrm{E}} = \hat{\mathcal{Q}}\hat{\rho}$), where $\hat{\rho}$ is the state of the composite system. The aim is to find a map $\hat{\rho} \mapsto \hat{\mathcal{P}}\hat{\rho}$ where $\hat{\mathcal{P}}\hat{\rho} = \mathrm{Tr}_{\mathrm{E}}(\hat{\rho}) \otimes \hat{\rho}_{\mathrm{E}} \equiv \hat{\rho}_{\mathrm{S}} \otimes \hat{\rho}_{\mathrm{E}}$.

It can be shown (REF. [49]) that the LvN equation (EQ. 2.6) can be written in the form

$$\begin{bmatrix} \dot{\hat{\rho}}_{\mathrm{S}} \\ \dot{\hat{\rho}}_{\mathrm{E}} \end{bmatrix} = \begin{bmatrix} \hat{\mathcal{P}}\hat{\hat{\mathcal{L}}}_{\mathrm{H}}\hat{\mathcal{P}} & \hat{\mathcal{P}}\hat{\hat{\mathcal{L}}}_{\mathrm{H}}\hat{\mathcal{Q}} \\ \hat{\mathcal{Q}}\hat{\hat{\mathcal{L}}}_{\mathrm{H}}\hat{\mathcal{P}} & \hat{\mathcal{Q}}\hat{\hat{\mathcal{L}}}_{\mathrm{H}}\hat{\mathcal{Q}} \end{bmatrix} \begin{bmatrix} \hat{\rho}_{\mathrm{S}} \\ \hat{\rho}_{\mathrm{E}} \end{bmatrix} \equiv \begin{bmatrix} \hat{\hat{\mathcal{L}}}_{\mathrm{SS}} & \hat{\hat{\mathcal{L}}}_{\mathrm{SE}} \\ \hat{\hat{\mathcal{L}}}_{\mathrm{ES}} & \hat{\hat{\mathcal{L}}}_{\mathrm{EE}} \end{bmatrix} \begin{bmatrix} \hat{\rho}_{\mathrm{S}} \\ \hat{\rho}_{\mathrm{E}} \end{bmatrix} \tag{2.16}$$

(remembering that $\hat{\hat{\mathcal{L}}}_{\mathrm{H}} = -i[\hat{H}, \hat{\rho}]$). The subscript H will henceforth be dropped for clarity purposes. Furthermore, $\hat{\rho}_{\mathrm{S}}$ and $\hat{\rho}_{\mathrm{E}}$ are both understood to be time dependent. EQ. 2.16 is the Nakajima-Zwanzig equation and can be seen as a generalisation of the master equation [33].

Evolution of the system is described by operators of the form $\hat{\mathcal{P}}\hat{\hat{\mathcal{L}}}$, which either leave dynamics in the subspace of the system (if followed by $\hat{\mathcal{P}}$) or project dynamics from the environment onto the system (if followed by $\hat{\mathcal{Q}}$). The converse is true for the evolution of the environment. $\hat{\mathcal{P}}\hat{\hat{\mathcal{L}}}\hat{\mathcal{P}}$ can act only on $\hat{\rho}_{\mathrm{S}}$ (as it keeps evolution within that subspace), and $\hat{\mathcal{P}}\hat{\hat{\mathcal{L}}}\hat{\mathcal{Q}}$ can act only on $\hat{\rho}_{\mathrm{E}}$ (as it projects dynamics from the environment onto the system), and the converse for the environment. Diagonal terms of EQ. 2.16 are constant, whereas off-diagonal terms represent time dependent interactions between the subspaces.

The condition for adiabatic elimination is that the environment evolves much faster than the system, and can therefore be assumed to have reached the steady state before the system 'sees' it. This is true if the equality

$$||\hat{\hat{\mathcal{L}}}_{\mathrm{ES}}|| \cdot ||\hat{\hat{\mathcal{L}}}_{\mathrm{SE}}|| \ll ||\hat{\hat{\mathcal{L}}}_{\mathrm{EE}}||^2 \tag{2.17}$$

holds [29]. The system sees of the environment only what the crossover projectors $\hat{\hat{\mathcal{L}}}_{\mathrm{ES}}$ and $\hat{\hat{\mathcal{L}}}_{\mathrm{SE}}$ communicate to it. If these are themselves much slower than the environment, it is impossible for them to convey all of the environment dynamics to the system.

2.3.3 Steady State Solution for the Environment

The equation of motion of the environment ($\dot{\hat{\rho}}_{\mathrm{E}} = \hat{\hat{\mathcal{L}}}_{\mathrm{ES}}\hat{\rho}_{\mathrm{S}} + \hat{\hat{\mathcal{L}}}_{\mathrm{EE}}\hat{\rho}_{\mathrm{E}}$) looks like an inhomogeneous linear differential equation with constant coefficient (since $\hat{\hat{\mathcal{L}}}_{\mathrm{EE}}$ is constant). This has a known solution

$$\hat{\rho}_{\mathrm{E}} = \mathrm{e}^{\hat{\hat{\mathcal{L}}}_{\mathrm{EE}}t}\hat{\rho}_{\mathrm{E}}(0) + \mathrm{e}^{\hat{\hat{\mathcal{L}}}_{\mathrm{EE}}t}\int_0^t \mathrm{e}^{-\hat{\hat{\mathcal{L}}}_{\mathrm{EE}}\tau}\hat{\hat{\mathcal{L}}}_{\mathrm{ES}}\hat{\rho}_{\mathrm{S}}(\tau)d\tau. \tag{2.18}$$

Dynamics are assumed to start in the system, so the first term in EQ. 2.18 is zero. Furthermore, since $\hat{\hat{\mathcal{L}}}_{\mathrm{EE}}$ is time-independent, $\mathrm{e}^{\hat{\hat{\mathcal{L}}}_{\mathrm{EE}}t}$ can be taken into the integral

$$\hat{\rho}_{\mathrm{E}} = \int_0^t \mathrm{e}^{\hat{\hat{\mathcal{L}}}_{\mathrm{EE}}(t-\tau)}\hat{\hat{\mathcal{L}}}_{\mathrm{ES}}\hat{\rho}_S(\tau)d\tau, \tag{2.19}$$

where normal exponent rules apply since $\hat{\hat{\mathcal{L}}}_{\mathrm{EE}}$ commutes with itself.

Next, the variable transformation $\tau' = t - \tau$, $d\tau' = -d\tau$ is applied to EQ. 2.19:

$$\hat{\rho}_{\mathrm{E}} = \int_0^t \mathrm{e}^{\hat{\hat{\mathcal{L}}}_{\mathrm{EE}}\tau'}\hat{\hat{\mathcal{L}}}_{\mathrm{ES}}\hat{\rho}_{\mathrm{S}}(t-\tau')d\tau'. \tag{2.20}$$

In the steady state limit ($t \to \infty$, $\tau' \to 0$) the reduced state of the system becomes independent of τ' and can be taken out of the integral. This can be shown using the Taylor series expansion of $\hat{\rho}_{\mathrm{S}}(t-\tau')$:

$$\hat{\rho}_{\mathrm{S}}(t-\tau') = \hat{\rho}_{\mathrm{S}}(t) + \sum_{n=0}^{\infty}\frac{\hat{\rho}_{\mathrm{S}}(t)^{(n)}}{n!}(t-\tau')^n. \tag{2.21}$$

In the long-time limit, the derivatives all go to zero since $\hat{\rho}_{\mathrm{S}}$ approaches the steady

state, such that $\hat{\rho}_{\mathrm{S}}(t-\tau') \to \hat{\rho}_{\mathrm{S}}(t)$. The term $\hat{\hat{\mathcal{L}}}_{\mathrm{ES}}\hat{\rho}_{\mathrm{S}}(t)$ can therefore be taken out of the integral, which is now easy to solve:

$$\hat{\rho}_{\mathrm{E}} = \hat{\hat{\mathcal{L}}}_{\mathrm{EE}}^{-1} \mathrm{e}^{\hat{\hat{\mathcal{L}}}_{\mathrm{EE}}\tau'}\Big|_0^{\infty} \hat{\hat{\mathcal{L}}}_{\mathrm{ES}}\hat{\rho}_{\mathrm{S}}(t) = -\hat{\hat{\mathcal{L}}}_{\mathrm{EE}}^{-1}\hat{\hat{\mathcal{L}}}_{\mathrm{ES}}\hat{\rho}_{\mathrm{S}}(t), \tag{2.22}$$

where it has been assumed that the eigenvalues of $\hat{\hat{\mathcal{L}}}_{\mathrm{EE}}$ have negative real parts that quickly cause the environment dynamics to reach their steady state.

Since it is assumed that all the system ever perceives of the environment is its steady state, EQ. 2.22 can be substituted into the equation of motion of the system:

$$\dot{\hat{\rho}}_{\mathrm{S}} = \hat{\hat{\mathcal{L}}}_{\mathrm{SS}}\hat{\rho}_{\mathrm{S}} - \hat{\hat{\mathcal{L}}}_{\mathrm{SE}}\hat{\hat{\mathcal{L}}}_{\mathrm{EE}}^{-1}\hat{\hat{\mathcal{L}}}_{\mathrm{ES}}\hat{\rho}_{\mathrm{S}}. \tag{2.23}$$

In EQ. 2.23 the environment has been eliminated (i.e. traced over), and in its place is a term that describes the effect of the dynamics of the environment on the dynamics of the system. An intuitive way to see this by examining the action of the operators: the second term is now a projection of the steady state dynamics of $\hat{\rho}_{\mathrm{E}}$ onto the subspace of the system by $\hat{\hat{\mathcal{L}}}_{\mathrm{SE}}$. Again, a central assumption of EQ. 2.23 is that the environment evolves so fast compared to the system that it reaches the steady state before the system sees it. Otherwise, it could not be adiabatically eliminated.

Kernel Function

The triple product in EQ. 2.23 can also be written in terms of the kernel function $\hat{\hat{K}}(t-\tau)$, known as the "memory function", which describes the effect of the dynamics in the environment on the dynamics of the system. Describing the system using the kernel function has practical applications that will become clear in the next section.

Starting from the equation of motion of the system in EQ. 2.16 with $\hat{\rho}_{\mathrm{E}}$ replaced by EQ. 2.19, and moving $\hat{\hat{\mathcal{L}}}_{\mathrm{SE}}$ into the integral, the equation of motion of the system is given by

$$\dot{\hat{\rho}}_{\mathrm{S}} = \hat{\hat{\mathcal{L}}}_{\mathrm{SS}}\hat{\rho}_{\mathrm{S}} + \int_0^t \hat{\hat{\mathcal{L}}}_{\mathrm{SE}} \mathrm{e}^{\hat{\hat{\mathcal{L}}}_{\mathrm{SS}}(t-\tau)} \hat{\hat{\mathcal{L}}}_{\mathrm{ES}}\hat{\rho}_{\mathrm{S}} d\tau. \tag{2.24}$$

The triple product in the integrand can be defined as the kernel function $\hat{\hat{K}}(t-\tau)$, which simplifies the equation of motion to [51, 52]

$$\dot{\hat{\rho}}_{\mathrm{S}} = \hat{\hat{\mathcal{L}}}_{\mathrm{SS}}\hat{\rho}_{\mathrm{S}} + \int_0^t \hat{\hat{K}}(t-\tau)\hat{\rho}_{\mathrm{S}}(\tau) d\tau. \tag{2.25}$$

2.3.4 Solution for the System

The inversion of $\hat{\hat{\mathcal{L}}}_{\mathrm{SS}}$ makes solving EQ. 2.23 in the time domain difficult, if not impossible. However, particularly in the form of EQ. 2.25, it is clear that the second part of EQs. 2.23 & 2.25 looks like a convolution of two functions. With equations of this form it is common to use the Laplace transform convolution theorem, which states that the Laplace transform of a pair of functions convolved in the time domain is equal to the point-wise product of the functions in the frequency domain: $\mathcal{L}\{(f \star g)(t)\} = \mathcal{L}\{f(t)\} \cdot \mathcal{L}\{g(t)\} = F(\epsilon)G(\epsilon)$, where in this instance $\mathcal{L}\{\cdot\}$ denotes the Laplace transform. It is taken by multiplying each side of EQ. 2.25 by $\mathrm{e}^{-\epsilon t}$ and integrating over the time interval $[0, \infty]$.

In the following, the solution for the system will be found in the frequency domain; the solution in the time domain is then found by performing a simple inverse Laplace transform. Once again, the large difference in time scales between the system and environment is exploited, this time to eliminate the kernel function. The result of this section is an effective master equation for the system closed in the subspace of the system only.

The Laplace transform of the left hand side of EQ. 2.25 is found using integration by parts:

$$\int_0^\infty \mathrm{e}^{-\epsilon t}\dot{\hat{\rho}}_{\mathrm{S}}dt = \hat{\rho}_{\mathrm{S}}\mathrm{e}^{-\epsilon t}\Big|_0^\infty - \int_0^\infty -\epsilon \mathrm{e}^{-\epsilon t}\hat{\rho}_{\mathrm{S}}dt = -\hat{\rho}_{\mathrm{S}}(0) + \epsilon\int_0^\infty \mathrm{e}^{-\epsilon t}\hat{\rho}_{\mathrm{S}}(t)dt. \quad (2.26)$$

Defining the Laplace transforms $\mathcal{L}\{\hat{\rho}_{\mathrm{S}}\} = l_{\hat{\rho}_{\mathrm{S}}}(\epsilon)$ and $\mathcal{L}\{\hat{\hat{K}}(t)\} = l_{\hat{\hat{\mathrm{K}}}}(\epsilon)$, EQ. 2.26 becomes

$$\int_0^\infty \mathrm{e}^{-\epsilon t}\dot{\hat{\rho}}_{\mathrm{S}}dt = -\hat{\rho}_{\mathrm{S}}(0) + \epsilon l_{\hat{\rho}_{\mathrm{S}}}(\epsilon). \quad (2.27)$$

The right hand side of EQ. 2.25 is then

$$\hat{\hat{\mathcal{L}}}_{\mathrm{SS}}\int_0^\infty \mathrm{e}^{-\epsilon t}\hat{\rho}_{\mathrm{S}}(t)dt + \int_0^\infty\int_0^t \mathrm{e}^{-\epsilon t}\hat{\hat{K}}(t-\tau)\hat{\rho}_{\mathrm{S}}(\tau)d\tau dt = \hat{\hat{\mathcal{L}}}_{\mathrm{SS}}l_{\hat{\rho}_{\mathrm{S}}}(\epsilon) + l_{\hat{\rho}_{\mathrm{S}}}(\epsilon)\cdot l_{\hat{\hat{\mathrm{K}}}}(\epsilon), \quad (2.28)$$

where the last equality is not trivial and is proven in Appendix A.

Putting together the left & right hand sides, the equation of motion of the system in the Laplace domain is:

$$-\hat{\rho}_{\mathrm{S}}(0) + \epsilon l_{\hat{\rho}_{\mathrm{S}}}(\epsilon) = \hat{\hat{\mathcal{L}}}_{\mathrm{SS}}l_{\hat{\rho}_{\mathrm{S}}}(\epsilon) + l_{\hat{\rho}_{\mathrm{S}}}(\epsilon)\cdot l_{\hat{\hat{\mathrm{K}}}}(\epsilon). \quad (2.29)$$

Solving for the system,

$$l_{\hat{\rho}_{\mathrm{S}}}(\epsilon) = \frac{\hat{\rho}_{\mathrm{S}}(0)}{\mathbb{1}\epsilon - \hat{\hat{\mathcal{L}}}_{\mathrm{SS}} - l_{\hat{\hat{\mathrm{K}}}}(\epsilon)}, \quad (2.30)$$

were ϵ is multiplied by the identity matrix to ensure its dimensions match those of the density matrix and projection operator.

The presence of $l_{\hat{\hat{\mathrm{K}}}}(\epsilon)$ in EQ. 2.30 suggests that the solution to the equation of motion for the system at a time t depends on its history over the interval $[0, t]$. However, evolution of the DNP system is assumed to be Markovian so this cannot be the case.

In the derivation of EQ. 2.23, the large difference in time scales between the system and environment was made use of. A similar approach is taken here to eliminate the kernel function. In the time domain, the kernel function can be expressed in diagonal form as a sum of eigenfunctions $\hat{\hat{K}}_k$ with eigenvalues ϵ_k:

$$\hat{\hat{K}}(t) = \sum_k \hat{\hat{K}}_k \mathrm{e}^{\epsilon_k t}. \tag{2.31}$$

This form of the kernel function is however difficult to find, even for a 2-spin system. Nonetheless, it will be used here to find the form of $l_{\hat{\hat{\mathrm{K}}}}(\epsilon)$:

$$l_{\hat{\hat{\mathrm{K}}}}(\epsilon) = \int_0^\infty \mathrm{e}^{-\epsilon t} \hat{\hat{K}}(t) dt = \sum_k \int_0^\infty \mathrm{e}^{-\epsilon t} \hat{\hat{K}}_k \mathrm{e}^{\epsilon_k t} = \sum_k \frac{\hat{\hat{K}}_k}{\epsilon - \epsilon_k}. \tag{2.32}$$

For adiabatic elimination to be applicable, the eigenvalues of the system must be much smaller than those of the kernel function (which includes the environment and cross-over projectors). This means that from the perspective of the kernel function, the region of eigenvalues corresponding to the system is $\epsilon \approx 0$. EQ. 2.32 can therefore be expanded as a Maclaurin series

$$l_{\hat{\hat{\mathrm{K}}}}(\epsilon) \approx l_{\hat{\hat{\mathrm{K}}}}(0) + \frac{\partial l_{\hat{\hat{\mathrm{K}}}}(0)}{\partial \epsilon}\epsilon + \frac{\partial^2 l_{\hat{\hat{\mathrm{K}}}}(0)}{\partial \epsilon^2}\frac{\epsilon^2}{2}... \tag{2.33}$$

However, since $\epsilon \approx 0$, the derivatives quickly tend to zero such that

$$l_{\hat{\hat{\mathrm{K}}}}(\epsilon) \approx l_{\hat{\hat{\mathrm{K}}}}(0) = -\sum_k \frac{\hat{\hat{K}}_k}{\epsilon_k}. \tag{2.34}$$

$\epsilon = 0$ in the frequency domain is equivalent to $t = \infty$ in the time domain. The result of EQ. 2.34 is thus that, as far as the system is concerned, the memory function is always in the steady state; the system does not 'see' any of the dynamics leading to the steady state. $l_{\hat{\hat{\mathrm{K}}}}(0)$ can be rewritten as a superoperator $\hat{\hat{\mathcal{M}}}$ describing the 'history-less' effect of the environment on the system, leading the equation of motion

$$l_{\hat{\rho}_\mathrm{S}}(\epsilon) = \frac{\hat{\rho}_\mathrm{S}(0)}{\mathbb{1}\epsilon - \hat{\hat{\mathcal{L}}}_\mathrm{SS} - \hat{\hat{\mathcal{M}}}} \tag{2.35}$$

in the eigenvalue (frequency) domain.

This can easily be taken back into the time domain using the relation $F(\epsilon) = \frac{1}{\epsilon-\alpha} \rightarrow f(t) = \mathrm{e}^{\alpha t}$. The effective master equation of the system in the time domain is therefore given by

$$\hat{\rho}_{\mathrm{S}}(t) = \mathrm{e}^{(\hat{\hat{\mathcal{L}}}_{\mathrm{SS}} + \hat{\hat{\mathcal{M}}})t} \hat{\rho}_{\mathrm{S}}(0). \tag{2.36}$$

This effective form of the master equation does not contain a memory function and its propagator $\hat{\hat{\mathcal{L}}}_{\mathrm{SS}} + \hat{\hat{\mathcal{M}}}$ is time-independent. EQ. 2.36 is the adiabatic approximation to EQ. 2.25. It is fully contained in the slow-evolving subspace, which is much smaller than the full subspace, thus significantly reducing the dimension of the problem.

2.4 Krylov-Bogolyubov Method of Averaging

The Krylov-Bogolyubov averaging (KBA) method is a method for replacing the exact differential equation of motion of a system with an averaged one [53]. It is most commonly used in celestial mechanics, but can also be applied in the context of quantum mechanics to average out fast-oscillating terms of a master equation [19, 27]. The method is used in the adiabatic elimination procedure to find the inversion $\hat{\hat{\mathcal{L}}}_{\mathrm{SS}}^{-1}$. It is also used in the derivation of the MAS simulation algorithm to derive an effective 2-level Hamiltonian for the CE event.

Krylov-Bogolyubov averaging can be applied to differential equations, for example the LvN equation, if they can be written in a dimensionless form with a small proportionality constant ε introduced on the right hand side

$$\frac{d}{dt}x = \varepsilon X(\varepsilon, t, x).$$

This can be done by a transformation of variables in which the time t is replaced by a dimensionless time variable τ reflecting the slow dynamics. ε should represent how

small interactions in the system are compared to the fast-oscillating terms.

The LvN equation in terms of τ is [19]

$$\frac{d}{d\tau}\hat{\rho} = \varepsilon(\hat{\hat{\mathcal{H}}}(\tau)\hat{\rho} + \hat{\hat{\mathcal{D}}}\hat{\rho}_{\text{th}}), \tag{2.37}$$

where the superoperator $\hat{\hat{\mathcal{H}}}(\tau)$ represents the coherent part of the master equation containing the fast-oscillating terms, and the superoperator $\hat{\hat{\mathcal{D}}}$ represents the time-independent dissipative part. Both are dimensionless due to the factor ε. The aim of the Krylov-Bogolyubov averaging method is to remove the time dependence in $\hat{\hat{\mathcal{H}}}(\tau)$ by averaging it out. After the averaging procedure, the time-independent equation of motion is

$$\frac{d}{d\tau}\hat{\rho}' = \varepsilon(\hat{\hat{\mathcal{H}}}_0(\varepsilon)\hat{\rho}' + \hat{\hat{\mathcal{E}}}(\varepsilon)\hat{\hat{\mathcal{D}}}\hat{\rho}_{\text{th}}), \tag{2.38}$$

where $\hat{\rho}$ and $\hat{\rho}'$ are related by the variable transformation

$$\hat{\rho} = \hat{\hat{\mathcal{B}}}(\varepsilon,\tau)\hat{\rho}' + \varepsilon\hat{\hat{\mathcal{C}}}(\varepsilon,\tau)\hat{\hat{\mathcal{D}}}\hat{\rho}_{\text{th}}. \tag{2.39}$$

Finding the form of $\varepsilon(\hat{\hat{\mathcal{H}}}_0(\varepsilon)$ and $\hat{\hat{\mathcal{E}}}(\varepsilon)$ forms the core of the KBA procedure.

The four superoperators in EQs. 2.38 and 2.39 can be expanded in powers of the smallness factor ε

$$\begin{gathered}\hat{\hat{\mathcal{H}}}_0(\varepsilon) = \hat{\hat{\mathcal{H}}}_1 + \varepsilon\hat{\hat{\mathcal{H}}}_2 + ..., \qquad \hat{\hat{\mathcal{E}}}(\varepsilon) = \hat{\hat{\mathcal{H}}}_1 + \varepsilon\hat{\hat{\mathcal{H}}}_2 + ... \\ \hat{\hat{\mathcal{B}}}(\varepsilon,\tau) = 1 + \varepsilon\hat{\hat{\mathcal{B}}}_1(\tau) + \varepsilon^2\hat{\hat{\mathcal{B}}}_2(\tau) + ... \\ \hat{\hat{\mathcal{C}}}(\varepsilon,\tau) = \hat{\hat{\mathcal{C}}}_1(\tau) + \varepsilon\hat{\hat{\mathcal{C}}}_2(\tau) + ...,\end{gathered} \tag{2.40}$$

where $\hat{\hat{\mathcal{H}}}_0(\varepsilon)$ and $\hat{\hat{\mathcal{E}}}(\varepsilon)$ are unknown. They are found by differentiating EQ. 2.39 with respect to time and then substituting for $\frac{d}{dt}\hat{\rho}$ and $\frac{d}{dt}\hat{\rho}'$ with the right hand side of EQs. 2.37 & 2.38, using the power series expansions in EQ. 2.40. By equating terms with the same order of ε, it is then possible to derive the explicit terms of the power

series expansions of $\hat{\hat{\mathcal{H}}}_0(\varepsilon)$ and $\hat{\hat{\mathcal{E}}}(\varepsilon)$ to the desired order of accuracy.

2.5 Classical Kinetic Monte Carlo Algorithm

The possibility of using a classical kinetic Monte Carlo (kMC) algorithm to simulate the DNP dynamics after adiabatic elimination offers enormous computational time-savings, allowing the simulation of large spin systems. In this section, the kMC algorithm is outlined. For a detailed derivation the reader is referred to Plenio & Knight [54] or Fichthorn & Weinberg [55].

kMC algorithms exist for both the quantum case, where they are used when the Lindblad master equation is difficult to solve or dynamics are not strictly Markovian in nature (see for example REF. [56]), and the classical case, where they can be used to significantly reduce the simulation time for appropriate classical-like dynamics [28, 29, 31]. Both cases simulate the Lindblad master equation in Hilbert space, but do so stochastically by averaging over a given number of possible trajectories the system can take, rather than evolving the density operator. In theory, the exact dynamics can be recovered by averaging over infinite trajectories. The computational advantage of the classical algorithms arises in part from the absence of coherent evolution in the dynamics they describe. Therefore, only the population dynamics, which can be efficiently simulated as a series of quantum jump operations, need to be simulated. Furthermore, because systems are assumed to be Markovian, only the current state of the system must be known, and memory usage scales linearly or in the worst case polynomially with N. This allows highly efficient simulation of very large spin systems [57].

2.5.1 Implementation of Variable Time-step Classical kMC

After adiabatic elimination, all coherences have been eliminated and the population dynamics can be fully described by instantaneous jump operations that move the system between eigenstates. Each jump operator has associated with it a jump rate

Γ_i that can be thought of as the probability of a particular jump occurring. If Γ_i is large, the associated jump is likely to happen, whereas if it is small, the jump is less likely to happen. The probability of a jump occurring depends on its jump rate only, and not on the history of the dynamics. Each state therefore depends on the current state only, and not on any previous states.

The variable time step kMC algorithm is implemented as follows:

1. Calculate the effective rates Γ_i. This will be done in detail in Chapter 3.

2. Generate two uniformly distributed random numbers r_1 and r_2 in the interval (0,1]. These will select the time step and the jump operation respectively. Care should be taken to ensure that the random numbers selected by the algorithm are not taken from a reproducible sequence. This can be done in Matlab for example by using the 'shuffle' seed for the random number generator. 'Shuffle' seeds the generator on the current time and therefore produces a different sequence of numbers each time the random number generator is called [58].

3. Using r_1 calculate the time step to the next jump operation [57]

$$\Delta t = \frac{-\log r_1}{\sum_i \Gamma_i}.$$

   In this form, the time step is drawn from a Poissonian distribution and ensures that the dynamics are neither oversampled, leading to unnecessarily long simulation times, nor undersampled, leading to unrepresentative dynamics. The time step is variable not only because of r_1, but also because the rates Γ_i can be state-dependent, and therefore change during evolution. The average time between events in the system $(1/\sum_i \Gamma_i)$ is therefore not constant [59].

4. Combine all effective rates into a single column vector normalised such that the cumulative sum of the rates is 1. This vector represents the probability of a particular jump operation taking place, where each jump operation is weighted by its rate. A graphical representation of the rate vector is shown in the top

panel of FIG. 2-1. Higher rates (such as Γ_S in this case) take up a larger fraction of the rate vector and are therefore more likely to be selected by the random number r_2 (next step). Small rates (such as Γ_{IS} here) take up a much smaller fraction of the rate vector and are less likely to be selected. The quantum jump corresponding to this rate is therefore also less likely to take place.

5. Using the normalised rate vector calculated in step four, find the first rate greater than r_2 and execute whichever jump this rate corresponds to. This is shown graphically in FIG. 2-1 for a 4-spin system consisting of two electrons and two protons in an initial configuration $|\uparrow\downarrow\uparrow\downarrow\rangle$ ($|S_1S_2I_1I_2\rangle$). After the first time step, the first quantum jump, selected by $r_2(1)$, is executed. As is shown in the top panel, $r_2(1)$ happens to fall in the region of Γ_S, which corresponds to an electron flip. In this instance, the second electron is flipped from the down state to the up state, changing the configuration of the system to $|\uparrow\uparrow\uparrow\downarrow\rangle$. Because the configuration has changed, those rates that are state-dependent must be recalculated, and the algorithm returns to step one.

6. Repeat steps one to five until the end of the experiment is reached. This forms a single trajectory. In the model system shown in FIG. 2-1, the trajectory consists of only five time steps evolving the system as follows: $r_2(2)$ selects Γ_I, corresponding to a nuclear flip. In this case the second proton is flipped taking the system to $|\uparrow\uparrow\uparrow\uparrow\rangle$. $r_2(3)$ selects an electron flip again, but this time flips the first electron, making the new configuration $|\downarrow\uparrow\uparrow\uparrow\rangle$. $r_2(4)$ falls on the electron-nuclear flip-flop rate Γ_{IS} causing the first electron and second proton to flip-flop: $|\uparrow\uparrow\uparrow\downarrow\rangle$, and finally $r_2(5)$ selects the nuclear flip-flop rate Γ_{II}, making the final configuration of the trajectory $|\uparrow\uparrow\downarrow\uparrow\rangle$. Note that each of the time steps has a different length, and that in this particular trajectory, the CE rate Γ_{ISS} was not selected since it is very small and the first five r_2 missed it.

7. Repeat steps one to six until the convergence criteria have been satisfied. This means that averaging over more trajectories does not change the results significantly. A protocol could for example be: once the difference between the results

of successive averages less than 1%, terminate the simulation.

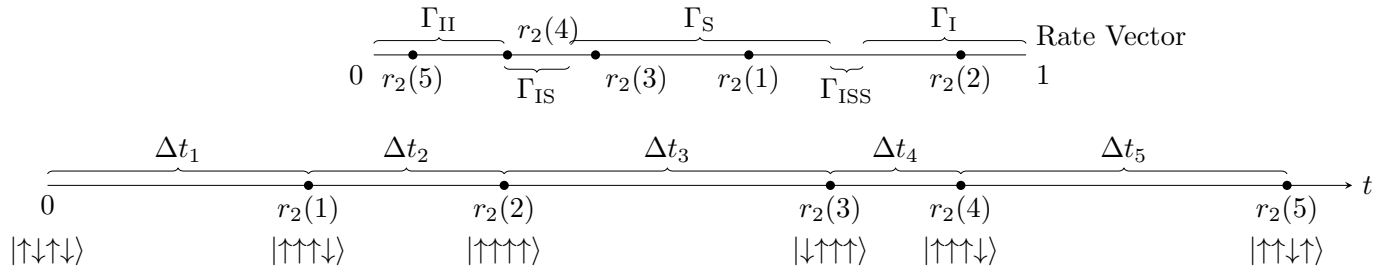


Figure 2-1: Schematic of the classical kMC algorithm with the configuration $|S_1S_2I_1I_2\rangle$. In the top figure, the rate vector of a fictitious system with five possible jumps is shown. The rate vector is normalised to 1. Γ_{II} corresponds to a nuclear flip-flop, Γ_{IS} corresponds to an electron-nuclear flip-flop, Γ_{S} to an electron flip, Γ_{ISS} to the CE triple spin flip, and Γ_{I} to a nuclear flip. $r_2(1)$ and $r_2(3)$ select the electron jump and flip the second and first electron respectively. $r_2(2)$ selects the nuclear flip and flips the second proton, $r_2(4)$ selects an electron nuclear flip-flop between the first electron and second proton, and finally $r_2(5)$ selects an proton flip-flop. This is one trajectory. A more detailed description is given in the text.

2.6 Landau-Zener Theory

In this section the Landau-Zener approximation [60, 61] used in the derivation of the MAS CE simulation algorithm is discussed. The Landau-Zener formula calculates the probability of a non-adiabatic transition occurring at an avoided level crossing between two states in a system with a time-dependent Hamiltonian. It is used in the MAS algorithm to simulate the dynamics at MAS events, when there is a change in polarisation somewhere in the system. The dynamics of interest in DNP are the polarisation dynamics, which are traditionally found by calculating the full dynamics of the system. By using the Landau-Zener transition probabilities, this lengthy and memory-intensive calculation is circumvented, thus permitting simulation of large spin systems.

2.6.1 Avoided Level Crossing

Before discussing the Landau-Zener approximation, it is important to understand what avoided level crossings are and why they occur [62]. Consider a two-state Hamiltonian with eigenvalues E_1 and E_2 and eigenstates v_1 and v_2. In the absence of any perturbation, the system will remain in the state that it is prepared in, and if E_1 happens to be equal to E_2 there is a degeneracy in the Hamiltonian. If a perturbation is applied to the system, the off-diagonal elements change the eigenstates and eigenvalues of the Hamiltonian. The new eigenvalues now depend on the perturbation, and the perturbed system no longer has degeneracies, even if the unperturbed energies are equal ($E_1 = E_2$). The perturbation therefore leads to an avoided level crossing.

2.6.2 Landau-Zener Formula

The Landau-Zener formula applies when the following three conditions are met:

1. The perturbation parameter (q) of the Hamiltonian must be known and vary linearly with time.

2. The separation of the energy levels must be a linear function of time.

3. The coupling in the non-adiabatic Hamiltonian matrix must be time-independent. This is equivalent to considering an infinitely fast transition during which the Hamiltonian has no time to change.

The second condition allows the substitution $E_2(t) - E_1(t) \equiv \alpha t$ where $E_{1,2}(t)$ are the energies of the two states at a time t, given by the incoherent (diagonal) elements of the Hamiltonian, and α is a constant.

In MAS CE, the perturbation parameter q is given by the time-dependent interactions in the Hamiltonian, and the separation of the energy levels is governed by the electron and nuclear Larmor frequencies. Note that neither of the two time dependences is linear, thus violating conditions 1 and 2. However, it can be assumed that in the region immediately surrounding an event, they are reasonably accurately described by a linear function.

The Landau-Zener transition probability P_{LZ} at an avoided level crossing, for which the third condition dictates $E_{1,2}(t) \equiv E_{1,2}$, is given by [63]

$$\begin{aligned} P_{\mathrm{LZ}} &= \mathrm{e}^{-2\pi\Gamma} \\ \Gamma &= \frac{a^2/\hbar}{\frac{\partial}{\partial t}|E_2 - E_1|} = \frac{a^2/\hbar}{\frac{\partial q}{\partial t}\frac{\partial}{\partial q}|E_2 - E_1|} = \frac{a^2}{\hbar|\alpha|}, \end{aligned} \tag{2.41}$$

where a is the coherent (off-diagonal) element of the 2-level Hamiltonian that couples the two energy states. It is half the separation between the unperturbed eigenenergies at the avoided crossing $E_1 = E_2$.

For a simple 2-level spin-1/2 Hamiltonian given by

$$\hat{H}(t) = \delta(t)\hat{L}_z + [\Omega(t)\hat{L}_+ + \Omega^*(t)\hat{L}_-], \tag{2.42}$$

where $\hat{L}$ is some spin operator, the exponent Γ is found from EQ. 2.41 to be

$$\Gamma = \frac{|\Omega(t_0)|^2}{|\dot{\delta}(t_0)|}, \tag{2.43}$$

where t_0 is the time of the crossing. In the basis of pure states $\psi_\pm$, $\hat{L}_z$ in EQ. 2.42 is the diagonal incoherent energy operator obeying $\hat{L}_z\psi_\pm = \pm\frac{1}{2}\psi_\pm$, and $\delta(t)$ is the energy difference between the pure states. The second term of EQ. 2.42 describes coherent dynamics mediated by the raising and lowering operators $\hat{L}_\pm$. These cause transitions between the states as: $\hat{L}_\pm\psi_\mp = \psi_\pm$, with a mixing rate $\Omega(t)$. With the exception of a very short interval around t_0, when $\delta(t_0) = 0$, the energy gap is generally much larger than the mixing rate. It is therefore generally the incoherent dynamics governed by $\hat{L}_z$ that dominate dynamics. However, at and around t_0, $|\delta(t)| << |\Omega(t)|$, and the dominant coherent dynamics can lead to a transition. The probability of this transition depends (from EQ. 2.43) on the "Rabi frequency" of the transition $\Omega(t)$, and the non-adiabatic passage velocity $\dot{\delta}(t)$ of the "detuning" $\delta(t)$ at $t = t_0$.

2.7 Nuclear Longitudinal Relaxation

The origin of nuclear longitudinal relaxation is the modulation of interactions due to time-varying local magnetic fields in the vicinity of each spin. This is often, though not always, related to motion of the spins. In solution this motion is quite literal in the form of molecular tumbling; as molecules 'tumble' past each other, their relative orientation with respect to each other and the static field B_0 changes, as does the length and direction of the vector joining any two spins. The former plays an important role when the interacting spins are from the same molecule (intra-molecular), and the latter when the spins are from different molecules (inter-molecular). In the solid state however, particularly at low temperature, most motional degrees of freedom are frozen out [64]. Classical molecular tumbling is therefore no longer able to contribute to relaxation.

Some of the earliest theories of nuclear relaxation in solids were Heitler's [2] and Waller's [65] theories in the 1930's, which worked reasonably well for solids with multiple types of thermal motion such as paraffins or ice, but broke down when applied to solids in which the only expected source of motion is lattice vibrations, such as insulating solids. In fact, when Waller first tried to describe the solid state T_1 of CaF_2 using only lattice vibrations, he predicted relaxation times in excess of 10^{19}s below 10K! Two decades later, Bloembergen, Purcell & Pound [66] introduced a new theory (BPP theory) which encompassed different types of motion that persist even to low temperatures and can loosely be referred to a kind of Brownian (i.e. random) motion [37]. When these 'Brownian' degrees of freedom are active, they are much more effective than the lattice vibrations proposed by Waller, and account for the relaxation times of minutes to hours observed experimentally. Under the right conditions, BPP theory holds in liquids and non-crystalline solids [64]. In the late 1950's BPP and Rollin & Hatton [67], who were the first to investigate NMR at low temperatures, independently came to the further conclusion that in many solids paramagnetic impurities play a dominant role in nuclear spin-lattice relaxation. Most of the groundwork for modern understanding of nuclear spin-lattice relaxation was developed in just over a decade, from about 1948 – 1960 by the likes of Bloembergen, Purcell & Pound, Wangsness & Bloch, Solomon, Abragam, Redfield and Tomita [68].

2.7.1 Inherent Nuclear Longitudinal Relaxation

There are four main spin-dependent electromagnetic interactions in the solid state that can lead to relaxation: spin-rotation, chemical shielding, quadrupolar interactions & dipolar interactions. The first three of these are generally not of interest for protons, leaving only the dipolar interaction [64]. The dipolar interaction is modulated by re-orientiation of the vector joining two nuclei and can be separated into inter-molecular interactions between spins on separate molecules, and intra-molecular interactions between spins within a molecule. Since intra-molecular interactions tend to be much stronger due to shorter spin separations, intra-molecular relaxation gen-

erally dominates the relaxation time. It should be noted at this time that unlike the spin diffusion process, where the dipolar interaction actively redistributes populations of spins, dipolar relaxation transfers energy between the lattice (which in this case is molecular motion) and the spins [37].

The relaxation rate constant depends three factors: the spin factor, which determines what transitions a particular interaction can cause, the size factor, which is a measure of how large the interaction is, and the spectral density $J(\omega)$, which describes how much of the molecular motion is at the correct frequency for a transition [64]. The spectral density is the Fourier transform of the correlation function $G(t, \tau)$, which characterises the 'memory' a system has of a particular configuration. For a homonuclear system undergoing random thermal motion, the correlation function generally only depends on the time τ between successive measurements of the ensemble average local field, and not on the time t. When τ is small, the correlation between successive measurements is high, and $G(\tau)$ (note that t has been dropped) is expected to be large. When τ is very long, there is little correlation between successive measurements and $G(\tau)$ approaches zero. By this time, the system has no memory of its previous configuration. The simplest form of the correlation function is [64]

$$G(\tau) = G_0 \mathrm{e}^{-|\tau|/\tau_\mathrm{c}}, \tag{2.44}$$

where τ_c is the correlation time, the time required for $G(\tau)$ to drop to approximately half its initial value G_0. For a correlation function such as EQ. 2.44 the spectral density is given by

$$J_\mathrm{BPP}(\omega, \tau_\mathrm{c}) = \frac{2\tau_\mathrm{c}}{1 + \omega^2 \tau_\mathrm{c}^2}, \tag{2.45}$$

and the motion is characterised entirely by the correlation time. It describes how much motion is present at different frequencies [37].

For the correlation time to be physical, it must be linked in some way to an observable

such as temperature or pressure. Here, it is linked to temperature, with which it is often assumed to have an Arrhenius-like relationship

$$\tau_{\mathrm{c}} = A\mathrm{e}^{E_{\mathrm{a}}/k_{\mathrm{B}}T}, \tag{2.46}$$

where A is some pre-exponential factor, E_{a} is an activation energy, and k_{B} is the Boltzmann constant [64]. What E_{a} activates depends on the system. In methyl groups for example it can be the activation energy for quantum mechanical hopping between different potential minima, in other systems it could be the activation of thermal re-orientation, etc. [64].

EQs. 2.44 to 2.46 clearly suggest that the inherent nuclear relaxation is temperature dependent at low temperatures and plateaus at higher temperatures. Although very simple, the model just described can be used to accurately describe non-crystalline solids in which there is only a single correlation function dependent on a single degree of freedom. In reality this is often not the case, and the system is better described by more complex theories involving more elaborate correlation functions. The building blocks of such theories however, are often still adaptations of the BPP model [64].

2.7.2 Paramagnetic Relaxation

In Section 2.7.1, the inherent nuclear relaxation was described. However, in order to have DNP, electrons (paramagnetic centres) are required. The effect of these paramagnetic centres on the nuclear relaxation is significant and must be taken into account when devising models for the relaxation of nuclei in DNP samples.

The presence of a paramagnetic centre in a matrix of protons creates a randomly fluctuating magnetic field that is 'felt' by the protons in its vicinity through the hyperfine interaction. There are two origins for the time dependence of this field: relative motion of the electron with respect to a nucleus, thus modulating the hyperfine interaction strength, and re-orienting of the electron spin operator, caused

by relaxation of the electron. When relaxation is brought about by modulation of the hyperfine interaction strength, the change in energy due to the flip-flop of an electron-nucleus pair ($\omega_S \pm \omega_I$) is compensated by the lattice, usually in the form of phonons. When it is the electron's relaxation that creates the fluctuating field, it is its coupling to the lattice that allows it to flip, generally at a much faster rate than a flip-flop [38]. At the low temperatures used in Chapter 8 many of the motional degrees of freedom are frozen out, and the correlation time of the random field is likely to be dominated by the electron relaxation time T_{1e} [38]. Indeed, Bloembergen goes so far as to say that in these situations "T_{1n} is not a characteristic of a chemical crystalline substance, but of its paramagnetic impurities" [69].

The nature of paramagnetic relaxation suggests that it should be dependent on the concentration of paramagnetic centres in the sample. If the concentration is very high, each centre only services a small number of protons and the dominant mechanism can be expected to be direct relaxation of the nuclei by an electron. In this case effects that the electrons have on each other when their dipolar interaction becomes non-negligible should also be taken into consideration. On the other hand, as will be shown in Section 8.3, even a very low concentration of paramagnetic centres can have a considerable effect on the nuclear relaxation. In this situation only a small fraction of the nuclei are in direct contact with the electron, with the majority of the nuclei experiencing it indirectly through spin diffusion. Spin diffusion thus evidently plays a pivotal role in the efficiency of paramagnetic relaxation in low concentration samples.

Taking into account the inherent nuclear relaxation R_{inh}, paramagnetic relaxation R_{PM}, and spin diffusion R_{SD}, the observed nuclear longitudinal relaxation rate can be separated into

$$R_{1n} = R_{inh} + R_{PM} + R_{SD}. \tag{2.47}$$

The inherent longitudinal relaxation provides temperature dependence, paramagnetic

relaxation provides concentration (of paramagnetic centres) dependence and is itself dependent on the electron relaxation, and spin diffusion is expected to be dependent on the number of nuclei each electron must serve and on the nuclear dipolar interaction.

2.8 Electron Longitudinal Relaxation

In the solid state, electron longitudinal relaxation arises from the exchange of energy between the spin system and the lattice, mostly in the form of phonons [70]. The two fundamental processes of electron relaxation in the solid state are the single-phonon direct process and the two-phonon Raman process, which were used by Waller [65] to describe the transfer processes in a system with modulated lattice vibrations [70]. Although Waller's approach was perhaps too simplistic, the framework provided by these two relaxation mechanisms can be used to describe many other mechanisms by changing the forces driving a transition. Nonetheless, there are many relaxation processes that fail to fall into any of the known relaxation mechanisms and characterisation of the mechanisms leading to electron relaxation is difficult [70].

The various types of relaxation processes can be differentiated by the number of phonons involved in the process and their temperature dependence. Only a brief overview of some of the processes is given here, a more detailed treatment can be found in REF. [70]. The two processes that tend to dominate at low temperatures are the direct and Raman processes [71].

The temperature dependence of R_{1e} can be found by fitting equation 2.48 to data [72]

$$\begin{aligned} R_{1e} = \frac{1}{T_{1e}} = A_{dir}T + A_{Ram}T^{\lambda} + A_{loc}\left[\frac{e^{\Delta_{loc}/T}}{(e^{\Delta_{loc}/T}-1)^2}\right] \\ + A_{Orb}\left[\frac{\Delta_{Orb}^3}{e^{\Delta_{Orb}/T}-1}\right] + A_{therm}\left[\frac{2\tau_c}{1+\omega^2\tau_c^2}\right], \end{aligned} \tag{2.48}$$

where A_{dir}, A_{Ram}, A_{loc}, A_{Orb}, A_{therm}, are coefficients of contribution for the direct [70], Raman [71, 73], local [74], Orbach [75] and thermal [76] processes respectively, T is the temperature in Kelvin, the factor λ is between $2 < \lambda < 9$, Δ_{loc} is the energy of the local mode (in Kelvin), Δ_{Orb} is the energy gap between the ground and excited states in the Orbach process, τ_{c} is the correlation time given already in EQ. 2.46, and finally ω is the transition frequency.

With some knowledge of the system, certain terms of the rate can be excluded from the fit since they are known not to contribute. For example, the thermal process is unlikely to play a big role at low temperatures. Similarly, if the temperature is below the Debye temperature, the local process is less likely to be involved.

2.8.1 Direct Process

The direct process is the simplest process and typically has a linear temperature dependence at low temperatures. At higher temperatures or for certain structures of energy levels, the temperature dependence may be exponential. In the direct process, energy is directly absorbed from or emitted into the lattice with the absorption or emission of a phonon respectively. For the process to be direct, the Zeeman energy of the system must be matched by the energy of the phonon [77, 78]. Although the absorption and emission energies are the same, the emission of a phonon into the lattice is slightly more likely than the absorption of a phonon by the system. The spin system that was originally 'heated' by an RF-pulse therefore 'cools' as it releases energy into the lattice. As a consequence, the lattice is heated as it absorbs phonons [70].

The direct process tends to dominate at temperatures below $\sim$ 10K [77, 78].

2.8.2 Raman Process

The Raman process is thus called due to its resemblance to the scattering of photons by molecules. Unlike in the direct process, there is no matching of energies between

the lattice and system. The Raman process is therefore a two-phonon process in which the system first absorbs a phonon from the lattice, thereby taking it into an intermediate higher-energy state, and subsequently emits a phonon, thereby dropping back down into a lower-energy state. The total energy change of the system must be equal to the Zeeman energy, and is equal to the difference in frequencies between the absorbed and emitted phonons [70, 78].

The Raman process can dominate in some spin-1/2 systems in a glassy matrix or magnetically dilute solids in the 10K to 200K range [78]. At very low temperatures, the temperature dependence tends to go as $\lambda = 9$, decreasing to $\lambda = 2$ as the temperature increases. The exact temperature dependence is heavily influenced by the lattice [70].

2.8.3 Orbach Process

The Orbach process was developed to treat electron relaxation in paramagnetic salts. It involves the simultaneous absorption/emission of two phonons by three or more electron states, collectively created by an electron ensemble. This is possible because Orbach treated the spin-lattice interaction as a perturbation that is able to connect states of the total spin Hamiltonian [75].

When applicable, the Orbach mechanism tends to become important at higher temperatures [77].

2.8.4 Local Mode Process

The previously described electron relaxation mechanisms all rely on lattice vibrations as treated by the Debye model (the Debye model treats vibrations of the lattice as phonons in a box). Such vibrations are not necessary for the local mode, which cou-

ples the system directly to the local phonon mode [74]. Because in the local mode process the phonon is localised, spin-lattice relaxation via the local mode tends to be slower than by other processes [79].

The local mode tends to take place at vibrational frequencies that are above the Debye temperature [80].

2.8.5 Thermal Process

Thermally activated processes include processes such as methyl group rotation or the movement of hydrogen-bonded protons. These processes can absorb energy from the spin system when the frequency of the process is approximately equal to the electron Larmor frequency [78].

Chapter 3

Static Cross Effect DNP

3.1 Introduction

In recent decades MAS DNP has taken the limelight in many aspects of DNP. Nonetheless, the static CE DNP mechanism remains experimentally relevant, covering for example the low temperature regime (<25K), which is not accessible to MAS DNP [81]. In this chapter the static CE mechanism is discussed in more detail, building on what was learned in Chapter 2. The adiabatic elimination procedure is then applied specifically to the CE. The derivation in this chapter follows the work of A. Karabanov and is published in REFs. [19, 27, 29]. A detailed derivation can be found in D. Wiśniewski's thesis [82]. Wiśniewski also wrote the core kMC simulation algorithm which was then adapted for the simulations in Chapter 4.

3.2 Static Cross Effect

The CE involves two coupled free electrons interacting collectively with a nuclear ensemble. Such an arrangement of electrons can be found either in systems with a high enough concentration of monoradicals that the inter-molecular electron coupling is significant, or in systems containing specifically designed biradicals with an optimised intra-molecular electron coupling. The proviso for CE DNP is that the inhomogeneous broadening of the EPR line must be approximately equal to the nuclear Larmor

frequency [23, 27]

$$\Delta\omega_{\mathrm{S}} =\mid \omega_{\mathrm{S}_1} - \omega_{\mathrm{S}_2} \mid\sim \omega_{\mathrm{I}}. \tag{3.1}$$

When this is the case, an electron flip-flop is energetically matched by a nuclear flip, and the triple spin flips characteristic of the CE become viable. Broadening of the EPR spectrum is achieved by changing the relative orientation of the electrons' g-tensors with respect to each other, so that their response to the static field differs and they precess at different Larmor frequencies. Because they precess at different rates, it is possible to saturate just one of the electrons by irradiating the system with microwaves on resonance ($\omega_{\mu\mathrm{w}} = \omega_{\mathrm{S}}$) with that electron. If the CE condition in EQ. 3.1 is met, the second electron is far off-resonance from the microwaves and therefore remains at approximately thermal polarisation. In this scenario the CE polarisation transfer is maximised, since the CE mechanism drives nuclear polarisation to equilibrate with the polarisation *difference* between the electrons. Effective CE DNP therefore requires electron offsets $\Delta_{1,2}$ (refer to EQ. 2.12) that satisfy [i]

$$\begin{aligned} \Delta_1 &=\mid \omega_{\mathrm{S}_1} - \omega_{\mu\mathrm{w}} \mid\sim 0 \\ \Delta_2 &=\mid \omega_{\mathrm{S}_2} - \omega_{\mu\mathrm{w}} \mid\sim \omega_{\mathrm{I}}. \end{aligned} \tag{3.2}$$

However, efficient microwave irradiation alone does not guarantee efficient CE DNP; other spin interactions and relaxation processes also play an important role. $T_{1\mathrm{e}}$ relaxation of the second electron for example, determines how quickly CE cycles can be repeated and therefore sets an upper limit on how many nuclei can be polarised by an electron in a given time. Nuclear $T_{1\mathrm{n}}$ on the other hand dictates the efficacy of spin diffusion. If the relaxation is fast compared to the propagating speed of the polarisation in the nuclear ensemble, much of the polarisation relaxes before it can be transferred between nuclei. As for the spin interactions, the triple spin flips underlying the CE mechanism are mediated by the electron dipolar and hyperfine interactions. If these are weak, the transfer of the polarisation from the electrons to nearby nuclei

[i] Note that throughout the rest of this thesis the microwave irradiation will be taken to be on resonance with the first electron.

is not efficient. Finally, the nuclear dipolar interaction is responsible for propagating polarisation within the nuclear ensemble. If this is weak, and in particular, if it is slower than T_{1n}, the polarisation cannot propagate and nuclei far from the electron pair do not become polarised.

At this point it is natural to make a distinction between nuclei that are polarised directly by the electrons via the triple spin flip, the *core*, and nuclei that are polarised by spin diffusion and are oblivious to the CE process, the *bulk*. Differentiation between the two categories of nuclear spins will be frequent in the coming chapters.

3.3 Energy Level Diagram

To get a more complete understanding of the CE on a microscopic level, it is instructive to study the energy level diagram for the simplest CE system: two electrons coupled to a single nucleus. FIG. 3-1 shows such a 3-spin system satisfying $\Delta\omega_S \sim +\omega_I$ in the lab frame. The first electron (e_1) is shown in blue, the second electron (e_2) in green and the nucleus in orange. Because the system satisfies EQ. 3.2, an electron flip-flop is energetically matched by a nuclear flip, and the central two energy levels become degenerate. Population exchange between these two levels is indirectly mediated by the electron dipolar and pseudo-secular hyperfine interactions (this will be discussed in more detail from the standpoint of the energy level diagram in the rotating frame). All other eigenstates are connected by the remaining non-Zeeman terms. When the microwave irradiation is switched on, the populations of states differing only in the state of the first electron equalise. This process is indicated by the magenta arrows and is driven by the ω_1 term for e_1 in the Hamiltonian. Combined with the CE triple spin flip that equalises the populations of the degenerate energy levels (yellow oval), this leads to an overall equalisation in population of the central four energy states (grey circle). In the microwave rotating frame, these four states are degenerate. At the same time, relaxation of e_2 tends to drive the system back to thermal equilibrium (dark green arrows), leading to an increased population of the

nuclear spin-up state. This is because energy levels $|6\rangle$ and $|8\rangle$ feed into the central four states, from which levels $|7\rangle$ and $|5\rangle$ then feed into $|1\rangle$ and $|3\rangle$. Since the central four levels are constantly re-equalising, every time $|7\rangle$ and $|5\rangle$ get depleted, $|2\rangle$ and $|4\rangle$ replenish them.

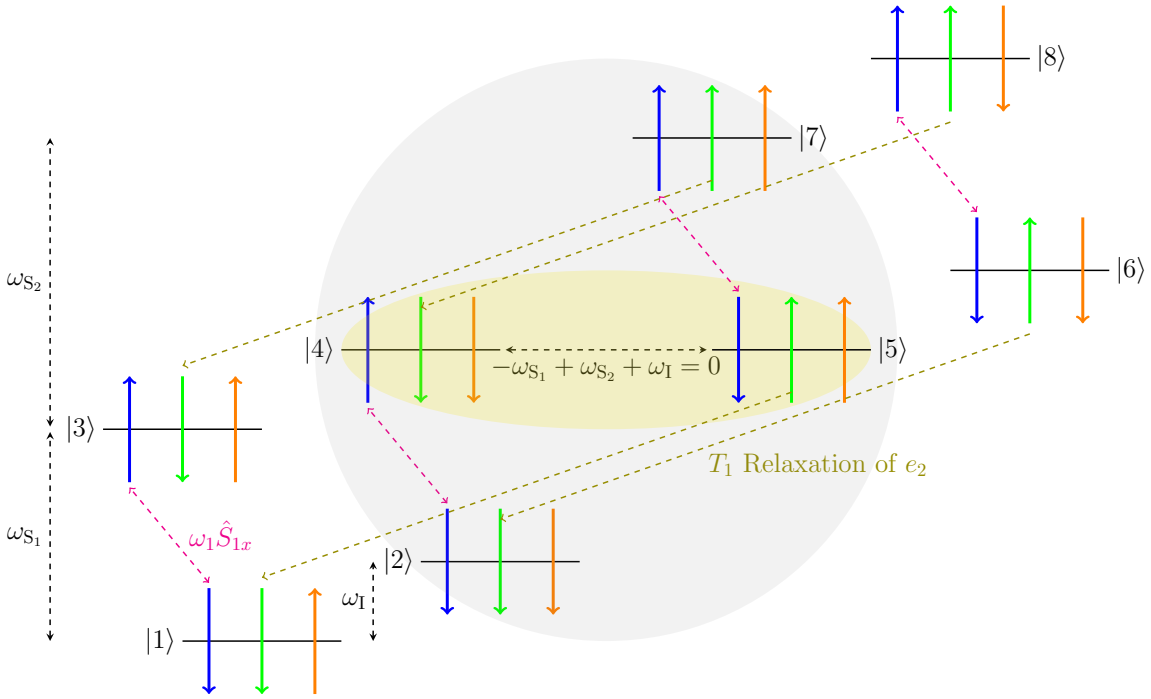


Figure 3-1: Energy level diagram for a 3-spin CE system satisfying the CE efficiency condition with $\Delta\omega_S \sim +\omega_I$. The first electron is shown in blue, the second electron in green and the nucleus in orange. Magenta arrows represent saturation of the first electron by the microwave irradiation, the yellow oval shows the pseudo-secular hfi and electron dipolar interaction mediated population equalisation of the degenerate states, and the grey circle shows the population equalisation of the 4 central energy levels. Dark green arrows indicate relaxation pathways of the second electron.

3.4 Efficient Cross Effect DNP and Incoherent Dynamics

When it comes to simulating the CE dynamics, a careful balance must be struck between creating a system that has efficient CE dynamics, thus leading to high polarisation enhancement, and ensuring that the dynamics are amenable to adiabatic elimination, and can thus be simulated efficiently with the kMC algorithm. As will

be shown in Section 3.4.3, it is possible to derive a set of inequalities that guarantees efficient CE dynamics that can also be efficiently simulated with the kMC algorithm.

3.4.1 Efficient CE DNP

The first hurdle to efficient CE DNP is the microwave irradiation. EQ. 3.1 assumes that the two electrons have exactly the energy prescribed to them by the Zeeman splitting. This would indeed be the case if they were completely isolated. However, since they are interacting with each other and the nuclear ensemble, their energies are shifted. Instead, the total detuning of each electron is found by collecting all $\hat{S}_z$ terms for each electron:

$$\begin{aligned}\hat{\Delta}_{1,\mathrm{Z}_1} &= \Delta_1 + 2D\hat{S}_{2z} + \sum_k A_{1z}\hat{I}_{kz} = 2D\hat{S}_{2z} + \sum_k A_{1z}\hat{I}_{kz} \\ \hat{\Delta}_{2,\mathrm{Z}_2} &= \Delta_2 + 2D\hat{S}_{1z} + \sum_k A_{2z}\hat{I}_{kz} = \omega_\mathrm{I} + 2D\hat{S}_{1z} + \sum_k A_{2z}\hat{I}_{kz}.\end{aligned} \tag{3.3}$$

From EQ. 3.3 it is evident that the efficacy of the microwave irradiation in fact depends not only on the microwave frequency, but also on the secular hyperfine and electron dipolar interactions, which shift the energy level from the Zeeman energy. The detuning is operator-valued, which means that it depends on the strength of the interactions as well as on the exact state of the entire system. It can therefore take on a discrete number of values, each corresponding to a particular configuration of the system.

3.4.2 Single Spin with Microwave-driven Dynamics

In this section, a system consisting of a single electron spin irradiated by a microwave field along the x-direction will be used to elucidate the conditions under which adiabatic elimination is applicable. These can then easily be adapted for the many-spin CE system.

The microwave-driven single spin Hamiltonian is given by

$$\hat{H} = \omega_1 \hat{S}_x + \Delta \hat{S}_z,$$

and the master equation in the microwave rotating frame is

$$\dot{\hat{\rho}} = -i[\hat{H}, \hat{\rho}] + \hat{\hat{\mathcal{D}}}_{\mathrm{TOT}} \hat{\rho},$$

where the dissipator is given by

$$\hat{\hat{\mathcal{D}}}_{\mathrm{TOT}} = \frac{R_{1\mathrm{e}}}{2}\big((1-p_{\mathrm{e}})\hat{\hat{\mathcal{D}}}[\hat{S}_+] + (1+p_{\mathrm{e}})\hat{\hat{\mathcal{D}}}[\hat{S}_-]\big) + 2R_{2\mathrm{e}}\hat{\hat{\mathcal{D}}}[\hat{S}_z],$$

and the density matrix can be expanded in terms of the X, Y & Z polarisation components

$$\hat{\rho} = \frac{1}{2} - p_{\mathrm{e}}(X\hat{S}_x + Y\hat{S}_y + Z\hat{S}_z).$$

If it is assumed that decoherence of the spin occurs on a much faster time scale than population exchange between eigenstates ($R_{2\mathrm{e}} \gg R_{1\mathrm{e}}$), the Bloch equations

$$\dot{X} = -\Delta Y - R_{2\mathrm{e}}X, \quad \dot{Y} = \Delta X - \omega_1 Z - R_{2\mathrm{e}}Y, \quad \dot{Z} = \omega_1 Y + R_{1\mathrm{e}}(1-Z) \tag{3.4}$$

can be found, and solved for the steady state

$$X = \frac{\Delta Z}{\omega_1 \eta'}, \quad Y = \frac{R_{2\mathrm{e}} Z}{\omega_1 \eta'}, \quad Z = (1 + \frac{\eta}{\eta'})^{-1}, \tag{3.5}$$

where

$$\eta' = \frac{R_{2\mathrm{e}}^2 + \Delta^2}{\omega_1^2}, \quad \eta = \frac{R_{2\mathrm{e}}}{R_{1\mathrm{e}}}. \tag{3.6}$$

The ratio $\frac{\eta}{\eta'}$ characterises how well the electron is saturated. For high saturation, $\frac{\eta}{\eta'} \ll 1$ and the z-component of the magnetisation $Z \sim 1$. For low saturation $\frac{\eta}{\eta'} \gg 1$ and $Z \sim 0$. These two inequalities lead directly to the many spin CE condition in EQ. 3.9. Next, the implications of this condition on the adiabatic elimination method

are examined.

From EQ. 3.4 it is seen that in the absence of microwave irradiation, the dynamics in the transverse (XY) plane are completely decoupled from the longitudinal (Z) dynamics. The $\dot{X}, \dot{Y}$ dynamics then simply describe precession of the spin (Δ term) along with a T_2 decay ($R_{2\mathrm{e}}$ term), whilst $\dot{Z}$ describes the T_1 buildup. The eigenvalues $\lambda_{\pm} = -R_{2\mathrm{e}} \pm i\Delta$ of the transverse dynamics are found by simultaneously solving $\dot{X}$ and $\dot{Y}$ in the absence of a microwave field. The exchange rate between longitudinal and transverse dynamics on the other hand is found from the mixing terms $\omega_1 Z$ and $\omega_1 Y$ to scale as ω_1. The condition for adiabatic elimination is that there is no coherence between the transverse and longitudinal dynamics. In other words, the transverse dynamics should occur on a much faster time scale than longitudinal dynamics and exchange between them

$$|\lambda_{\pm}|^2 = R_{2\mathrm{e}}^2 + \Delta^2 \gg \omega_1^2, R_{1\mathrm{e}}^2.$$

Recall from the derivation of the steady state solution of the environment in Section 2.3.3 that in adiabatic elimination the initial dynamics in Z are taken to be incoherent. This is the case when $\eta' \gg 1$. Substituting the steady state value of Y into $\dot{Z}$ and rearranging to group terms of Z, the longitudinal dynamics starting from the thermal state are well approximated by

$$\dot{Z} = R_{1\mathrm{e}} - (R_{1\mathrm{e}} + \frac{R_{2\mathrm{e}}}{\eta'})Z, \tag{3.7}$$

describing an exponential recovery of the steady state with a effective rate $R_{1\mathrm{e}} + \frac{R_{2\mathrm{e}}}{\eta'}$. Squaring EQs. 3.5 ($X^2 + Y^2 \sim Z^2/\eta'$), it is evident that the dynamics become incoherent ($X^2 + Y^2 \sim 0$) when $\eta' \gg 1$.

If the condition $\eta' \gg 1$ is satisfied, the uninformative (for the purpose of calculating polarisation) transverse dynamics can be adiabatically eliminated. EQ. 3.7 can then be written in Lindblad form, where $Z \to p_{\mathrm{e}}$, and the relaxation terms are regrouped

into R_{1e} and R_{2e}

$$\dot{\hat{\rho}}' = \hat{\hat{\mathcal{D}}}'_{\mathrm{TOT}}\hat{\rho}', \qquad \hat{\hat{\mathcal{D}}}'_{\mathrm{TOT}} = \Gamma_+\hat{\hat{\mathcal{D}}}[\hat{S}_+] + \Gamma_-\hat{\hat{\mathcal{D}}}[\hat{S}_-], \qquad \Gamma_\pm = \frac{R_{1e}(1 \pm p_e)}{2} + \frac{R_{2e}}{2\eta'}. \tag{3.8}$$

EQ. 3.8 is the incoherent Lindblad equation in the subspace of the longitudinal dynamics only (indicated by the prime $'$). The transverse dynamics have been adiabatically eliminated. The second term in the $\Gamma_\pm$ rates accounts for the incoherent rate caused by the microwave irradiation. If the condition $\eta' \gg 1$ is not satisfied, coherences in the form of Rabi oscillations cause the adiabatic elimination procedure to break down.

3.4.3 Efficient Simulation of the Cross Effect

The conditions for effective CE dynamics that are eligible for adiabatic elimination (and therefore efficient simulation) are given by

$$1 \ll \hat{\eta}_1 \ll \eta \ll \hat{\eta}_2, \qquad \hat{\eta}_j = \frac{R_{2e}^2 + \hat{\Delta}_{j,\mathrm{Z}_j}^2}{\omega_1^2}, \qquad \eta = \frac{R_{2e}}{R_{1e}}, \tag{3.9}$$

and follow directly from EQ. 3.3, and EQ. 3.6 & the ensuing discussion. EQ. 3.9 ensures both maximum polarisation difference between the electrons, and incoherent longitudinal dynamics. The latter is important, as if dynamics are coherent, the longitudinal ($\langle \hat{S}_z \rangle$) and transverse ($\langle \hat{S}_{x,y} \rangle$) dynamics of the first electron become mixed and the adiabatic elimination procedure cannot be applied. A more detailed discussion of each part of EQ. 3.9 follows.

- $1 \ll \eta$ constrains the experimental regime in which the adiabatic elimination is valid. Static CE DNP is usually performed at low temperatures (< 90K) to increase thermal polarisation of the spins. At very low temperatures R_{2e} is indeed several orders of magnitude higher than R_{1e}. However, as the temperature increases, they converge and this condition is no longer satisfied [32].

- $1 \ll \hat{\eta}_1$ ensures that microwave irradiation of the first electron does not entail coherent Rabi oscillations. Rabi oscillations result in strong correlation between the transverse and longitudinal dynamics, thus preventing the use of adiabatic elimination. This is equivalent to the condition $\eta' \gg 1$ after EQ. 3.7. The square of the microwave irradiation strength in the denominator suggests that weak microwave irradiation should be used. Too strong a field can lead to undesirable population inversion.

- $\hat{\eta}_1 \ll \eta$ guarantees that the first electron is fully saturated. This follows from the discussion after EQ. 3.5 ($Z \sim 0$).

- $\eta \ll \hat{\eta}_2$ guarantees that the second electron remains approximately at thermal polarisation. This follows from the discussion after EQ. 3.5 ($Z \sim 1$).

3.5 Adiabatic Elimination

In this section the adiabatic elimination (AE) procedure introduced in general terms in Chapter 2 is applied specifically to static CE DNP. The elimination proceeds in two steps: in the first the system dynamics are projected onto the zero coherence subspace, and in the second the remaining coherent dynamics are projected onto the Zeeman subspace. The result is that dynamics are completely enclosed in the Zeeman subspace and therefore represent classical-like population exchange between the Zeeman eigenstates. In this form, dynamics are suited to simulation using a classical kMC algorithm, and thus simulation of large spin systems.

Before delving into the details of the AE, the energy level diagram is revisited, this time in the rotating frame, to understand why the CE DNP system lends itself to AE.

3.5.1 Rotating Frame Energy Level Diagram

When FIG. 3-1 is taken into the microwave rotating frame, all states connected by $\omega_1 \hat{S}_{1x}$ become degenerate, and the pair of states already degenerate remains so. The microwave frame energy level diagram thus has three sets of degenerate states at $-\omega_{\mathrm{I}}, 0$ & ω_{I}, as seen in FIG. 3-2.

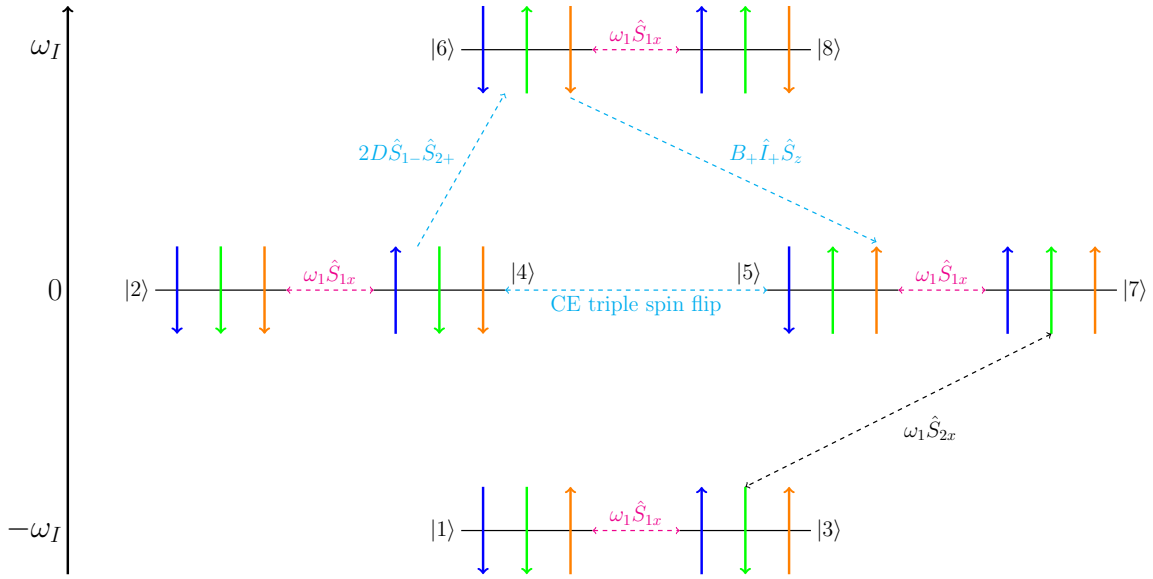


Figure 3-2: Energy level diagram for the 3-spin system in FIG. 3-1 in the microwave rotating frame. Since in this frame the first electron is saturated (magenta), the 4 central levels are degenerate. States $|4\rangle$ and $|5\rangle$ are indirectly connected via the CE triple spin flip (cyan), which takes place between non-degenerate eigenstates.

The dynamics in FIG. 3-2 can be split into two types: dynamics taking place within degenerate states, and dynamics between non-degenerate states. In both cases it is the non-Zeeman terms of the Hamiltonian that effect transitions between eigenstates and cause population exchange between them. Transitions between non-degenerate states are mediated by the microwave term of the second electron, the pseudo-secular hyperfine interaction and the flip-flop part of the electron dipolar interaction. Since these are all much smaller than the energy gap ω_{I}, population exchange is rather slow. Furthermore, although states $|4\rangle$ and $|5\rangle$ are degenerate, they are not connected by $\omega_1 \hat{S}_x$. Instead, they are connected by a 2-step triple spin flip as shown in FIG. 3-2. Although the net result is still an exchange within a manifold, the process occurs

between manifolds and is therefore slower than the saturation process, which occurs within a manifold. As long as the condition $\hat{\eta}_1 \gg 1$ is satisfied, the fast dynamics of saturation remain incoherent such that AE can be applied.

3.5.2 Zero Quantum Coherence Projection

The first step in the AE procedure is to eliminate all terms with non-zero coherences. If performed at the CE resonance (EQ. 3.1), the resultant dynamics take place in the subspace of the second electron and the nuclei, since at resonance $\hat{H}_{\mathrm{Z}} = \omega_{\mathrm{I}}(\hat{S}_{2z} + \sum \hat{I}_{kz})$, and the fast dynamics of the irradiated electron are eliminated.

The total state space of the system can be separated into subspaces identifiable by their coherence number q,

$$\mathfrak{L} = \sum \mathfrak{L}_q,$$

each of which contains corresponding elements of the density operator: $\hat{\rho}^{(q)} \in \mathfrak{L}_q$. The zero coherence space contains elements with no flips e.g. $\hat{S}_{jz}$ or a flip-flop e.g. $\hat{S}_{1+}\hat{S}_{2-}$, the single coherence spaces $q = 1$ and $q = -1$ contain single flip or flop terms e.g. $\hat{S}_{1+}$ and $\hat{S}_{1-}$ respectively, and so on. The Zeeman Hamiltonian contains only $\hat{S}_z$ and $\hat{I}_z$ terms, and is therefore unable to change the coherence order of the density matrix. The commutation $[\hat{H}_{\mathrm{Z}}, \hat{\rho}^{(q)}]$ however, has different eigenvalues depending on the coherence order q

$$[\hat{H}_{\mathrm{Z}}, \hat{\rho}^{(q)}] = -iq\omega_{\mathrm{I}}\hat{\rho}^{(q)}.$$

The subspace of interest, $\hat{\rho}^{(0)}$, is the one that commutes with the Zeeman Hamiltonian. It contains not only the diagonal Zeeman terms, but also flip-flop terms from the dipolar and hyperfine interactions. However, since these, and indeed any other, interactions are much smaller than the nuclear Zeeman interaction ω_{I}, by which the eigenvalues of the complementary subspace scale, $\mathfrak{L}_{q>0}$ necessarily evolves on a much faster time scale than the subspace of interest $\mathfrak{L}_0$, or interaction between them. The

inequality

$$\mid \omega_{\mathrm{I}} \mid \gg \mid D \mid, \mid B_{jk} \mid, \mid A_{jk} \mid, \mid d_{kk'} \mid, \mid \omega_1 \mid, R_{1\mathrm{n}}, R_{2\mathrm{n}}, R_{1\mathrm{e}}, R_{2\mathrm{e}},$$

thus plays the role of EQ. 2.17 and the subspace $\mathfrak{L}_{q>0}$ can be eliminated. Furthermore, since it is assumed that the condition $\hat{\eta}_1 \gg 1$ is satisfied, dynamics start from the thermal state $\hat{\rho}_{\mathrm{th}}$ (EQ. 2.3), which is in the Zeeman subspace.

EQ. 2.23 can be written in terms of the dissipative LvN equation in the zero coherence subspace

$$\dot{\hat{\rho}}_0 = -i[\hat{H}_0, \hat{\rho}_0] + \hat{\hat{\mathcal{D}}}_0 \hat{\rho}_0, \tag{3.10}$$

where the coherent part $-i[\hat{H}_0, \hat{\rho}_0]$ plays the role of the projector $\hat{\hat{\mathcal{L}}}_{\mathrm{SS}}$ and the dissipator $\hat{\hat{\mathcal{D}}}_0$ plays the role of the triple product $\hat{\hat{\mathcal{L}}}_{\mathrm{SE}} \hat{\hat{\mathcal{L}}}_{\mathrm{EE}}^{-1} \hat{\hat{\mathcal{L}}}_{\mathrm{ES}}$. The expressions for $\hat{\hat{\mathcal{L}}}_{\mathrm{SS}}$, $\hat{\hat{\mathcal{L}}}_{\mathrm{SE}}$ and $\hat{\hat{\mathcal{L}}}_{\mathrm{ES}}$ can be found directly from the initial Hamiltonian (EQ. 2.12) by examining the effect of each term in the Hamiltonian on the zero and non-zero coherence elements of the density matrix. Traditionally, the inversion $\hat{\hat{\mathcal{L}}}_{\mathrm{EE}}^{-1}$ is found by taking the system into the Laplace domain and solving the dynamics there, as described in Section 2.3. A. Karabanov et al. however, have shown that it is also possible to do this using the Krylov-Bogolyubov method of averaging [19, 27] with $\varepsilon = 1/\omega_{\mathrm{I}}$ and $\tau = \omega_{\mathrm{I}} t$ (refer to Section 2.4). They have also shown that it is possible to truncate the series expansions at the 4^{th} spin correlation order, thus further reducing the state space from $\mathfrak{L}_0$.

After averaging, the explicit form of $\hat{H}_0$ is given by

$$\begin{aligned}\hat{H}_0 = &\sum_{k'<k} d_{kk'}\big(2\hat{I}_{kz}\hat{I}_{k'z} - \frac{\hat{X}_{kk'} + \hat{X}^\dagger_{kk'}}{2}\big) + \frac{\omega_1}{2}\big(1 - \frac{D}{\omega_{\rm I}}\hat{S}_{2z}\big)(\hat{S}_{1+} + \hat{S}_{1-})... \\ &+ \big(\frac{D^2}{4\omega_{\rm I}} + 2D\hat{S}_{2z} + \sum_k A_{1k}\hat{I}_{kz}\big)\hat{S}_{1z} + \big(\frac{2\omega_1^2 - D^2}{4\omega_{\rm I}} + \sum_k A_{2k}\hat{I}_{kz}\big)\hat{S}_{2z}... \\ &+ \sum_k \big[(b_{k0} + b_{1k}\hat{S}_{1z}\hat{S}_{2z})\hat{I}_{kz} - \frac{\omega_1}{4\omega_{\rm I}}(B_{2k}\hat{Y}_k + B^*_{2k}\hat{Y}^\dagger_k) - \frac{D}{4\omega_{\rm I}}(\bar{B}_k\hat{Z}_k + \bar{B}^*_k\hat{Z}^\dagger_k)\big],\end{aligned}$$

where $\hat{X}_{kk'}$, $\hat{Y}_k$ and $\hat{Z}_k$ are the fictitious spin operators

$$\hat{X}_{kk'} = \hat{I}_{k+}\hat{I}_{k'-}, \qquad \hat{Y}_k = \hat{I}_{k+}\hat{S}_{2-}, \qquad \hat{Z}_k = \hat{I}_{k+}\hat{S}_{1+}\hat{S}_{2-}.$$

Note the appearance of the triple spin flip $\hat{Z}_k$ that is not present in the original Hamiltonian. It is modulated by the electron dipolar interaction and the difference in pseudo-secular hyperfine interaction between the two electrons, emphasising the importance of asymmetry in the system. The pseudo-secular interaction has been grouped into three terms

$$b_{k0} = \frac{\mid B_{1k} \mid^2 + \mid B_{2k} \mid^2}{8\omega_{\rm I}}, \qquad b_{k1} = \frac{B_{1k}B^*_{2k} + B^*_{1k}B_{2k}}{2\omega_{\rm I}}, \qquad \bar{B}_k = B_{1k} - B_{2k}.$$

The dissipator is given by

$$\hat{\hat{\mathcal{D}}}_0 = \sum_j \big(\bar{\Gamma}^{\rm S}_{j+}\hat{\hat{\mathcal{D}}}[\hat{S}_{j+}] + \bar{\Gamma}^{\rm S}_{j-}\hat{\hat{\mathcal{D}}}[\hat{S}_{j-}]\big) + \sum_k \hat{\Gamma}^{\rm I}_k(\hat{\hat{\mathcal{D}}}[\hat{I}_{k+}] + \hat{\hat{\mathcal{D}}}[\hat{I}_{k-}]) + \Gamma^{\rm SS}(\hat{\hat{\mathcal{D}}}[\hat{K}] + \hat{\hat{\mathcal{D}}}[\hat{K}^\dagger]), \tag{3.11}$$

where the form of $\hat{\hat{\mathcal{D}}}$ is given by EQ. 2.10, $\hat{K} = \hat{S}_{1+}\hat{S}_{2-}$ is the fictitious electron spin operator, and the explicit form of the rates is

$$\begin{aligned}\Gamma^{\rm S}_{1\pm} = \frac{R_{1\rm e}(1 \mp p_{\rm e})}{2}, \qquad \bar{\Gamma}^{\rm S}_{2\pm} = \frac{R_{1\rm e}(1 \mp p_{\rm e})}{2} + \frac{\omega_1^2 R_{2\rm e}}{2\omega_{\rm I}^2} \\ \hat{\Gamma}^{\rm I}_k = \frac{R_{1\rm n}}{2} + \frac{(b_{k0} + b_{k1}\hat{S}_{1z}\hat{S}_{2z})(R_{2\rm n} + R_{2\rm e})}{\omega_{\rm I}}, \qquad \Gamma^{\rm SS} = \frac{D^2 R_{2\rm e}}{\omega_{\rm I}^2}.\end{aligned} \tag{3.12}$$

In EQs. 3.10 to 3.11 the fast-evolving non-zero coherences have been eliminated.

3.5.3 Zeeman Projection

The second step of the elimination procedure is to eliminate any non-Zeeman orders remaining after the zero coherence projection. This ensures that all the relevant dynamics take place in the longitudinal subspace only, i.e. along the diagonals of the density matrix in the Zeeman eigenbasis. The orders to be eliminated are $\hat{S}_{1\pm}$, and the fictitious spin operators $\hat{X}_{kk'}$, $\hat{Y}_k$, & $\hat{Z}_k$ forming the coherent ($[\hat{H}_0, \hat{\rho}_0]$) part of EQ. 3.10. Once these are eliminated, only the incoherent dissipative part of the master equation is left

$$\dot{\hat{\rho}}' = \hat{\hat{\mathcal{D}}}'\hat{\rho}'.$$

In this projection, the elimination of the non-Zeeman orders follows the procedure outlined in Section 3.4.2 for the elimination of transverse dynamics in a single-spin system with microwave-driven dynamics. As for the single-spin case, the detuning Δ, transverse relaxation R_{2e}, and microwave driving ω_1 are found for each of the four quantum jumps $\hat{S}_{1\pm}$, $\hat{X}_{kk'}$, $\hat{Y}_k$, $\hat{Z}_k$ and used to find their respective jump rate Γ. Notation follows that of EQ. 3.8, and to differentiate between the single-spin dynamics in EQ. 3.8 and many-spin dynamics, a superscript of $^{(1)}$ will be used for the single-spin case. The detuning $\Delta^{(1)}$ is found by collecting Zeeman components of the spins involved in the quantum jump, the Rabi frequency $\omega_1^{(1)}$ is given by the coefficient of the jump operators, and $R_{2e}^{(1)}$ is the effective transverse relaxation.

$\hat{\mathbf{S}}_{\mathbf{1}\pm}$

These operators cause jumps between the up and down orientations of the first electron. The transverse relaxation rate, Rabi frequency and detuning are given by

$$R_{2e}^{(1)} \equiv R_{2e}, \qquad \omega_1^{(1)} \equiv \frac{\omega_1}{2}\big(1 - \frac{D}{\omega_I}\hat{S}_{2z}\big),$$
$$\Delta^{(1)} \equiv \hat{P}_1 = \frac{D^2}{4\omega_I} + 2D\hat{S}_{2z} + \sum_k (A_{1k} + b_{k1}\hat{S}_{2z})\hat{I}_{kz}.$$

$\hat{\mathbf{Y}}_\mathbf{k}$

The $\hat{Y}_k$ operators cause flip-flops between a nucleus and the second electron. Their detuning, Rabi frequency and relaxation are given by

$$R_{2e}^{(1)} \equiv R_{2e}, \qquad \omega_1^{(1)} \equiv \left|\frac{\omega_1 B_{2k}}{2\omega_I}\right|,$$
$$\Delta^{(1)} \equiv \hat{P}_{2k} = b_{k0} + \big(\sum_k A_{1k} - 2D\big)\hat{S}_{1z} + \sum_{k'<k}(d_{kk'} - A_{2k'} - b_{k1}\hat{S}_{1z})\hat{I}_{kz}.$$

$\hat{\mathbf{Z}}_\mathbf{k}$

$\hat{Z}_k$ are the CE triple spin flips. When the CE condition is met, an electron flip-flop is energetically matched by a nuclear flip. Their detuning, Rabi frequency and relaxation are given by

$$R_{2e}^{(1)} \equiv 2R_{2e}, \qquad \omega_1^{(1)} \equiv \left|\frac{D\bar{B}_k}{2\omega_I}\right|,$$
$$\Delta^{(1)} \equiv \hat{P}_{3k} = b_{k0} + \frac{D^2 - \omega_1^2}{2\omega_I} + \sum_{k'<k}(2d_{kk'} - A_{2k} + A_{1k})\hat{I}_{kz}.$$

$\hat{\mathbf{X}}_{\mathbf{kk'}}$

Finally, the nuclear spin diffusion operator $\hat{X}_{kk'}$ causes flip-flops between nuclear spins. This term is responsible for propagating polarisation within the bulk.

$$R_{2e}^{(1)} \equiv 2R_{2n}, \qquad \omega_1^{(1)} \equiv d_{kk'},$$
$$\Delta^{(1)} \equiv \hat{P}_{kk'} = b_{k0} - b_{k'0} + (b_{k1} - b_{k'1})S_{1z}\hat{S}_{2z} + \sum_k (A_{jk} - A_{jk'})\hat{S}_{jz} + 2\sum_{s\neq k,k'}(d_{ks} - d_{k's}).$$

Here the condition $R_{2e} \gg R_{1e}, R_{1n}, R_{2n}$ was used. This is generally true at the low temperatures relevant to DNP experiments.

Master Equation

Using EQ. 3.8 with the notation $\eta' = ((R_{2e}^{(1)})^2 + (\Delta^{(1)})^2)/(\omega_1^{(1)})^2$, the master equation in the Zeeman subspace has thus been found, where

$$\begin{aligned}\hat{\dot{\mathcal{D}}}' =& \hat{\dot{\mathcal{D}}}_0 + \hat{\bar{\Gamma}}^{S_1}\big(\hat{\dot{\mathcal{D}}}[\hat{S}_{1+}] + \hat{\dot{\mathcal{D}}}[\hat{S}_{1-}]\big) + \sum_k \hat{\Gamma}_k^{SI}\big(\hat{\dot{\mathcal{D}}}[\hat{Y}_k] + \hat{\dot{\mathcal{D}}}[\hat{Y}_k^\dagger]\big) \\ & \sum_{k<k'} \hat{\Gamma}_{kk'}^{II}\big(\hat{\dot{\mathcal{D}}}[\hat{X}_{kk'}] + \hat{\dot{\mathcal{D}}}[\hat{X}_{kk'}^\dagger]\big) + \sum_k \hat{\Gamma}_k^{ISS}\big(\hat{\dot{\mathcal{D}}}[\hat{Z}_k] + \hat{\dot{\mathcal{D}}}[\hat{X}_k^\dagger]\big).\end{aligned}$$

The rates for each of the quantum jumps are given by

$$\begin{aligned}\hat{\bar{\Gamma}}^{S_1} &= \frac{\omega_1^2}{2} R_{2e}\big(1 - \frac{D}{\omega_I}\big)^2 (R_{2e}^2 + \hat{P}_1^2)^{-1}, \qquad \hat{\Gamma}_k^{SI} = \frac{1}{2}\left|\frac{\omega_1 B_{2k}}{2\omega_I}\right| R_{2e}(R_{2e}^2 + \hat{P}_{2k}^2)^{-1} \\ \hat{\Gamma}_{kk'}^{II} &= d_{kk'}^2 (4R_{2n}^2 + \hat{P}_{kk'}^2)^{-1}, \qquad \hat{\Gamma}_k^{ISS} = \left|\frac{D\bar{B}_k}{2\omega_I}\right| R_{2e}(4R_{2e}^2 + \hat{P}_{3k}^2)^{-1},\end{aligned} \tag{3.13}$$

where the property $\hat{\dot{\mathcal{D}}}[\hat{X}] + \hat{\dot{\mathcal{D}}}[\hat{X}^\dagger] = \hat{\dot{\mathcal{D}}}[\hat{X} + \hat{X}^\dagger]$ is used.

3.6 Interpretation of the Effective Rates

In the form of EQs. 3.12 & 3.13, the rates give a transparent understanding of the mechanisms underlying CE dynamics. In this section each of the rates will be discussed in detail. The rates $\hat{\bar{\Gamma}}^{S_1}$, $\hat{\Gamma}_k^I$, $\hat{\Gamma}_k^{SI}$, $\hat{\Gamma}_{kk'}^{II}$ & $\hat{\Gamma}_k^{ISS}$ are operator-valued, which means that they depend on the state of the entire system. They therefore modulate the dynamics differently at different stages in the evolution.

- $\Gamma_{1\pm}^S$: Describes the longitudinal relaxation of the first electron that drives it back to thermal equilibrium. Since longitudinal processes reshuffle the populations of Zeeman eigenstates, they are mediated by the spin flipping operators $\hat{S}_\pm$. The up and down rates are unevenly weighted by the thermal polarisation. At

maximal polarisation (p_{th}), the flip up rate vanishes and the spin is driven into the spin-down state only. When the polarisation is negligible, the up and down rates are equivalent and the spin is not preferentially driven into either of its two spin states.

- $\hat{\bar{\Gamma}}^{\text{S}_1}$: Describes the saturation of e_1 by the on-resonance microwave irradiation. When the microwave irradiation is strong, this term dominates over $\Gamma^{\text{S}}_{1\pm}$ and the up and down flips become equally probable. The resulting dynamics are rapid spin flips of e_1. The dependence of $\hat{\bar{\Gamma}}^{\text{S}_1}$ on the electron dipolar coupling D and hyperfine interactions A_{1k} and b_{k1} implies that strong coupling of e_1 to any of the surrounding spin ensemble leads to a less efficient saturation process.

- $\Gamma^{\text{S}}_{2\pm}$: The first term in this rate describes the longitudinal relaxation of the second electron. Recall from FIG. 3-1 that this rate helps lead to nuclear polarisation enhancement by driving e_2 to thermal equilibrium. Here the imbalance between the flip up and flip down rates is crucial because it ensures that the second electron always drives the system into the same states (nuclear spin-up in the case of FIG. 3-1).

  The second term is a perturbative correction to the relaxation due to the microwave irradiation, which tilts the quantisation axis of e_2 away from the Zeeman axis. The perturbation corrects for this by approximating the dynamics in a diagonal frame.

- $\hat{\Gamma}^{\text{I}}_k$: As with the electron rates, the first term in the nuclear relaxation rate describes relaxation back to thermal equilibrium. Since the thermal nuclear polarisation is negligible, the nuclear relaxation rate is not weighted.

  The second term is a perturbative correction accounting for tilting of the nuclear quantisation axis away from the Zeeman axis. In the nuclear case this is caused not by the microwave irradiation but by the pseudo-secular hfi. This term is not relevant for nuclei far removed from the electrons, where the hfi is negligible. In proximity to the electrons however, the state of the electrons will affect the nuclear relaxation. Paramagnetic relaxation is discussed extensively in the

experimental chapters.

- Γ^{SS}: Effective cross-relaxation between the two electrons due to the dipolar coupling between them. This rate is constant and results from the projection of the dynamics onto the Zeeman subspace. The presence of the transverse electron relaxation rate $R_{2\mathrm{e}}$ suggests that the underlying processes leading to the cross-relaxation are of a coherent nature.

- $\hat{\Gamma}_k^{\mathrm{SI}}$: Interaction rate between the unsaturated electron and a nucleus. It is equivalent to the SE polarisation transfer rate and describes diffusive dynamics. The presence of this rate in the CE dynamical equation shows that the SE is active even under CE conditions. The dependence of $\hat{\Gamma}_k^{\mathrm{SI}}$ on the nuclear and electronic transverse relaxation rates shows that, even though the effective dynamics are modelled by classical rate equations, the underlying processes are quantum mechanical. The coefficients $\hat{P}_{2k}$ are operator-valued and depend on the bulk polarisation. Since it appears in the denominator, it is clear that as the bulk polarisation increases, the double flip electron-nuclear rate decreases. This manifests in the polarisation buildup curve as a slowing of the dynamics as the nuclear steady state is approached.

- $\hat{\Gamma}_{kk'}^{\mathrm{II}}$: The nuclear interaction rate is responsible for propagating nuclear polarisation within the bulk via spin diffusion. The bulk nuclei are far from the electrons and cannot be polarised by them directly since they don't 'see' them. The operator-valued coefficient $\hat{P}_{kk'}$ has a dependence on the difference in secular interaction between two spins. This dependence arises from the shifting of nuclear Larmor frequencies due to their coupling to the electrons. If the frequency difference is large, the nuclear interaction is quenched and the spin diffusion mechanism inefficient. This is because spins that are far off resonance from each other do not interact efficiently.

- $\hat{\Gamma}_k^{\mathrm{ISS}}$: Triple spin flip operator mediating the CE. It is indirectly dependent on the microwave irradiation amplitude and offset from CE resonance through the

operator-valued coefficient $\hat{P}_{3k}$. The rate is reduced if the difference between the secular couplings to each electron is large, especially as the ensemble becomes more polarised. There is also a dependence on the squares of the pseudo-secular hyperfine interactions of a nucleus with each electron. If the hfi is strong, the rate is reduced.

The jump rates Γ^{SS} and $\hat{\Gamma}_k^{\mathrm{ISS}}$ should be much smaller than $R_{2\mathrm{e}}$ to ensure that separation in time scales is significant and the polarisation dynamics are well-approximated by longitudinal dynamics.

3.7 kMC Algorithm Implementation

Elimination of coherences means that the system dynamics can be described by classical rate equations that only affect the dynamics of the populations in Hilbert space. This in turn means that the kMC algorithm described in Section 2.5 can be applied as follows:

1. The first step is to create a spin system and define all parameters. This includes interaction parameters, which are determined from the geometry of the spin system, system parameters, such as T_1, T_2, ω_1, & Δ, and simulation parameters such as the number of trajectories to average and the duration of the simulation experiment.

2. Next, the system configuration is initialised based on the Boltzmann distributions of the electrons and nuclei. This must be done at the beginning of each trajectory because some of the rates are operator-valued and therefore depend on the exact up-down configuration of the spins at a given point in time.

3. Once the state of the system has been set, all jump rates described in Section 3.6 can be calculated. These are then collected in a cumulative sum normalised to one. In this way, rates that have a higher value make a larger contribution to the sum and are therefore statistically more likely to be selected.

4. Next, two random numbers r_1 and r_2 are generated from a uniform random distribution in the interval (0,1]. The first of these numbers is used to calculate the time to the next jump operation:

$$\Delta t = \frac{-\log r_1}{\sum_i \Gamma_i},$$

where $\sum_i \Gamma_i$ is the sum over all the possible jump rates in the system. Using a variable time step like this ensures that the dynamics are sampled efficiently without being under-sampled.

5. r_2 on the other hand is used to determine which jump process takes place in the current time step. The jump rate selected is the first to have a value greater than r_2 in the cumulative rate vector created in step 3.

6. Once the selected jump is carried out, operator-valued rates must be re-evaluated for the new system configuration, since one, two or three spins could have flipped in the jump process.

7. Steps three to six are repeated until the sum of all the time steps reaches the chosen duration of the experiment. This is one trajectory.

8. Steps three to seven must be repeated until a meaningful number of trajectories has been averaged. This last step is crucial. If the number of trajectories averaged is too small, the dynamics are noisy and do not converge to the true value. Conversely, there is no need to continue adding trajectories after the desired convergence criteria have been met. Simulations in Chapter 4 were terminated after the discrepancy between successive averages was less than 5%.

Chapter 4

Application of the kinetic Monte Carlo Algorithm

In this chapter the simulation results of static CE DNP dynamics are discussed. The first section uses the full master equation (EQs. 2.8, 2.9 & 2.12) to study the dependence of CE efficiency in a 3-spin system on a number of CE parameters. In the second section, the Zeeman projection is compared to the full LvN equation for a 5-spin system. The third section returns to the 3-spin system to examine how various parameters affect the polarisation dynamics. In these three sections the system has to be kept small due to the exponential complexity scaling of the CE DNP problem. The fourth section then applies the kMC algorithm developed in the previous chapter to study the dynamics of a 120-spin system. The simulation is shown to scale polynomially rather than exponentially with respect to system size. Finally, the last two sections examine how the geometry of a 125-spin nuclear ensemble affects the polarisation process. All simulations assume proton spins.

4.1 Cross Effect DNP Efficiency

The primary aim of these small-scale simulations is to determine an appropriate parameter regime for CE DNP. Since the full master equation is used, each of the three DNP mechanisms (CE, SE, and TM) can be active under the right conditions. Sim-

plifications have been made by choosing a geometry that minimises interactions. By placing the proton far from e_1, and at the magic angle ($\theta_{\mathrm{M}} = \arccos 1/\sqrt{3}$) with respect to the static field, it is coupled to e_2 only and the secular hfi is zero (refer to EQ. 2.14). The proton need not be coupled to both electrons for the CE to be active. In fact, the dependence of $\hat{\Gamma}^{\mathrm{ISS}}$ on $\bar{B}_k$ suggests that it is favourable to be coupled to one of the electrons only. The proton is coupled to the second electron because, due to its ω_{I} offset from the microwave frequency, the SE mechanism is also active in this case and can be made the sole DNP pathway by letting $D = 0$. The secular hfi is set to 0 because, although it does affect the CE efficiency, it acts as an offset, and does not directly contribute to the CE DNP transfer process.

The effect of 4 parameters on the CE efficiency will be shown in the next section: the electron dipolar interaction D, the microwave irradiation strength ω_1, the electron transverse relaxation $R_{2\mathrm{e}}$, and the temperature T, which also affects the electron longitudinal relaxation $R_{1\mathrm{e}}$. In all cases the electron polarisation difference (Δp_{e}) is plotted since efficient CE DNP equilibrates the nuclear polarisation (p_{n}) with Δp_{e}. In this and all future simulations, the electron polarisation and nuclear polarisation enhancement are normalised to the electron thermal polarisation.

4.1.1 Electron Dipolar and Pseudo-secular Hyperfine Interactions

Along with the pseudo-secular hfi, the electron dipolar interaction mediates the CE triple spin flip. If its strength D is too weak, the electrons do not communicate well and the less efficient SE DNP process dominates ($\hat{\Gamma}_k^{\mathrm{SI}} > \hat{\Gamma}_k^{\mathrm{ISS}}$). If it is too strong, the states of the electrons become strongly coherent and they begin to act as one. This makes it difficult to saturate just one of the electrons, even when the microwave irradiation is weak. In this case, thermal mixing can become the dominant process.

The pseudo-secular hyperfine interaction also has an optimal range. Its strength B

must be strong enough to effectively participate in the triple spin flip, but not so strong as to make the saturation inefficient by mixing the electron and nuclear states. Both D and B appear to the fourth power in the denominator of the rate $\hat{\Gamma}_k^{\mathrm{ISS}}$, and quench CE DNP if too strong.

In FIG. 4-1, the effect of $0 < D < 500$kHz is tested for four values of B: 0.1MHz, 1MHz, 2MHz & 10MHz at 1K temperature. Other simulation parameters are given in the caption. Dashed lines show Δp_{e} and solid lines show p_{n}. It is clear that at 1K, the optimal D lies somewhere between 75 to 160kHz, and B should be $\sim$ 1MHz. $D = 100$kHz will be used for the rest of this chapter, and $B = 1$MHz for the rest of this section.

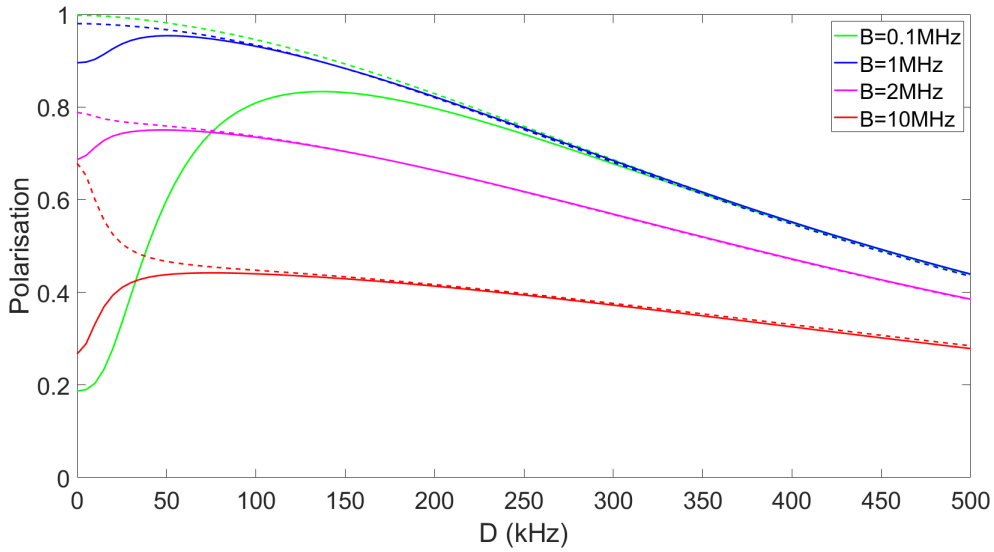


Figure 4-1: 3-spin simulation testing the effect of D and B on the polarisation dynamics. Dashed lines are Δp_{e} and solid lines are p_{n}. Simulation parameters are $B_0 = 3.4$T, $T = 1$K, $\omega_1 = 10$kHz, $T_{1\mathrm{e}} = 1$s, $T_{2\mathrm{e}} = 10\mu$s, $T_{1\mathrm{n}} = 100$s, $T_{2\mathrm{n}} = 1$ms.

In this and the following three figures, the steady state polarisations are plotted as functions of the relevant parameters. The steady states were calculated by evolving the systems until the change in polarisation between successive time steps was less than 1%. This approach works well here because each individual simulation (for example for each value of D) took very little time an the systems quickly reach the

steady state. A better approach for larger systems however, would be to solve EQ. 2.1.6 for the steady state ($\dot{\hat{\rho}} = 0$).

4.1.2 Microwave Irradiation Amplitude

Ideally, the microwave irradiation should saturate e_1 and leave e_2 at approximately thermal polarisation. If the microwave irradiation is too weak, $\Gamma^{\mathrm{S}}_{1\pm}$ dominates over $\hat{\bar{\Gamma}}^{\mathrm{S}_1}$ and e_1 is not saturated. This leads to a small Δp_{e} and thus low nuclear polarisation enhancement. From FIG. 4-2, this appears to be the case for $\omega_1 < 4$kHz. In this regime the nuclear polarisation enhancement is not limited by the electron polarisation difference. The triple spin flip rate is decreased for small ω_1 due to the $D^2 - \omega_1^2$ dependence in the denominator. From about 6kHz onward, the CE becomes active and there is highly efficient polarisation transfer. This continues through to very large ω_1 (see inset), although for irradiation amplitudes exceeding $\sim$ 50kHz, the polarisation starts to decrease. When the microwave strength is too high, the second term in $\bar{\Gamma}^{S}_{2\pm}$ starts to dominate and e_2 becomes saturated as well. The polarisation difference between the electrons is thus reduced, as is the nuclear polarisation, despite the process being highly efficient.

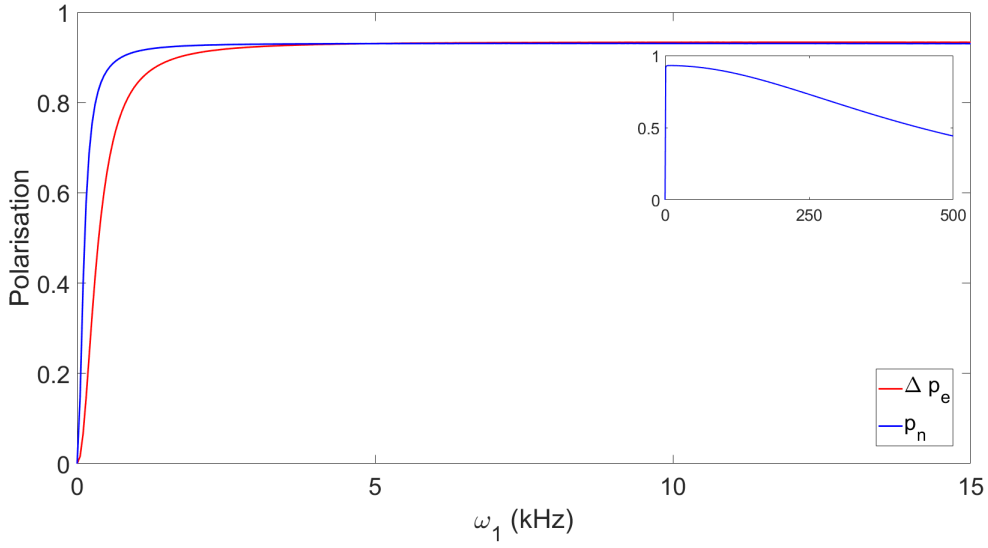


Figure 4-2: 3-spin simulation testing the effect of the microwave irradiation amplitude ω_1 on the polarisation dynamics. Simulation parameters are $B_0 = 3.4\text{T}$, $T = 1\text{K}$, $D = 100\text{kHz}$, $T_{1\text{e}} = 1\text{s}$, $T_{2\text{e}} = 10\mu\text{s}$, $T_{1\text{n}} = 100\text{s}$, $T_{1\text{n}} = 1\text{ms}$, $B = 1\text{MHz}$.

4.1.3 Effect of Temperature

Temperature affects the thermal polarisation of the electrons, which is given by

$$p_{\text{th}} = \tanh\left(\frac{\hbar\gamma_{\text{I}}B_0}{2k_{\text{B}}T}\right).$$

As the temperature increases, thermal energy starts to even out the up and down spin populations, thereby decreasing the thermal polarisation and the maximum Δp_{e}. Crucially, the electron longitudinal relaxation rate also increases with increasing temperature. For efficient DNP, $R_{1\text{e}}$ should be fast, thus allowing the polarisation of many nuclei in a short time. The condition $1 \ll \hat{\eta}_1 \ll \frac{R_{2\text{e}}}{R_{1\text{e}}}$ however, sets an upper limit on how fast $R_{1\text{e}}$ can be without violating the conditions for adiabatic elimination or interfering with the saturation of e_1. If $\Gamma^{\text{S}}_{1\pm}$ dominates over $\hat{\bar{\Gamma}}^{\text{S}_1}$, the up and down flip rates are not equal and e_1 is not saturated. This is seen clearly in FIG. 4-3 for high temperatures (short relaxation times). For very low temperatures on the other hand (slow relaxation times), $R_{1\text{e}}$ is small and the condition $\eta \ll \hat{\eta}_2$ is violated. Note that although in FIG. 4-3 the peak nuclear polarisation is at $\sim 10\text{K}$, 1K temperatures will

continue to be used in some simulations. This is because in this very low temperature regime, the condition $\frac{R_{2e}}{R_{1e}} \gg 1$ is most applicable (refer to FIG. 4-6).

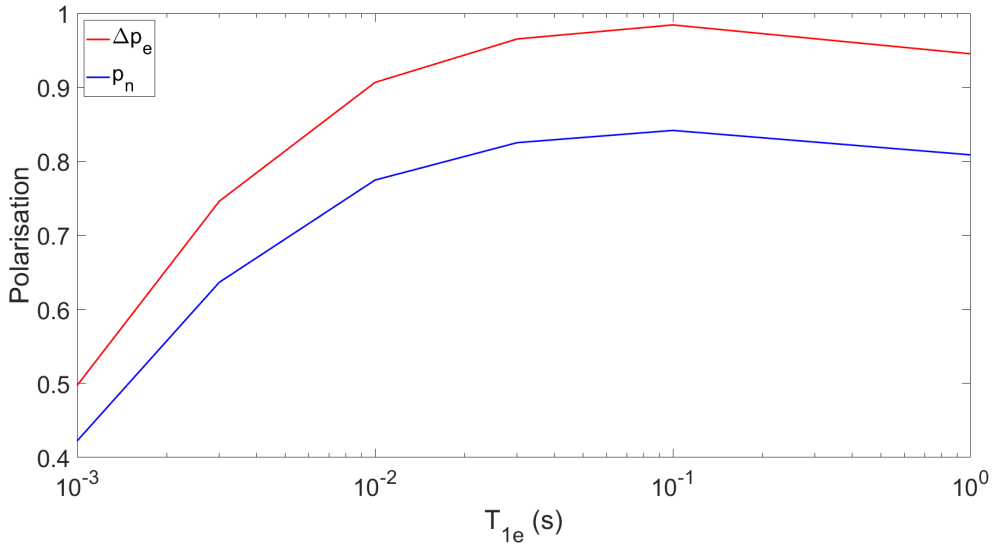


Figure 4-3: 3-spin simulation testing the effect of temperature on the polarisation dynamics. Simulation parameters are $B_0 = 3.4$T, $D = 100$kHz, $\omega_1 = 10$kHz, $T_{2e} = 10\mu$s, $T_{1n} = 100$s, $T_{2n} = 1$ms, $B = 1$MHz. The temperature – T_{1e} relations are (in pairs of [T(K), T_{1e}(s)]): [1, 1], [10, 0.1], [30, 0.03], [50, 0.01], [70, 0.003], [90, 0.001].

The electron longitudinal relaxation time depends not only on temperature, but also on other parameters such as the type of radical. The T_{1e} values given in the caption of FIG. 4-3 are therefore intended as approximate order-of-magnitude indications of T_{1e} only, not as exact values. In REF. [83] for example D. Shimon et al. measured the T_{1e} relaxation time of the biradical TOTAPOL at 3.38T for temperatures between 6K to 40K. They reported T_{1e} values of 0.15s to 1ms respectively. REF. [84] goes to lower temperatures with T_{1e} reported as 13ms, 30ms & 240ms for 20K, 7K & 2.7K respectively for TEMPOL in a 3.34T magnet. F. Mentink-Vigier et al. in REF. [39] use T_{1e}s of 0.1ms to 1ms for TOTAPOL-like simulations at 100K at 9.39T.

4.1.4 Effect of Electron Transverse Relaxation

Following closely from the previous subsection, the effect of the electron transverse relaxation is now studied. R_{2e} is heavily dependent on the immediate environment of the electrons, but is not so much temperature dependent. When R_{2e} is very large (T_{2e} very short), the condition $\frac{R_{2e}}{R_{1e}} \ll \hat{\eta}_2$ becomes difficult to satisfy and e_2 also becomes saturated. If it is too slow, the condition $R_{2e} \gg \Gamma^{SS}, \hat{\Gamma}^{ISS}_k$ is violated, leading to coherent dynamics in the triple spin and electron cross-relaxation jump processes. R_{2e} is present in the denominators of most of the rates, the transfer efficiency therefore decreases with increasing rate.

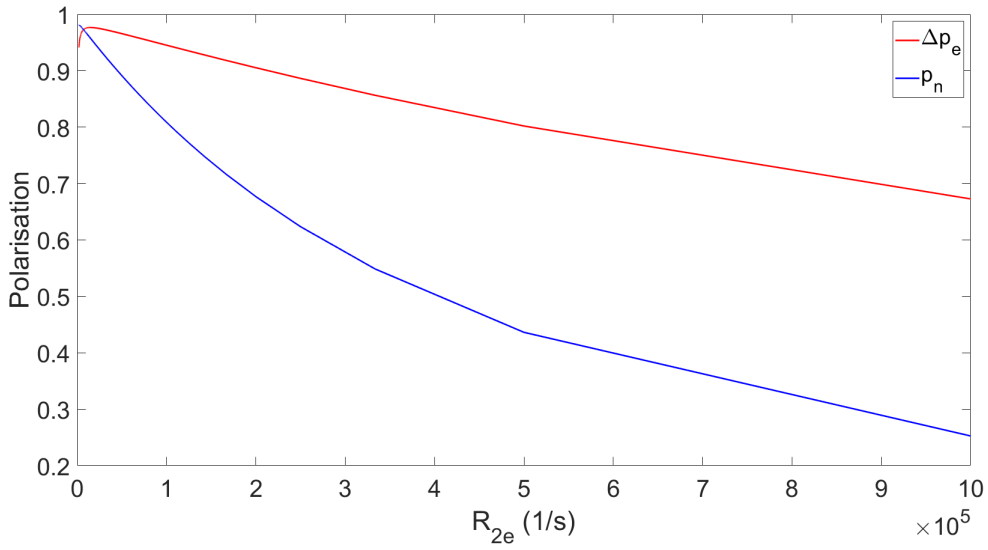


Figure 4-4: 3-spin simulation testing the effect of T_{2e} on the polarisation dynamics. Simulation parameters are $B_0 = 3.4$T, $D = 100$kHz, $\omega_1 = 10$kHz, $T_{1e} = 1$s, $T_{1n} = 100$s, $T_{2n} = 1$ms, $B = 1$MHz.

4.1.5 Discussion

In the last section a parameter regime for efficient CE DNP was found. The dipolar interaction and pseudo-secular hyperfine interactions should be $D \sim 100$kHz and $B \sim 1$MHz respectively, and the microwave irradiation amplitude should be between 6 to 50kHz. Low temperatures with relatively slow R_{1e} are preferable as are relatively low values of R_{2e}. Although a difference between the longitudinal and transverse relaxation rates is required, they should not be too dissimilar. If $R_{1e} \ll R_{2e}$, the condition $\eta \ll \hat{\eta}_2$ becomes difficult to satisfy, and e_2 is also saturated. Conversely, if $R_{1e} \gg R_{2e}$, the condition for adiabatic elimination ($1 \ll \eta$), and for effective saturation of e_1 ($\hat{\eta}_1 \ll \eta$) become difficult to satisfy. The latter condition furthermore requires R_{2e} to be moderate since it is squared in the numerator of $\hat{\eta}_1$. ω_1^2 appears in the denominator of $\hat{\eta}_1$ & $\hat{\eta}_2$ and should therefore also be moderate to ensure that $1 \ll \eta$ and $\eta \ll \hat{\eta}_2$ can be satisfied. Finally, although the pseudo-secular interaction strength does not appear in the CE efficiency conditions, it should be strong enough to participate effectively in the CE triple spin flip, but not so strong as to mix the electron and nuclear states, thereby interfering with the saturation of e_1.

4.2 Error Testing the Zeeman Projection

In this section the Zeeman projection resulting from the adiabatic elimination is error tested by comparison to the full master equation. A 5-spin system consisting of the electrons, two core protons and a bulk proton is used. Section 3.2 provides a definition of the terms core and bulk. Again, the secular hfi is set to zero, and the two core protons interact only with the electron nearest to them. The bulk proton interacts only with the two core protons with $d = 10$kHz. Simulations were also run with $d = 0$ to check how well the Zeeman projection captures spin diffusion. The core protons are coupled to the electrons via the pseudo-secular interaction with $B = 1$MHz. The dipolar interaction between the electrons is varied between $0 < D < 500$kHz. A schematic of the spin system is shown in FIG. 4-5.

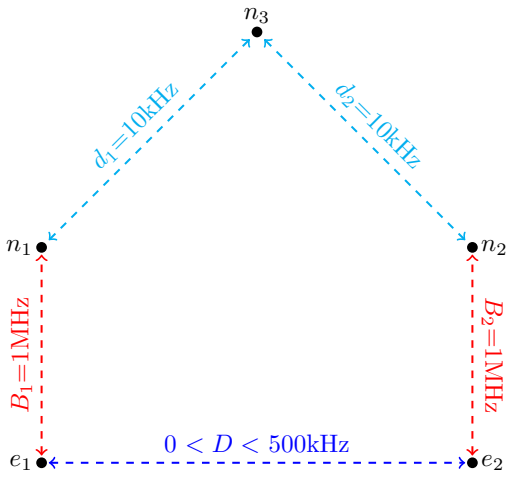


Figure 4-5: 5-spin system used to test the Zeeman projection against the full master equation.

The Zeeman projection and full master equation are compared by their nuclear polarisations p_{ZP} and p_{FE} respectively. The percent difference (Max. % error= $(p_{\mathrm{FE}} - p_{\mathrm{ZP}})/p_{\mathrm{FE}}$) is calculated at the steady state, where the maximal buildup error occurs.

In addition to varying the electron dipolar interaction, different temperatures and microwave irradiation amplitudes are tested. The microwave amplitudes are 5kHz, 10kHz, 15kHz, 20kHz & 25kHz. The temperatures, and corresponding $T_{1\mathrm{e}}$, are given in the caption of FIG. 4-8 along with the remaining parameters.

Results of the 5-spin simulations are shown in FIGs. 4-6 & 4-7 for different ω_1 with and without d respectively, and in FIGs. 4-8 & 4-9 for different temperatures with and without d respectively. Simulations varying ω_1 are performed at 10K, and for the case with d at 1K as well, to demonstrate that at 1K the error is lower. Simulations varying T are performed at $\omega_1 = 10$kHz.

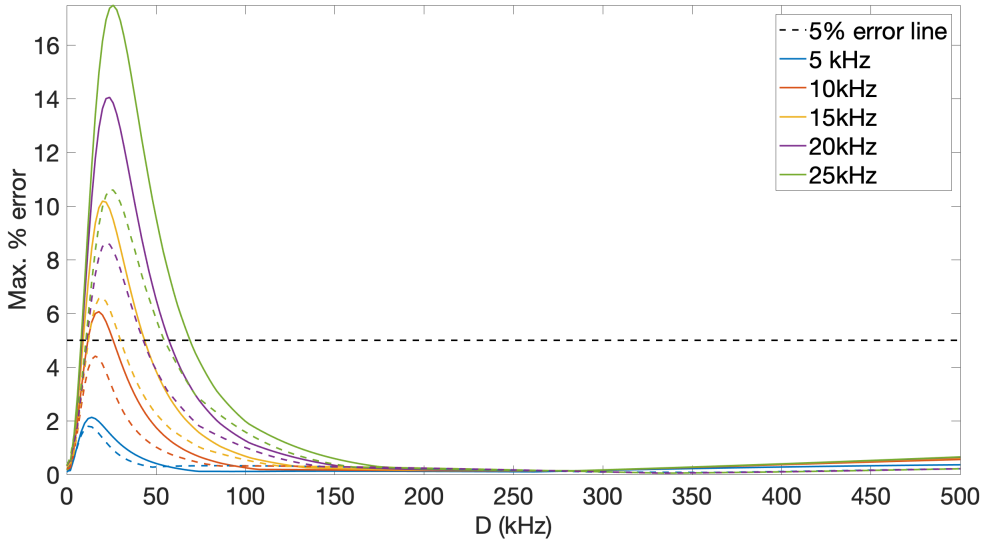


Figure 4-6: Error between Zeeman projection and full master equation for different microwave irradiation amplitudes and T=1K (dashed lines) & T=10K (solid lines). Nuclear dipolar interactions are assumed. The remaining parameters are $B_0 = 3.4\text{T}$, $T_{1\text{e}}(1K) = 1\text{s}$, $T_{1\text{e}}(10K) = 0.1\text{s}$, $T_{2\text{e}} = 10\mu\text{s}$, $T_{1\text{n}} = 100\text{s}$, $T_{2\text{n}} = 1\text{ms}$, $d = 10\text{kHz}$.

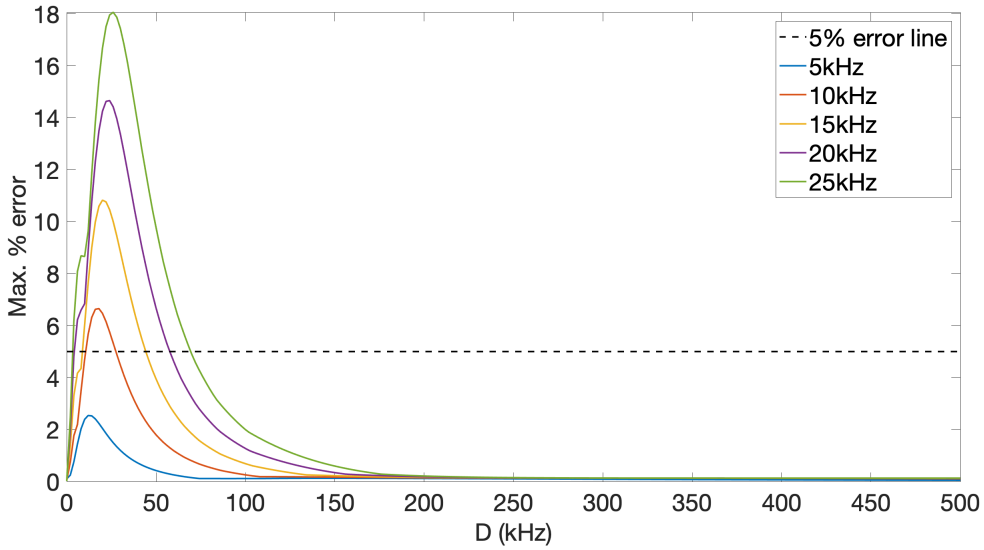


Figure 4-7: Error between Zeeman projection and full master equation for different microwave irradiation amplitudes. No nuclear dipolar interactions are assumed. The remaining interactions are $B_0 = 3.4\text{T}$, $T = 10\text{K}$, $T_{1\text{e}} = 0.1\text{s}$, $T_{2\text{e}} = 10\mu\text{s}$, $T_{1\text{n}} = 100\text{s}$, $T_{2\text{n}} = 1\text{ms}$, $d = 0$.

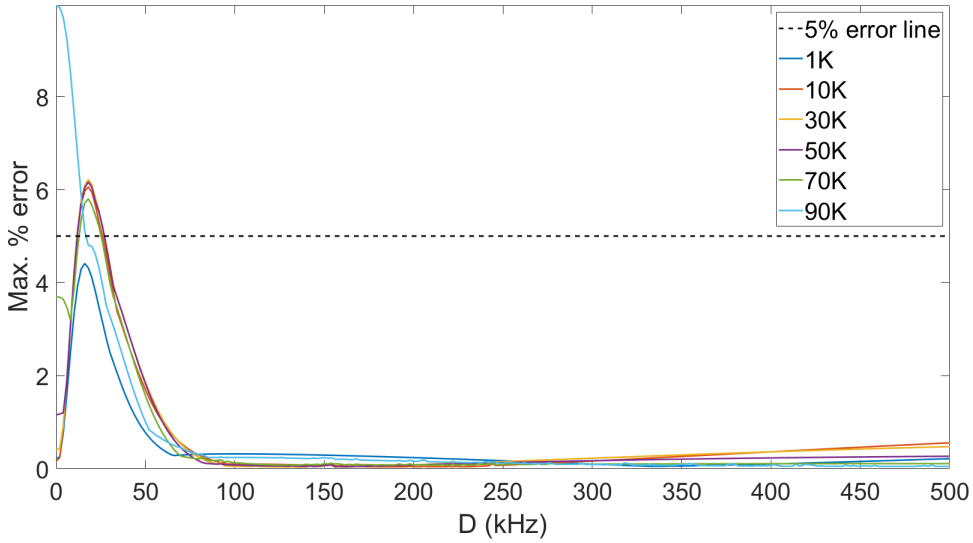


Figure 4-8: Error between Zeeman projection and full master equation for different temperatures. Nuclear dipolar interactions are assumed. The remaining parameters are $B_0 = 3.4\text{T}$, $\omega_1 = 10\text{kHz}$, $T_{2\text{e}} = 10\mu\text{s}$, $T_{1\text{n}} = 100\text{s}$, $T_{2\text{n}} = 1\text{ms}$, $d = 10\text{kHz}$. The temperature - $T_{1\text{e}}$ relations are (in pairs of [T(K), $T_{1\text{e}}$(s)]): [1, 1], [10, 0.1], [30, 0.03], [50, 0.01], [70, 0.003], [90, 0.001].

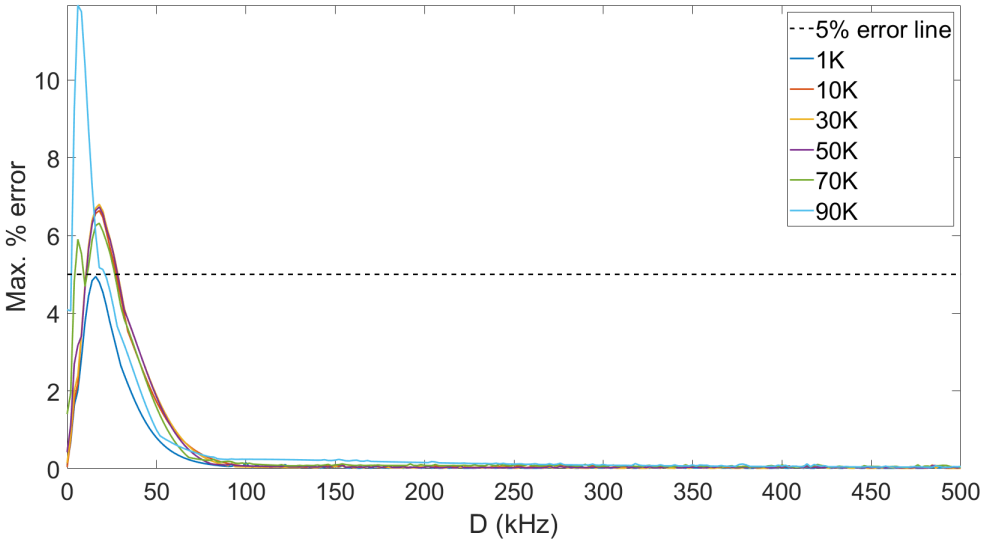


Figure 4-9: Error between Zeeman projection and full master equation for different temperatures. No nuclear dipolar interactions are assumed. The remaining interactions are $B_0 = 3.4\text{T}$, $\omega_1 = 10\text{kHz}$, $T_{2\text{e}} = 10\mu\text{s}$, $T_{1\text{n}} = 100\text{s}$, $T_{2\text{n}} = 1\text{ms}$, $d = 0$. The temperature - $T_{1\text{e}}$ relations are (in pairs of [T(K), $T_{1\text{e}}$(s)]): [1, 1], [10, 0.1], [30, 0.03], [50, 0.01], [70, 0.003], [90, 0.001].

4.2.1 Discussion

In all four cases it is clear that for $D < 100$kHz the error is larger. This is because if D is small, the condition $1 \ll \hat{\eta}_1$ becomes more difficult to satisfy. When this condition is not met, the longitudinal and transverse dynamics become mixed by Rabi oscillations and the adiabatic elimination breaks down, since it assumes that the slow longitudinal dynamics can be decoupled from the fast transverse dynamics (refer to Section 3.4.2). $\Gamma^{\mathrm{SS}} \ll R_{2\mathrm{e}}$ may also no longer be true, so the electron flip-flop jumps can no longer be represented by incoherent Markovian processes. Furthermore, for very low values of D, the CE becomes so weak that the SE becomes the dominant process. Note that the SE is always present, but is typically negligible compared to the CE. In FIG. 4-6 the ω_1 dependence is shown for both $T = 1$K and $T = 10$K. Recall from the discussion in Section 4.1.3 that the most efficient CE DNP temperature is approximately 10K. However, it is clear from FIGs. 4-6 & 4-8 that the error at 10K is significantly higher than at 1K. Temperature affects the electron longitudinal relaxation rate. Higher temperatures have higher $R_{1\mathrm{e}}$, so if $R_{2\mathrm{e}}$ is assumed to be temperature independent, high temperatures make the condition $1 \ll \hat{\eta}_1 \ll \eta$ difficult to satisfy. In this case the saturation of e_1 is inefficient and engenders Rabi oscillations, which are not captured by the adiabatic elimination. Finally, lower microwave amplitudes have smaller errors because they make the condition $1 \ll \hat{\eta}_1$ easier to satisfy. Very strong microwave amplitudes lead to mixing of the longitudinal and transverse dynamics.

The temperature dependence of the error is non-monotonic and more complex. At the two extremes of temperature, the two inequalities $1 \ll \hat{\eta}_1 \ll \eta$ (for high temperature) and $\eta \ll \hat{\eta}_2$ (for low temperature) become difficult to satisfy, and at D relevant for CE DNP they have higher error —albeit still small. The interesting behaviour at low D is testament to the complex interplay between the various interaction and relaxation parameters in the system.

In both cases the error is approximately the same for the cases with and without nuclear dipolar interactions, suggesting that the Zeeman projection accurately captures the effect of nuclear spin diffusion. This becomes of importance when studying large spin systems, where the vast majority of nuclei are polarised indirectly by their neighbours rather than being polarised directly by the electrons.

4.3 Steady State Polarisation and Buildup Time

Ultimately, the two parameters of most interest experimentally are the steady state nuclear polarisation (p_{n}) and the buildup time. The buildup time τ_{DNP} is usually taken to be the time constant of the exponential buildup (and will indeed be used as such later in this chapter), but is defined here as the time $\tau_{90\%}$ taken to reach 90% of the steady state. Using this definition of the buildup time, $\tau_{90\%}$ is not limited to monoexponential buildup curves but can reasonably be applied to biexponential buildups, which would have two independent τ_{DNP}. The goal of DNP is to increase the steady state polarisation by orders of magnitude to maximise enhancement (ϵ_{DNP}). However, this is only useful experimentally if the steady state is reached in a reasonable time. Long buildup times are the consequence of a weak dipolar network in the bulk. They lead to time consuming experiments and more loss of polarisation in the transfer process due to nuclear relaxation. The steady state polarisation is more subtle. It critically depends on the efficacy of the DNP process in the core. The polarisation in the core must then be efficiently transferred to the bulk, where the dipolar network propagates it to the outer reaches of the system. If any one of these steps is ineffective, the steady state polarisation is negatively affected.

To create a truly experimentally relevant DNP model system, there must be a careful balance between the steady state nuclear polarisation and $\tau_{90\%}$. FIGs. 4-10 to 4-13 show the buildup curves for some select values of D, B, T & ω_1 for the 3-spin system in Section 4.1. These simulations are all performed at 1K. The polarisation of the saturated electron is shown in dashed lines, that of the unsaturated electron in

dotted lines, and the nuclear polarisation in solid lines. The blue nuclear polarisation curves across the four plots have consistent parameters. It should be noted that since only one transfer process is being simulated, the buildup times are very fast. In a larger spin systems more transfer processes are required to reach the steady state and the buildup time is longer. The reader is reminded that the electron polarisations and nuclear polarisation enhancement are always normalised by the electron thermal polarisation.

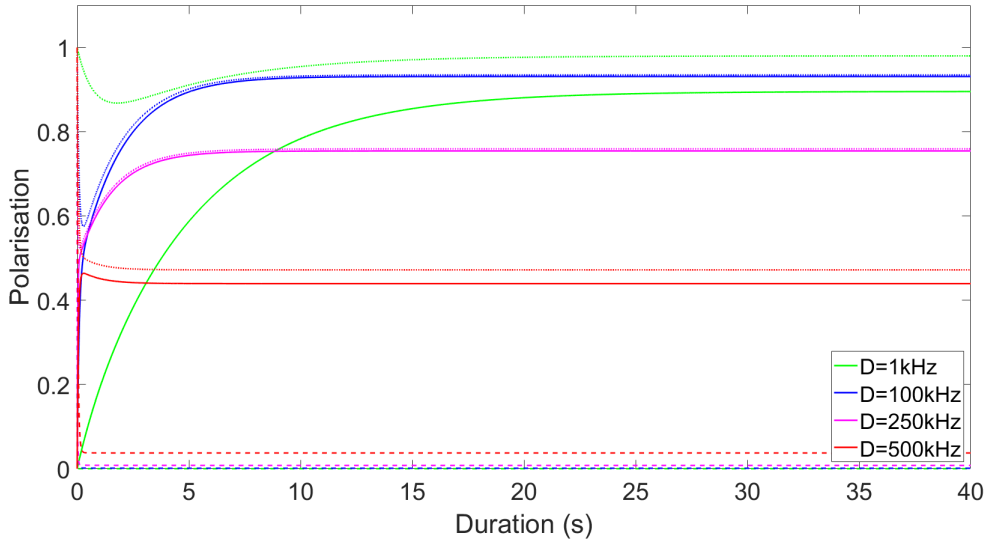


Figure 4-10: Buildup curves for the 3-spin system with $D = 1$kHz, $D = 100$kHz, $D = 250$kHz, and $D = 500$kHz. The remaining parameters are $B_0 = 3.4$T, $B = 1$MHz, $\omega_1 = 10$kHz, $T = 1$K, $T_{1e} = 1$s, $T_{2e} = 10\mu$s, $T_{1n} = 100$s, $T_{2n} = 1$ms. Solid lines are the nuclear polarisation, dashed lines are the polarisation of the saturated electron, and dotted lines are the polarisation of the unsaturated electron.

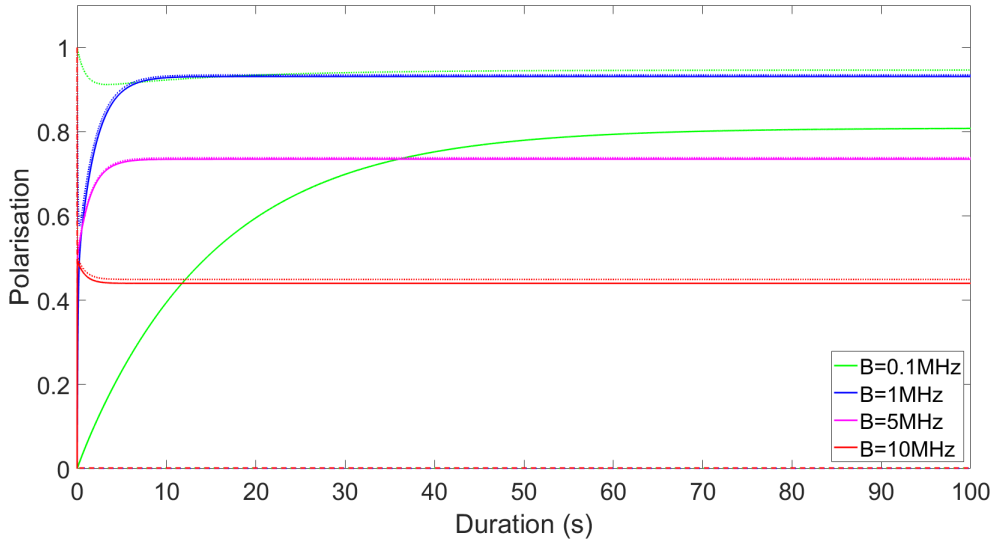


Figure 4-11: Buildup curves for the 3-spin system with $B = 0.1$MHz, $B = 1$MHz, $B = 5$MHz, and $B = 10$MHz. The remaining parameters are $B_0 = 3.4$T, $D = 100$kHz, $\omega_1 = 10$kHz, $T = 1$K, $T_{1e} = 1$s, $T_{2e} = 10\mu$s, $T_{1n} = 100$s, $T_{2n} = 1$ms. Solid lines are the nuclear polarisation, dashed lines are the polarisation of the saturated electron, and dotted lines are the polarisation of the unsaturated electron.

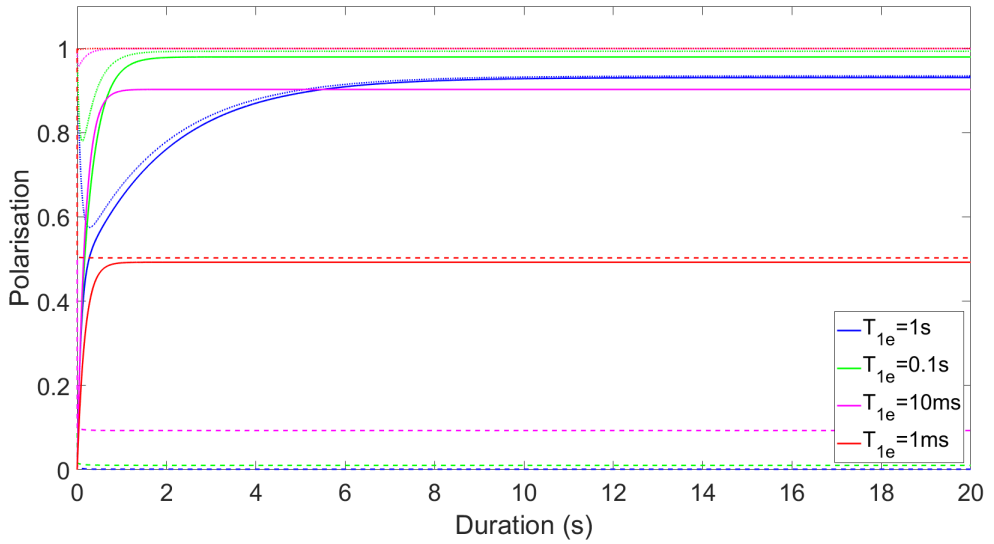


Figure 4-12: Buildup curves for the 3-spin system at $T_{1e} = 1$s, $T_{1e} = .1$s, $T_{1e} = .01$s and $T_{1e} = .001$s. The corresponding temperatures are $T = 1$K, $T = 10$K, $T = 50$K, and $T = 90$K respectively. The remaining parameters are $B_0 = 3.4$T, $B = 1$MHz, $D = 100$kHz, $B = 1$MHz, $\omega_1 = 10$kHz, $T_{2e} = 10\mu$s, $T_{1n} = 100$s, $T_{2n} = 1$ms. Solid lines are the nuclear polarisation, dashed lines are the polarisation of the saturated electron, and dotted lines are the polarisation of the unsaturated electron.

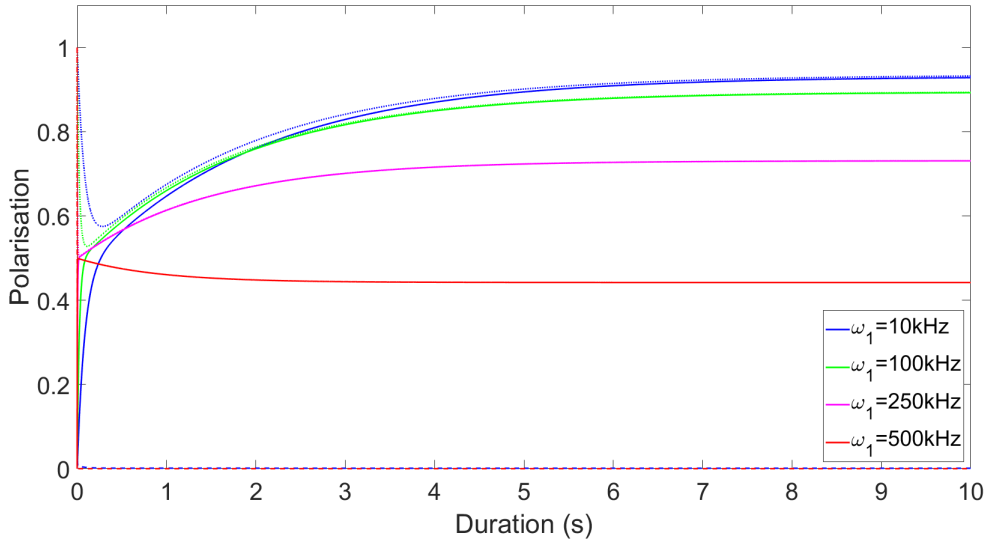


Figure 4-13: Buildup curves for the 3-spin system with $\omega_1 = 10$kHz, $\omega_1 = 100$kHz, $\omega_1 = 250$kHz, and $\omega_1 = 500$kHz. The remaining parameters are $B_0 = 3.4$T, $B = 1$MHz, $D = 100$kHz, $T = 1$K, $T_{1e} = 1$s, $T_{2e} = 10\mu$s, $T_{1n} = 100$s, $T_{2n} = 1$ms. Solid lines are the nuclear polarisation, dashed lines are the polarisation of the saturated electron, and dotted lines are the polarisation of the unsaturated electron.

4.3.1 Discussion

For low values of D, B, and R_{1e}, the condition $\eta \ll \hat{\eta}_2$ becomes more difficult to satisfy and e_2, which is off-resonant with respect to the microwave irradiation frequency, is initially also saturated to some degree. For the microwave irradiation, the opposite is true. The stronger the irradiation, the larger the initial drop in polarisation of e_2. The second electron then recovers its thermal polarisation via relaxation processes.

For low electron dipolar interactions (FIG. 4-10) the buildup time of the nucleus is slow (green solid line) because the triple spin flip rate $\hat{\Gamma}_k^{\mathrm{ISS}}$ is low. The CE is also not as effective as it could be ($p_{\mathrm{n}} < \Delta p_{\mathrm{e}}$) because in this regime $\hat{\Gamma}_k^{\mathrm{ISS}} < \hat{\Gamma}_k^{\mathrm{SI}}$ and the less efficient SE process dominates. As the dipolar interaction increases, so does $\hat{\Gamma}_k^{\mathrm{ISS}}$, and the buildup time decreases to the point where, at $D = 500$kHz, it is almost instantaneous. However, increasing D also increases the electron cross-relaxation rate Γ^{SS} so the electron states become strongly mixed. e_2 therefore also starts to

become saturated. For the case of $D = 500$kHz the interaction is so strong that e_1 becomes less saturated, implying that the condition $\hat{\eta}_1 \ll \eta$ is no longer fully satisfied.

The pseudo-secular hfi (FIG. 4-11) follows a very similar trend. If B is too low, the CE rate is small so the buildup is long. The higher B, the faster the rate, until at $B = 10$MHz it is almost instantaneous. In this case e_1 is always saturated, since neither η nor $\hat{\eta}_1$ are B-dependent.

Temperature (FIG. 4-12) affects not only $T_{1\mathrm{e}}$, but also the electron thermal polarisation (EQ. 2.3). As the temperature increases from 1K (blue) to 90K (red), the thermal polarisation of the electrons drops from ~ 1 to ~ 0.03. This decreases the difference between the flip up and flip down rates ($\Gamma^{\mathrm{S}}_{1\pm}$ and the first term in $\bar{\Gamma}^{\mathrm{S}}_{2\pm}$) of the electrons, in theory making it easier to saturate them. This is true for e_2, which becomes more saturated at higher temperature, where the condition $\eta \ll \hat{\eta}_2$ is more easily achieved. e_1 on the other hand becomes less saturated because, although $\Gamma^{\mathrm{S}}_{1+} \sim \Gamma^{\mathrm{S}}_{1-}$, the condition $\eta \ll \hat{\eta}_1$ is no longer fully satisfied. The buildup time is only slightly affected by the temperature and is dictated primarily by the time it takes e_2 to reach its steady state. The position of the e_2 steady state is governed by the microwave irradiation.

Finally, the effect of the microwave irradiation on the buildup dynamics is studied (FIG. 4-13). The effect on the dynamics of e_2 are quite simple: the stronger ω_1, the more it tips e_2 away from the Zeeman polarisation axis (second term in $\Gamma^{\mathrm{S}}_{2\pm}$) and saturates it, leading to efficient DNP ($p_{\mathrm{n}} \sim \Delta p_{\mathrm{e}}$) with low enhancement. For high ω_1 the saturation of e_2 is almost instantaneous, with the nuclear buildup following closely. e_1 is easily saturated in all cases.

4.4 Many-body kMC Simulation

In this section results from the first large-scale kMC simulation are shown. The choice of geometry will be discussed and the time-savings compared to the full master equation shown. This simulation was run on a 20-core Intel Xeon E5-2690V2 3.00GHz processor. The 120-spin simulation took 18 days to run with 100 trajectories of 600s each per core.

4.4.1 Geometry for Large-scale Simulation

Armed with detailed knowledge of how the DNP parameters affect the nuclear polarisation process, the next step is to find an appropriate geometry. The ideal parameters identified so far are: $B_0 = 3.4$T, $D = 100$kHz, $\omega_1 = 10$kHz, $T = 1$K, $T_{1e} = 1$s $T_{2e} = 10\mu$s, $T_{1n} = 100$s and $T_{2n} = 1$ms. The static field strength corresponds to that of the polariser magnet here at the University of Nottingham. D is equivalent to an electron concentration of approximately 3mM, which is in the range of concentrations used later in this thesis for experiments run on the polariser. The remaining parameters are typical of static CE DNP experiments and simulations as presented in Section 4.1.3.

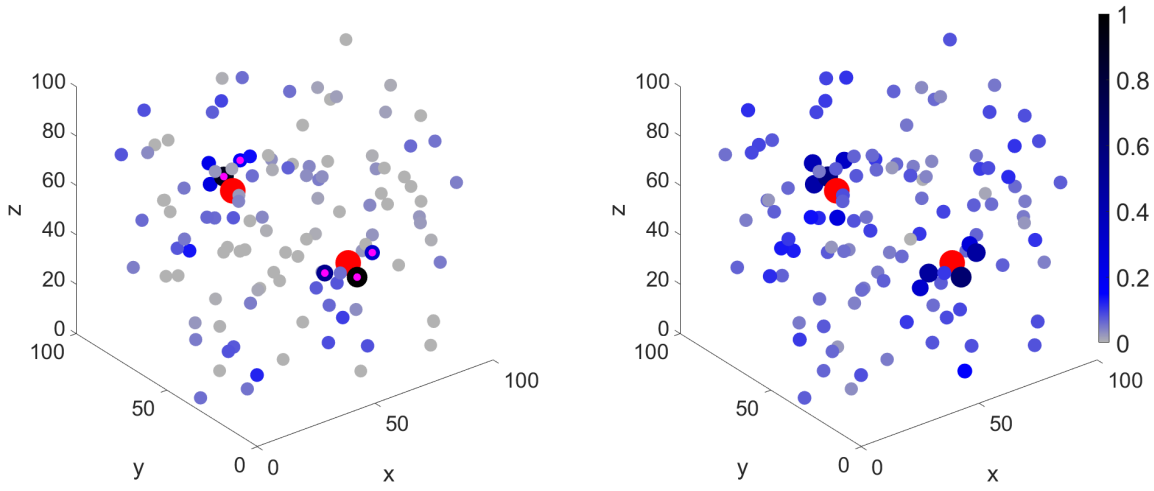
To prevent loss of generality and to avoid symmetry effects, the nuclear spin ensemble is formed of a uniform random distribution of 118 protons with the two electrons in the centre. The random distribution mimics glass formation of the water/glycerol solutions typically used in solid state DNP experiments. To ensure efficient polarisation transfer, two of the core protons (one for each electron) are strategically placed close to the electrons and at the magic angle with the static field. This reduces the secular hfi coupling to zero (EQ. 2.14), therefore facilitating transfer from that proton to neighbouring protons. The only condition placed on the random geometry is that the nuclei should be no closer than 2Å to each other. This is slightly less than the density of pure water or a 50/50 water/glycerol solution (2.5Å). With this proton separation, the average nearest six neighbours proton interaction is ~ 110Hz, and the

average nearest neighbour interaction $\sim$ 490Hz. The protons closest to the electrons are at $\sim$ 6Å to be sure that the secular hyperfine interaction does not exceed 1MHz. This can be achieved experimentally by building 'cages' around the electrons in the mono- or biradical molecules. For Carbon-13 NMR, the cages could for example be formed of bulky aromatic rings such as in Trityl [28]. In proton NMR, the radical molecules can be deuterated such as in deuterated bTbk [85].

Before starting the full 120-spin simulation, the geometry was checked on a random selection of 4 and 10 spins (both times including the two positioned spins) to ensure that it was suitable for efficient CE DNP.

4.4.2 Large-scale Simulation Results

In FIG. 4-14 the spatial distribution of the nuclear polarisation is shown after 10s and 220s. The same simulation as in FIG. 4-14 was run again without nuclear dipolar interactions to demonstrate the importance of spin diffusion in propagating polarisation through the bulk. This is shown in FIG. 4-15



(a) Nuclear polarisation after 10s.

(b) Nuclear polarisation after 220s.

Figure 4-14: Spatial polarisation of the 120-spin system after 10s (FIG. 4-14a) and 220s (FIG. 4-14b). Simulation parameters are $B_0 = 3.4$T, $D = 100$kHz, $\omega_1 = 10$kHz, $T = 1$K, $T_{1e} = 1$s, $T_{2e} = 10\mu$s, $T_{1n} = 100$s & $T_{2n} = 1$ms. 2000 trajectories of the system are averaged to obtain the polarisations at each point in time. The electrons are shown in red. The size and colour of each proton indicate its polarisation. The 5 protons with magenta centres in FIG. 4-14a are the core, for which the CE rate is faster than all other rates.

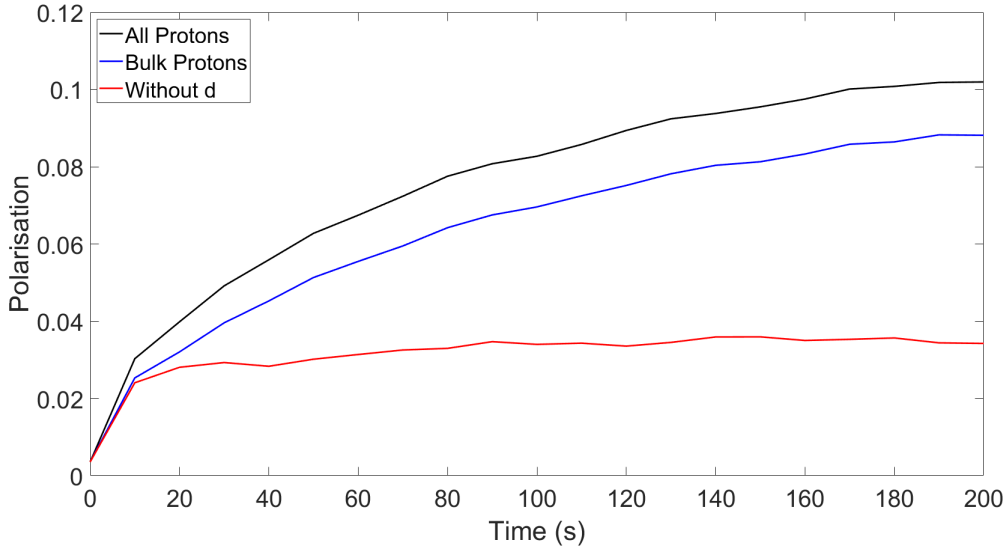


Figure 4-15: Average nuclear polarisation of the kMC simulation with (black) and without (red) nuclear dipolar interactions. $\varepsilon_{\mathrm{DNP}}$ and τ_{DNP} are found by fitting a monoexponential function of the form $p_{\mathrm{I}} = \varepsilon_{\mathrm{DNP}}(1-\exp[-\mathrm{t}/\tau_{\mathrm{DNP}}])$ to the buildup curve. $\varepsilon_{\mathrm{DNP}}$ and τ_{DNP} are 0.12 and 63s respectively for the case with dipolar interactions and 0.04 and 49s respectively for the case without. The blue curve is the buildup with protons hyperfine shifted by more than 25kHz removed.

Discussion

Because the spin system consists of both core protons and a significant number of bulk protons in a random spatial distribution, it can be used to study spin diffusion in a glassy matrix. To the author's knowledge this had not yet been possible to the same extent at the time of publication. Hovav, Feintuch & Vega published a paper in 2011 focusing on DNP-assisted spin diffusion in the SE [24]. However, their system consisted only of one electron hyperfine coupled to one core nucleus, which in turn was dipolar coupled to a linear chain of 8 bulk nuclei. With A. Karabanov's formalism, it is possible to take into account the effect of radical and solvent geometry at a scale that has not been possible before [29].

The importance of the dipolar network in the bulk is evident in FIG. 4-14. At short times (FIG. 4-14a), only protons in close proximity to the electrons are polarised. These are the core protons (magenta centre), polarised directly by the electrons via

the CE triple spin flip, and their immediate neighbours. The protons next to each electron that have very high polarisation are the two positioned protons. At later times (FIG. 4-14b), the polarisation has had time to travel through the dipolar network of the bulk and reach nuclei remote from the electrons. Although virtually all protons have enhanced their polarisation, the enhancement is not uniform. Protons that still have a very low polarisation after 220s, when the system has almost reached the steady state, lie in 'holes' in the dipolar network. They are not well-connected to other protons and therefore struggle to acquire polarisation before it relaxes. The effect of the dipolar network will be discussed in more detail in the next two sections.

The plots in FIG. 4-15 show the enhancement of the nuclear ensemble's polarisation with (black) and without (red) nuclear dipolar coupling. When the dipolar coupling is zero, the enhancement is much lower and the buildup faster. This scenario corresponds to FIG. 4-14a in that only the core protons (and some of their immediate neighbours) become polarised. Since they are strongly coupled to the electrons, this process happens quickly and the system soon reaches its steady state. The case with dipolar coupling is more similar to FIG. 4-14b. The enhancement is much higher because all spins in the dipolar network receive some enhancement. The buildup time however, is now much longer because the system is continuously evolving as the polarisation moves outwards. The buildup in this case depends mostly on the strength of the dipolar coupling between protons. If the coupling is strong, transfer is fast and the buildup short. Pockets of isolated spins however have weak dipolar interactions, thus slowing the buildup time and decreasing the average enhancement. This will become clearer in the next sections where the geometry of the bulk is examined in more detail. Another factor impacting the buildup time is the nuclear relaxation. If it is fast compared to the dipolar interaction pathways, it relaxes polarisation before it can be transferred. The buildup curve then becomes more similar to that in the absence of dipolar coupling.

From an experimentalist's perspective, it is the behaviour of the bulk polarisation

that is of interest because this is what is measured. The resonance of nuclei in the core is strongly hyperfine shifted by the secular hfi and therefore usually falls outside the receiver bandwidth of the pick-up coil. The blue line in FIG. 4-15 shows the average polarisation enhancement when protons hyperfine shifted by more than 25kHz are removed. This corresponds to 5 protons, 3 of which belong to the core. It is evident that the removal of these protons not only reduces the overall enhancement, but also leads to a slower buildup, since many of the core protons, which are efficiently polarised, have been removed.

The ability to perform many-body simulations that encompass a large proportion of bulk nuclei opens the door to experimentally relevant simulations. It is now possible to target specific DNP parameters (similarly to the first few sections of this chapter) and see how they affect the bulk dynamics. In Sections 4.5 & 4.6, the kMC algorithm will be used to study how solution geometry and biradical design affect static CE DNP.

4.4.3 Time Saving with kMC Algorithm

To pose an advantage compared to simulation of the full master equation, the simulation time of the kMC algorithm should scale less than exponentially with the number of spins in the system. If this is the case, it is possible to simulate systems even larger than 120 spins. The scaling of simulation time with number of spins is found by simulating 5 to 2000 spins undergoing 500 quantum jumps averaged over 30 trajectories for 19 uniform random geometries. The simulations are averaged over different systems to smooth out geometry effects. Just like with the previous geometry, two spins are optimally located to maximise polarisation transfer. FIG. 4-16 was obtained in a reasonable time frame by simulating over a given number N of quantum jumps (which occur on a fast time scale) rather than simulating over a chosen duration of experiment. Only 6 geometries were run in parallel on the 20-core processor to ensure that it was below capacity. If the computer reaches capacity, memory and power effects that are unrelated to the efficiency of the algorithm start to contribute to the

simulation time.

FIG. 4-16 shows exponential and polynomial fits to the scaling of simulation time with number of spins. All parameters have been kept the same is in FIG. 4-14.

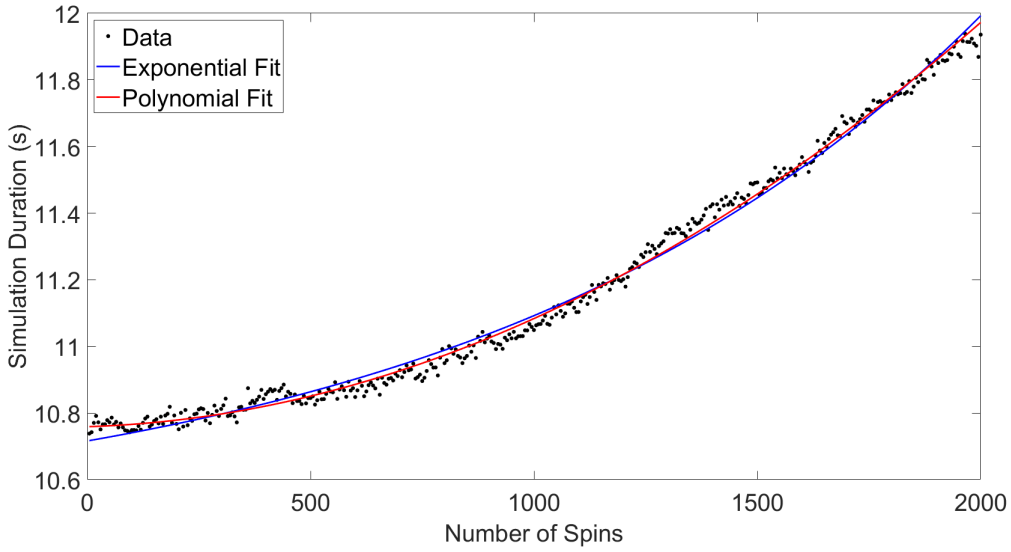


Figure 4-16: Quadratic and exponential fits to simulation time as a function of number of spins. The fit parameters are for a quadratic fit of the form $y = ax^2 + bx + c$ with $a = 2.8\text{e}^{-7}$, $b = 4.2\text{e}^{-5}$, & $c = 10.76$, and a monoexponential fit of the form $y = a * \exp(\text{bx}) + \text{c}$ with $a = 0.27$, $b = 8.7\text{e}^{-4}$, & $c = -10.45$. The R^2 value of the quadratic fit is 0.995 and that of the exponential fit is 0.992.

Discussion

FIG. 4-16 suggests that the polynomial fit is slightly better than the exponential fit ($R^2 = 0.995$ vs. $R^2 = 0.992$), although the difference is small and both overestimate the simulation time for large systems. This may imply that a larger number of spins and/or quantum jumps should be simulated. Since the number of states in the system scales exponentially with system size, polynomial scaling indicates slower growth than the number of states. Furthermore, if the scaling is quadratic, it is proportional to the effective number of kMC jumps in each kMC step; at each step, the number of possible kMC jumps from a particular state is proportional to the square of the number of spins, since each state can have either a single or double spin flip.

The simulation time depends not only on the number of states in the system, but also on the strength of nuclear dipolar interactions. Weak interactions slow down spin diffusion and decrease the effective rates, thereby increasing simulation time.

4.5 Effect of Solution Geometry on Nuclear Polarisation

It is customary in solid state DNP to dissolve DNP radicals in solutions of pure water and some form of glassing agent such glycerol or dimethyl sulfoxide. This mitigates inhomogenous distribution of radicals caused by the water's crystalline lattice pushing impurities to its domain boundaries as it freezes [86]. Glassing agents prevent the formation of a crystal lattice and instead form an amorphous glassy matrix. When the mole fraction of these compounds is high in an aqueous solution, the hydrogen bonds that would typically lead to the formation of a large crystal are perturbed. In a water/glycerol solution for example, the dominant bonds are instead glycerol-glycerol and water-glycerol, which do not form a lattice [87, 88].

In this section the kMC algorithm is used to study how nuclear polarisation dynamics develop as the spin geometry moves from a perfect cubic lattice to a randomised one. 5%, 10%, 15%, & 20% linear randomisations are applied to the cubic lattice to simulate the increasingly broken lattice as more glassing agent is added to a solution. Only geometry-dependent parameters change between solutions, all other parameters are constant. Note that although a cubic lattice has been used here, ice actually forms a hexagonal lattice [89].

Simulations in this section were run on the 20-core processor already mentioned and an additional 16 cores from an Intel Xeon E5-2643 v2 3.30GHz processor.

4.5.1 Creation of Grid Geometry

The starting point for these simulations is an optimised $5 \times 5 \times 5$ cubic grid of protons that is able to accommodate the large separation between electrons while also providing reasonably good DNP enhancement. The grid was optimised using the CE efficiency condition (EQ. 3.9) as a guide. If relaxation rates are chosen from experimental observation and D & ω_1 by considerations of effective DNP, $\hat{\eta}_1$ & $\hat{\eta}_2$ can be tuned through the secular hyperfine interaction. At the high fields relevant to DNP, $\hat{\eta}_2$ is dominated by the nuclear Larmor frequency, and is therefore well approximated by ω_I^2/ω_1^2. The geometry that best satisfies the CE efficiency condition can therefore be found by tuning A_{1k} only, which in turn is adjusted by changing the grid spacing. This can be achieved experimentally by deuterating the solvent and/or radical. To keep the size of the spin grid at a minimum (thereby maximising the nuclear dipolar interactions), the electrons lie on the diagonal of the grid. The angle between the $e-e$ vector and the z-axis is set to $\pi/3$. In the xy-plane the $e-e$ vector is at an angle $\pi/4$.

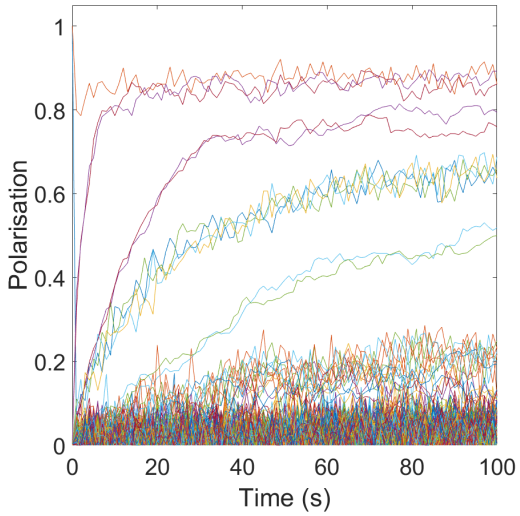
Optimised Spin Separation

Finding the optimal grid spacing for the nuclear spins was an iterative process. For each grid spacing $\hat{\eta}_1$ was calculated using the 8 strongest [i] secular hyperfine couplings. The grid spacing was adjusted until one was found that satisfactorily obeyed $\hat{\eta}_1 \ll \eta$ while providing a suitably strong dipolar network and accommodating the electrons. An optimal grid spacing of 8.4Å was found. This corresponds to 2% water in a heavy water and deuterated glycerol solution, which is perhaps a lower nuclear concentration than would typically be used in low temperature static CE DNP, but is still experimentally relevant. Because the dipolar interaction is quite weak at such large spin separations, the buildup times are long, and the system more susceptible to relaxation losses. This problem can be circumvented by adjusting the relaxation parameters.

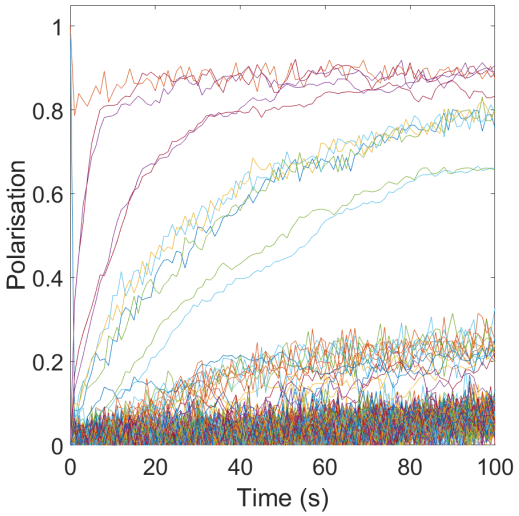
[i] After the 8^{th} strongest interaction, A_{1k} was found to drop off and contribute little to the sum in $\hat{\Delta}_{1,\mathrm{z}_1}$.

Effect of T_{1n}

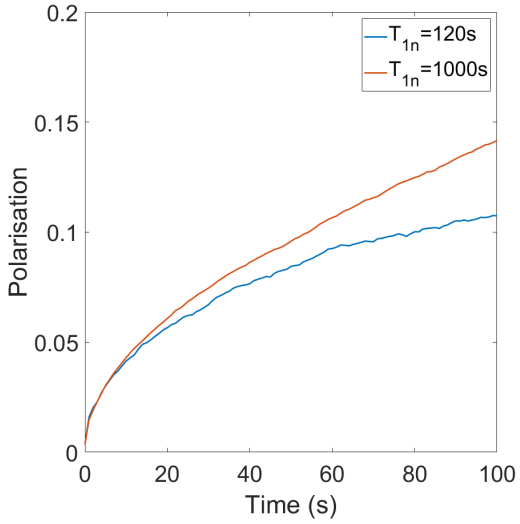
In FIG. 4-17 the nuclear longitudinal relaxation time is increased from $T_{1n} = 120$s to $T_{1n} = 1000$s to counter the effect of the large grid spacing.



(a) Individual spin dynamics, T_{1n}=120s.



(b) Individual spin dynamics, T_{1n}=1000s.



(c) Average spin dynamics.

Figure 4-17: Effect of T_{1n} on polarisation dynamics in the 8.4Å grid spacing geometry. Non-geometric parameters are $B_0 = 3.4$T, $D = 100$kHz, $\omega_1 = 10$kHz, $T = 1$K, $T_{1e} = 1$s $T_{2e} = 10\mu$s, $T_{2n} = 1$ms. 1000 trajectories were averaged to obtain FIGs. 4-17a, where $T_{1n} = 120$s, & 4-17b, where $T_{1n} = 1000$s. In FIG. 4-17c the average nuclear buildup is shown for the two T_{1n}.

FIG. 4-17 is the trajectory representation of FIG. 4-14 (albeit with longer T_{1n}). Like in FIG. 4-14a, it is clear from FIG. 4-17 that only a few nuclei, those well-connected to the electrons, become highly polarised. The vast majority of nuclei have much lower polarisation. The core is unaffected by an increase in T_{1n} because it is polarised very quickly and does not rely on the nuclear dipolar interaction. In the bulk however, there is a clear change in dynamics with the increase in T_{1n}. For $T_{1n} = 120$s the bulk nearly reaches its steady state in the 100s simulation time (FIG. 4-17c), suggesting that the propagation of polarisation has been curtailed by relaxation. For $T_{1n} = 1000$s on the other hand,the bulk has clearly not reached the steady state in 100s. Since the relaxation time is a lot longer, polarisation has time to travel to the further reaches or more weakly connected pockets of the system before it relaxes, the dynamics therefore continue to develop for much longer.

The other relaxation parameters were also adjusted slightly to give good results for this geometry. Still within reasonable experimental values they are: $T_{1e} = 0.2$s, $T_{2e} = 1\mu$s, $T_{1n} = 1000$s, $T_{2n} = 20$ms.

Randomisation of Geometry

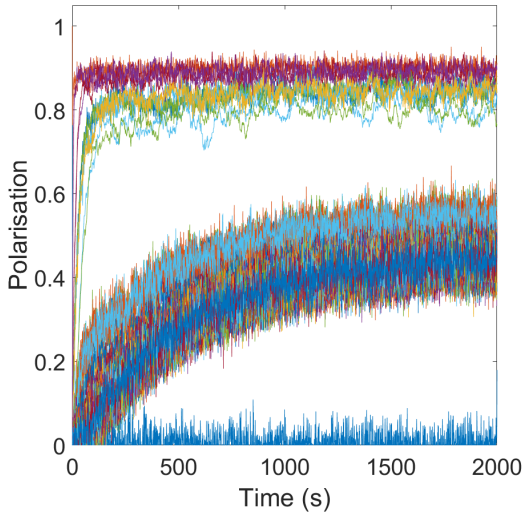
To create the linear randomisation on the position of the spins, an array of random numbers from a normal distribution with a mean of 0 and standard deviation of σ_{ideal} =Randomisation $\times$ 8.4Å was generated for x, y, and z. This array was then subtracted from the perfect spin grid to give the randomised coordinates of the nuclear spins. For each realisation of a geometry, a new set of random numbers was chosen. Matching of the CE conditions was checked for each realisation, as was the actual standard deviation (calculated from the spread of spin separations). Electrons were kept in the same position as for the 0% randomisation case.

4.5.2 Randomisation Simulations

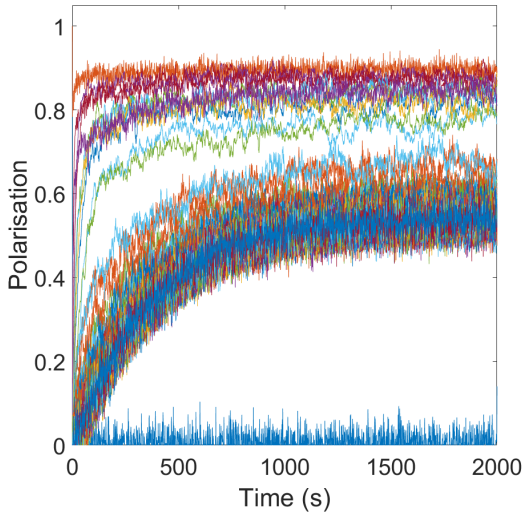
FIGs. 4-18 to 4-20 show the kMC simulations of the 5 solutions. The perfect grid simulation was run only once and averaged over 1200 trajectories. The 5%, 10%, 15% & 20% randomisations were each averaged over 12 different realisations of the geometry, totalling 1176 trajectories. FIG. 4-20b shows the average nuclear polarisations of the 5 solutions. The buildup times are marked by dots and were calculated by applying a biexponential fit to the average polarisation and extrapolating to 8000s to make sure the steady state has been reached. The buildup times and nuclear polarisation enhancements are also shown in TAB. 4.1.

Randomisation	**End Polarisation**	**Buildup Time (s)**
0%	0.49	1051
5%	0.57	789
10%	0.50	1041
15%	0.42	1099
20%	0.39	1058

Table 4.1: End polarisation and buildup time (time to reach 90% of the steady state polarisation) for the 0% to 20% randomisation cases, calculated from a biexponential fit of the form $p_{\mathrm{I}} = a(1 - \exp(t/b) + c(1 - \exp(t/d))$ extrapolated to 8000s to ensure the steady state has been reached.

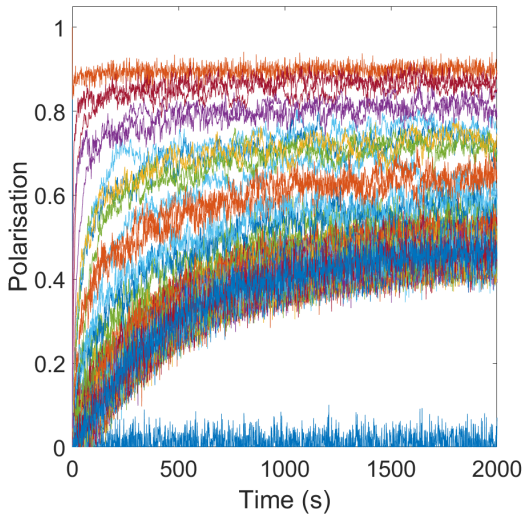


(a) Perfect grid.

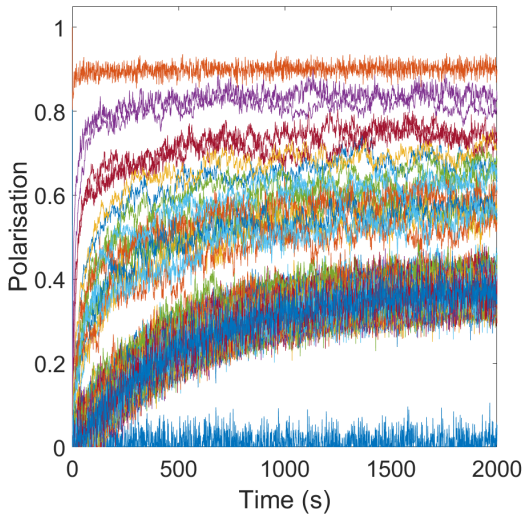


(b) 5% randomisation.

Figure 4-18: Individual spin polarisation in a 125-spin grid with 8.4Å grid spacing. FIG. 4-18a: 0% randomisation, FIG. 4-18b: 5% randomisation. The 0% randomisation simulation is averaged over 1200 trajectories and the 5% randomisation simulation over 1176 trajectories.

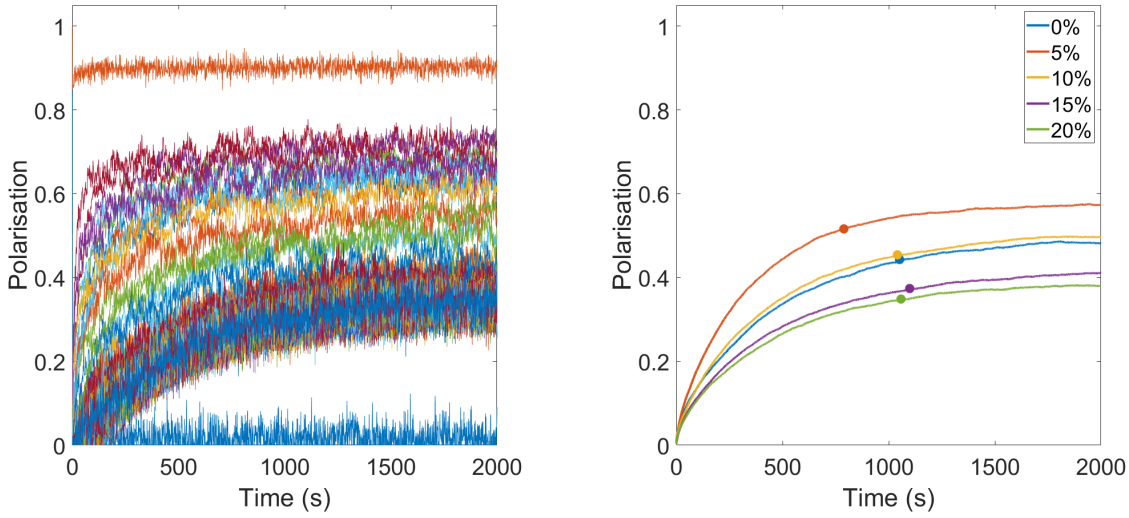


(a) 10% randomisation.



(b) 15% randomisation.

Figure 4-19: Individual spin polarisation in a 125-spin grid with 8.4Å grid spacing. FIG. 4-19a: 10% randomisation, FIG. 4-19b: 15% randomisation. Both simulations are averaged over 1176 trajectories.



(a) 20% randomisation.

(b) Average polarisations 0 – 20%.

Figure 4-20: Individual spin polarisation in a 125-spin grid with 8.4Å grid spacing. FIG. 4-20a: 20% randomisation averaged over 1176 trajectories, FIG. 4-20b: average polarisation buildup for 0% to 20% randomisations. Dots mark the buildup time (time to reach 90% of the steady state polarisation), calculated from a biexponential fit of the form $p_{\mathrm{I}} = a(1 - \exp(t/b) + c(1 - \exp(t/d))$ extrapolated to 8000s.

4.5.3 Discussion

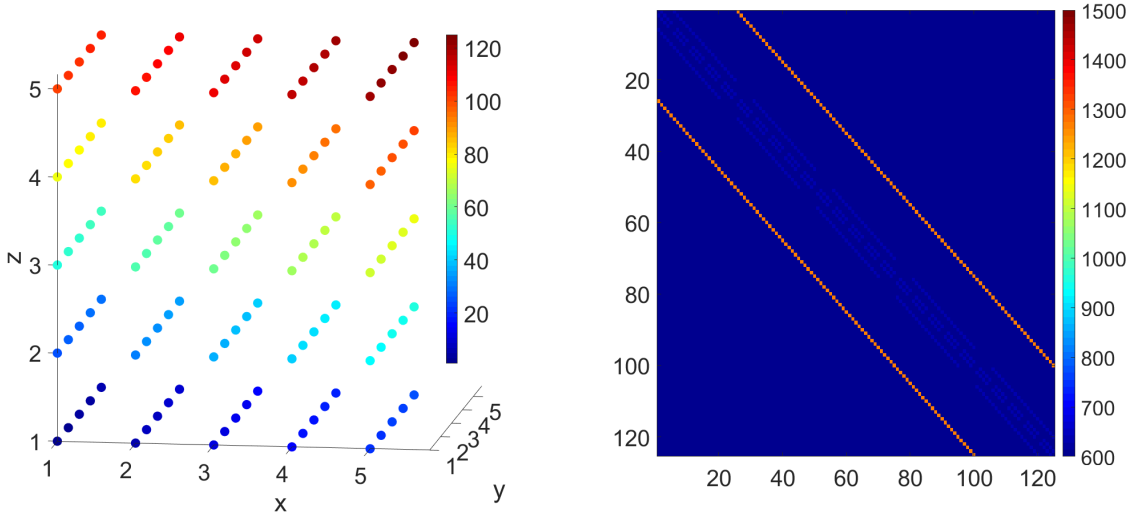
In FIG. 4-18 there is clear clustering of spins into two distinct polarisation groups: one for the core, which is highly polarised with a very fast buildup, and one for the bulk, which is much larger, has slower buildup and lower polarisation. In FIG. 4-20a, the core and bulk are indistinguishable. In the perfect grid geometry, the propagation of polarisation is highly directional, which is why there is such a clear distinction between the core and the bulk. As the randomisation increases, this distinction starts to blur, since protons are no longer confined to sets of equal angle θ to the magnetic field (EQs. 2.13 to 2.15). At high randomisations, protons previously at an unfavourable angle can move to a more favourable angle and vice versa. At 5% and 10% randomisation, the nuclear polarisation is enhanced, and the buildup time shortened compared to the perfect grid, with 5% randomisation giving the optimal result.

The buildup times and end polarisation are given in TAB. 4.1. From 15% randomi-

sation onwards, increasing randomisation leads to less favourable DNP again. The CE efficiency conditions were tested on all 5 geometries and satisfied. To understand why 5% randomisation yields the best DNP, one must therefore turn to the dipolar network.

The ideal case is a perfectly isotropic dipolar network with relatively strong interactions. Then the polarisation can travel quickly and there are no pockets of isolated spins. Clearly, this is not the case for the perfect grid. Although the system is very ordered, the dipolar interactions are highly directional. Polarisation therefore propagates efficiently in a few specific directions, but poorly everywhere else. In a more disordered system on the other hand, pockets of isolated spins form. These have long buildups and low enhancement, thereby reducing the DNP efficiency of the sample. For intermediate randomisations, the distribution of dipolar interactions lies somewhere between these two extremes. Some spins will have moved in such a way to encourage transfer between layers, and some will have isolated themselves. However, since the randomisation is small, the more 'isolated' spins in the system are still connected to the rest of the system and the decrease in transfer to these spins is more than balanced out by the increase in transfer between groups.

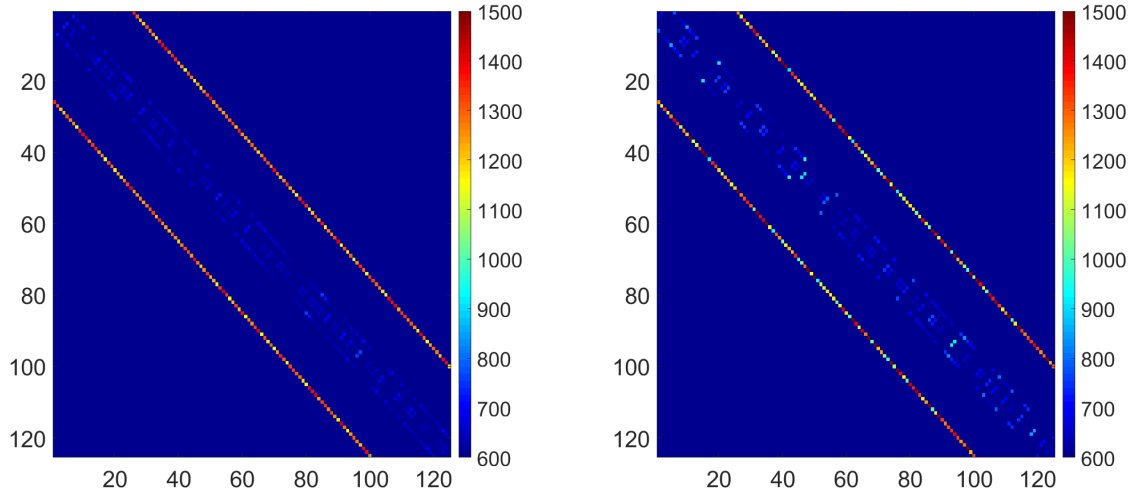
This is easier understood by considering the connectivity matrices for the 5 different solutions (FIGs. 4-21 to 4-23). Each point on these plots corresponds a dipolar interaction of one spin with another. To create better contrast, the map is truncated at 600Hz. The number ordering of the protons is shown in FIG. 4-21a.



(a) Numbering order of protons.

(b) Perfect grid.

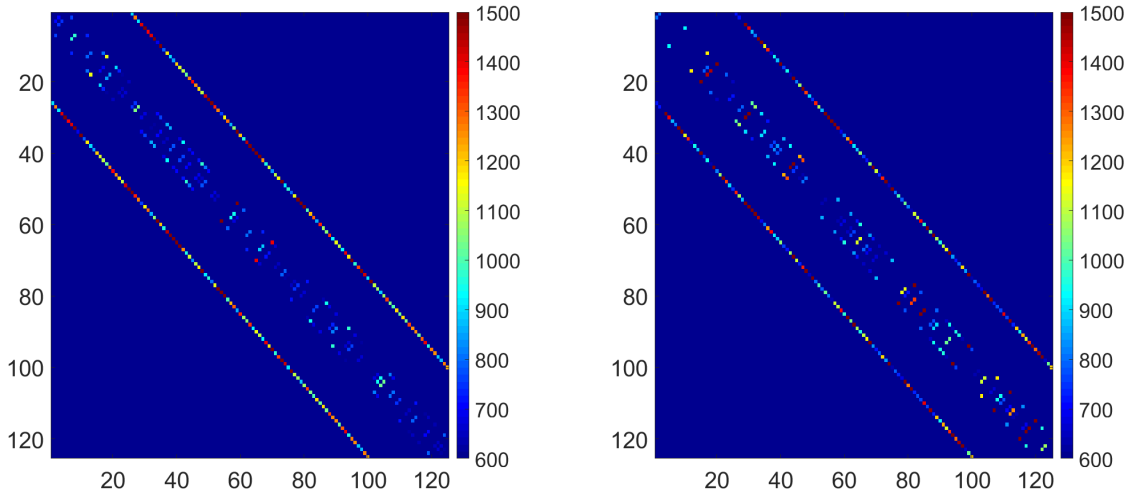
Figure 4-21: FIG. 4-21a: Numbering order of the protons, FIG. 4-21b: connectivity matrix for the perfect grid. The colour scale is in Hz.



(a) 5% randomisation.

(b) 10% randomisation.

Figure 4-22: FIG. 4-22a: connectivity matrix for 5% randomisation, FIG. 4-22b: connectivity matrix for 10% randomisation. The colour scale is in Hz.



(a) 15% randomisation.

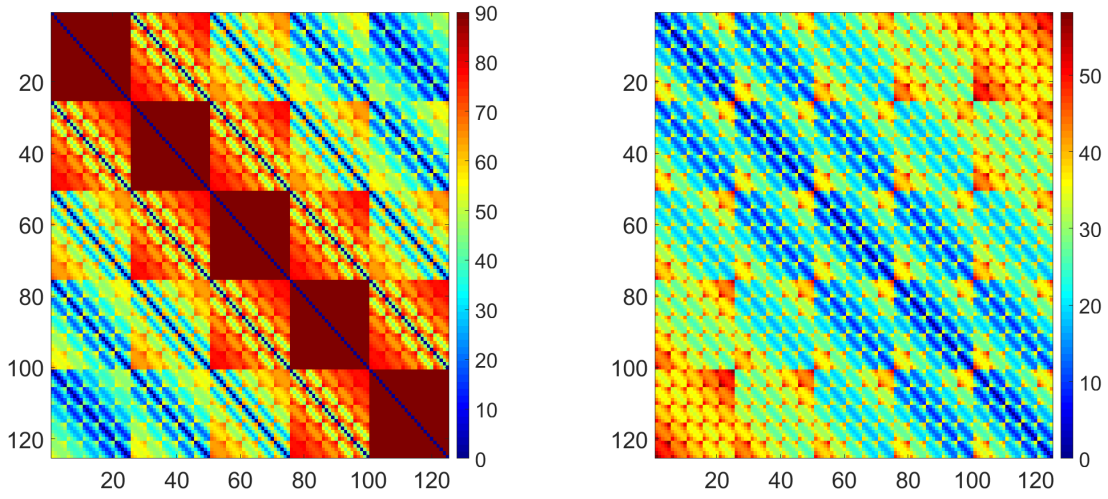
(b) 20% randomisation.

Figure 4-23: FIG. 4-23a: connectivity matrix for 15% randomisation, FIG. 4-23b: connectivity matrix for 20% randomisation. The colour scale is in Hz.

To understand the distribution of dipolar interactions in FIGs. 4-21 to 4-23, it is instructive to look also at the proton separations (r) and the angle formed by the vector connecting a proton pair and the static magnetic field (θ). As a reminder, the nuclear dipolar interaction is given by:

$$d = \frac{\mu_0}{4\pi}\frac{\hbar^2\gamma_I^2}{2r^3}(1 - 3\cos^2\theta),$$

(refer to Section 2.2.2).



(a) Angle matrix.

(b) Distance matrix.

Figure 4-24: FIG. 4-24a: Matrix of proton angles θ in the perfect grid, where θ is the angle between the static field and the vector joining two protons. The colour scale is in degrees. FIG. 4-24b: Matrix of proton distances in the perfect grid. The colour scale is in Å.

FIGs. 4-21 to 4-23 show that each proton interacts significantly (>600Hz) with somewhere between 3 and 6 other protons. In the grid geometry (FIG. 4-21b) there are only two significant interactions strengths. The first is relatively strong at 1274Hz (orange strips), and the second is just over half of this at 637Hz (light blue strips). From FIG. 4-24 these correspond respectively to the nearest neighbours (8.4Å) at angles of 0° and 90°. Propagation is therefore efficient within planes parallel and perpendicular to the static field, but inefficient in all other directions. How quickly polarisation is transferred between the parallel planes depends on the strength of the central light blue strips, since these cut across the parallel planes. For the cases of 5% and 10% randomisation, some of the parallel plane nearest neighbour interactions become slightly stronger, and some slightly weaker (outer strips in FIGs. 4-22a & 4-22b). However, crucially, some of the next nearest neighbours in the perpendicular planes are now better connected, facilitating propagation between orthogonal planes. For the high randomisations (FIGs. 4-23a & 4-23b), some of the interactions become very strong, and some of them very weak. 'Holes' of weak interaction start to appear between nearest neighbours, meaning that some spins are cut off from the rest. These

stop the polarisation from propagating and lead to less favourable DNP.

This section has shown that the addition of a glassing agent that randomises the geometry of the nuclear bulk can affect the bulk polarisation. Typically, glassing agents are used to ensure homogeneous distribution of radical in the sample. The formation of glass however also changes the dipolar network and can therefore be used to modulate transfer efficiency in the bulk. Again, it should be noted that in these simulations a cubic lattice was used, whereas ice forms a hexagonal lattice. However, results for a hexagonal lattice are expected to follow a similar trend, though perhaps with a more complex dipolar structure. The absence of powder averaging, which is so important in MAS DNP simulations, should also be justified. In MAS, the constant re-orientation of the spin ensemble as it goes through a rotor period means that at different points in time, different orientations of electron pairs contribute to signal. In static CE on the other hand, this is not the case, and any electron pairs not oriented favourably with respect to the static field contribute minimally to the signal. There is therefore no need to perform a full powder average since many of the orientations will be negligible in terms of their participation in the DNP enhancement.

4.6 Effect of Radical Geometry on Nuclear Polarisation

In this section the kMC algorithm is used to take a closer look at radical design. The very strong secular hyperfine shift of protons very close to electrons both splits the DNP resonance and quenches spin diffusion. The former can be mitigated by adjusting the microwae frequency, and the latter by constructing 'cages' made of non-DNP active atoms around the electrons of the radical that prevent solution protons from coming too close. Examples of this are the large aromatic rings in Trityl [28] or proton replacement in deuterated bTbk [85]. These 'cages' are simulated by removing protons in pairs (one for each electron) from the immediate environment

of the electrons and seeing how this affects the polarisation enhancement and buildup.

The electrons are in contact with the nuclear ensemble through the secular and pseudo-secular hyperfine interactions. The secular hfi, along with the secular part of the electron dipolar interaction causes a shift in the electrons' resonance frequency (EQ. 3.3), therefore affecting their response to the microwave irradiation. Furthermore, A_{jk} terms show up in the denominators of the CE rate $\hat{\Gamma}_k^{\mathrm{ISS}}$, the SE rate $\hat{\Gamma}_k^{\mathrm{SI}}$ and the microwave saturation rate $\hat{\bar{\Gamma}}^{\mathrm{S}_1}$ [ii]. The polarisation efficiency is therefore expected to be improved if nuclei with high A_{jk} are removed. Conversely, the pseudo-secular interaction appears in the numerator of the above rates. Removing nuclei with high B_{jk} is therefore expected to negatively impact DNP.

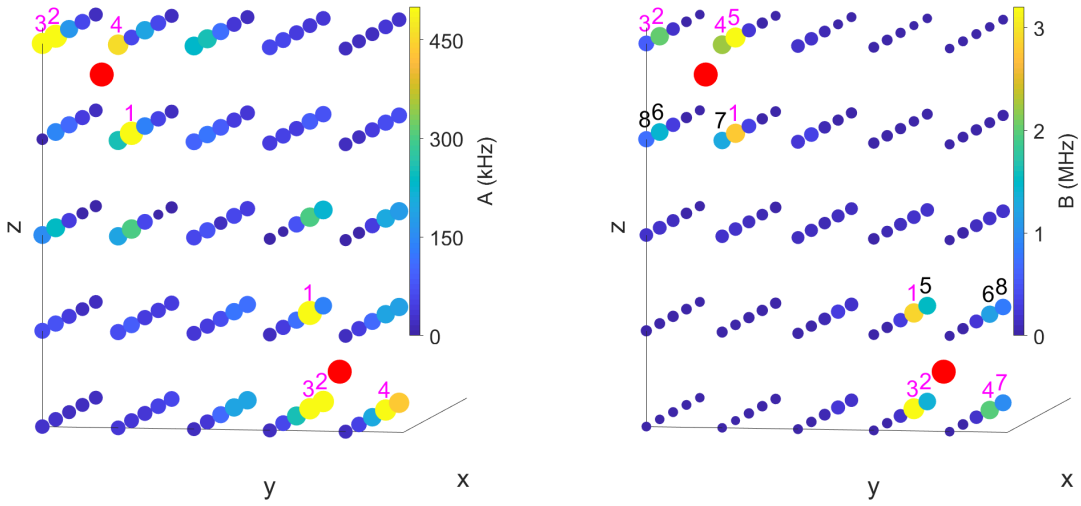
Simulations in this section were run on both the 20-core and the 16-core processors. The geometry used is the most efficient (fastest buildup, highest enhancement) of the 5% randomisation realisations from the previous section with all parameters kept the same. Figures are shown on the perfect spin grid to guide the eye more easily.

4.6.1 Removing Spins

The approximate symmetry of the spin system suggests removal of spins in pairs: one from each electron. Because they are so far apart (∼4.2nm), it is assumed that there is no overlap in the spheres of influence of the two electrons. Changing the immediate environment of one of the electrons should therefore not influence the immediate environment of the other. First, the 4 pairs with the highest secular interactions are removed in decreasing order. All of these spins belong to the core, where the core is defined as those protons for which $\hat{\Gamma}_k^{\mathrm{ISS}} > \hat{\Gamma}_{kk'}^{\mathrm{II}}\ \forall\ k, k'$. This is no surprise since many of them also have high pseudo-secular interactions (which increase $\hat{\Gamma}_k^{\mathrm{ISS}}$), and the secular interaction quenches the spin diffusion rate $\hat{\Gamma}_k^{\mathrm{II}}$. Next, the 4 remaining pairs with the highest pseudo-secular couplings are removed in decreasing order. The order in which the 8 pairs of spins are removed is shown in FIG. 4-25. Magenta

[ii] They are also present in the diffusion rate $\hat{\Gamma}_{kk'}^{\mathrm{II}}$, but this is not the point of discussion here.

numbers correspond to core nuclei. Only 8 protons are removed from each electron since after the 8^{th} proton the hyperfine interactions become very weak and removal of further spins has little effect on the dynamics.



(a) Secular HFI strengths.

(b) Pseudo-secular HFI strengths.

Figure 4-25: Spatial dependence of the secular hyperfine (FIG. 4-25a) and pseudo-secular hyperfine (FIG. 4-25b) interactions. Pairs 1 to 4 correspond to the highest secular hfi, and 5 to 8 to the highest pseudo-secular hfi, in decreasing order. Magenta numbers are core nuclei.

FIG. 4-26 shows the buildup of the bulk polarisation after each pair of spins is removed.

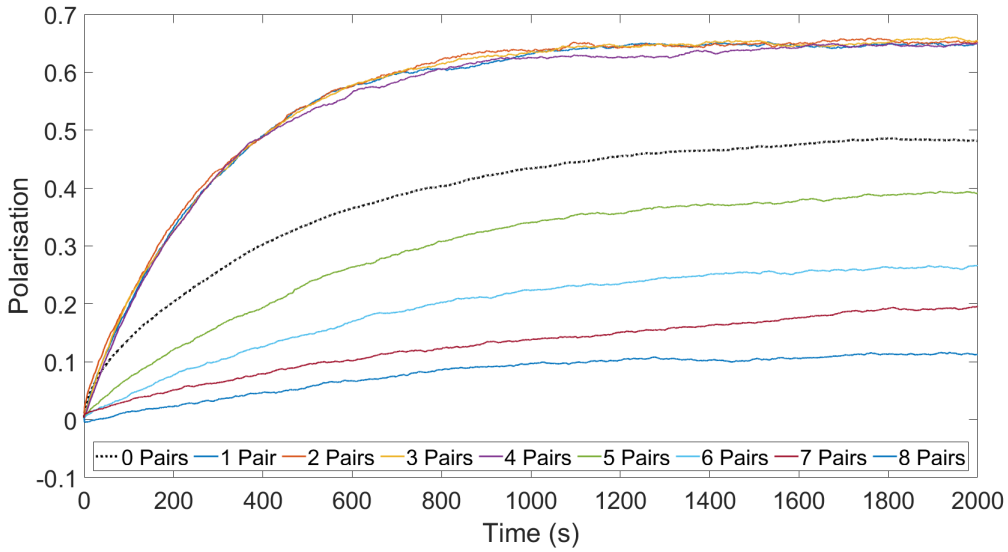
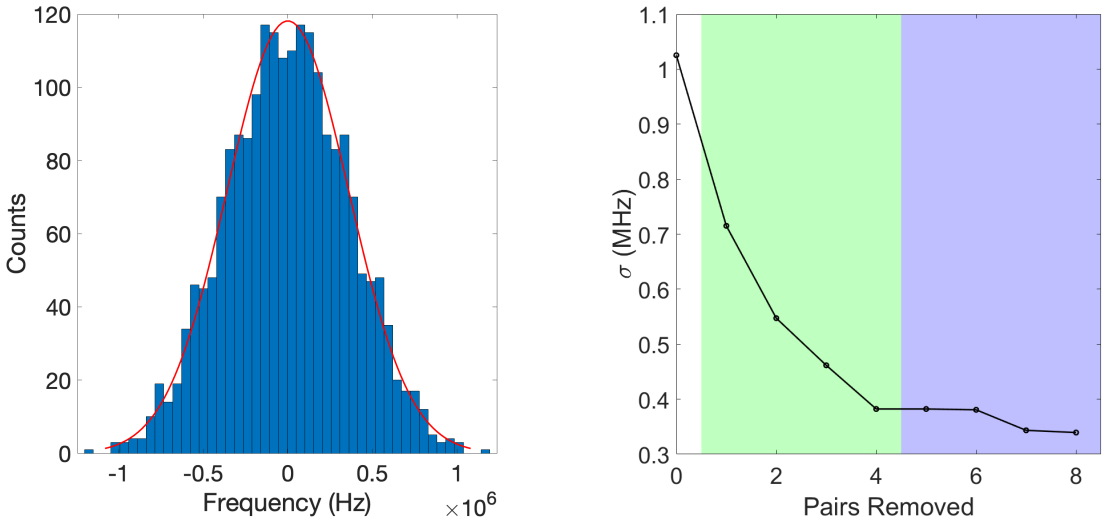


Figure 4-26: Bulk polarisation buildup of the spin system as each pair of protons is removed.

The secular hyperfine interaction leads to a discrete, state-dependent distribution of possible offsets $\hat{\Delta}_{1,Z_1}$ and $\hat{\Delta}_{2,Z_2}$ that the electrons can have (EQ. 3.3). This offset shifts them from resonance with the microwave irradiation. Since the secular hfi contributes to this offset, the distribution is expected to narrow as spins with high A_{jk} are removed. This is shown in FIG. 4-27. FIG. 4-27a shows an example frequency spread of the second electron after 4 pairs of protons were removed. The standard deviation is calculated by applying a normal fit (red line) to the histogram. FIG. 4-27b shows the average standard deviation between the two electrons as spins are removed from the system.



(a) Frequency distribution.

(b) Standard deviation distribution.

Figure 4-27: FIG. 4-27a: Frequency distribution (blue) and normal fit (red) for the second electron after the first 4 pairs of spins have been removed, FIG. 4-27b: average standard deviation between the two electrons after each pair of spins has been removed. The green shaded area corresponds to the 4 highest secular interactions removed, and the blue shaded area to the remaining 4 highest pseudo-secular interactions removed.

Order	$\mathbf{A_1} \times \mathbf{10^6}$ (rad)	$\mathbf{A_2} \times \mathbf{10^6}$ (rad)	$\mathbf{B_1} \times \mathbf{10^6}$ (rad)	$\mathbf{B_2} \times \mathbf{10^6}$ (rad)
1	**1.64**	.002	2.85	.016
1	.002	**1.29**	.016	2.75
2	**.651**	.002	1.37	.008
2	.001	**1.16**	.008	2.00
3	**.643**	.005	5.33	.010
3	0.00	**.581**	.006	.574
4	**.624**	.002	1.96	.008
4	.002	**.460**	.008	2.24
5	.133	0.00	**1.51**	.010
5	.005	.056	.010	**3.84**
6	.193	0.00	**1.17**	.011
6	0.00	.147	.010	**1.42**
7	.430	0.00	**.986**	.006
7	.001	.256	.010	**1.27**
8	.185	.001	**.802**	.007
8	.002	.005	.007	**.730**

Table 4.2: Order of spins removed including their secular and pseudo-secular hfi strengths. For each spin, the interaction in bold marks the reason for removing the spin. Magenta spins form the core.

TAB. 4.2 shows the hyperfine interactions (in radians) of the spins removed. Again, magenta indicates core protons. The interactions in bold are the reason for removing a spin.

4.6.2 Discussion

As expected, the removal of pairs of spins with high secular interactions leads to an increase in bulk polarisation, and the removal of pairs of spins with high pseudo-secular interactions leads to a drastic decrease (FIG. 4-26). In this particular geometry, removing the first pair with strong secular interaction has the largest effect. Removing the subsequent 3 pairs of spins has little effect. Evidently the first pair strongly shifts the electrons from resonance, thereby decreasing the DNP efficiency. Once this pair has been removed, removal of the next 3 pairs has little effect on the polarisation. This is because for these protons the spin diffusion rate $\hat{\Gamma}^{\mathrm{II}}_{kk'}$ is small due to its $A_{jk} - A_{jk'}$ dependence. This means that even if they have very high polarisation,

they are ineffective at transferring it to the bulk (which has low A_{jk}), and therefore do not influence polarisation dynamics. Once pairs of spins with high pseudo-secular interactions start to be removed, the bulk polarisation immediately starts to drop off. By removing these spins, a crucial step in the polarisation transfer from the electrons to the core has been removed, and if the core has low polarisation, so does the bulk. The importance of the pseudo-secular interaction is captured by the B_{jk} dependence of the SE transfer rate $\hat{\Gamma}_k^{\mathrm{SI}}$, and the $\bar{B}_k$ dependence of $\hat{\Gamma}_k^{\mathrm{ISS}}$. Note that since the spheres of influence of the two electrons are assumed to be independent, $\bar{B}_k \sim B_k$.

FIG. 4-27a shows how the removal of spin pairs affects the frequency offsets of the two electrons. It is evident that removing spins with high pseudo-secular interactions does not have much of an effect on the standard deviation of the frequency offset. This is unsurprising since the largest secular interactions have already been removed. After the first pair (with the highest secular interactions) is removed on the other hand, there is significant narrowing of the frequency distribution. This is because the largest term in the sum of EQ. 3.3 has been removed. As more pairs with high secular interactions are removed, the electrons approach their optimal offsets Δ_1 & Δ_2 (EQ. 3.2). Their offset is then determined by the electron dipolar interaction only, which is easier to mitigate since it is not state-dependent.

In this section the kMC algorithm has been used to show that geometry plays an important role in the CE DNP efficiency of radicals. Protons very close to the electrons with high secular interactions shift the electrons from their optimal offset and are ineffective at transferring polarisation. It is therefore convenient to remove such protons from the radical by building 'cages' around electrons that prevent protons from coming too close. Care must be taken however not to remove too many protons with high pseudo-secular interactions as it is these that propagate polarisation to the bulk. The transfer process to the bulk is optimised for protons with approximately the same secular hyperfine interaction. Similar results were found by D. Wiśniewski for simulations using the SE equivalent of the kMC algorithm [28].

Chapter 5

Magic Angle Spinning DNP

5.1 Introduction

MAS spectroscopy has in the last few decades become a powerful tool in many fields of research. It has proven its worth particularly in fields such as biology, where the study of large, insoluble biomolecules – whose anisotropic interactions cannot be averaged out by rotational averaging alone – has been made possible by sample spinning. Because it does not rely on fast tumbling of molecules in solution for its high resolution, MAS NMR is not hampered by molecular size or by entering the solid state [17]. Nonetheless, like static NMR, it suffers from low sensitivity. This can be mitigated by lowering the temperature, increasing the magnetic field (and therefore radio frequency of the tipping pulse), and increasing spinning frequency [90, 91, 92]. Or, more crucially, with MAS DNP. Spinning of the sample relaxes the conditions for DNP to take place, since periodic variation of anisotropic interaction constants means that more spins are likely to meet DNP conditions at some point in the rotor period. Furthermore, the emergent temporal separation of CE resonance and microwave resonance matching events means that the CE conditions no longer need to be met simultaneously, so more electron pairs in the system are likely to match them and participate in the DNP process [17].

The first MAS DNP experiments were performed as early as 1985 by Wind et al. [7]

and in 1992 by Schaefer et al. [93, 94, 95]. Early MAS experiments were limited by the available hardware, required to achieve high spinning & microwave frequencies, and low temperature. Pioneering work by Griffin and his group however, has pushed the boundaries to much higher microwave frequencies (and hence magnetic fields) with the development of gyrotron microwave sources [8, 96]. Efforts by de Paëpe's group on the other hand have taken MAS NMR to temperatures as low as 30K [81]. Combined with the enhancement obtained from DNP, these developments have led to a compelling means to study a wide range of samples. Today, MAS DNP has found application from the detection of small magnetic moments to the detection of nuclei in low concentration [17]. However, as with the static case, the development of a MAS DNP theory has taken much longer.

For many years, the major hold-back of CE MAS theory was that theorists were attempting to build MAS theory from the static theory. Whilst this has been shown to work well for the solid effect [25, 97, 98, 99], the CE cannot be adapted from the static case, as the polarisation dynamics are dictated by different interaction dynamics [17]. The first true descriptions of CE MAS that did not rely on the static case dynamics were presented almost concurrently by Thurber & Tycko [100] and Mentink-Vigier et al. in 2012 [25]. In 2015 Mance et al. proposed a theory similar to that of Mentink-Vigier [101]. All three described the dynamics in terms of avoided level crossings. Mance et al. were even able to predict the nuclear depolarisation observed experimentally and explain the strong dependence of nuclear polarisation enhancement on spinning frequency. Although taking slightly different approaches, all three groups used simulations that were built using the full master equation, which in MAS faces even more severe computational and temporal issues because the dynamics must be tracked throughout a rotor period. Thurber & Tycko were the first to introduce large-scale simulations in 2014. Their 3000-spin simulation consisted of 1000 3-spin systems coupled by the electron dipolar interaction [102]. In 2017 Mentink-Vigier et al. presented a fast simulation algorithm based on a reduced state space and Landau-Zener transitions [26]. In 2018 Perras & Pruski simulated MAS DNP using a Monte

Carlo algorithm [103]. Here a new, highly efficient simulation algorithm developed by A. Karabanov is introduced and its performance tested.

This chapter starts by revisiting the CE mechanism, this time under MAS conditions and with particular focus on the rotor events that lead to polarisation exchange. Next, the Landau-Zener and Krylov-Bogolyubov approximations that simplify the calculation of the dynamics are discussed, along with the conditions under which they apply. Finally, A. Karabanov's fast simulation algorithm is outlined.

5.2 MAS Cross Effect Hamiltonian & Simulation

The form of the MAS CE Hamiltonian is the same as for the static case (EQ. 2.12), but with time-dependent interaction parameters due to the sample spinning. In the microwave rotating frame it is given by

$$\begin{aligned}\hat{H} = {} & \Delta_1(t)\hat{S}_{1z} + \Delta_2(t)\hat{S}_{2z} + \omega_{\mathrm{I}}\sum_k \hat{I}_{kz}... \\ & + D(t)(2\hat{S}_{1z}\hat{S}_{2z} - \frac{1}{2}\hat{S}_{1+}\hat{S}_{2-} - \frac{1}{2}\hat{S}_{1-}\hat{S}_{2+})... \\ & + \sum_{k<k'} d_{kk'}(t)(2\hat{I}_{kz}\hat{I}_{k'z} - \frac{1}{2}\hat{I}_{k+}\hat{I}_{k'-} - \frac{1}{2}\hat{I}_{k-}\hat{I}_{k'+})... \\ & + \sum_j \sum_k (A_{jk}(t)\hat{I}_{kz} + \frac{B_{jk+}(t)}{2}\hat{I}_{k+} + \frac{B_{jk-}(t)}{2}\hat{I}_{k-})\hat{S}_{jz}... \\ & + \sum_j \frac{\omega_1}{2}(\hat{S}_{j+} + \hat{S}_{j-}).\end{aligned} \tag{5.1}$$

The offsets $\Delta_{1,2}(t)$ are defined by isotropic (Δ_0) and anisotropic ($\Delta_j^{(g)}(t)$) terms. The isotropic part $\Delta_0 = \bar{\omega}_{\mathrm{S}_j} - \omega_{\mu\mathrm{w}}$ is the offset between the average electron Larmor frequency ($\bar{\omega}_{\mathrm{S}}$) and the microwave frequency ($\omega_{\mu\mathrm{w}}$). It is equivalent to the offset in the static case. The anisotropic term depends on the principal components of the electrons' g-tensors and their orientation with respect to the other electron (refer to FIG. 5-1). Its time dependence arises due to the variation of the angle between the g-tensor's principal axis system (PAS) and B_0 as the sample rotates.

FIG. 5-1 shows a typical setup of a MAS system. The static field is conventionally oriented along the lab frame z-axis, and forms the magic angle ($\theta_{\mathrm{M}} = \arccos(1/\sqrt{3})$) with the spinning axis of the MAS rotor. The MAS rotor spins at the MAS frequency ν_{MAS}. For CE DNP to be effective, pairs of electrons (e_1 & e_2) participating in the CE must have differently aligned PAS. In FIG. 5-1, the electrons show the ideal orientation of the principal axes in bTbk, a commonly used MAS DNP biradical [86]. Unless otherwise specified, all simulations have this orientation of the principal axes with respect to each other.

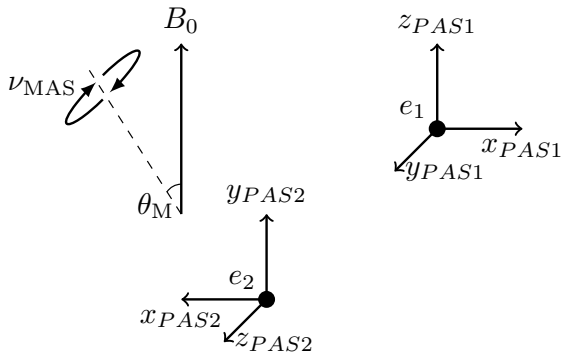


Figure 5-1: Typical MAS DNP setup. The sample is spun at a frequency ν_{MAS} at the magic angle (θ_{M}) with respect to the static field, with B_0 conventionally pointing along the lab frame z-axis. e_1 and e_2 show the ideal orientation of the principal axes in the bTbk molecule, a commonly used MAS DNP biradical [86].

Just as in the static case, the equation of motion in MAS DNP is given by the dissipative Lindblad master equation (EQs. 2.8 & 2.9). However, despite static and MAS DNP looking almost identical on paper, the mechanisms leading to DNP and the implementation of the master equation in simulations are very different. In MAS the time dependence of the Hamiltonian leads to time dependent eigenvalues (the energy levels), which vary periodically with the rotor motion. These changes in the energy levels lead to avoided level crossings, which in turn give rise to new ways of polarisation exchange that are not present in the static case. Furthermore, in MAS DNP an additional time scale must be taken into account, the rotor period. The rotor period is

for example pertinent to the dissipators representing relaxation, which can be taken to be time-independent because the fluctuations in the Hamiltonian due to interactions with the environment (leading to relaxation), occur on a much faster time scale (on the order of ω_{I} or ω_{S}, MHz to GHz) than the rotor period (on the order of 10's of kHz).

The time dependence of the Hamiltonian also changes the way in which MAS DNP is simulated. The first distinction is that in MAS it is necessary to take into account the powder average, since at different points in the rotor period different orientations of a molecule contribute to the enhancement. The first step is therefore to define a powder averaging protocol. In this and the following chapter, the protocol used is "circle" in α and "repulsion" in β & γ, where the angles are given in zyz Euler notation. The repulsion method [104, 105] is highly efficient and converges for a minimal number of crystallite orientations, which drastically reduces simulation time. It is so named because it is based on fictive inter-crystallite repulsive forces that, by an iterative process, evenly distribute a chosen number of points on a sphere. Unless stated otherwise, 72 angles are averaged, 6 in α and 12 in β & γ.

The next step is to build the time- and orientation- independent Lindbladians and the relaxation superoperator in the Zeeman frame so that these are not re-calculated with each powder and time step loop. Then, the powder loop is started. For each iteration of the loop, the re-oriented spin geometry in the lab frame is calculated. This is then the starting geometry for the rotor loop. Only the electrons and core nuclei need to be powder re-oriented, since the bulk is assumed to be a uniform random distribution of spins. In the rotor loop, the Hamiltonian is piece-wise integrated with time steps small enough that the Hamiltonian can be taken to be constant. For each time step the interaction parameters are re-calculated and the time-dependent Liouvillian built. This is then added to the time-independent Liouvillian defined outside the rotor loop to create the propagator for the current loop. Once the desired number n of rotor periods has been reached, the polarisation dynamics from the current powder orientation are added to those of the previous powder angles and the next powder loop

is started. Finally, after the powder loop is finished, the average of the polarisation dynamics over all powder angles is taken. A good summary of MAS NMR simulation is given in REF. [106].

The piece-wise integration of the Hamiltonian to create a propagator $\hat{M}$ that is representative of the entire rotor loop is possible because the model MAS DNP master equation given by EQs. 5.1 & 2.9 is a linear system with periodic coefficients in Liouville space. The periodic (stroboscopic) dynamics can therefore be described by a system with constant coefficients. Such an approach has already been taken by Mentink-Vigier et al. in REF. [26]. Let the density matrix after n rotor periods (T_r) be given by $\hat{\rho}(nT_\mathrm{r})$. If the stroboscopic dynamics can be represented by a system with constant coefficients, then $\hat{\rho}(nT_\mathrm{r})$ can written in terms of the initial density matrix $\hat{\rho}(0)$ and the periodic propagator $\hat{M}$:

$$\hat{\rho}(nT_\mathrm{r}) = \mathrm{e}^{n\hat{M}T_\mathrm{r}}\hat{\rho}(0). \tag{5.2}$$

Although the equation looks simple, finding the propagator $\hat{M}$ is not easy, and often requires numerical methods, even for small systems. This is where the piece-wise integration comes in. If the rotor period is divided into small time intervals in which the MAS Hamiltonian can be assumed to be constant, $\hat{M}$ can be found by multiplying the propagator for each time step with the propagators from the previous time steps, resulting in the propagator $\hat{M}$ describing the dynamics throughout the entire rotor period. For each powder angle, $\hat{M}$ is calculated once only, and the dynamics over many periods are calculated with EQ. 5.2.

5.2.1 Polarisation Events

In the static case, population exchange between the Zeeman eigenstates is due to flip-flops by the hyperfine and dipolar interactions. The microwave irradiation also plays a role and the polarisation transfer is dependent on the CE resonance condition $|\omega_{\mathrm{S}_1} - \omega_{\mathrm{S}_2}| \sim \omega_\mathrm{I}$ being met. For polarisation transfer to be efficient, the microwave

irradiation should additionally be on resonance with one of the electrons. In the MAS case, Zeeman eigenstates are coupled by the time dependence of interaction parameters. If conditions are right, polarisation can be transferred during an avoided level crossing via non-adiabatic quantum jumps known as rotor events. Rotor events are generally temporally well-separated and occur at specific times in the rotor period, determined by the electron offsets $\Delta_j(t)$. Three events lead to the CE mechanism being active in MAS DNP:

- **microwave events**: lead to microwave saturation of one of the two electron spins when $\Delta_j(t) = 0$. This can happen for medium values of the isotropic microwave offset Δ_0, which can then periodically be matched by the time-dependent anisotropic offset $\Delta_j^{(g)}(t)$. Microwave events maximise the polarisation difference between electrons as the large g-tensor anisotropy typical of CE biradicals causes them to occur at different times for each electron.

- **electron events**: lead to polarisation exchange between pairs of electrons when their offsets are equal: $\Delta(t) = \Delta_1(t) - \Delta_2(t) = 0$. The polarisation transfer is mediated by the electron dipolar interaction.

- **CE events**: transfer the electron polarisation difference to a nucleus via CE triple spin flips when $|\Delta(t)| = \omega_{\mathrm{I}}$.

Under the right conditions, all three events demonstrate non-adiabatic jump-like behaviour, allowing the use of approximation methods that significantly reduce simulation time. They are furthermore all reversible, and can be represented by a unitary operator. The periodic polarisation dynamics that lead to enhancement are therefore a consequence of irreversible processes, engendered by dissipation, accumulating over many periods.

To examine in more detail the effect of rotor events on the polarisation dynamics, it is instructive to look first at the simplest CE system: two coupled electrons and a nucleus coupled to e_1 only. For the sake of simplicity, only spin interactions causing

transitions will be considered initially. These are the flip-flop ($\hat{S}_{1\pm}\hat{S}_{2\mp}$) part of the electron dipolar interaction and the nuclear flip part of the pseudo-secular hyperfine interaction ($\hat{I}_{\pm}\hat{S}_{1z}$). The Zeeman term causing splitting of the energy levels into 8 product states is also kept. In the discussion that follows, the product states are given by $|e_1\ e_2\ n\rangle$.

Microwave events

When e_1 is saturated at $\Delta_1(t) = 0$, its up and down orientations within the four pairs of states

$$(|\uparrow\uparrow\uparrow\rangle, |\downarrow\uparrow\uparrow\rangle), \quad (|\uparrow\downarrow\uparrow\rangle, |\downarrow\downarrow\uparrow\rangle),$$
$$(|\uparrow\uparrow\downarrow\rangle, |\downarrow\uparrow\downarrow\rangle), \quad (|\uparrow\downarrow\downarrow\rangle, |\downarrow\downarrow\downarrow\rangle),$$

become equivalent. Microwave irradiation of the first electron ($\omega_1\hat{S}_{1x}$) causes population-equalising mixing in the pairs, thereby saturating it. When $\Delta_2(t) = 0$, the microwave term of the second electron ($\omega_1\hat{S}_{2x}$) causes mixing of states that differ only in the orientation of e_2, and e_2 is saturated. The population exchange between pairs of states occurs when $|\Delta_j(t)| \ll |\omega_1|$, and is non-adiabatic if $\dot{\Delta}_j(t) \neq 0$. The former must be the case for the microwave irradiation to be able to cause mixing between states. If the latter is true, the system is far from a stable point (refer to the discussion after EQ. 5.3) and the level crossing is very rapid, with no change of polarisation before or after the event. As will be elaborated in Section 5.4, the jump-like nature of the events is well-described within the framework of Landau-Zener transitions.

Electron events

When the two electron offsets match ($\Delta(t) = 0$), the up-down and down-up orientations of the electrons have the same energy within the two pairs of states whose nuclear orientation is the same:

$$(|\uparrow\downarrow\uparrow\rangle, |\downarrow\uparrow\uparrow\rangle), \quad (|\uparrow\downarrow\downarrow\rangle, |\downarrow\uparrow\downarrow\rangle).$$

In this case, state mixing is mediated by the flip-flop part of the electron dipolar interaction ($-\frac{1}{2}D(t)[\hat{S}_{1+}\hat{S}_{2-} + \hat{S}_{1-}\hat{S}_{2+}]$) and leads to an exchange of polarisation between the electrons. The exchange can occur when $|\Delta(t)| \ll |D(t)|$, and again $\dot{\Delta}(t) \neq 0$ is required for the system to rapidly cross the mixing interval and experience a non-adiabatic jump of the electron polarisation difference.

Both electronic jumps rely on the large amplitudes of the offsets $\Delta_j(t)$ & $\Delta(t)$ and their time derivatives with respect to the microwave irradiation and electron dipolar coupling to ensure that the quantum jumps are of a non-adiabatic nature. The large difference in amplitudes arises due to the large g-anisotropy of the electrons, particularly at high magnetic fields and relatively high MAS frequencies.

CE events

When the electron offset difference is matched by the nuclear Larmor frequency, CE triple spin flips mediated by the combined effect of the flip-flop electron dipolar interaction ($-\frac{1}{2}D(t)[\hat{S}_{1+}\hat{S}_{2-} + \hat{S}_{1-}\hat{S}_{2+}]$) and the pseudo-secular hyperfine interaction ($\frac{1}{2}[B_{1+}(t)\hat{I}_+ + B_{1-}(t)\hat{I}_-]\hat{S}_{1z}$) lead to mixing of one of the pairs of states

$$(|\uparrow\downarrow\downarrow\rangle, |\downarrow\uparrow\uparrow\rangle), \quad (|\uparrow\downarrow\uparrow\rangle, |\downarrow\uparrow\downarrow\rangle),$$

where the pair on the left corresponds to $\Delta(t) = \omega_{\mathrm{I}}$ and the pair on the right corresponds to $\Delta(t) = -\omega_{\mathrm{I}}$. Again, non-adiabaticity of this transition requires $\dot{\Delta}(t) \neq 0$, and the transition can only occur when $|\Delta(t)| \ll |D(t), B(t)|$. Just as in the static case, the triple spin flip $\hat{S}_{1+}\hat{S}_{2-}\hat{I}_+$ is not present in the Hamiltonian and drops out of Krylov-Bogolyubov averaging of the CE transition dynamics. The averaging procedure produces an effective dynamics within a two-level system that can accurately be treated with Landau-Zener theory.

5.3 Energy Level Diagram

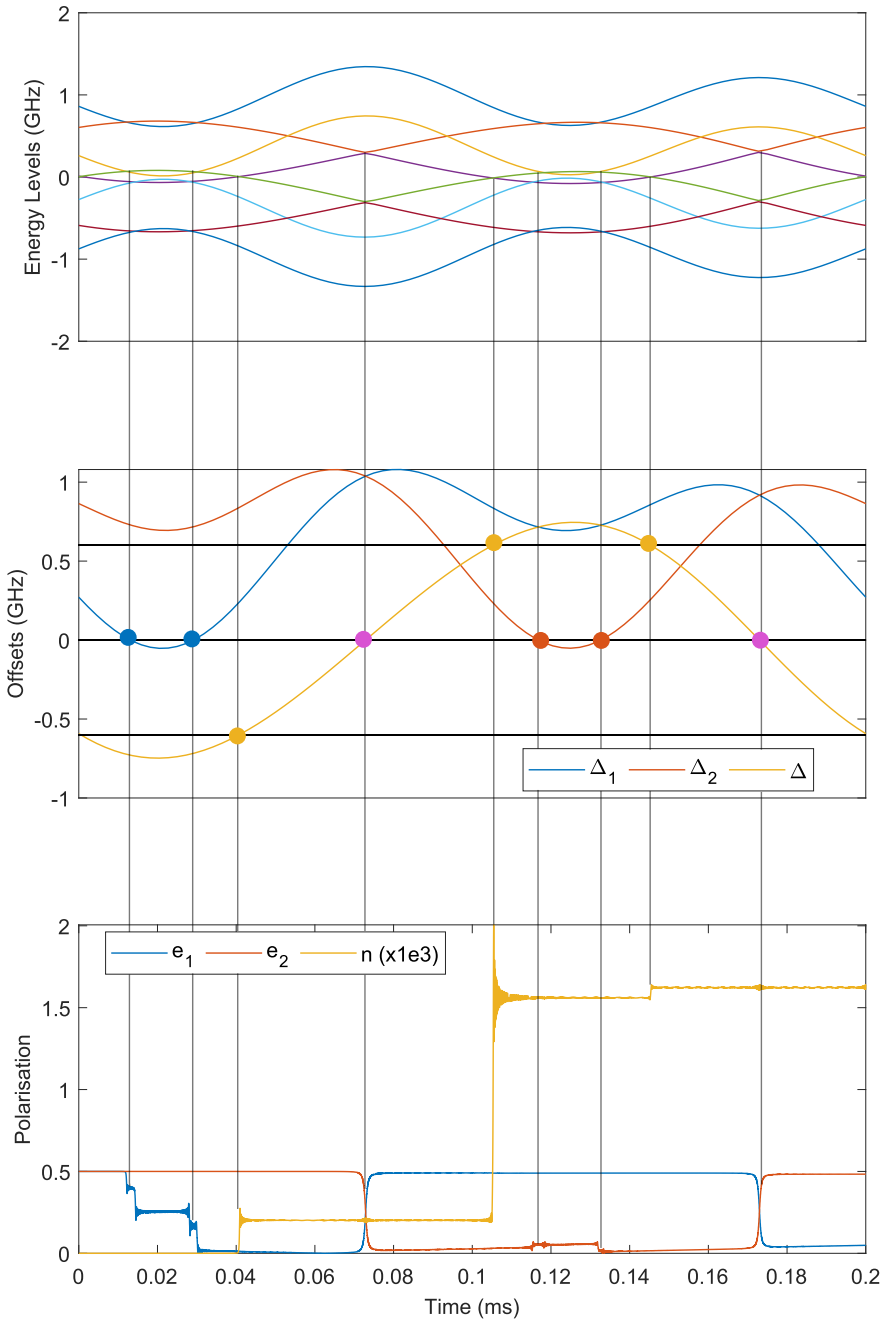


Figure 5-2: Caption on next page.

Figure 5-2: Simulation of a basic 3-spin ($n - e_1 - e_2$) single crystallite system. The proton is coupled only to e_1. The principal components of the electron g-tensors are $g_X = 2.009$, $g_Y = 2.006$ & $g_Z = 2.002$. PAS_1 & PAS_2 are oriented as in FIG. 5-1 and the initial Euler angles of the system in the lab frame are ($\pi/3$, $\pi/6$, 0) in zyz notation. The $e - e$ distance is 1.22Å, similar to that of bTbk [86]. The $e_1 - n$ vector is $[\sin(\pi/3),\ 0,\ \cos(\pi/3)]\times 0.3$Å. The physical parameters are $B_0 = 14.1$T, $T = 100$K, $R_{1\text{e}} = 10^3\text{s}^{-1}$, $R_{2\text{e}} = 10^4\text{s}^{-1}$, $R_{1\text{n}} = 0.1\text{s}^{-1}$, $R_{2\text{n}} = 10^3\text{s}^{-1}$, $\nu_{\text{MAS}} = 5$kHz, $\Delta_0 = 650$MHz, $\omega_1 = 0.6$MHz. The three panels show the dynamics within a period. The top panel shows the 8 energy levels of the system, the central panel shows the offsets $\Delta_1(t)$, $\Delta_2(t)$ & $\Delta(t)$ and the bottom panel shows the polarisation dynamics within the first period. The 3 horizontal lines in the middle panel denote 0 & $\pm\omega_{\text{I}}$. Vertical lines connect moments in time across the three panels at which a polarisation exchange takes place.

FIG. 5-2 shows the time dependence of the energy levels (top panel), the time dependence of the offsets $\Delta_1(t)$, $\Delta_2(t)$ & $\Delta(t)$ (middle panel), and the polarisation dynamics (bottom panel) within the first period for a single crystallite 3-spin system. To simplify the dynamics, the nucleus is coupled to e_1 only. The relevant physical and geometric parameters are in the figure caption. Starting from the highest energy, the energy levels in the top panel are as follows (in $|e_1\ e_2\ n\rangle$ notation): dark blue = $|\uparrow\uparrow\uparrow\rangle$, orange = $|\downarrow\uparrow\uparrow\rangle$, yellow = $|\uparrow\uparrow\downarrow\rangle$, green = $|\downarrow\uparrow\downarrow\rangle$, purple = $|\uparrow\downarrow\uparrow\rangle$, light blue = $|\downarrow\downarrow\uparrow\rangle$, red = $|\uparrow\downarrow\downarrow\rangle$, dark blue = $|\downarrow\downarrow\downarrow\rangle$. Although not visible in this figure, matching of the energy levels is not exact due to perturbations caused by off-diagonal hyperfine interaction, dipolar, and microwave terms. In the central panel, the 3 horizontal lines show 0 & $\pm\omega_{\text{I}}$. Polarisation exchanges happen when the offsets cross one of these lines (as shown by the dots). Blue and orange dots indicate microwave events at $\Delta_j(t) = 0$, when one of the electrons becomes saturated. For e_1, the matching pair of states is $|\uparrow\uparrow\downarrow\rangle \leftrightarrow |\downarrow\uparrow\downarrow\rangle$ and for e_2 it is $|\downarrow\downarrow\uparrow\rangle \leftrightarrow |\downarrow\uparrow\uparrow\rangle$. Magenta dots show electron events at $\Delta(t) = 0$, when the two electrons switch polarisation. For these events the pairs $|\uparrow\downarrow\downarrow\rangle \leftrightarrow |\downarrow\uparrow\downarrow\rangle$ and $|\downarrow\uparrow\uparrow\rangle \leftrightarrow |\uparrow\downarrow\uparrow\rangle$ experience an avoided level crossing. Finally, yellow dots indicate CE events, in which the polarisation difference between the electrons is transferred to the nucleus. At these times $\Delta(t) = \pm\omega_{\text{I}}$ and the pair of energy levels exchanging is $|\downarrow\uparrow\downarrow\rangle \leftrightarrow |\uparrow\downarrow\uparrow\rangle$. There is also a solid effect transition at $\Delta_1(t) = \omega_{\text{I}}$. However, since the SE transition ($\sim |\omega_1 B(t)|/|\omega_{\text{I}}|$) occurs on a much slower time scale

than the CE transition ($\sim |D(t)B(t)|/|\omega_{\mathrm{I}}|$), it is much less effective in the short jump period and makes a negligible contribution to the polarisation.

5.4 Approximations to the Master Equation

One of the inherent limiting factors of any large-scale DNP simulation is the exponential complexity scaling of state space with system size. For MAS simulations this is exacerbated by the need to track parameters over time. However, the non-adiabatic nature of the polarisation jumps in most relevant cases, means that dynamics within a rotor period can be calculated using Landau-Zener theory. Subsequent long-time dynamics can then be calculated stroboscopically at the end of each rotor period using an average propagator [26, 100]. Combined, these two powerful approximations greatly simplify the dynamics, allowing simulation of many-body systems. The Landau-Zener approximation [60, 61] in particular is useful because it relies only on probabilities of transitions between two relevant levels, which can be calculated very efficiently. However, since there is no direct 2-level transition describing CE transitions in the Hamiltonian, the CE dynamics must be Krylov-Bogolyubov averaged to obtain an effective Hamiltonian that is suitable for the Landau-Zener approximation. Initially, the simplest 3-spin system with only the indispensable interactions will be studied and the importance of fast coherent decay emphasised. This is later expanded to include more nuclei and the secular hyperfine interaction.

The Landau-Zener theory for two-level systems was already introduced in the Theory Toolbox (Chapter 2). In the following it is applied specifically to the rotor events in MAS.

5.4.1 Non-adiabaticity and Coherent Decay of Electron Events

The adiabaticity of rotor events depends on the instantaneous values of the interactions & offsets, and the spin relaxation rates. The former define the magnitudes of the jumps, whereas the latter describe relaxation to thermal equilibrium (longitudi-

nal relaxation) and the decay of quantum coherences (transverse relaxation). MAS tends to decrease transverse relaxation rates as it averages out homogeneous broadening. Though this is good for increased resolution, it removes one of the relaxation mechanisms from T_2, which then depends primarily on field inhomogeneity and less on spin-spin interactions, and is therefore slower. Coherences are then more likely to persist over multiple jump events and introduce a random phase to the dynamics. If the coherences are strong enough, different pairs of states participate in a jump event than predicted by Landau-Zener theory, with different rates. The longitudinal relaxation also plays an important role. A very short T_{1e} prevents the electrons from being brought out of equilibrium, thus quenching DNP since no polarisation difference is created between them. Very long T_{1e} on the other hand means that the system never resets, and eventually both electrons are saturated, again quenching DNP.

The interval τ in which $\delta(t) \ll \Omega(t)$ and mixing can occur (refer to Section 2.6 for a definition of the detuning $\delta(t)$ and the mixing rate $\Omega(t)$), is calculated from the Taylor expansion of $\delta(t)$ near the jump at $t = t_0$:

$$|\delta(t)| \sim |\dot{\delta}(t_0)\big[t - t_0\big]| \sim \Omega(t_0),$$

where the first term of the expansion disappears since $\delta(t_0) \sim 0$, and $\delta(t)$ must be $\sim \Omega(t_0)$ near the crossing for an exchange to take place. The mixing interval τ is therefore given approximately by

$$\tau = |t - t_0| \sim \frac{\Omega(t_0)}{\dot{\delta}(t_0)}. \tag{5.3}$$

At a stable point $\dot{\delta}(t_0) = 0$ and the mixing interval is undefined, since it is impossible for the mixing rate to overcome the energy gap. When the system is far from a stable point, τ is short because $\dot{\delta}(t_0)$ is large, and transitions that take place must have a jump-like nature. When τ is large, transitions need not be adiabatic to take place within the mixing interval.

For the Landau-Zener approximation to be valid, spin relaxation should be negligible

within τ and the various jump events should be well separated in time:

$$\frac{|\Omega(t_0)|}{\dot{\delta}(t_0)}\max\{R_{1e},\ R_{2e}\} \ll 1, \quad \frac{|\Omega(t_0)|}{\dot{\delta}(t_0)} \ll |t_+ - t_-|, \tag{5.4}$$

respectively, where R_{1e} & R_{2e} are characteristic electron relaxation rates and $t_\pm$ are the time shortly before and after the non-adiabatic event. Together, these two conditions ensure that dynamics remain incoherent and are not characterised by a random phase. Applying EQ. 5.4 directly to the electron spin transitions, the non-adiabaticity condition is given by

$$\max\left\{\frac{|\omega_1|}{|\dot{\Delta}_j(t_0)|}, \frac{|D(t_0)|}{|\dot{\Delta}(t_0)|}\right\} \ll \min\left\{\frac{2\pi}{10\nu_{\mathrm{MAS}}}, T_{2e}\right\}. \tag{5.5}$$

The factor of 10 arises because (as seen in FIG. 5-2) there are $\sim$10 events within a rotor period of $T_r = 2\pi/\nu_{\mathrm{MAS}}$. The restrictiveness of this and the remaining conditions of the fast simulation algorithm will be discussed in Section 5.5.

For the CE transition, finding the adiabaticity and coherence conditions is not so simple, as it is not a direct 2-level process. In order to bring it into a form appropriate for Landau-Zener treatment, the time-dependent Hamiltonian must first be Krylov-Bogolyubov averaged.

5.4.2 Non-adiabaticity and Coherent Decay of CE Events

This subsection starts by briefly considering the 3-spin energy level diagram first in the static case and then in the MAS case to determine what terms in the Hamiltonian contribute to the CE events. Once an appropriate CE Hamiltonian is found, it is Krylov-Bogolyubov averaged so that the Landau-Zener approximation can be used. Finally, the Landau-Zener and coherence conditions are given.

Krylov-Bogolyubov Averaging of CE Events

For a static 3-spin system with the first electron saturated by the microwave irradiation, the four pairs of states differing only in the orientation of e_1 rapidly equalise (FIG. 5-3). The left hand side of FIG. 5-3 corresponds to the nuclear spin-up state, and the right hand side to the spin-down state. The top half on the other hand corresponds to e_2 retaining its thermal polarisation.

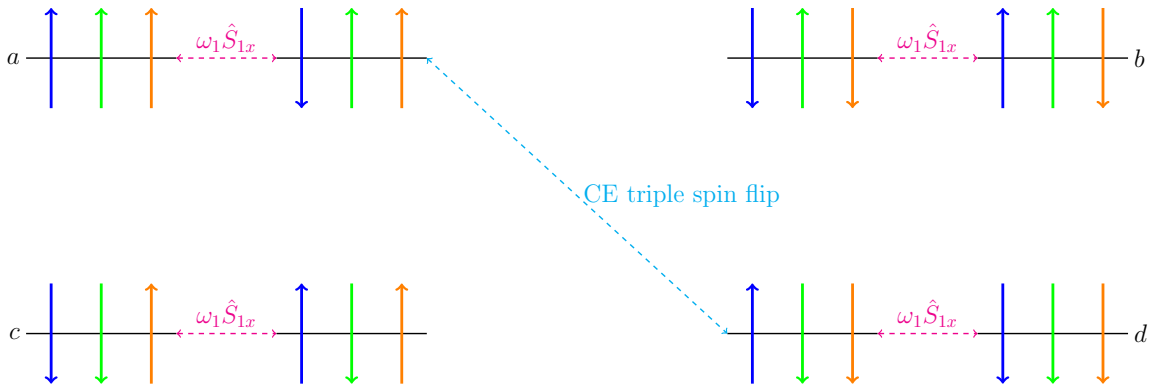


Figure 5-3: Schematic of the CE mechanism for a static 3-spin system ($|e_1\ e_2\ n\rangle$ notation) with the first electron saturated.

Ideally, the saturation of e_1 should not affect e_2 or n, which should remain at $p_{\mathrm{e}_2} \sim p_{\mathrm{e,th}} = |\uparrow\rangle$ and $p_{\mathrm{n}} \sim 0$ respectively. Saturation of e_1 therefore leads to states a & b in FIG. 5-3 dominating over states c & d, since these are the levels in which e_2 remains polarised. CE triple spin flips $\hat{S}_{1+}\hat{S}_{2-}\hat{I}_{-}$ subsequently equilibrate the populations of states a & d. Combined, the saturation and CE flips thus lead to a depopulation of states a & c, and an increased population of states b & d. The nuclear spin-down state is therefore enhanced.

One of the key assumptions throughout this chapter is that rotor events are independent. Under this assumption, the MAS CE event is well separated from the single spin microwave event, and at a CE transition $|\Delta_j(t)| \gg |\omega_1|$. This means that the microwave irradiation is ineffective during the CE transition and need not be considered. Re-examining FIG. 5-3 in the context of MAS, it is clear that the symmetric single

spin Zeeman order $\hat{S}_{1z} + \hat{S}_{2z}$ in EQ. 5.1 is also redundant, as there is no longer a Zeeman splitting of the electron energies (since at CE events $\Delta(t) = \Delta_1(t) - \Delta_2(t) = 0$). It therefore acts trivially on the pairs a & d. Finally, since the double spin electron Zeeman order $\hat{S}_{1z}\hat{S}_{2z}$ commutes with the rest of the Hamiltonian, it too can be discarded. The remaining effective CE Hamiltonian is therefore non-secular, 4-level and 2-spin, where the two electrons have been combined to create one fictitious spin $\hat{K}$:

$$\hat{H}_{\mathrm{CE}} = \omega_{\mathrm{I}}\hat{I}_z + \Delta(t)\hat{K}_z - \frac{D(t)}{2}(\hat{K}_+ + \hat{K}_-) + \frac{1}{2}(B_+(t)\hat{I}_+ + B_-(t)\hat{I}_-)\hat{K}_z,$$
$$\hat{K}_z = \frac{1}{2}(\hat{S}_{1z} - \hat{S}_{2z}), \qquad \hat{K}_\pm = \hat{S}_{1\pm}\hat{S}_{2\mp},$$

where $B_+(t) = B_{1+}(t) - B_{2+}(t)$ is the asymmetry of the pseudo-secular hyperfine interaction. In the rotating frame of the resonance CE Hamiltonian $\omega_{\mathrm{I}}(\hat{I}_z + \hat{K}_z)$, the effective CE Hamiltonian becomes

$$\hat{H}'_{\mathrm{CE}} = \delta(t)\hat{K}_z + \mathrm{e}^{i\omega_{\mathrm{I}}t}\hat{H}_+ + \mathrm{e}^{-i\omega_{\mathrm{I}}t}\hat{H}_-,$$
$$\hat{H}_+ = \hat{H}_-^\dagger = \frac{1}{2}[B_+(t)\hat{I}_+\hat{K}_z - D(t)\hat{K}_+], \quad \delta(t) = \Delta(t) - \omega_{\mathrm{I}},$$

where $\hat{H}_\pm$ cause transitions between eigenstates. In high magnetic fields, the Zeeman splitting dominates over all other interactions, so near the non-adiabatic jump ($\Delta(t) = \omega_{\mathrm{I}}$), $|\omega_{\mathrm{I}}| \gg |D(t)|$, $|\delta(t)|$, $|B(t)|$. Krylov-Bogolyubov averaging can therefore be employed to find the average CE Hamiltonian in the rotating frame, given here to second order

$$\bar{\hat{H}}'_{\mathrm{CE}} = \delta(t)\hat{K}_z + \frac{1}{\omega_{\mathrm{I}}}[\hat{H}_+, \hat{H}_-] \sim \delta(t)\hat{K}_z + \Omega(t)\hat{L}_+ + \Omega^*(t)\hat{L}_-, \tag{5.6}$$

where

$$\Omega(t) = \frac{D(t)B(t)_-}{4\omega_{\mathrm{I}}}, \quad \hat{L}_\pm = \hat{I}_\mp\hat{K}_\pm.$$

Note that the right hand side of EQ. 5.6 is in the same form as the Landau-Zener Hamiltonian in EQ. 2.42.

Given that the detuning in this case is $\delta(t) = \Delta(t)$, the Landau-Zener probability of a transition between states is given from EQ. 2.43 as

$$1 - \epsilon = \mathrm{e}^{-2\pi\Gamma}, \quad \Gamma = \frac{|\Omega(t_0)|^2}{|\dot{\Delta}(t_0)|}.$$

If it is assumed that coherent terms have no effect on the dynamics caused by strong transverse electron relaxation, the observables before ($\hat{L}_z$) and after ($\hat{L}'_z$) the transition are related by $\langle \hat{L}'_z \rangle = (1 - 2\epsilon)\langle \hat{L}_z \rangle$, where ϵ is the probability of staying in the same state (no transition). Furthermore, if the fictitious electron Zeeman operator commutes with the averaged Hamiltonian $\bar{\hat{H}}'_{\mathrm{CE}}$, the nuclear Zeeman observable after the transition ($\langle \hat{I}_z \rangle'$) is given by

$$\langle \hat{I}_z \rangle' = (1 - \frac{\epsilon}{2})\langle \hat{I}_z \rangle + \frac{\epsilon}{2}\langle \hat{S}_{1z} - \hat{S}_{2z} \rangle + 2\epsilon\langle \hat{S}_{1z}\hat{S}_{2z}\hat{I}_z \rangle. \tag{5.7}$$

For experimental reasons, MAS DNP is mostly carried out at relatively high temperatures of > 30K [81]. This means that the initial polarisation is very low ($\langle \hat{S}_{1z}\hat{S}_{2z}\hat{I}_z \rangle \sim p_{\mathrm{e}}^2 p_{\mathrm{n}} \ll 1$), so the triple spin Zeeman operators $\hat{S}_{1z}\hat{S}_{2z}\hat{I}_z$ have a negligible effect on the spin dynamics. The evolution is thus dominated by the polarisation difference between the electrons, and EQ. 5.7 is well-approximated by

$$\langle \hat{I}_z \rangle' = (1 - \frac{\epsilon}{2})\langle \hat{I}_z \rangle + \frac{\epsilon}{2}\langle \hat{S}_{1z} - \hat{S}_{2z} \rangle. \tag{5.8}$$

From EQ. 5.8 it is clear that during a CE rotor event, a nucleus gains the polarisation difference between electrons at a rate $\epsilon/2$. If the double quantum case ($\Delta(t_0) = -\omega_{\mathrm{I}}$) had been considered rather than the single quantum case, the nucleus would have had opposite polarisation:

$$\langle \hat{I}_z \rangle' = (1 - \frac{\epsilon}{2})\langle \hat{I}_z \rangle - \frac{\epsilon}{2}\langle \hat{S}_{1z} - \hat{S}_{2z} \rangle.$$

Non-Adiabaticity and Coherent Decay

CE rotor events are characterised by an energy difference $\delta(t) = \pm\omega_{\mathrm{I}}$ and a mixing rate $\Omega(t) = \frac{D(t)B(t)_-}{4\omega_{\mathrm{I}}}$. The CE event analog to EQ. 5.5 is therefore

$$\max\left\{\frac{|B(t_0)D(t_0)|}{4\omega_{\mathrm{I}}\dot{\Delta}(t_0)}\right\} \ll \min\left\{\frac{2\pi}{10\nu_{\mathrm{MAS}}},\ T_{2\mathrm{e}}\right\}, \tag{5.9}$$

which ensures that events are well-separated in time and coherences decay quickly. Again, it is assumed that $T_{2\mathrm{e}} \ll T_{1\mathrm{e}},\ T_{1\mathrm{n}},\ T_{2\mathrm{n}}$, dominating not only over $e-e$ and $n-n$ coherences, but also over $e-n$ coherences.

5.4.3 Hyperfine and Nuclear Dipolar Interactions

So far, the simplest single-nucleus CE system containing only interactions that are directly relevant to the rotor events has been examined. The next step is to incorporate further nuclei and interactions. Inclusion of the secular hyperfine interaction leads to the splitting of spin resonance frequencies of the electron-nuclear interaction, $\hat{H}_{\mathrm{A}} = \sum_{jk} A_{jk}(t)\hat{I}_{kz}\hat{S}_{jz}$. Extending the system to more nuclei on the other hand introduces the nuclear dipolar coupling $\hat{H}_{\mathrm{II}} = -\frac{1}{2}\sum_{k<k'} d_{kk'}(t)(\hat{I}_{k+}\hat{I}_{k'-} - \hat{I}_{k-}\hat{I}_{k'+})$, responsible for mediating polarisation exchange between nuclear spins. Both of these effects become important when spin separations ($e-n$ for the former and $n-n$ for the latter) are small.

Hyperfine Splitting

Given the typically high magnetic fields of MAS DNP and the strong g-anisotropy of biradicals, the hyperfine splitting of electron dynamics by A_{jk} is generally negligible [26]. An important exception is the presence of spin-1 ^{14}N close to the free radical electrons in nitroxyl biradicals. Here, the nitrogen and delocalised unpaired electron from the oxygen are close enough that both the Fermi contact term (otherwise generally negligible in the context of DNP) and the anisotropic dipole-dipole force must be taken into account [107]. Depending on the orientation of the $e-^{14}$N pair, the secular hyperfine interaction can take values up to $\sim$ 100MHz, comparable to the electron

g-anisotropy in static fields less than 5T.

To account for the ^{14}N spins, the hyperfine splitting electron-nitrogen terms $A_j(t)\hat{J}_{jz}\hat{S}_{jz}$ should be included in the electron spin Hamiltonian, where $\hat{J}_{jz}$ are the nitrogen spin operators. Note that each electron interacts only with the nitrogen in its nitroxyl group, not with both. Since nitrogen has spin-1, the spin operators are given by the equally probable scalar projections $\hat{J}_{jz} = 0, \pm 1$. This means that a nitroxide biradical has 9 possible combinations of nitrogen orientations, each of which produces different dynamics. A rigorous simulation should therefore average over all 9 combinations of $\hat{J}_{1z}$ & $\hat{J}_{2z}$, making the simulation time 9 times longer.

Nuclear Exchange

Spin diffusion mediated by the nuclear dipolar flip-flop term $\hat{H}_{\mathrm{II}}$ propagates polarisation to nuclei far removed from the electrons. In close proximity to electrons, the diffusion process is quenched by the hyperfine splitting $\hat{H}_{\mathrm{A}}$, which creates energy gaps between the $|\uparrow\downarrow\rangle - |\downarrow\uparrow\rangle$ orientations of the interacting nuclear spin pairs that are larger than the nuclear interaction strength. However, the proximity of these nuclei to the electrons also means that their pseudo-secular hyperfine interactions are strong, and that they tend to be polarised directly by CE events. Spin diffusion is also quenched by the sample rotation at the magic angle (refer to EQ. 2.13), which tends to average the dipolar interaction to zero. While this is desirable for high resolution spectroscopy, it hinders the polarisation from propagating, thus limiting the effect of DNP. Ways to mitigate this include reducing the MAS spinning frequency so that fewer interactions are averaged out, or recovering the couplings by applying resonant RF-pulses [108].

The analytic formulae describing the nuclear spin diffusion process including both dipolar and hyperfine effects are found by considering a projection of the model system given by EQs. 5.1 & 2.9 onto the subspace of two arbitrary nuclear spins $\hat{\mathbf{I}}_k,\ \hat{\mathbf{I}}_{k'}$. The two spins are coupled by the nuclear Hamiltonian term $\hat{H}_{\mathrm{II}}$. For the purpose of

examining the inter-nuclear exchange, the pseudo-secular interaction, Zeeman splitting and Zeeman orders of the nuclear dipolar interaction can be omitted, as these all commute with the rest of the Hamiltonian. Only the transverse relaxation term is kept, as the longitudinal term acts equally on both nuclei. The Hamiltonian and dissipator of this simplified system are thus given by

$$\begin{aligned}\hat{H}_{kk'}(t) &= \hat{a}_k(t)\hat{I}_{kz} + \hat{a}_{k'}(t)\hat{I}_{k'z} - \frac{d(t)}{2}(\hat{I}_{k+}\hat{I}_{k'-} + \hat{I}_{k-}\hat{I}_{k'+}),\\ \hat{a}_s(t) &= \sum_{j=1}^{2} A_{js}(t)\hat{S}_{jz}, \quad s = k, k' \ , \\ \hat{\hat{\mathcal{D}}}_{kk'} &= R_{2\mathrm{n}}[\hat{\hat{\mathcal{D}}}(\hat{I}_{kz}) + \hat{\hat{\mathcal{D}}}(\hat{I}_{k'z})].\end{aligned} \tag{5.10}$$

The z-component of the total nuclear spin $\hat{I}_z = \hat{I}_{kz} + \hat{I}_{k'z}$ commutes with $\hat{H}_{kk'}$ and therefore does not participate in the exchange process or dissipation. The effective exchange dynamics are therefore 2-level and fully described in terms of the fictitious operators

$$\hat{K}_z = \frac{1}{2}(\hat{I}_{kz} - \hat{I}_{k'z}), \qquad \hat{K}_\pm = \hat{I}_{k\pm}\hat{I}_{k'\mp}$$

(note the similarity to the treatment of the CE Hamiltonian). This leads to an effective Hamiltonian

$$\begin{aligned}\bar{\hat{H}}_{kk'}(t) &= \hat{a}(t)\hat{K}_z - d(t)\hat{K}_x\\ \hat{a}(t) &= \hat{a}_k(t) - \hat{a}_{k'}(t).\end{aligned}$$

$\hat{a}(t)$ is operator-valued due to the electron spins $\hat{S}_{jz}$ in the $\hat{a}_s(t)$ terms of EQ. 5.10, which have eigenvalues of $\pm 1/2$. The magnitude of $\hat{a}(t)$ in the effective Hamiltonian therefore depends on the orientation of the electrons and can take 4 different values. However, since the sign of $\hat{a}(t)$ bears no consequence on the exchange dynamics, only two effective values need be considered, and the dynamics averaged over only these two values. At typical experimental conditions of $T \sim 90$K and $B_0 < 20$T, the electron spin polarisations are $p_\mathrm{e} \sim 0.1$ (EQ. 2.3). The probability of finding the electrons in the up or down state is then given by $\frac{1}{2}(1 \pm p_\mathrm{e}) \sim 0.45$ or $0.55 \sim 0.5$, so

the electronic up and down states are more or less equally probable. It is therefore possible to take an equally weighted average over the two values of $\hat{a}(t)$. Note that this is no longer true for Cryo-MAS at 30K, where $p_{\mathrm{e}} \sim 0.3$.

Assume that one of the two $\hat{a}(t)$ values is chosen. The dissipator acts on the spin components as

$$\hat{\hat{\mathcal{D}}}\hat{K}_z = 0, \qquad \hat{\hat{\mathcal{D}}}\hat{K}_{\pm} = -R_{2\mathrm{n}}\hat{K}_{\pm},$$

and the effective master equation in the subspace of the two nuclei then describes the free decay of the spin observables $\langle p_\alpha(t)\rangle,\ \alpha = x, y, z$ obeying the Bloch equations

$$\begin{aligned}
\dot{p}_x(t) &= -\hat{a}(t)p_y(t) - R_{2\mathrm{n}}p_x(t), \\
\dot{p}_y(t) &= \hat{a}(t)p_x(t) + d(t)p_z(t) - R_{2\mathrm{n}}p_y(t), \\
\dot{p}_z(t) &= -d(t)p_y(t),
\end{aligned} \tag{5.11}$$

where $\hat{a}(t)$ and $d(t)$ have zero time-averages. In the Bloch notation, $p_z(t) = \langle K_z\rangle$ characterises the decay of the polarisation difference between two nuclei i.e. the polarisation equilibration process between each pair of nuclear spins. In addition to the spin diffusion process, there are also coherent dynamics in the form of the transverse terms $p_{x,y}(t) = \langle K_{x,y}\rangle$, generated by the nuclear flip-flop orders.

The value of $\hat{a}(t)$ dictates whether detailed analysis of EQ. 5.11 is possible. It is common in MAS DNP to use partially deuterated glassy matrices to mitigate fast nuclear relaxation [17]. Two common solvents are the so-called DNP juice (d8-glycerol/D_2O/H_2O, 60:30:10%) and d6-dimethyl sulfoxide/H_2O [17]. In DNP juice, the average nuclear separation is 6.18Å (including 3% residual protons from the deuterated glycerol and water, and if it is assumed that all nuclei are equally distributed in a cubic lattice). This leads to an average minimum dipolar interaction between neighbours of around 6Hz and an average maximum of around 660Hz. These values of d were calculated by averaging over 1e4 realisations of a 100 spin system

with an $n-n$ separation of (6.18 + 5%)Å and forming a random angle θ with the static magnetic field (refer to EQ. 2.13). The secular hyperfine interaction, and consequently $\hat{a}(t)$, on the other hand can take on a much broader range of values. The secular hyperfine interaction was calculated in shells of distance $(2.8 + n_{\mathrm{s}}6.18 + 5\%)$Å from an electron, where n_{s} is the shell number. $n_{\mathrm{s}} = 0$ corresponds to the average $e-n$ separation of the structural protons of bTbk [109]. In each shell, the average difference in the secular hyperfine interaction was calculated for 1e4 random pairs forming a random angle θ with the static magnetic field (refer to EQ. 2.14), and with both electrons oriented in the same direction. In the first shell the average difference is on the order of 10's of MHz, in the second $\hat{a}(t)$ is in the high 100's of kHz, the third shell has $\hat{a}(t)$ in the low 100's of kHz, and in the fourth it is 10's of kHz. Even with such a low concentration of nuclei (13%), the $\hat{a}(t)$ term dominates for nuclei in close proximity to the electrons. Too large of a separation between $\hat{a}(t)$ and $d(t)$ & $R_{2\mathrm{n}}$ however renders a detailed analysis of EQ. 5.11 impossible. This work will therefore focus on low proton concentration solvents such as DNP juice. For reference, the equivalent values of $\hat{a}(t)$ in a water/glycerol sample (with an $n-n$ separation of 2.5Å), are (starting from the second shell) mid MHz, low MHz, and 100's kHz.

Stroboscopic Nuclear Dynamics

The electron stroboscopic dynamics are calculated from the average propagator $\hat{M}$ that describes the dynamics within a rotor period. This is however not possible for the nuclei, whose polarisation dynamics are much slower. A different approach must therefore be taken.

If the condition

$$d_{\mathrm{max}}^2 T_{\mathrm{r}} \ll R_{2\mathrm{n}} \tag{5.12}$$

is met, then

$$p_z(nT_\mathrm{r}+t) \sim p_z(nT_\mathrm{r}),\ t \in [0, T_\mathrm{r}],$$

where d_max is the maximum nuclear dipolar interaction and nT_r is the n^th rotor period. In other words, the inter-nuclear exchange has a negligible effect on the nuclear spin dynamics within a rotor period. It is therefore possible to coarse-grain the dynamics and describe them stroboscopically. For typical spinning frequencies of ν_MAS <100kHz, typical R_2n of 5000s^{-1} at 100K [25, 26], and an average maximum dipolar interaction of 660Hz (as calculated above), the condition in EQ. 5.12 is easily satisfied.

A further simplification to the dynamics can be achieved by calculating the nuclear exchange rate numerically. For any given spin pair, the effective nuclear exchange rate $r_{kk'}$ can be found by fitting a monoexponential to the stroboscopic dynamics:

$$p_{k,\alpha}(nT_\mathrm{r}) \sim p_{k,\alpha}(0)\mathrm{e}^{-r_{kk'}nT_\mathrm{r}}, \qquad \alpha = x, y, z.$$

This numerical scheme involves only 3×3 operators and is therefore highly efficient. The nuclear polarisation of the k^th spin after the n^th MAS period is then

$$p_k^{(n)} = \tilde{p}_k^{(n)} + \frac{1}{2}\sum_{k<k'}(1-\mathrm{e}^{-r_{kk'}T_\mathrm{r}})(\tilde{p}_{k'}^{(n)} - \tilde{p}_k^{(n)}). \tag{5.13}$$

EQ. 5.13 is the correction to the stroboscopic nuclear polarisation calculated by the purely incoherent Landau-Zener approximation ($\tilde{p}_k^{(n)}$). It takes into account the nuclear dissipation that acts over many periods and modulates the polarisation exchange between two nuclei by their polarisation difference.

The incoherence condition for the nuclear dynamics is

$$\frac{\nu_\mathrm{MAS}}{2\pi} \ll R_\mathrm{2n} \ll \frac{|\dot{\hat{a}}_{kk'}(t)|}{|d_{kk'}(t)|},$$

when the detuning $\hat{a}(t)$ is zero.

5.5 Incoherent Decay in Landau-Zener Theory

For the Landau-Zener approximation to be valid, coherences must decay quickly, particularly those generated by electronic spin-spin relaxation. If T_{2e} is longer than the characteristic temporal separation between rotor events, quantum coherences persisting over multiple events affect the magnitude of the polarisation jump. Since coherences are highly dependent on the energy difference $\delta(t)$, and between jumps $\delta(t)$ dominates over the mixing rate, a slow T_{2e} decay introduces a random phase to the dynamics. This random phase accumulates between jumps and, in conjunction with the fact that different pairs of states now participate in the non-adiabatic jumps with different transition rates, makes the application of the Landau-Zener approximation impossible.

If however coherences decay quickly, i.e. the relaxation time is much shorter than the inter-jump length ($T_{2e} \ll 2\pi/10\nu_{MAS}$), then the coherent terms rapidly decay between jumps and can be neglected as they have here. Combined, the three conditions

1. Incoherent dynamics:
$$T_{2e} \ll \frac{2\pi}{10\nu_{MAS}},$$

2. Microwave and electron events:
$$\max\left\{\frac{|\omega_1|}{|\dot{\Delta}_j(t_0)|}, \frac{|D(t_0)|}{\dot{\Delta}(t_0)|}\right\} \ll \min\left\{\frac{2\pi}{10\nu_{MAS}}, T_{2e}\right\}$$

3. And CE events:
$$\max\left\{\frac{|B(t_0)D(t_0)|}{4\omega_I\dot{\Delta}(t_0)}\right\} \ll \min\left\{\frac{2\pi}{10\nu_{MAS}},\ T_{2e}\right\},$$

lead to purely incoherent spin dynamics represented by a sequence of non-adiabatic Landau-Zener transitions.

5.5.1 Application of the Incoherence Conditions

In this section, approximate values for the microwave, electron and CE transition times are calculated for the model system in FIG. 5-2 to evaluate how restrictive the incoherence conditions are.

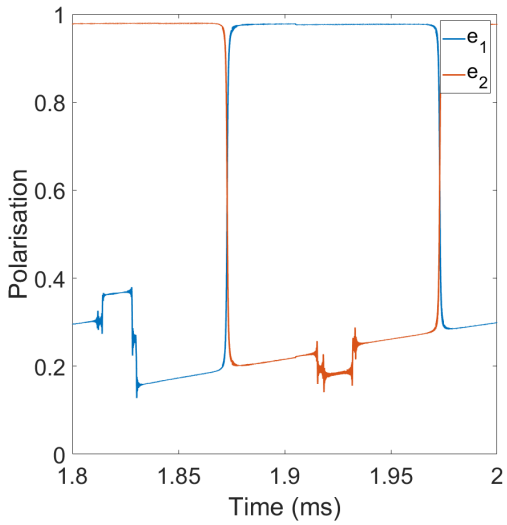
The derivative of the two electron offsets at the microwave exchange ($\partial\Delta_j(t_0)/\partial t$) is on the order of 1.3e13s^{-2}, comparable to values obtained by Thurber & Tycko [100]. The dipolar and pseudo-secular hyperfine interactions are approximately 0.1GHz and 10MHz respectively at the transitions, leading to a transition time of a few nanoseconds, while the rotor period is on the order of 10's of microseconds and the electron T_{2e} can be expected to be on the order of microseconds [100]. The CE incoherence condition is therefore easily satisfied. It remains satisfied at spinning frequencies of up to 100kHz, though at such high frequencies the first condition is violated, and electron coherences do not have time to decay between events.

The two electron saturation transition times are on the order of tens of nanoseconds and the electron polarisation exchange is on the order of 0.5μs. The electron exchange is quite slow compared to the electron T_{2e} relaxation, which is why the transitions in FIG. 5-2 are quite smooth.

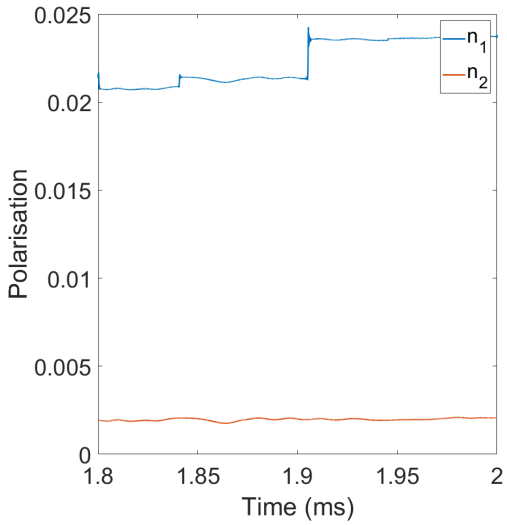
5.5.2 Dynamics in One Rotor Period

To understand better the effect of violating the incoherence conditions, it is instructive to examine the electron and nuclear dynamics within a single rotor period (FIG. 5-4). The parameters are given in the caption of FIG. 5-2. The additional proton is located at $[\cos(\pi/3),\ 0,\ \sin(\pi/3)] \times 0.6$Å from e_1. Dynamics are shown in the 9$^{\text{th}}$ rotor period, by which time the electrons have reached their stroboscopic steady state. Once they reach their stroboscopic steady state, the microwave and electron events are compensated by T_{1e} and the electrons no longer change polarisation between rotor periods (though they change polarisation within a period) [110]. Many more periods

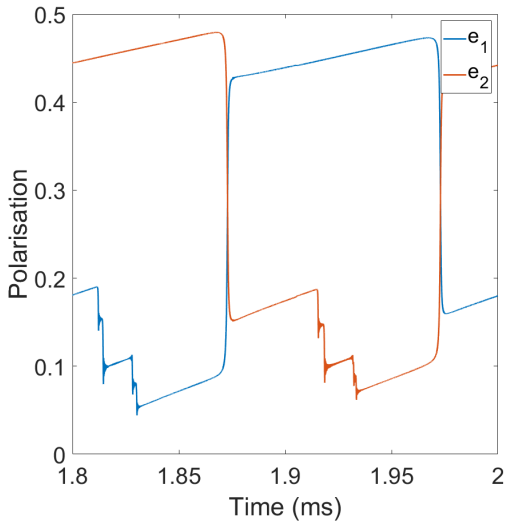
are required for the protons to reach their stroboscopic state.



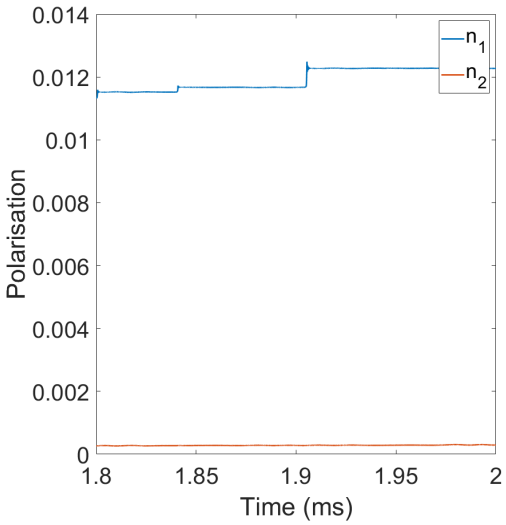
(a) Electron dynamics for $R_{2e} = 1 \times 10^3 s^{-1}$.



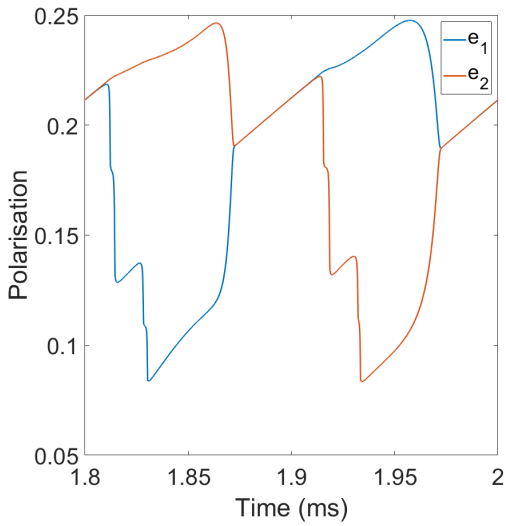
(b) Proton dynamics for $R_{2e} = 1 \times 10^3 s^{-1}$.



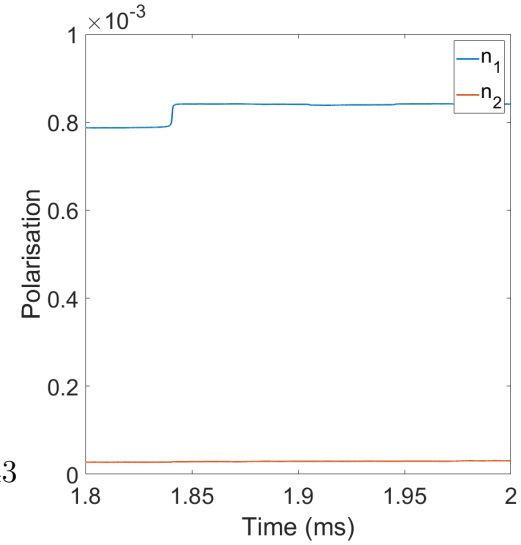
(c) Electron dynamics for $R_{2e} = 1 \times 10^5 s^{-1}$



(d) Proton dynamics for $R_{2e} = 1 \times 10^5 s^{-1}$.



(e) Electron dynamics for $R_{2e} = 1 \times 10^7 s^{-1}$.



(f) Proton dynamics for $R_{2e} = 1 \times 10^7 s^{-1}$.

Figure 5-4: Dynamics within the 9^{th} rotor period for the 3-spin system in FIG. 5-2, the second nucleus is located at $[\cos(\pi/3),\ 0,\ \sin(\pi/3)] \times 0.6$Å from e_1.

In FIG. 5-4, the electron (a,c,e) and proton (b,d,f) dynamics are shown for different values of the electron transverse relaxation. $T_{2\text{e}}$ plays an important role in the transition dynamics and can either carry coherences between events when it is too slow, violating the condition $T_{2\text{e}} \ll 2\pi/10\nu_{\text{MAS}}$, or act within a rotor event, making the it less efficient. In FIGs. 5-4a & 5-4b, $T_{2\text{e}}$ is 1ms, while the rotor period is 2ms. In FIG. 5-4a coherences clearly persist between polarisation events, and as a result the nuclear dynamics are not smooth, albeit high in polarisation. The fast simulation algorithm (see Section 5.6) however assumes completely incoherent dynamics and is not able to capture the effect of the random phase, thus incurring an error. In FIGs. 5-4c & 5-4d $T_{2\text{e}}$ is 10μs and therefore satisfies the incoherence condition. Although the polarisation is slightly lower, transitions are sharp and the nuclear dynamics smooth. For the very short $T_{2\text{e}}$ of 0.1μs in FIGs. 5-4e & 5-4f, the adiabaticity conditions are violated and the relaxation acts within a transition. The transitions are no longer sharp and the nuclear polarisation is much lower. The Landau-Zener approximation no longer applies and again, the fast simulation algorithm (Section 5.6) breaks down. In all cases, the polarisation of the second nucleus, located further away from the electron, only becomes appreciable after many more periods.

5.6 Fast Simulation Algorithm

The analytic methods outlined in the previous sections pave the way to a highly efficient simulation algorithm that requires only the indispensable effective dynamics. In the following paragraphs the fast simulation algorithm will be outlined and the conditions for its application specified.

The applicability of the fast simulation algorithm is dependent on a stringent set of conditions on the electron and nuclear dynamics. The dynamics themselves depend not only on inherent properties of the spins in question, but also on the experimental

parameters used. Care must be taken to ensure that the algorithm is used only when appropriate. The conditions are:

- Electrons must reach their stroboscopic steady state before nuclei start their polarisation dynamics.

- With the exception of ^{14}N nuclei in nitroxyl groups, nuclear dynamics do not affect electronic dynamics. It must be possible to treat the two separately. (Section 5.4.3)

- The dominating mechanism by which nuclear spins gain polarisation from the electrons is the non-adiabatic Landau-Zener jump that occurs at the CE resonances $\Delta(t) = \pm\omega_{\mathrm{I}}$. (Section 5.2.1)

- Nuclear quantum coherences (transverse dynamics) have a negligible effect on the polarisation dynamics and the longitudinal spin-lattice relaxation acts on time scales much longer than a rotation period. (Section 5.5)

- The thermal nuclear polarisation is negligible compared to the electron thermal polarisation and can therefore be neglected. (Section 5.4.2)

The combination of these assumptions and the analytic equations resulting from the Landau-Zener and Krylov-Bogolyubov approximations, along with the average propagator provide the basis for the fast simulation algorithm detailed below:

1. Numerically find the instances $\{t_1, ...t_m\},\ t_s \in [0, T_{\mathrm{r}}]$ of CE resonances $\Delta(t_s) = \pm\omega_{\mathrm{I}}$.

2. Numerically calculate the polarisation difference of the electrons at the CE resonances for the stroboscopic stationary state. This requires solving the full master equation of the pair of electrons for only one rotor period:

$$P_s = \pm 1(\langle \hat{S}_{1z} \rangle - \langle \hat{S}_{2z} \rangle)\Delta(t_s), \qquad \Delta(t_s) = \pm\omega_{\mathrm{I}}.$$

3. Calculate the Landau-Zener probability of the non-adiabatic CE jumps for the k^{th} nucleus at $t = t_s$ by

$$\epsilon_{sk} = 1 - \mathrm{e}^{-2\pi\Gamma_{sk}}, \qquad \Gamma_{sk} = \frac{D^2(t_s)|(B_{1k} - B_{2k})(t_s)|^2}{16\omega_{\mathrm{I}}^2|\dot{\Delta}(t_s)|}$$

4. Apply the recurrent formula

$$p_{sk} = (1 - \frac{\epsilon_{sk}}{2})p_{s,k-1} + \frac{\epsilon_{sk}P_s}{2}, \qquad s = 1, ..., m \tag{5.14}$$

within the rotation period for each nucleus k to calculate the nuclear polarisation before and after the s^{th} CE transition.

5. Let $p_k \equiv p_k^{n-1}$ be the polarisation of the k^{th} nucleus after the $(n-1)^{\text{th}}$ rotation period. The polarisation after the n^{th} period is then calculated using EQ. 5.14. The nuclear spin lattice relaxation is taken into account by letting $\tilde{p}_k^{(n)} \equiv \mathrm{e}^{-r_1 T_{\mathrm{r}}} p_{km}$. The nuclear exchange correction in EQ. 5.13 is applied to the values $\tilde{p}_k^{(n)}$, leading to the nuclear polarisation $p_k^{(n)}$ at the end of each period.

6. The algorithm starts from $p_k^{(0)}$ and is repeated for n rotations. The evolution interval is therefore nT_{r}.

5.7 Comparison to Other Groups

To the author's knowledge only three other groups have attempted large-scale simulations of MAS DNP systems. Thurber & Tycko were the first in 2014, followed by Mentink-Vigier et al. in 2017 [26], and finally Perras & Pruski in 2018 [103]. Thurber & Tycko's model is the simplest, consisting of 1000 3-spin systems coupled by the electron dipolar interaction. The aim of the large-scale simulation is to study the effect of electron spin diffusion on nuclear depolarisation. Each 3-spin system is simulated using the Landau-Zener formula rather than the full master equation. Although suitable for its purpose, this approach is rather limited, as it cannot take into

account nuclear spin diffusion for example. Mentink-Vigier et al.'s simulation is much more versatile. It is based on a reduced Liouville subspace that scales linearly with system size, and two types of events. These are Bloch-type events, in which relaxation process cannot be neglected (generally microwave and intra-molecular dipolar events) and Landau-Zener transitions, which can be considered to be infinitely sharp (generally SE, CE and inter-molecular events). They then propose a hybrid Bloch-Landau-Zener propagator that accounts for both types of events. With this approach they were able to simulate a 30-point field sweep of a 40 biradical system averaged over 10 realisations in approximately an hour. They also simulated a single biradical with 400 nuclei (60 core, 340 bulk) in 200s, a 20-fold improvement to the full LvN approach. Because they take into account Bloch-type transitions, they are not restricted by the condition of non-adiabaticity which is so crucial to A. Karabanov's fast simulation algorithm. Finally, Perras & Pruski have presented a Monte Carlo approach. They treat electron events with the Landau-Zener formalism, and use low-order correlations in Liouville space to model the spin diffusion. The Monte Carlo method is then applied to determine the steady state enhancement factor. Because they are limited to low-order correlations for the spin diffusion, the frequency range in which their simulation can be applied is restricted to 2.5 to 50kHz spinning frequencies, and spin diffusion times must be short. Nonetheless they were able to study the effects of spinning frequency on spin diffusion, and solvent/radical deuteration on the enhancement for systems as large as 87 spins. The fast simulation algorithm presented here aims to compete with the algorithm proposed by Mentink-Vigier et al. in terms of efficiency and applicability.

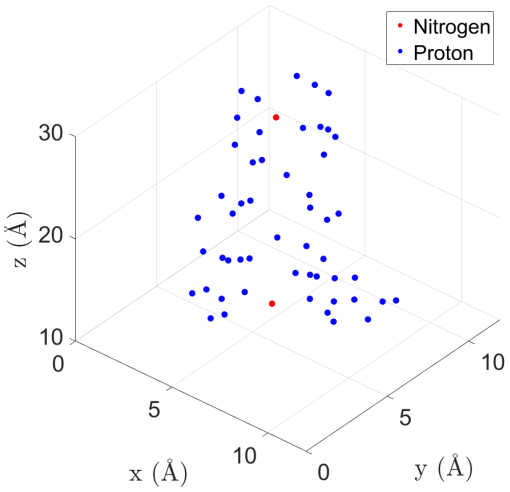
Chapter 6

Application of MAS Fast Simulation Algorithm

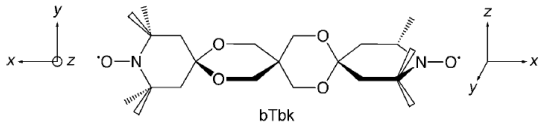
Following a similar structure to that of Chapter 4, this chapter presents an in silico study of the CE under MAS DNP conditions. The first section describes the geometry used for simulations. In the second section, the fast algorithm is compared with the full equation for a 3-spin system. The algorithm is tested as a function of spinning frequency and the electron transverse relaxation rate, and the importance of the number of integration steps and powder angles is highlighted. In the next section, the accuracy of the nuclear exchange dynamics is tested on a 4-spin system. The fourth section then starts to use the simulation algorithm predictively. Here, microwave frequency sweeps are presented for different static magnetic field strengths and spinning frequencies. Using the optimal microwave offset found from these 3-spin simulations, the first large-scale simulations comprising all 52 structural protons of bTbk are then performed for a similar set of parameters. Finally, a 152-spin simulation of all 52 structural protons of bTbk and an additional 100 solvent nuclei is used to examine in more detail the effect of the proton concentration in the solvent on MAS DNP.

6.1 bTbk Geometry

So far, the choice of electron geometry has been driven by optimisation considerations rather than true molecular geometries. This is possible in the static CE because there one can assume that as long as the concentration of electrons is high enough, sufficient pairs of electrons match the CE condition and give rise to DNP. In the MAS case, things are more complicated because of the constant re-orientation of molecules due to the sample spinning. One of the most popular biradicals used in MAS DNP is the nitroxide-based bis-TEMPO-bisketal (bTbk) [86]. The bisketal tether holding together the two TEMPO moieties in bTbk gives it a relatively rigid structure, which leads to increased enhancement since the electrons re-orient as a pair and retain their orientations relative to each other. The two TEMPO moieties form a dihedral angle of 82°, which is just 8° off the ideal 90° used in all simulations throughout this chapter [86]. For some simulations, the exact coordinates of the 52 structural protons and the two electrons are used. These are taken from REF. [109] and were loaded into the Spinach GUI (SpinDynamics - Southampton, UK) to calculate spin separations. In FIG. 6-1a the 52 structural protons (blue) and two nitrogen atoms (red) in bTbk are shown. 24 of the 52 structural protons come from methyl groups in close vicinity to the electrons. These are the protons closest to the electrons and on average have an $e - n_c$ distance of 2.8Å. Since the electrons are delocalised over the oxygen-nitrogen bond, the average $e - e$ distance is calculated from the centre of the two O-N bonds, and is ∼1.22nm [107]. The relative orientation of the electron g-tensor principal axes is taken from REF. [86] and is shown in the 3D structure of bTbk (FIG. 6-1b). The principal axis components are $g_X = 2.010$, $g_Y = 2.006$, $g_Z = 2.002$ [26]. Unless otherwise specified, all simulations have g-tensor orientations & principal axis components, and $e - e$ & $e - n_c$ distances corresponding to those of bTbk.



(a) bTbk coordinates.



(b) 3D structure of bTbk.

Figure 6-1: FIG. 6-1a shows the coordinates of the two nitrogen atoms (red) and 52 structural protons (blue) in bTbk. The geometry is taken from [109]. FIG. 6-1b shows the 3D structure of bTbk [86]. For the remainder of this chapter the principal axis systems of the two electrons will have this orientation with respect to each other.

6.2 Error Testing of the Fast Algorithm

The CE efficiency and non-adiabaticity conditions presented in Chapter 5 all depend on the electron transverse relaxation rate R_{2e} and the MAS spinning frequency ν_{MAS}. The fast simulation algorithm is therefore tested against the full master equation (EQs. 5.1 & 2.8) as a function of each of these parameters. This section starts however with a study of two additional sources of error in MAS simulations: the integration time step and the powder averaging protocol. In this section, simulations are limited to 24 powder angles (except Section 6.2.2), and only one nitrogen spin orientation ($J_{1z} = J_{2z} = 0$). Nonetheless, good agreement is observed between the fast and full algorithms, although averaging over more powder angles and all nitrogen orientations may be necessary to match experimental data.

6.2.1 Integration Time Step

The piece-wise integration of the MAS Hamiltonian used to calculate the dynamics within a rotor period assumes that the integration time step is short enough that the Hamiltonian is constant in that time. If this is not the case, this approach is no longer accurate and the dynamics become random and characterised by a low polarisation. Simulations with low spinning frequencies require a larger number of time steps to ensure that they are short enough, whereas simulations with high spinning frequencies can have fewer steps and still be accurate. This is shown in FIG. 6-2, where the stroboscopic nuclear steady state polarisation calculated by the full master equation is plotted for different spinning frequencies as a function of N, the number of time steps. When N is large enough, the dynamics converge and the polarisation stays constant. If N is too small however, the polarisation is lower than it should be and the nuclear dynamics show an unphysical dependence on the integration time step. Care must therefore be taken when setting up simulations to ensure that the time step is sufficiently short (N sufficiently large).

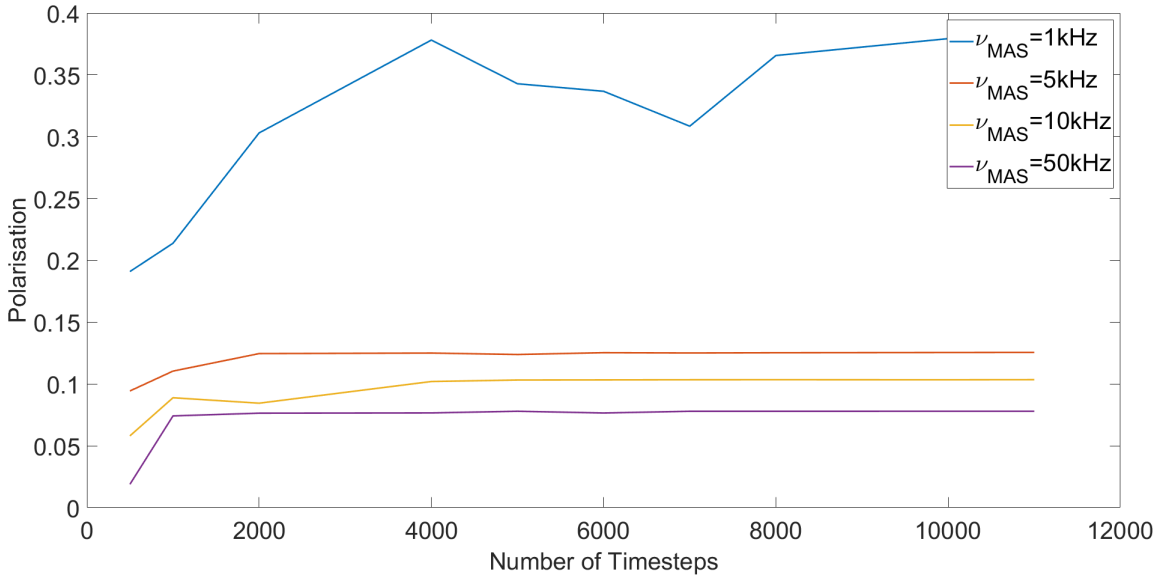


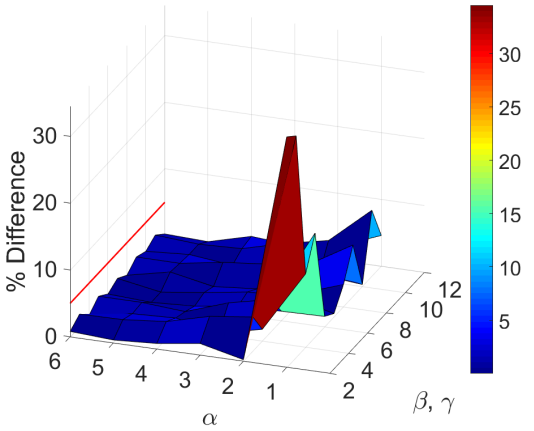
Figure 6-2: Stroboscopic nuclear steady state polarisation as a function of number of integration steps for different spinning frequencies. The geometry is similar to that of bTbk: the $e-e$ distance is 1.22nm, the e_1-n vector is $[\sqrt{(2/3)},\ 0,\ \sqrt{(1/3)}]\times$0.3nm. The proton interacts with e_1 only. The electron g-tensors are oriented as in FIG. 5-1, and the initial Euler angles are all 0. The principal components of the electron g-tensors are $g_X = 2.010,\ g_Y = 2.006,\ g_Z = 2.002$. The dynamics are averaged over 24 powder angles, but not over the 9 nitrogen orientations ($J_{1z} = J_{2z} = 0$). The physical parameters are: $B_0 = 14.1$T, $T = 100$K, $R_{1e} = 10^3 s^{-1}$, $R_{2e} = 1.7 \times 10^5 s^{-1}$, $R_{1n} = 0.1 s^{-1}$, $R_{2n} = 10^3 s^{-1}$, ν_{MAS} =0.1kHz to 50kHz, N=500 to 11000, $\Delta_0 = 650$MHz, $\omega_1 = 0.6$MHz.

6.2.2 Powder Averaging Protocol

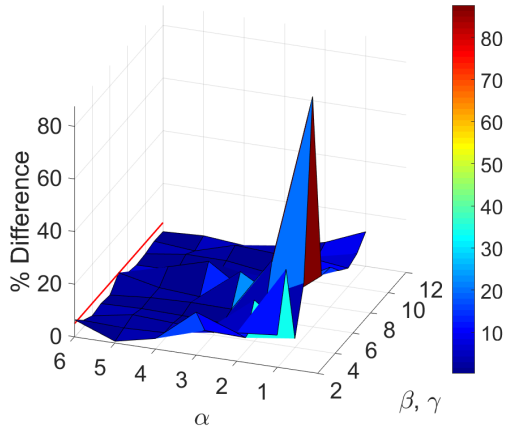
Powder averaging is an essential component of MAS simulations due to the periodic re-orientation of the interaction parameters as the sample rotates. However, the necessity for averaging over powder angles also drastically increases simulation time. It is therefore imperative to choose efficient powder averaging protocols that converge for a minimal number of powder angles. The powder protocol chosen for most simulations in this chapter is based on the "repulsion" protocol with 72 powder angles [104, 105]. Another popular protocol is the ZCW protocol [111, 112, 113].

FIG. 6-3 shows the percent difference between the end nuclear polarisation (of the 3-spin system described in Section 6.2.1) of successive $\beta,\ \gamma$ pairs for each α. The red

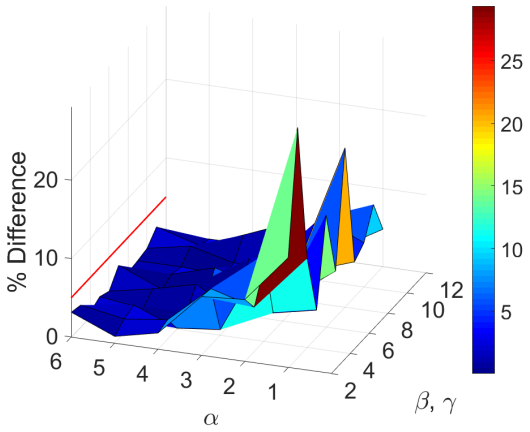
line marks 5% difference. From the figure it is clear that averaging over 6 α angles and β, γ pairs, leads to convergence below 5% for spinning frequencies ranging from 1kHz to 15kHz.



(a) $\nu_{\mathrm{MAS}} = 1\mathrm{kHz}$.



(b) $\nu_{\mathrm{MAS}} = 5\mathrm{kHz}$.



(c) $\nu_{\mathrm{MAS}} = 15\mathrm{kHz}$.

Figure 6-3: Surface plots showing the percent difference between successive averages of β, γ pairs for each alpha. FIG. 6-3a: $\nu_{\mathrm{MAS}} = 1\mathrm{kHz}$, $N = 7\mathrm{e}3$, FIG. 6-3b: $\nu_{\mathrm{MAS}} = 1\mathrm{kHz}$, $N = 5\mathrm{e}3$, FIG. 6-3c: $\nu_{\mathrm{MAS}} = 15\mathrm{kHz}$, $N = 5\mathrm{e}3$. The remaining parameters are as in FIG. 6-2.

6.2.3 Electron Relaxation Rate Scan

FIG. 6-4 shows the stroboscopic nuclear steady state polarisation as a function of the electronic transverse relaxation for MAS frequencies of 0.1kHz, 5kHz, & 10kHz calculated with the full (dashed) and fast (solid) algorithms. The error stays below 10% over the entire range of relaxation rates except for very fast relaxation at low spinning frequency. Lines are to guide the eye only.

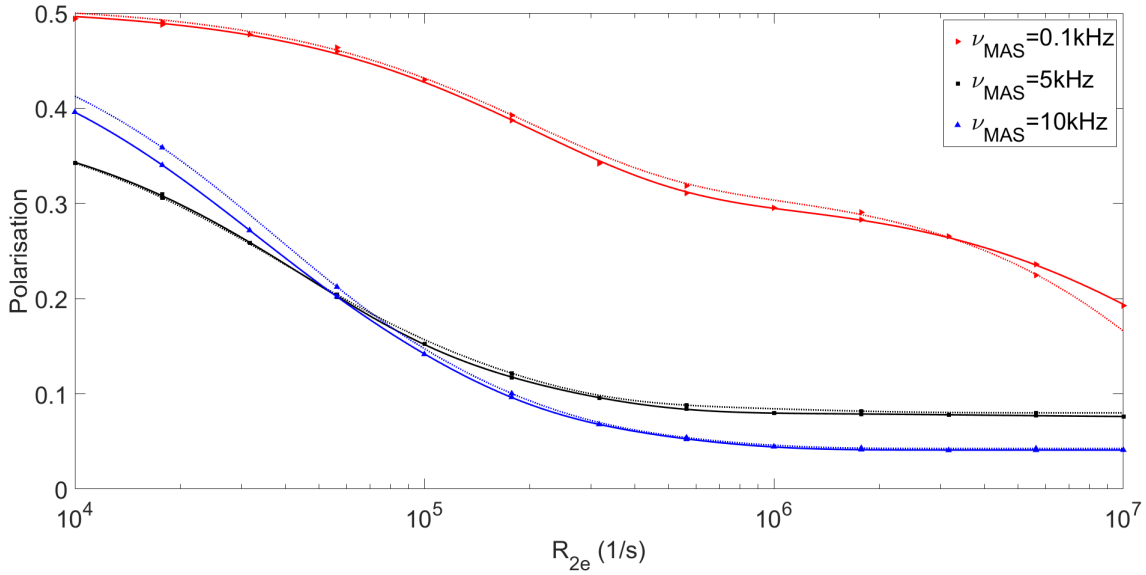


Figure 6-4: Stroboscopic nuclear steady state polarisation as a function of the electron transverse relaxation R_{2e} for the full (dashed) and fast (solid) algorithms at ν_{MAS} =5kHz & N =5e3 (black squares), ν_{MAS} =10kHz & N =1e3 (blue triangles) and ν_{MAS} =0.1kHz & N =1e4 (red triangles). See caption in FIG. 6-2 for the system parameters.

At ν_{MAS} =5kHz, the error between the full and the fast algorithms is negligible over the entire range of relaxation rates. When ν_{MAS} =10kHz, there is an increase in error for slow relaxation rates because the incoherence condition in EQ. 5.5 is violated. When electron relaxation times are long and the rotor period short, coherences do not have time to decay between rotor events. The dynamics at the events therefore pick up a random phase which not only tends to decrease the polarisation, but is also not captured by the fast algorithm, thus incurring an error. The faster the spinning frequency, the faster relaxation rates must be for the dynamics to remain incoherent. However, relaxation rates faster than $\sim 10^6 \text{s}^{-1}$ are not experimentally relevant for

the systems studied here [100]. Focus will therefore be on spinning frequencies of 40kHz or less. For very low spinning frequencies, when the transitions are slow, the error is larger for fast relaxation. This is because in this regime, relaxation acts within a rotor event. When this happens, as was shown in FIG. 5-4e, the polarisation jumps become smaller and lose their jump-like nature. They are therefore no longer accurately captured by the Landau-Zener formalism, and would require treatment using the Bloch-like formalism introduced by Mentink-Vigier et al. [26].

6.2.4 MAS Frequency Scan

FIG. 6-5 shows the stroboscopic nuclear steady state of the full (dashed) and fast (solid) algorithms as a function of the spinning frequency. The electron transverse relaxation rate is kept fixed at $R_{2e} = 1.7 \times 10^6 s^{-1}$, although in theory it should decrease with increasing ν_{MAS} as more dipolar interactions are averaged out. The number of integration steps was adjusted according to FIG. 6-2 for each spinning frequency.

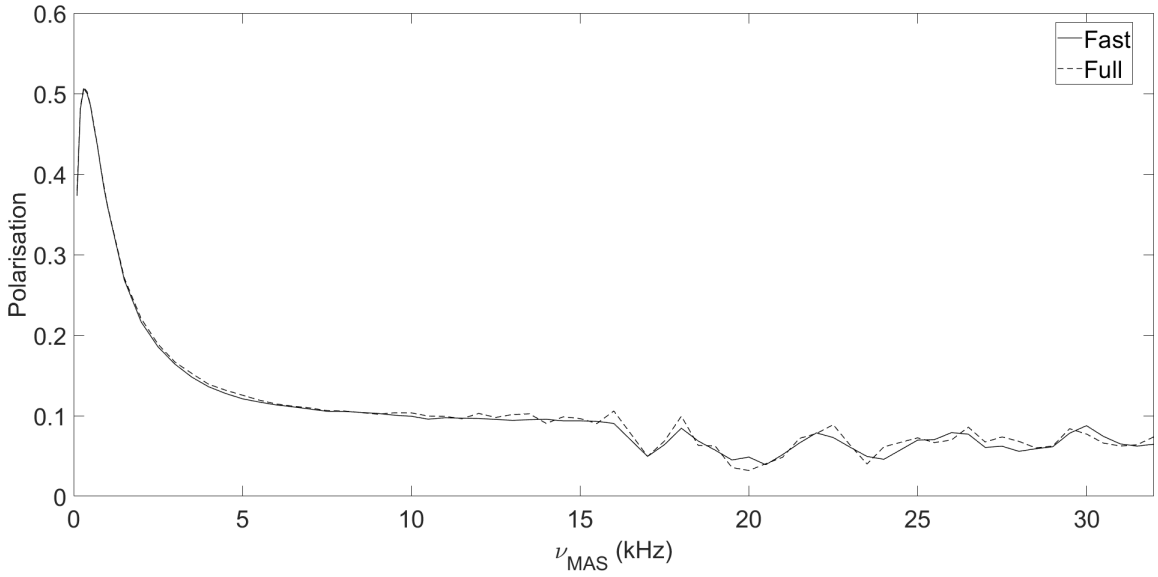


Figure 6-5: Stroboscopic nuclear steady state polarisation as a function of the spinning frequency ν_{MAS} for the full (dashed) and fast (solid) algorithms. $R_{2e} = 1.7 \times 10^5 s^{-1}$, refer to Fig. 6-2 for the remaining parameters.

The fast simulation algorithm shows very good agreement with the full equation

for ν_{MAS} <10kHz. Notably, it captures the non-monotonic behaviour of the nuclear polarisation as a function of the spinning frequency, which arises from the electronic longitudinal relaxation. For very low spinning frequencies, the longitudinal relaxation time is much shorter than the rotor period, $T_{\mathrm{r}}/T_{1\mathrm{e}} \gg 1$, so the electrons reach their (equal) thermal polarisation at the beginning of the MAS period, and remain there for the rest of it. Since the CE transfers the polarisation *difference* of the electrons to the nuclei, the nuclear polarisation is low in this regime. As the spinning frequency increases, the electrons spend more of their time with different polarisations, thus increasing CE DNP. However, if the spinning frequency is too fast, and $T_{\mathrm{r}}/T_{1\mathrm{e}} \ll 1$, the electrons never reach thermal equilibrium. This leads to both of them being saturated because the system never resets, thereby again quenching CE DNP because no polarisation difference is created between the electrons. Furthermore, for very fast spinning frequencies transverse coherences are more likely to persist over multiple jump events, introducing a random phase that makes the dynamics non-smooth, and tend towards lower polarisation. This is seen in FIG. 6-5 for spinning frequencies above 10kHz. Above 10kHz, the fast simulation algorithm is no longer as accurate for this combination of spinning frequency and $R_{2\mathrm{e}}$ because it cannot describe well the coherent dynamics.

The optimal spinning frequency for MAS CE DNP depends on the electron relaxation times and thus varies from system to system. In the ideal case, the electron polarisation difference is maximised for a significant part of the MAS period and the electronic transverse relaxation does not affect the dynamics.

6.3 Nuclear Exchange Dynamics

In this section, the nuclear exchange dynamics in the fast algorithm are tested against the full master equation for a single crystallite 4-spin system.

6.3.1 Geometry

The 4-spin geometry used is shown in FIG. 6-6. In the lab frame, the electron pair is fixed along the x-axis with a separation of 1.22nm and the $e_1 - n_\mathrm{c}$ pair is fixed along the y-axis with a separation of 0.28nm. The $e_1 - n_\mathrm{b}$ pair has fixed separation of 0.9nm and forms a variable angle ϕ with the $e_1 - n_\mathrm{c}$ pair in the xy-plane. The n_c and n_b distances are typical of bTbk in DNP juice, where the core (n_c) corresponds to the average $e - n$ distance to the methyl group protons and the bulk (n_b) to the average distance to the first shell of solvent protons (refer to Section 5.4.3).

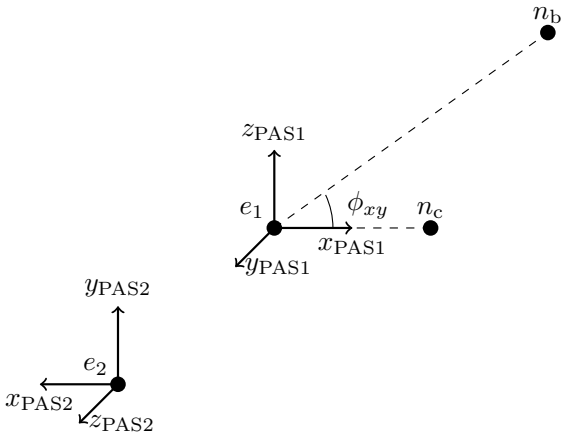
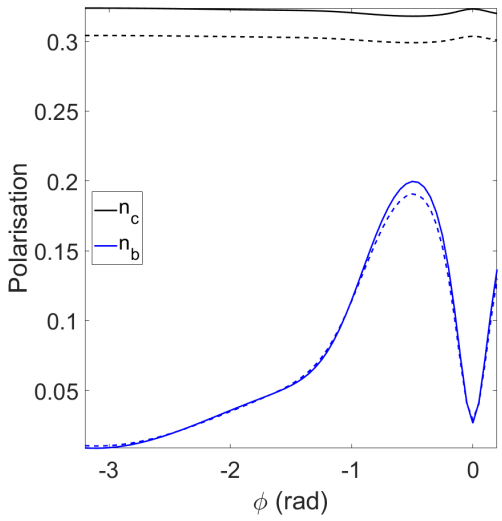


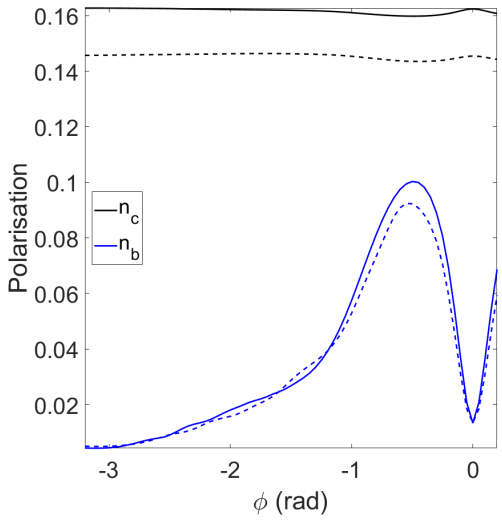
Figure 6-6: 4-spin system used to study nuclear exchange dynamics. The $e_1 - n_\mathrm{c}$ vector is $[0,\ 1,\ 0] \times 0.28$nm, the $e_1 - n_\mathrm{b}$ distance is 0.9nm.

6.3.2 Simulations

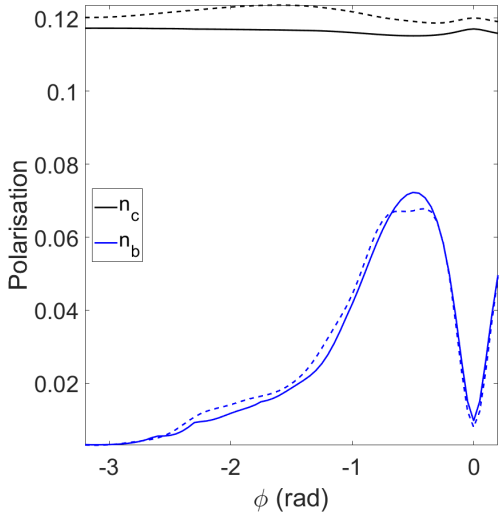
FIG. 6-7 shows the stroboscopic nuclear polarisation of the core (blue) and bulk (black) protons for the full (dashed) and fast (solid) simulation algorithms for a 14.1T static field, with $R_{2\mathrm{e}} = 1 \times 10^5 \mathrm{s}^{-1}$, $R_{2\mathrm{n}} = 2 \times 10^4 \mathrm{s}^{-1}$, and ν_MAS =1kHz, 5kHz, 10kHz & 20kHz.



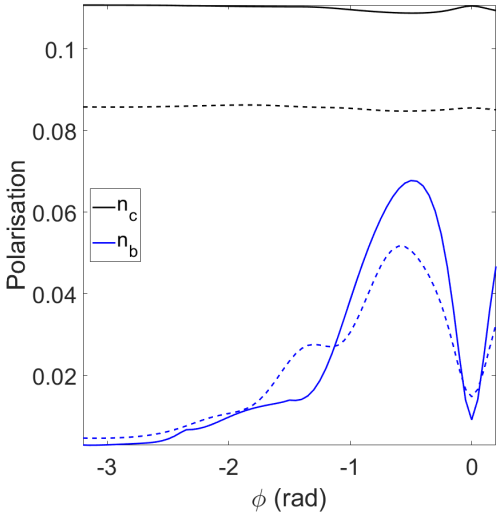
(a) Enhancement for ν_{MAS}=1kHz.



(b) Enhancement for ν_{MAS}=5kHz.



(c) Enhancement for ν_{MAS}=10kHz.



(d) Enhancement for ν_{MAS}=20kHz.

Figure 6-7: Single crystallite core (blue) and bulk (black) enhancement for the full (dashed) and fast (solid) algorithms as a function of the angle ϕ between the $e_1 - n_c$ and $e_1 - n_b$ vector. The geometry is shown in FIG. 6-6. $R_{2e} = 10^5 s^{-1}$, $R_{2n} = 2 \times 10^4 s^{-1}$. The remaining parameters are as it FIG. 6-2.

6.3.3 Discussion

Effect of ϕ

When the angle ϕ between the two nuclei is large, they are far apart and spin dif-

fusion is inefficient because the nuclear dipolar interaction is weak. Since the bulk proton is polarised primarily by spin diffusion, it thus has low polarisation. As ϕ decreases, the dipolar interaction increases and n_{b} becomes more polarised. However, because even at their closest the two protons are still relatively far apart (0.68nm), the bulk is never able to achieve the same polarisation as the core, since much of the polarisation relaxes before reaching it. Decreasing the angle further, an interesting feature is observed as ϕ approaches zero. When $\phi = 0$, the unit vectors of $e_1 - n_{\mathrm{c}}$ and $e_1 - n_{\mathrm{b}}$ have the same angular dependence. As a consequence, the time $t_{kk'}$ when the energy gap between the nuclear states ($\hat{a}(t)$) is zero coincides with the time the dipolar interaction ($d(t)$) is zero. Therefore, no transition takes place. However, for higher spinning frequencies, the coherences that are carried over from the electron events alter the energy level diagram in such a way that even when $\phi = 0$, the bulk receives some polarisation. This is seen in the full simulation algorithm, but not the fast algorithm.

Effect of ν_{MAS}

By changing the spinning frequency, the effects of coherent decay on the nuclear dynamics can be examined. When the spinning frequency is relatively low (FIG. 6-7a), transitions are diabatic, and all coherences, both nuclear and electronic, decay between jump events and do not carry over into the next event. The fast simulation algorithm is therefore able to accurately capture the nuclear dynamics of the bulk, although it tends to overestimate the polarisation of the core. This is possibly because for short $e - n$ distances, the pseudo-secular hyperfine interaction is very strong, thus potentially violating the incoherence condition for CE transitions (EQ. 5.9), especially when the spinning frequency is high. As the spinning frequency increases, the polarisation of both the core and the bulk decreases, as expected. However, while the full algorithm shows the non-smooth dynamics due to electron and nuclear coherences, the dynamics of the fast algorithm retain the same angular dependence for all four spinning frequencies. Nuclear coherences become particularly relevant in FIG. 6-7d, where the nuclear transverse relaxation is equal to the 20kHz spinning frequency, vi-

olating the condition $2\pi/\nu_{\mathrm{MAS}} \ll R_{2\mathrm{n}}$.

In any full MAS simulation, the dynamics are powder averaged, and thus the detailed geometry dependences described in this section disappear. Nonetheless, the importance of incoherent dynamics has once again been shown, and the accuracy of the fast simulation algorithm verified in an appropriate parameter regime.

6.4 bTbk Core Simulations

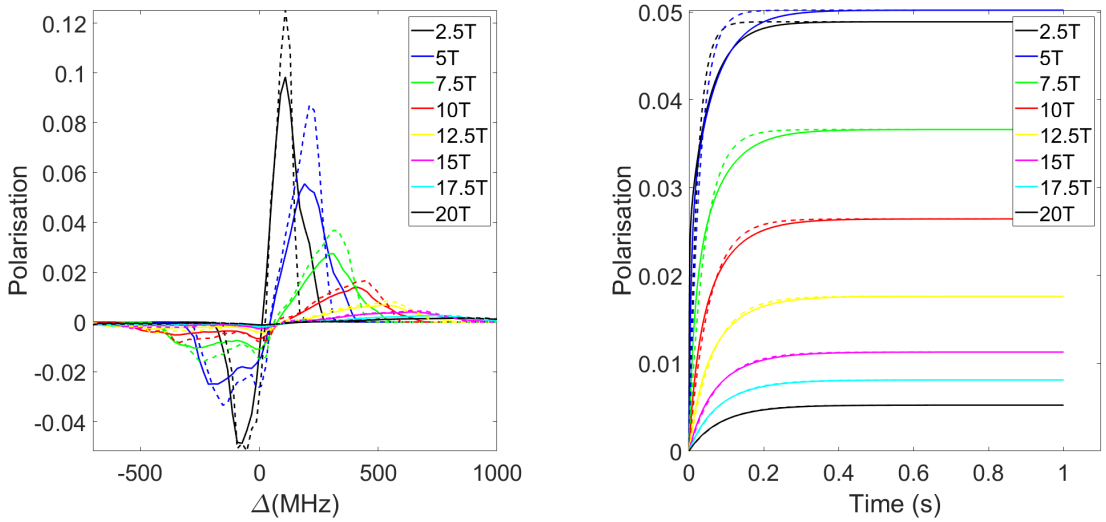
This section is the first to use the fast simulation algorithm for predictive purposes. Here the geometry first returns to the 3-spin system to simulate frequency sweeps of the microwave irradiation $\omega_{\mu\mathrm{w}}$ (manifested in the offset Δ_0) for different static field strengths and spinning frequencies. The optimal microwave offset found using these small-scale simulations is then used to inform simulations of the 52 structural protons of bTbk, also for different static field strengths and spinning frequencies. The 3-spin simulations are averaged over 72 powder angles and all 9 nitrogen orientations and will be used to demonstrate the time-savings achieved by using the fast simulation algorithm. The single proton is attached to the e_1 by the vector $[\sqrt{2/3},\ 0,\ \sqrt{1/3}]\times$ 0.5nm. The 52-spin simulations are averaged over 72 powder angles but not the 9 nitrogen orientations ($J_{1z} = J_{2z} = 0$).

6.4.1 Static Field Sweep

FIG. 6-8a shows the the offset sweeps for static fields ranging from 2.5T to 20T with (solid) and without (dashed) nitrogen averaging. For the case without nitrogen averaging, $J_{1z} = J_{2z} = 0$. For each static field, the powder & nitrogen averaged simulation over all microwave offsets, with 1e3 integration steps and 100 MAS periods took only ∼6 hours. In contrast, simulation over a single microwave offset of a single crystallite for the same number of integration steps and periods using the full equation takes ∼2.5s. Multiplying this by 72×9 for the powder & nitrogen averages yields 27 minutes for each microwave frequency. The 46-point frequency sweep would then take about

21 hours. Due to the exponential complexity scaling of system size with number of spins, the difference in simulation times between the fast and full algorithms becomes even more pronounced for larger spin systems.

FIG. 6-8b shows the buildup of the 52 structural protons of bTbk over the same range of magnetic fields and using the optimal offset seen in FIG. 6-8a.



(a) 3-spin system.

(b) 52 spin system.

Figure 6-8: FIG. 6-8a: Stroboscopic nuclear steady state enhancement of a 3-spin system as a function of the offset Δ for different B_0 using the fast algorithm with (solid) and without (dashed) nitrogen averaging. The $e-n$ vector is $[\sqrt{2/3}, 0, \sqrt{1/3}] \times 0.5$ nm. $T = 95$K, $R_{1e} = 3 \times 10^3 \text{s}^{-1}$, $R_{2e} = 10^6 \text{s}^{-1}$, $R_{1n} = 10 \text{s}^{-1}$, ν_{MAS}=5kHz. The hyperfine tensor components of nitrogen are $A_x = 17$MHz, $A_y = 20.5$MHz, $A_z = 95.9$MHz [26]. Other parameters are the same as in FIG. 6-2. FIG. 6-8b: Average stroboscopic nuclear steady state enhancement of the 52 structural protons of bTbk for different B_0 using the optimal Δ observed in FIG. 6-8a using the same parameters. These simulations are not nitrogen averaged ($J_{1z} = J_{2z} = 0$). Dashed lines show a monoexponential fit to the polarisation dynamics. In both cases 72 powder angles are averaged. Remaining parameters are as in FIG. 6-2.

6.4.2 Discussion

3-spin Simulations

From FIG. 6-8a it is evident that the strength of the static magnetic field affects not only the position of the optimal microwave offset, but also the maximum enhancement. The electron Zeeman splitting $\Delta_j(t)$ is dependent on the electron Larmor

frequency, which is in turn dependent on the static field as $\omega_S = \gamma_S B_0$, where γ_S is the electron gyromagnetic ratio. Larger offsets are therefore required to achieve resonance at higher magnetic fields. The reduction in enhancement at high fields is due to increased inhomogeneous broadening of the EPR spectrum. This accelerates the transverse relaxation and increases the passage velocity ($\dot{\delta}(t)$ in EQ. 2.43). Since the Landau-Zener transition probability is inversely proportional to the passage velocity, polarisation exchange at avoided level crossings becomes less probable and the enhancement decreases. Nonetheless, MAS DNP is often performed at high magnetic fields (the MAS DNP facility at the University of Nottingham for example has a magnetic field of 14.1T) because this increases the NMR resolution [17].

Near the peaks of the offset sweeps, the simulations without nitrogen averaging (dashed) overestimate the nuclear enhancement. This is because the chosen nitrogen orientation $J_{1z} = J_{2z} = 0$ is such that the nitrogen has no effect on the electrons. However, in the remaining 8 configurations, one or both of the electrons are hyperfine shifted by their respective nitrogen atom and therefore no longer on resonance. This diminishes the efficiency of the DNP process since they are no longer fully saturated by the microwave field. This effect is much more pronounced at low magnetic fields, where the hyperfine shift due to the nitrogen is proportionally larger. At high magnetic fields however, the Zeeman splitting is so large that the hyperfine shift has minimal effect. Indeed, for B_0=20T there is barely any difference between the two simulations. This suggests that for simulations with large magnetic fields it is not necessary to average over all 9 nitrogen orientations to obtain reasonably accurate nuclear dynamics. The choice of nitrogen orientation for the non-averaged case also causes the enhancement to drop to zero at much smaller positive offsets at low fields. With only a single orientation, the system loses resonance much faster than if all combinations, each with a different resonance, were taken into account.

Finally, it is noted that the $B_0 = 5$T offset sweep with nitrogen averaging closely matches the experimentally observed bTbk spectrum at $B_0 = 5$T [86].

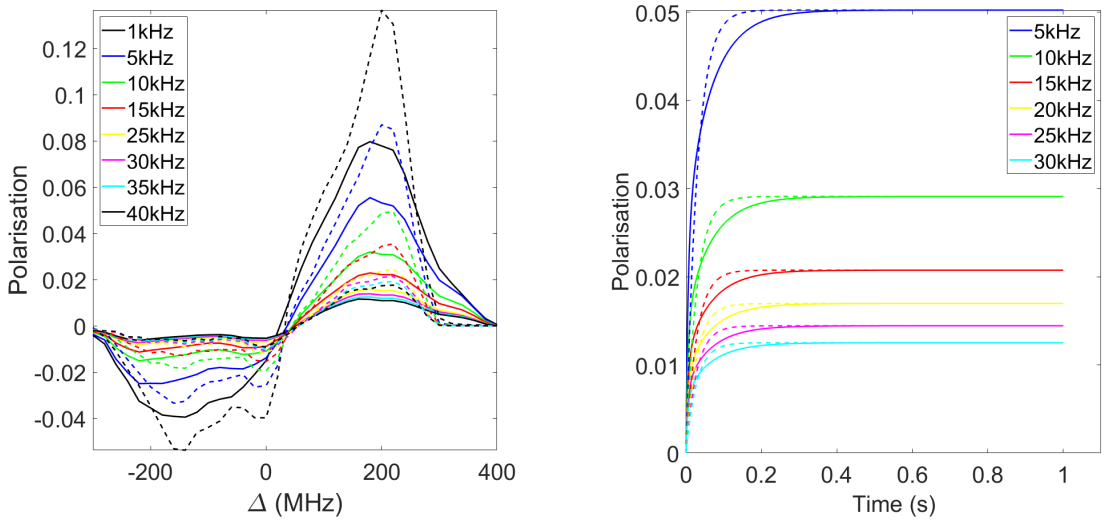
52-spin Simulations

In FIG. 6-8b, the optimal offsets observed in FIG. 6-8a are used to simulate the polarisation dynamics of the 52 structural protons of bTbk. In these simulations the enhancement has a peak somewhere between 2.5T and 5T that is not observed for the 3-spin system. This is possibly because, with a compact molecule like bTbk (the furthest protons are 0.8nm from an electron), if the Zeeman splitting of the energy levels is too small, the secular hyperfine interaction creates unfavourable degeneracies. Small static fields therefore have a reduced enhancement.

For high magnetic fields the buildup is well-fit by a monoexponential, suggesting that the proton polarisation equilibrates across the entire molecule before approaching the steady state. At low fields, where the monoexponential fit is not as good, different protons approach the steady state at different rates. This may be because when the magnetic field is low, the Zeeman splitting is small, and the detuning due to the secular hyperfine interaction is more significant. Since large differences in the hyperfine shifts quench the nuclear exchange, nuclei in the further reaches of the bTbk molecule may no longer be polarised as effectively, and thus have a slower buildup time. At high fields, the same hyperfine shift is smaller compared to the energy gap, and the nuclear exchange is more active.

6.4.3 MAS Frequency Sweep

FIG. 6-9a shows the offset sweeps for MAS spinning frequencies ranging from 1 to 40kHz with (solid) and without (dashed) nitrogen averaging for the 3-spin system. As before, for the case without nitrogen averaging the orientations are $J_{1z} = J_{2z} = 0$. FIG. 6-9b shows the average buildup for the 52 structural protons of bTbk over the frequency range 5kHz to 30kHz. In both cases the static field strength is 5T.



(a) 3-spin system.

(b) 52-spin system.

Figure 6-9: FIG. 6-9a: Stroboscopic nuclear steady state enhancement of a 3-spin system as a function of the offset Δ for different ν_{MAS} using the fast algorithm with (solid) and without (dashed) nitrogen averaging. B_0=5T. FIG. 6-9b: Average stroboscopic nuclear steady state enhancement of the 52 structural protons of bTbk for different ν_{MAS} using the optimal Δ observed in FIG. 6-9a using the same parameters. These simulations are not nitrogen averaged ($J_{1z} = J_{2z} = 0$). Dashed lines show monoexponential fits to the polarisation dynamics. In both cases 72 powder angles are averaged. Remaining parameters are as in FIG. 6-8.

6.4.4 Discussion

3-spin Simulations

The decrease in nuclear polarisation at high spinning frequencies was already observed in FIG. 6-5 and is observed again in FIG. 6-9a. In comparison to FIG. 6-8a though, the shape of the offset sweep for different spinning frequencies is different. Firstly, the optimal offset is not frequency dependent, as the frequency does not affect the energy level structure of the system but the transition probabilities. Also in contrast to FIG. 6-8a, the peaks all have similar shape, the only difference being a reduction in the enhancement as the spinning frequency increases. As was already discussed in Section 6.2.4, for high spinning frequencies CE transitions become less probable and are more likely to be encumbered by coherences carrying over from previous rotor events. Because the static field does not change, in FIG. 6-9a the case without

nitrogen averaging significantly over-estimates the enhancement for all spinning frequencies.

52-spin Simulations

As the spinning frequency increases, the 52-spin steady state is increasingly accurately predicted by the nitrogen averaged 3-spin model. Higher spinning frequencies average out more of the nuclear dipolar interactions, thus quenching spin diffusion, so that the only nuclei to become polarised are those polarised directly by the CE process. It may then be possible to represent the core nuclei with a single representative nucleus. This will be discussed in more detail in the next section. The fact that the 52-spin enhancement matches the nitrogen averaged enhancements of the 3-spin model is likely a coincidence. It could however suggest that an $e-n$ distance of 0.5nm is too short for a representative core nucleus. From a geometric stand point, a smaller enhancement is typically indicative of larger $e-n$ or $n-n$ separations. The matching of the 52-spin model with the lower-enhancement, nitrogen-averaged 3-spin model may therefore suggest that a larger $e-n$ separation is required.

6.5 Simulations of bTbk in Solvent

In this final section, a large-scale simulation of the 52 bTbk protons and 100 solvent protons is used to study in more detail the effect of the proton concentration in the solvent on the MAS DNP dynamics.

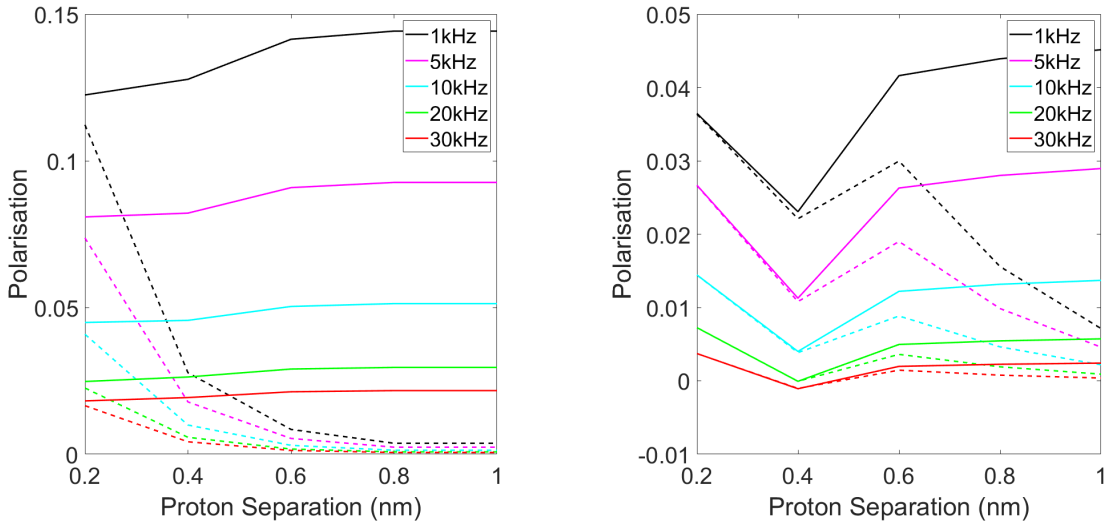
6.5.1 Geometry

The solvent is formed of a uniform random distribution to model the lack of crystalline structure due to glassing agents. 5 concentrations of protons were studied: 2Å, 4Å, 6Å, 8Å, & 10Å, corresponding approximately to proton concentrations of 207M, 25M, 8M, 3M, & 1.7M respectively. For reference, a 50/50 water/glycerol mixture is approximately 111M, and DNP juice is approximately 5M. The molarity is reduced experimentally by deuteration.

6.5.2 Simulations

These simulations were distributed over the 20-core and 16-core processors (refer to Chapter 4). However, due to the enormity of the propagation matrices, only 15 and 10 cores respectively were used, and the simulations offset, to avoid having multiple large matrices stored at the same time. For a system of 152 spins, the matrices used to calculate the propagators have dimensions $92416 \times 153 \times 153$, equating to approximately 16.1GB each. Although the matrices are only stored temporarily, the available RAM must be enough to handle this memory usage. The average simulation time for each powder angle with 1e3 integration steps was 3.3 hours.

Two sets of simulations were run. In parameter set 1, the parameters are $B_0 = 5\text{T}$, $R_{1\text{e}} = 3 \times 10^3\text{s}^{-1}$, $R_{1\text{n}}$=10s^{-1}, $R_{2\text{e}} = 10^6\text{s}^{-1}$ (FIG. 6-10a). In parameter set 2, the parameters are $B_0 = 14.1\text{T}$, $R_{1\text{e}} = 10^4\text{s}^{-1}$, $R_{1\text{n}}$=0.1s^{-1}, $R_{2\text{e}} = 10^6\text{s}^{-1}$ (FIG. 6-10b). The simulations are powder averaged but the nitrogen orientations are fixed at $J_{1z} = J_{2z} = 0$. This is justified because although the nitrogen spins have an effect on the overall enhancement by changing the electron offsets, they do not affect spin diffusion. The spinning frequency, however, does affect spin diffusion, so the simulations were run for spinning frequencies from 1kHz to 30kHz.



(a) Parameter set 1.

(b) Parameter set 2.

Figure 6-10: Steady state enhancement of the 52 structural protons of bTbk (solid), and 100 solvent protons (dashed). The minimum separation between protons in the solvent is 2Å, 4Å, 6Å, 8Å& 10Å. In FIG. 6-10a the parameters are $B_0 = 5\text{T}$, $R_{1\text{e}} = 3 \times 10^3 \text{s}^{-1}$, $R_{1\text{n}}$=10s^{-1}, $R_{2\text{e}} = 10^6 \text{s}^{-1}$. In FIG. 6-10b the parameters are $B_0 = 14.1\text{T}$, $R_{1\text{e}} = 10^4 \text{s}^{-1}$, $R_{1\text{n}}$ =0.1s^{-1}, $R_{2\text{e}} = 10^6 \text{s}^{-1}$. The remaining parameters are as in FIG. 6-2.

6.5.3 Discussion

Following from the discussion in Section 6.4.2, the enhancement is expected to be lower for the second parameter set, where B_0 is 14.1T, than for the first, where B_0 is 5T. Also as expected, the enhancements of both bTbk and the solvent decrease with increasing spinning frequency, and the solvent enhancement decreases as the proton concentration decreases. In the next paragraphs the two parameter sets will be examined separately to see how the above trends, combined with different electron and proton longitudinal relaxation rates affect the bTbk–solvent dynamics.

Parameter Set 1

Parameter set 1 has ideal parameters for enhancement of the bTbk protons, but is not optimal for the solvent protons. In addition to the small B_0, another contributor to the bTbk enhancement is the electron longitudinal relaxation time, which is longer than in parameter set 2. This means that the CE process is more efficient,

since the electrons spend more time out of equilibrium, and therefore with different polarisation. The faster nuclear longitudinal relaxation time means that the bTbk enhancement becomes independent of the solvent enhancement at higher proton concentrations. The solvent protons are assumed to be polarised primarily via spin diffusion, which is affected both by the proton separation, which in turn determines the dipolar interaction strength, and the spinning frequency, which determines how many of the dipolar interactions are averaged out. When the R_{1n} is fast, $d(t)$ must be strong in order for the polarisation to diffuse before it relaxes. The system therefore quickly loses enhancement as the spin separation and spinning frequency increase.

Parameter Set 2

The smaller R_{1n} in this parameter set causes the bTbk and solvent dynamics to be more co-dependent. For proton separations less than 4Å, bTbk and the solvent are strongly coupled and achieve the same enhancement. The dip at 4Å occurs because the bTbk protons are losing some of their polarisation to the solvent. Beyond 4Å, the nuclear exchange is no longer strong enough to equilibrate the polarisation of the entire spin system and the dynamics decouple. As with parameter set 1, the bTbk protons recover the polarisation they were losing to the solvent and eventually become independent of the solvent dynamics. The solvent protons however retain some enhancement even for large proton separations, particularly at low spinning frequencies.

The simulations in FIG. 6-10 emphasise the importance of spin diffusion, even in MAS, where dipolar interactions are averaged out by the sample spinning. The effect of the solvent geometry and spin relaxation rates has been examined, and shown to have a significant impact on the enhancement of a system. Finally, a useful property of the bTbk-solvent dynamics can be gleaned from the large-scale simulations: for the spin separations typical of MAS DNP (6Å or higher), the bTbk and solvent dynamics evolve quite separately. This suggests that it may be possible to replace the full bTbk core with a single, representative core proton, thus further reducing the simulation time.

Chapter 7

Experiment Toolbox

This chapter marks the beginning of the experimental part of this thesis. The first section focuses on the NMR hardware and software. This is followed by a section describing data acquisition and the pulse sequence used for NMR data. Section 3 discusses error propagation and sources of error, and the final section briefly describes the EPR magnet and EPR pulse sequence.

7.1 Hardware & Software

All NMR experiments were performed using a custom-built polariser magnet (Oxford Instruments - Abingdon, UK) and an NMR probe built by R. Shakhovy. Shakhovy also made the Temperature Controller software used to control the temperature of experiments. Data was processed with Topspin 1.3 (Bruker GmBh - Karlsruhe, Germany) and a home-made programme written in Python 3.7 (Anaconda Inc.). This section describes the hardware and software.

Polariser Magnet

The 3.35T shielded polariser magnet is able to perform both NMR and DNP experiments. The high magnetic field is generated by a superconducting solenoid kept below its critical temperature by a 4.2K helium dewar, which is in turn insulated by a nitrogen dewar. A needle valve allows liquid helium to flow from the dewar into

the variable temperature insert in the bore of the magnet, allowing experiments to be performed at liquid helium temperatures. The bore of the magnet is kept under a constant vacuum ($\sim 2 \times 10^{-4}$mbar pressure) by a Trivac D 65 B (Leybold GmBh - Cologne, Germany) rotary vane vacuum pump. Pumping on the system removes high energy particles on the liquid-gas interface and reduces the boiling point of helium, such that temperatures as low as ~1K can be achieved. The NMR probe sits inside the variable temperature insert.

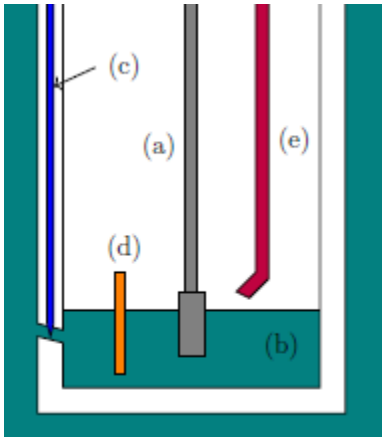


Figure 7-1:

Figure 7-2: Schematic diagram of the polariser magnet. a) NMR probe b) Helium bath for experiments at liquid helium temperatures c) Needle valve opening into the variable temperature insert from the helium dewar d) Capacitor to measure liquid helium level e) Waveguide for microwave irradiation (DNP). Parts d) and e) are not relevant for the experiments performed here.

NMR Probe & Spectrometer

The NMR sample sits inside a 4-loop coil that acts both as transmitter and receiver. The sample is contained in a $\sim$ 60μL teflon cup that fits snugly in the coil thus maximising sensitivity in receiver mode. The $B_1(t)$ field created in transmitter mode is orthogonal to the static field B_0. The temperature at the sample is controlled by changing the current flowing through a heating element that sits directly below the sample. This is done via the Temperature Controller software. The sample temperature is measured with a CERNOX (Lake Shore Cryotronics Inc. - Westerville, USA) temperature sensor located behind the coil and no further than 5mm from the fur-

thest parts of the sample. The temperature sensor can accurately read temperatures down to 2.6K. The probe is interfaced with the Temperature Controller software via a DAQ board (National Instruments Corporation - Austin, USA), and connects to the spectrometer via a pre-amplifier and amplifier. The NMR probe is tuned to the proton frequency ($\sim$ 142.64MHz at 3.35T) by a resonant circuit (FIG. 7-3b) composed of the receiver coil (inductor), and two trimmer capacitors, one in series and one in parallel with the inductor. The parallel capacitor tunes the circuit's resonance frequency to the proton resonance, and the series capacitor matches the circuit by changing its Q-factor [32]. The NMR probe is shown in FIG. 7-3a.

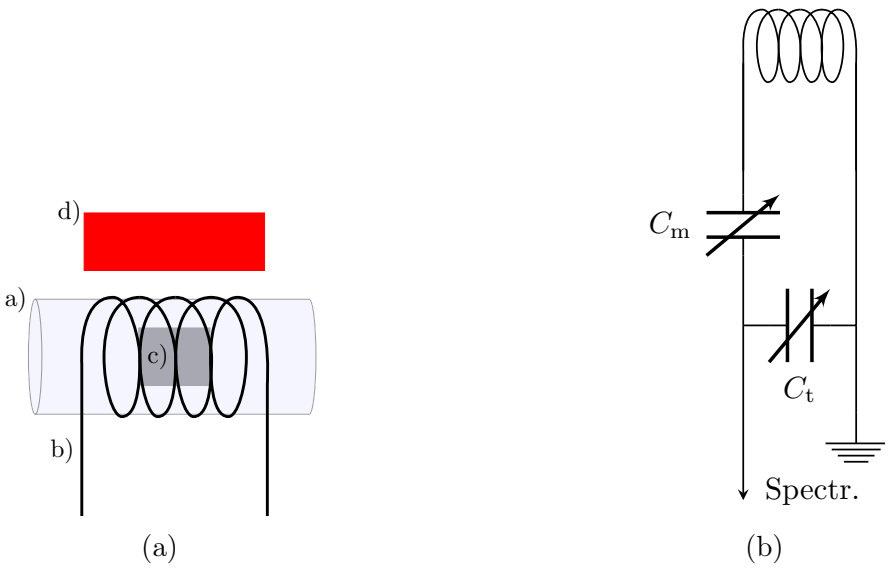


Figure 7-3: FIG. 7-3a: a) Sample cup b) Receiver/transmitter coil c) CERNOX temperature probe d) Heating element. FIG. 7-3b: Tuning and matching circuit. The receiver coil acts as the inductor, the trimmer capacitor in series with it (C_{m}) matches the circuit and the capacitor in parallel tunes it (C_{t}).

The pulse sequences are applied through a Bruker Avance DSX 400 console (Bruker GmBh - Karlsruhe, Germany) interfaced with Topspin 1.3 (Bruker GmBh - Karlsruhe, Germany).

Software

The Temperature Controller software (Microsoft Visual Studio, Microsoft) is based on a PID feedback loop [114]. This monitors the difference between a user-input desired temperature and the temperature measured by the temperature sensor on a secondly basis and adjusts the current through the heating element accordingly. With this setup it is possible to keep the temperature at the sample stable to within 0.1K over the range 2.6K to 30K (FIG. 7-9). The Temperature Controller is interfaced with the current source for the heating element and the Lake Shore temperature monitor via the DAQ board.

The NMR pulse programmes and data files are handled by Topspin 1.3. However, although Topspin can perform data analysis, this was done using a self-made Python script. Processing included zero-filling, line-broadening, phase correction & calculation of T_{1n} [115]. The phase correction was found automatically by finding the phase for which the integral of the real part of the spectrum is maximised and that of the imaginary part minimised. Where necessary, the phase was further adjusted manually. Topspin is interfaced with the probe via the spectrometer.

A schematic of the NMR setup is shown in FIG. 7-4.

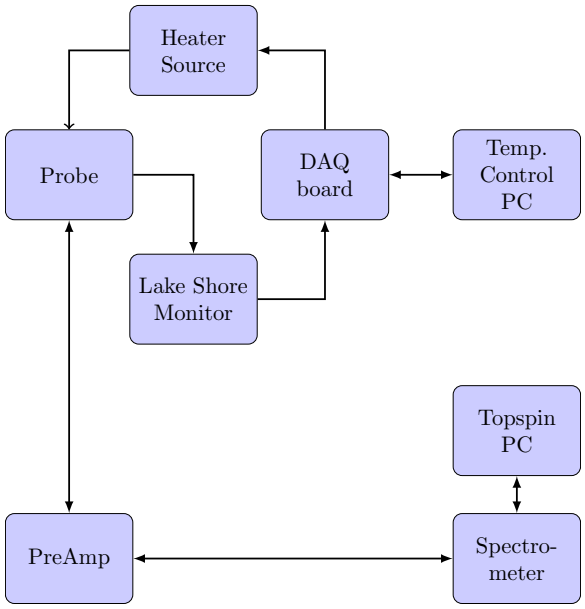


Figure 7-4: Schematic diagram of the NMR setup.

7.2 NMR measurement

Magnetic resonance experiments measure the signal induced in a receiver coil by the coherent precession of spins in a magnetic field. It is the transverse component of this precession, arising from a disturbance from equilibrium, that creates the signal. In the rotating frame and at thermal equilbrium, the magnetisation is aligned with B_0 and cannot be detected. However, when $B_1(t)$ is applied, the magnetisation starts to tip onto the transverse plane, with the transverse component precessing about B_0 at the Larmor frequency. This precession is coherent for the duration of $B_1(t)$ and only starts to dephase after the end of the pulse. The change in magnetic flux due to the precession causes, via Faraday's law of induction, an electromotive force in the receiver coil. This in turn creates a voltage across the terminals of the coil that oscillates at the frequency of precession. The amplitude of the oscillation depends on the magnitude of the transverse magnetisation, thus decreasing as the spins dephase and giving rise to the typical shape of the NMR signal, known as the Free Induction Decay (FID) [116], shown in FIG. 7-5. Note that because the receive and transmit coils are one and the same, the NMR signal is measured after the termination of the

RF-pulse, with some instrumental dead-time allowed to protect the highly sensitive pick-up electronics from the high power pulses.

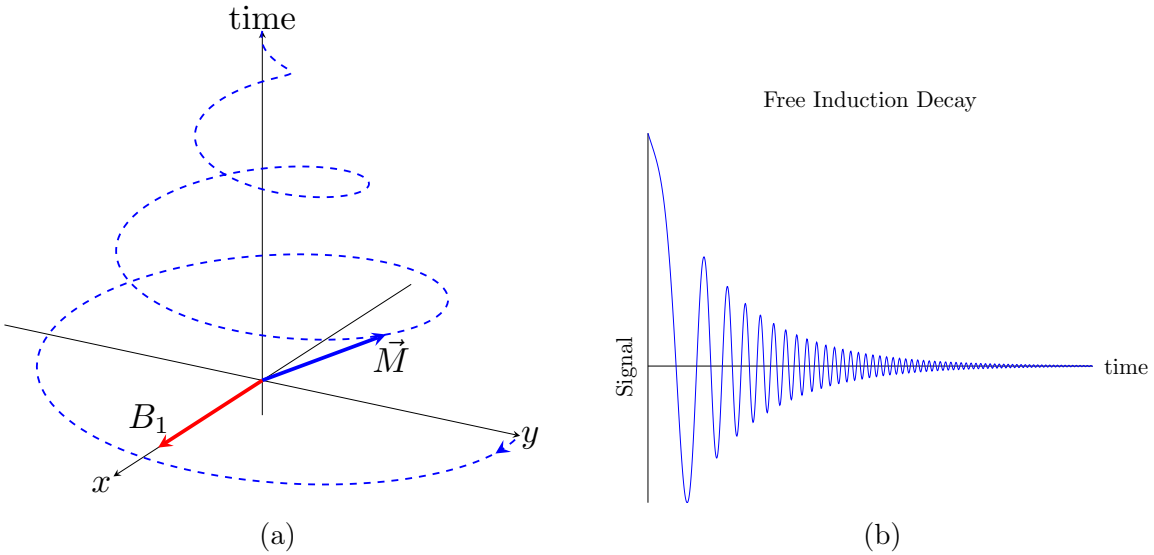


Figure 7-5: FIG. 7-5a: Decay of sample magnetisation ($\vec{M}$) in the transverse plane of the rotating frame after removal of B_1. FIG. 7-5b: Free induction decay induced in the receiver coil by the decaying transverse magnetisation.

RF-pulses

In general it is assumed that the $B_1(t)$ field is on resonance with the spins and therefore appears static along the x-axis in the rotating frame ($B_1(t) \rightarrow B_1$). In this resonant case, B_0 is effectively eliminated from the rotating picture and the only magnetic field affecting the spins is B_1 (FIG. 7-5a). RF-pulses exploit the much slower precession of spins about B_1 (generally $B_1 \ll B_0$) to tip the magnetisation by a specific amount in the yz-plane. For example, applying a pulse for $1/4$ of the precession period ($\pi/2$-pulse) flips the magnetisation onto the y-axis, whereas applying a pulse for $1/2$ a period (π-pulse) inverts the magnetisation onto the $-z$-axis. The flip angle (θ_{flip}) is given in the lab frame by [32]

$$\theta_{\text{flip}} = -\gamma B_1(t) t_{\text{p}},$$

where t_{p} is the duration of the pulse.

Spectrum

The FID is acquired in the time domain and is then zero-filled, Fourier transformed and phase corrected to yield a spectrum in the frequency domain [115]. The shape and integral of the spectrum contain spectral information about chemical groups [32]. The observed transverse relaxation T_2^* for example, is inversely proportional to the full-width-half-maximum of the spectrum. T_1 on the other hand can be measured by tracking how the integral of the spectrum changes as the sample magnetisation recovers towards equilibrium.

Saturation Recovery Pulse Sequence

All T_1 data in Chapter 8 was collected using a saturation recovery pulse sequence [32]. The simplest saturation recovery sequence consists of a train of closely spaced $\pi/2$-pulses alternating along x and y (the saturation loop), followed after some recovery time τ_{r} by a single $\pi/2$-pulse along x (the acquisition pulse). The saturation loop completely destroys the longitudinal magnetisation and the acquisition pulse tips it onto the transverse plane for measurement. As τ_{r} increases, the magnetisation has more time to recover before the acquisition pulse, thus increasing the amplitude of the FID and hence the integral of the spectrum. The longitudinal relaxation time T_1 is then found by acquiring many FIDs with different τ_{r} and fitting EQ. 7.1 to the integrals ($I(t)$) of the spectra:

$$I(t) = I_0\big[1 - \exp(-t/T_1)\big], \tag{7.1}$$

where I_0 is the integral at thermal equilibrium and the time t starts after the end of the saturation loop. Although rigorous, calculating T_1 using this approach is time consuming, since after each acquisition pulse the longitudinal magnetisation must be allowed to fully recover before starting the next saturation loop with a new τ_{r}.

A faster approach is to tip only a fraction of the magnetisation onto the y-axis, leaving the rest to recover normally [117]. Because most of the magnetisation survives the

acquisition pulse, another acquisition pulse can be applied after some delay time τ_{d}, and another after $2\tau_{\mathrm{d}}$, and so on. With this method the entire T_1 buildup can be observed with only one saturation loop, followed by a train of small flip angle acquisition pulses, making it much faster than a $\pi/2$-pulse saturation recovery. The measured T_1 however, now depends on the flip angle and number of pulses:

$$I_n(t) = I_0\big[1 - \exp(-t/T_1)\cos^n(\theta_{\mathrm{flip}})\big], \tag{7.2}$$

where $I_n(t)$ is the integral after the n^{th} acquisition pulse. The $\cos^n(\theta_{\mathrm{flip}})$ term accounts for the unrecoverable magnetisation lost with each acquisition pulse.

The pulse sequence used for NMR experiments in Chapter 8 consisted of a saturation loop with 50 closely spaced x- & y-pulses, followed by 16 acquisition pulses with a 2° flip angle (FIG. 7-6). With this flip angle only 0.1% of the magnetisation is lost by the 16^{th} pulse, so EQ. 7.1 can be used to calculate T_1 without incurring significant error.

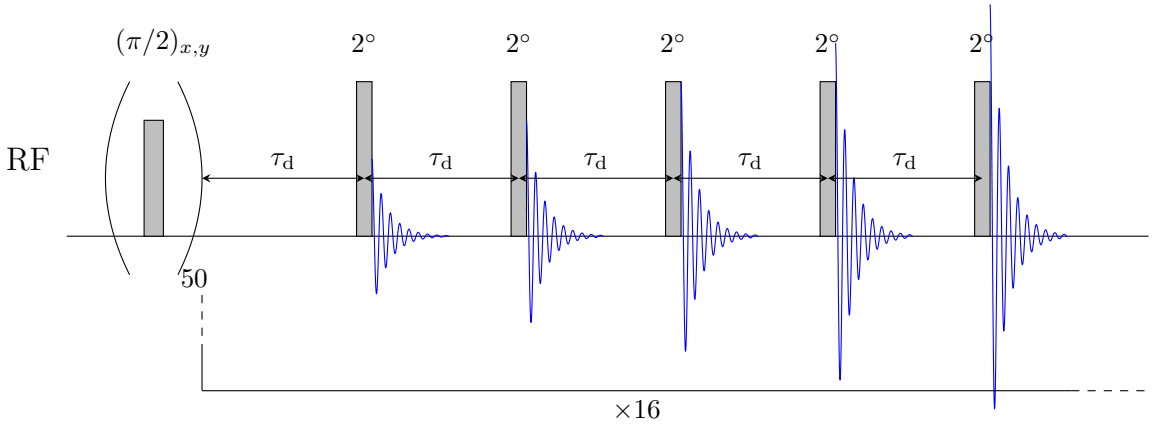


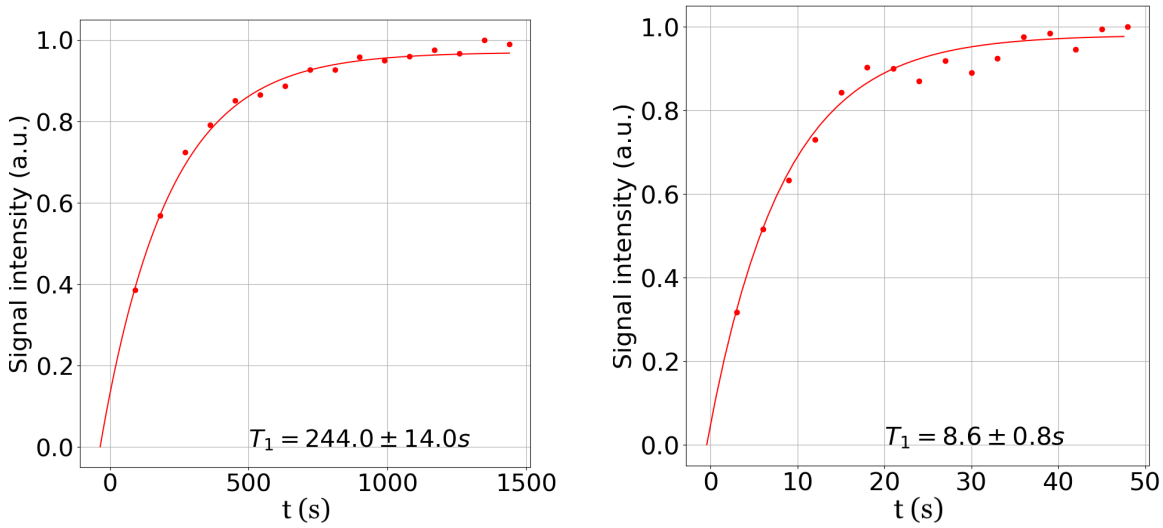
Figure 7-6: Pulse sequence for the NMR saturation recovery. The saturation loop is formed of 50 x- & y-pulses. After saturation, the 16-pulse acquisition train starts, with 2° pulses applied at regular intervals τ_{d}. With each successive pulse, the longitudinal magnetisation, and therefore the FID (blue), grows.

FIG. 7-6 shows how with each successive acquisition pulse the FID grows, since the magnetisation has had more time to recover. To accurately capture this buildup, τ_{d}

should be $\sim T_1/3$, so that it samples both the initial buildup, and the start of the plateau as $I(t)$ approaches I_0. Since τ_d depends on T_1, it depends on temperature and radical concentration, and for the work presented here ranges from 3s at high temperatures and concentrations, to over 900s at low temperatures and concentrations.

Magnetisation Buildup

FIG. 7-7 shows examples of processed 30mM buildups at 3K (FIG. 7-7a) and 30K (FIG. 7-7b). They are normalised to 1 to facilitate curve-fitting. Points on the buildup are separated by τ_d and track the increasing integrals of the spectra as the longitudinal magnetisation recovers (refer to the increasing amplitude of the FIDs in FIG. 7-6). T_1 is calculated by fitting EQ. 7.1 to the buildups. The error shown is the standard deviation.



(a) (b)

Figure 7-7: Buildup curve at 3K (FIG. 7-7a) and 30K (FIG. 7-7b) for the 30mM sample.

7.3 Error Analysis and Uncertainty

The list of error sources in NMR experiments is long, and contains several errors that are difficult to quantify such as thermal noise, temperature instability, & low signal-to-noise ratio (SNR) [115]. One easily quantifiable error however, is that incurred

from the fitting of data with EQ. 7.1.

Most T_1 times shown in Chapter 8 are calculated from an average over N_{runs} experiments. The error on the averaged T_1 ($\bar{T_1}$) is then given by

$$\delta\bar{T_1} = \frac{1}{\sqrt{N_{\text{runs}}}}\sqrt{\sum_{runs}(\delta T_1)^2}, \tag{7.3}$$

where δT_1 is the standard deviation of the fit with EQ. 7.1 for each experiment. δT_1 increases when the SNR is low (at high temperatures) and when the temperature is not constant throughout the buildup [i].

FIG. 7-8 shows the processed spectra (zero-filled & line-broadened) of a 50mM Tempol sample at 3K and 30K. At 3K the signal much stronger because the thermal polarisation is higher, and thermal noise is negligible. Thermal (Johnson-Nyquist) noise is inherent to any circuit, has zero average and increases with increasing temperature [118], compounding the issue of low SNR at high temperatures, where the signal is reduced anyway due to the lower thermal polarisation. The Johnson-Nyquist noise is seen clearly in FIG. 7-8b.

Another source of error in the data is temperature instability. FIG. 7-9 shows the temperature history over a set of four 3K experiments. The inset shows the temperature history over that entire day of experiments. The red lines mark the ±0.1K limits.

[i] Since T_1 is temperature dependent, each point on the plot then represents a different temperature, and thus buildup curve.

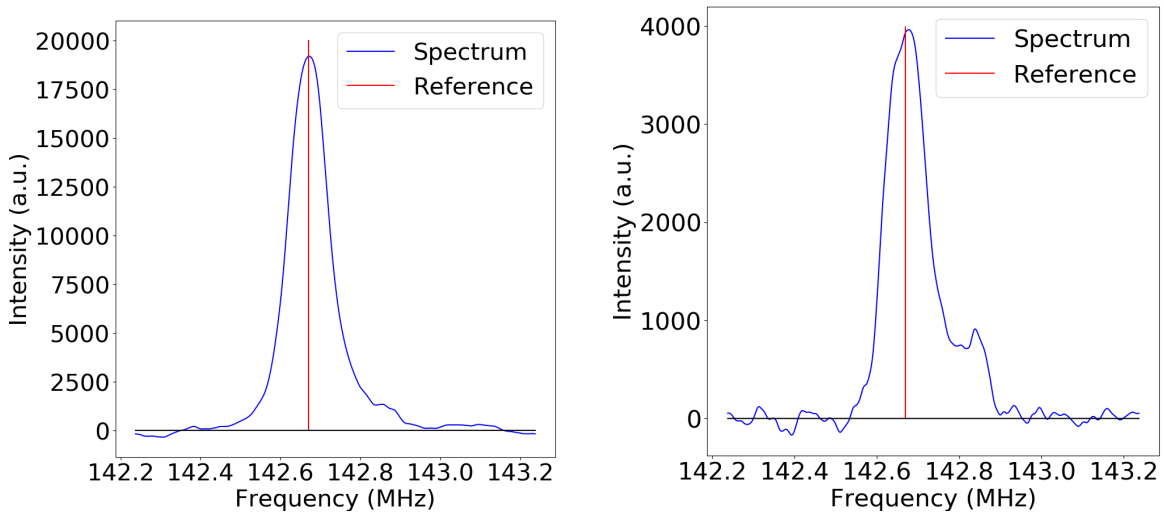


Figure 7-8: Processed spectra of a 50mM Tempol sample at 3K (a) and 30K (b). The noise seen clearly in the 30K spectrum is Johnson-Nyquist noise from the hardware.

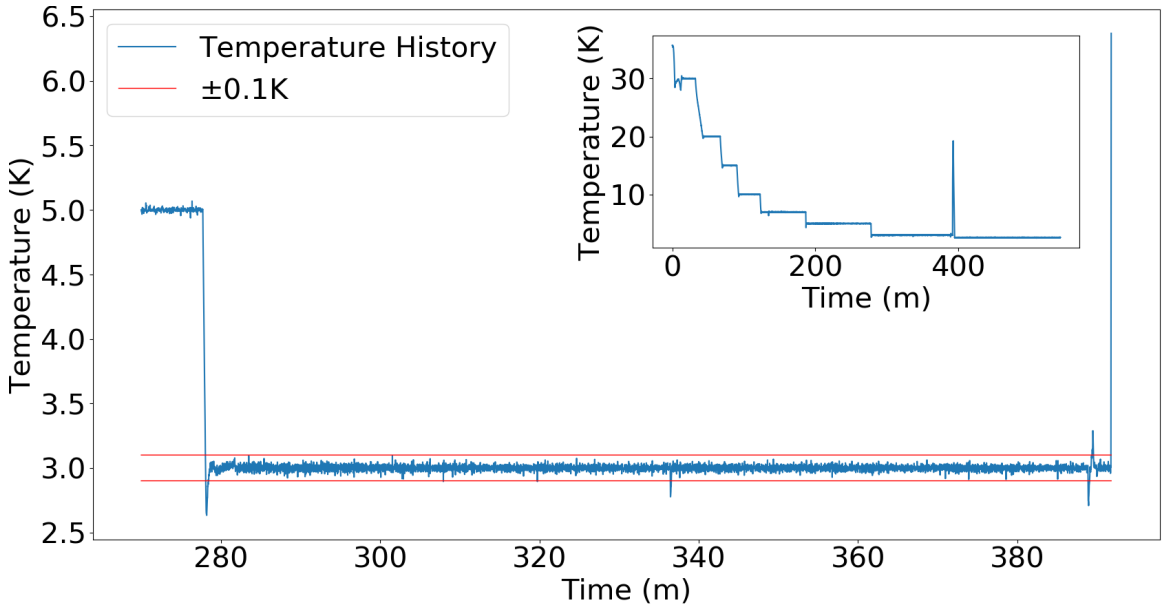


Figure 7-9: Temperature history over four 3K experiments. The red lines mark the ±0.1K limits. The inset shows the entire temperature history for that day of experiments.

7.4 Electron Paramagnetic Resonance

All T_{1e} data was acquired by R. Shakhovy using the EPR magnet. The principles of EPR measurement are largely the same as those of NMR, with some exceptions due to the typically broad spectra in EPR and the fast decay of EPR FIDs. Most EPR experiments for example make use of the spin echo rather than the FID. This is because the (in most cases) very large inhomogeneous broadening of the EPR spectrum causes the FID to decay very quickly, often within the instrumental dead-time required to protect the receiver from the strong RF-pulse [119]. This adjustment is reflected in the pulse sequence used for EPR measurement.

EPR magnet

The EPR magnet (Oxford Instruments - Abingdon, UK) is a 3.4T superconducting magnet. Like the polariser its bore can be cooled below 4.2K by opening a needle valve to allow liquid helium to flow into the sample space and pumping on it with a rotary vane vacuum pump (Leybold GmBh - Cologne, Germany). The sample temperature is measured by a CERNOX temperature sensor (Lake Shore Cryotronics Inc. - Westerville, USA) mounted on the probe, and controlled by an ITC console (Intelligent Temperature Controller ITC503, Oxford Instruments - Abingdon, UK). Unlike with the NMR probe, the heating element of the ITC is not located on the EPR probe, but on the magnet itself. The sample temperature is therefore much more difficult to control. The microwave field for $B_1(t)$ (94.895GHz) is generated by a Krymov microwave bridge that also acts as the receiver. The pulse sequences and data collection are controlled with a home-written LabVIEW program (National Instruments Corporation - Austin, USA).

EPR Saturation Recovery

The longitudinal relaxation of electrons is fast even in the low temperature regime. This means that the magnetisation can be tipped by a $\pi/2$-pulse without much loss of time since the longitudinal magnetisation recovers quickly. Furthermore, temperature

stability is less of an issue because experiments are much shorter. FIG. 7-10 shows the pulse sequence used to acquire EPR data. It differs from the NMR sequence in that it measures the decay of the echo (a pair of back-to-back FIDs as the spins refocus and then dephase again) rather than the FID. The saturation loop consists of 1000 x- & y-pulses and lasts about 100μs. This is followed by a $\pi/2$-pulse after a given recovery time τ_{r}. The spins are then allowed to dephase for a fixed time T_{e} before applying a rephasing π-pulse. The echo is acquired at $2T_{\mathrm{e}}$. The whole process is then started again with a different τ_{r} to acquire the next point. Unlike with the NMR sequence, the recovery time τ_{r} (τ_{d} in FIG. 7-6) is not fixed, but is given by

$$\tau_{\mathrm{r}} = N \times t_{\mathrm{block}},$$

where t_{block} is a fixed time block e.g. 400μs at 2K and 10μs at 30K, and N is an array of numbers that samples frequently at the beginning of the buildup and more sparsely as the plateau is reached: $N = 1, 2, 3, 4, 6, ...16384, 23170, 32768$.

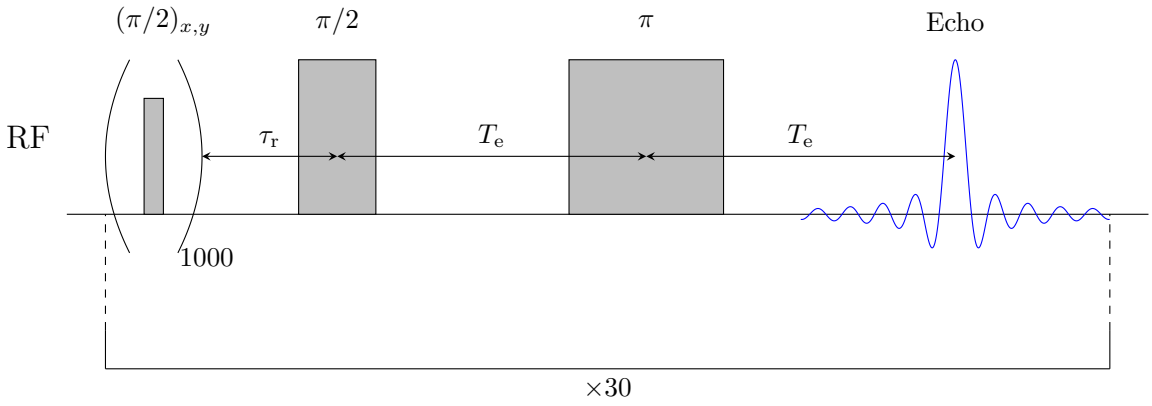


Figure 7-10: Pulse sequence for the EPR saturation recovery. The saturation loop is formed of 1000 x- & y-pulses. The experiment is repeated 30 times with different recovery times τ_{r}. The recovery times are such that the beginning of the buildup is sampled more frequently than the plateau. As τ_{r} increases, the signal increases as does the echo (blue). A time T_{e} after the $\pi/2$-pulse, a π-pulse is applied to refocus the spins. The echo forms a time $2T_{\mathrm{e}}$ after the $\pi/2$-pulse.

Chapter 8

NMR Experiments

In this penultimate chapter, experimental results are presented. First, the sources of paramagnetic centres in the samples used are discussed. The chapter is then divided into four further sections, one for each investigation. In the first section, the temperature and concentration dependence of nuclear T_1 in Tempol-doped water/glycerol mixtures is examined. In the next section, a water/glycerol sample is degassed to study the effect of oxygen in solution on the nuclear T_1. At the end of this section there is a detailed interpretation of the effect of paramagnetic centres on the Tempol and degassed samples. The third section examines the inherent nuclear relaxation by looking at water/glycerol samples in which the water, glycerol, or both have been deuterated. In the final section, the nuclear T_1 collected in Section 8.2 is combined with EPR data collected by R. Shakhovy to examine the correlation between electron T_{1e} and nuclear T_{1n}.

To the author's knowledge there has been no such in-depth study of proton relaxation dynamics in the presence of Tempol spanning to such low temperatures. Shimon et al. [120] studied the nuclear T_1 of degassed 10mM and 40mM Tempol samples as well as a non-degassed 40mM Tempol sample. However, the 10mM T_1 was measured only for temperatures between 60K to 80K, and the 40mM samples between 6K to 50K. Chen & Tycko [121] studied the T_{1n} behaviour for temperatures below 10K, but were using 5mM, 10mM & 15mM concentrations of the nitroxide triradical DOTOPA

rather than Tempol.

Understanding how T_{1n} is affected by DNP parameters such as temperature and radical concentration is important because it plays a crucial role in the efficiency of DNP enhancement; even the most efficient DNP process can have minimal enhancement if the nuclear matrix relaxes before the polarisation propagates. It is also helpful to have a broad understanding of the behaviour of nuclear T_1 when choosing the relaxation parameters for DNP simulations such as the two presented in this thesis.

8.1 Paramagnetic Centres

There are two sources of paramagnetic centres in the samples: Tempol, and the natural presence of oxygen in solution. Both will be discussed briefly.

8.1.1 Tempol

Nitroxides such as Tempol and bTbk are popular in DNP experiments for their high enhancement factors, high solubility in water, and cost-effectiveness. They are futhermore non-toxic, making them amenable for use with biological samples [122]. Over half a dozen nitroxide mono-, bi-, & tri-radicals exist, each catering to particular systems and experimental conditions [123]. Like bTbk, Tempol (4-hydroxy-TEMPO) is a TEMPO derivate, and its molecular structure (FIG. 8-1) is similar to that of bTbk. As with bTbk, the spin density of the unpaired electron on the nitrogen bonded oxygen is spread over the O-N bond, with virtually no delocalisation over the rest of the molecule, causing it to be strongly hyperfine shifted by the nitrogen [107]. Tempol is both light and temperature sensitive and should be kept in the dark between 2°C & 8°C [124].



Figure 8-1: Molecular structure of Tempol [124].

8.1.2 Dissolved Oxygen

Molecular oxygen (O_2) is naturally non-polar, but can become polarised in the presence polar molecules such as water. When this occurs, the resulting dipole-induced dipole force creates a weak attraction between the two molecules that causes the oxygen to dissolve in the water. Because the attraction is only weak, the amount of oxygen that can be dissolved is highly temperature and pressure dependent [125, 126]. At 0°C and atmospheric pressure, the maximum oxygen in solution in distilled water is ∼14.6mg/L, or ∼0.91mM [127, 128]. Though to a lesser degree, dissolved oxygen is also present in glycerol, with distilled water at 20°C and atmospheric pressure saturating at ∼9mg/L, while glycerol saturates at ∼2mg/L [129]. If it is assumed that once the sample freezes the oxygen concentration remains unchanged, a ball park estimate of the amount of oxygen dissolved in a 50/50 water/glycerol mixture is 0.5mM. The dominant source of paramagnetic centres in non-degassed samples is therefore Tempol.

8.2 Tempol Experiments

In this section the effect of temperature and Tempol concentration on the T_{1n} relaxation of a 50/50 water/glycerol mixture is studied.

8.2.1 Sample Preparation

The six samples used in this section are 10mM, 20mM, 30mM, 40mM, & 50mM of Tempol (Sigma Aldrich; Missouri, USA; 176141) dissolved in a 50/50 water/glycerol (water: distilled in-house, glycerol: Fischer Scientific; Loughborough, UK; G/0600/08) (v/v) solution, as well as a 50/50 water/glycerol (v/v) sample without Tempol (0mM sample). Samples were prepared by mixing appropriate proportions of 0mM stock and 50mM stock to minimise error in the Tempol concentrations. Samples were kept in the dark at $\sim 5°$C to mitigate sample degradation.

8.2.2 Experiment Procedure

Loading the Sample

To ensure an even distribution of Tempol in the sample, samples were mixed with a vortexer and left to rest until gas entering solution in this process bubbled out before being loaded into the sample cup. This in turn was filled completely to maximise sensitivity. After inserting the NMR probe in the magnet it was left to cool to $\sim$100K before slowly engaging the vacuum pump. This guarantees that the sample is frozen and cannot be sucked out of the sample cup when the vacuum is applied.

Temperature Profile

A significant concern with low temperature NMR measurements is temperature stability. It affects the cooling rate and order of experiments, and can have a considerable effect on the T_1 relaxation. In this and the next section, experiments were performed in the order 5K, 7K, 10K, 15K, 20K, 30K & 3K. This temperature ordering is easy to achieve and allows fast cooling of the sample at a rate of approximately 3.8Kmin^{-1}. The 3K experiment is left until last to give the elements surrounding the sample space time to cool, thus making the experiment more stable. Temperature stability is particularly important at 3K because experiments are up to 45min long, and the low temperature T_1 is highly temperature dependent.

The temperature at the sample space was monitored throughout all experiments to ensure fluctuations did not exceed ±0.1K. For optimal temperature stability, the system must be given time to equilibrate at each new temperature before starting experiments. The temperature was changed by manually adjusting the needle valve and/or adjusting the heating current via the Temperature Controller. For temperatures above 7K, the temperature remained stable for all 4 runs of an experiment. For 3K and 5K on the other hand, heat entering the sample space by thermal conduction through the NMR probe frequently required the needle valve to be opened more between runs. When this was the case, the magnet was given 5 minutes to re-stabilise before starting the next run. Where possible, experiments were performed on a single day to minimise variability in the temperature environment.

T_{1n} Measurement

The nuclear longitudinal relaxation time was measured for each concentration (0mM to 50mM) at each temperature (3K to 30K) using the saturation recovery pulse sequence described in Section 7.2. Recall from this section also that to accurately capture the T_1 buildup, τ_d should be approximately $T_1/3$, and is therefore temperature and Tempol concentration dependent. In this set of experiments, τ_d ranges from under 5s at high temperatures and concentrations to over 100s at low temperatures and concentrations. A table of relevant acquisition parameters can be found in Appendix B.

For each sample, 4 experiments (with adjusted τ_d if necessary) were performed consecutively at each temperature. For the 0mM and 10mM concentrations, experiments were performed on two different samples from different stocks. These two concentrations therefore have a total of 8 experiments at each temperature (four each for the two samples).

8.2.3 Results

T_{1n} was calculated for each sample and temperature using Python's non-linear least squares curve-fitting algorithm to fit EQ. 7.1 to the buildup curves. The average T_{1n} ($\bar{T}_{1n}$) was then calculated for each temperature and the error propagated using EQ. 7.3 to yield FIG. 8-2.

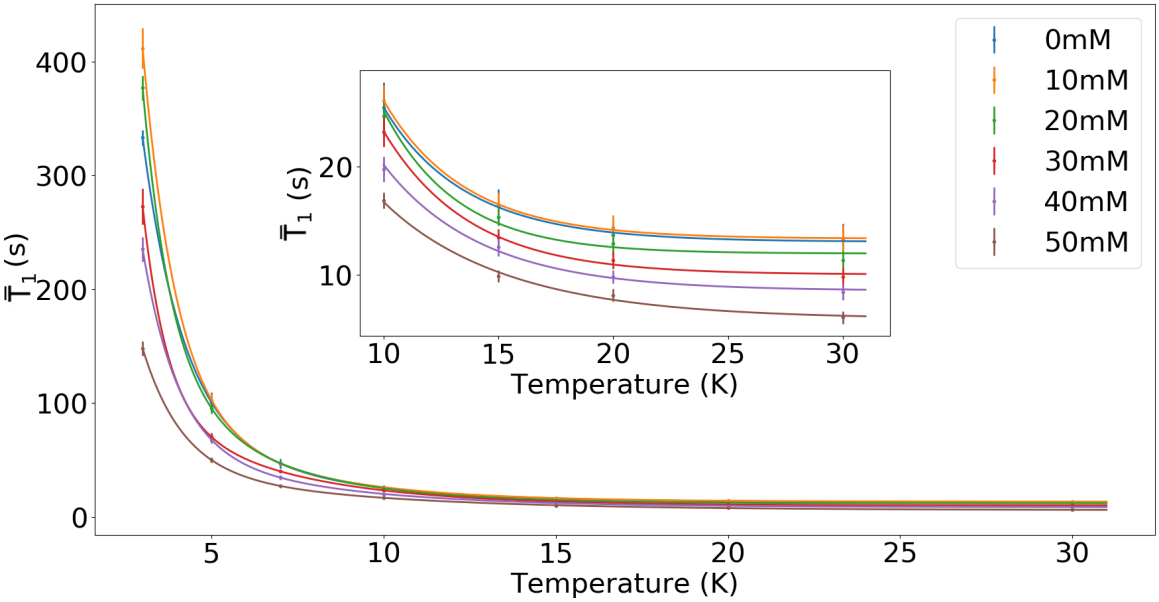


Figure 8-2: T_{1n} times averaged over all experiments at each temperature and concentration (4 experiments for 20mM to 50mM, 8 experiments for 0mM & 10mM).

To capture the temperature dependence of the average nuclear relaxation, biexponential fits of the form

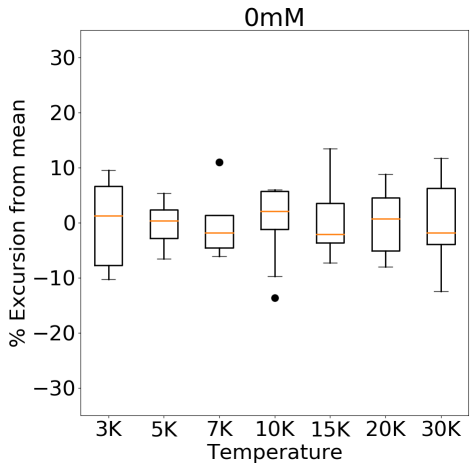
$$ae^{-bT} + ce^{-dT} + e \tag{8.1}$$

were applied to the data for each sample, where T is the temperature in Kelvin. The fitting parameters $a - e$ along with the R^2 value of the fits are shown in TAB. 8.1.

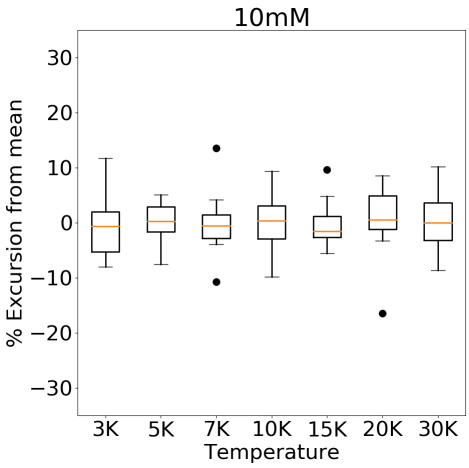
Sample	a	b	c	d	e	R^2
0mM	3307.9	0.9	165.2	0.3	13.1	0.999
10mM	6864.6	1.0	195.7	0.3	13.4	0.999
20mM	9804.6	1.2	291.6	0.3	11.9	0.999
30mM	13116.2	1.4	190.1	0.3	10.0	0.999
40mM	3354.0	1.0	112.9	0.3	8.6	0.999
50mM	1463.9	0.9	6.4	0.2	5.9	0.999

Table 8.1: Fitting parameters for the biexponential fit (EQ. 8.1) to the temperature dependence of $\bar{T}_{1n}$ for different concentrations of Tempol.

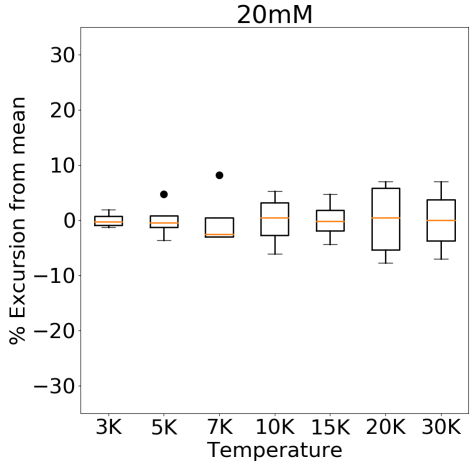
There was significant variability in the measured relaxation times, despite all efforts to keep the sample temperature consistent between runs. The origin of the variability is unkown, but it is possible to shed light on its nature using a statistical approach. However, though useful to get an overview of the data, the statics should not be given undue importance because the sample sizes (4 or 8 data points) are so small. FIG. 8-3 shows the excursion (in %) of the T_{1n} measured in each experiment from the average nuclear relaxation time at that temperature and concentration. When the measured value is equal to the mean, the excursion is 0%, whereas if it is 10% greater than or smaller than $\bar{T}_{1n}$, the excursion is $+10\%$ or -10% respectively. The orange line shows the median of the data, the edges of the box are the first and third quartiles, the whiskers extend to 1.5 times the interquartile range and the circles show outliers.



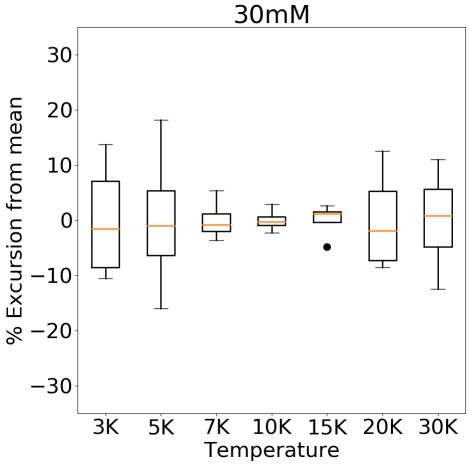
(a) 0mM.



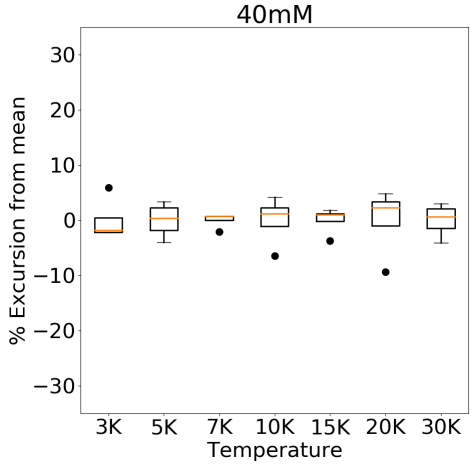
(b) 10mM.



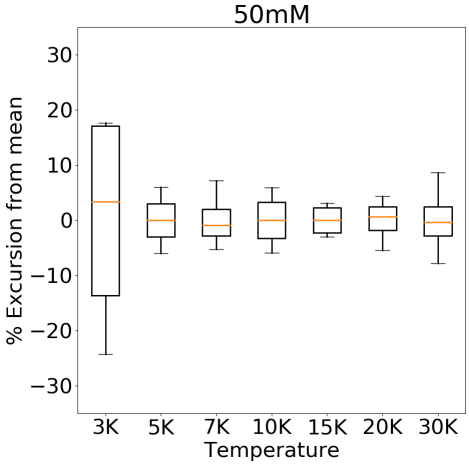
(c) 20mM.



(d) 30mM.



(e) 40mM.



(f) 50mM.

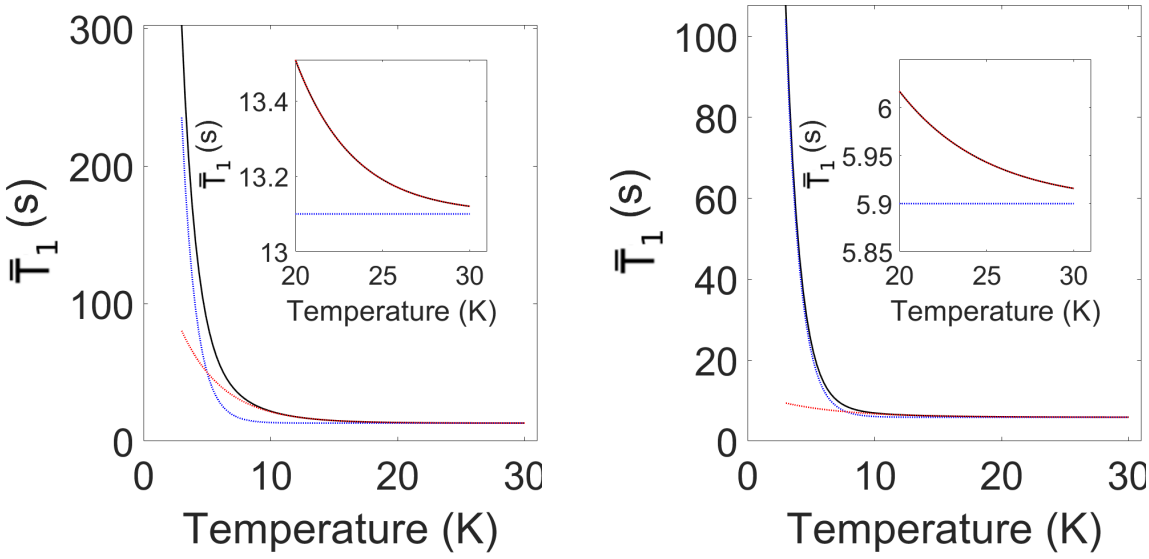
Figure 8-3: Effect of temperature and concentration on the variability of the T_{1n} data.

8.2.4 Discussion

Temperature Dependence

From FIG. 8-2 it is evident that below 15K there is a steep rise in the temperature dependence, with $\bar{T}_{1n}$ more than doubling as the temperature is decreased from 5K to 3K. At such low temperatures many of the relaxation mechanisms are frozen out [64], but clearly any mechanisms remaining are highly temperature dependent. Above 15K, the relaxation appears to become virtually temperature independent, and is offset by the concentration of Tempol; the 50mM sample plateaus at 6s while the 0mM & 10mM samples plateau at 13s. The near perfect fits of the biexponential curves in FIG. 8-2 suggest that the temperature dependence is well described by two competing mechanisms, one which dominates at low temperatures (b in EQ. 8.1), and one that becomes relevant at higher temperatures (d in EQ. 8.1).

FIG. 8-4 shows the low temperature (blue) and high temperature (red) exponential fits for the 0mM and 50mM samples. In all 6 samples, the $\bar{T}_{1n}$ dependence above 15K is modelled accurately by the high temperature exponent (d, red) only, while the low temperature exponent (b, blue) consistently underestimates the plateau temperature. The fitting at low temperatures on the other hand is more subtle. As the concentration of Tempol increases, the low temperature part of the curve is increasingly well described by the low temperature exponent alone, suggesting that some mechanism related to the electrons dominates in this regime. For low Tempol concentrations however, a good fit is only obtained if both the low temperature and high temperature exponents contribute. From this it can be concluded that the mechanism represented by the high temperature exponent is always present and accurately captures the plateau, while the mechanism represented by the low temperature exponent is only accurate at low temperatures, and becomes increasingly dominant as the concentration of paramagnetic centres increases.



(a) 0mM Sample (b) 50mM Sample

Figure 8-4: Low temperature (blue, b exponent) and high temperature (red, d exponent) components of the biexponential fit (black) of the $\bar{T}_{1n}$ temperature dependence given in EQ. 8.1.

It is noted that the temperature dependence of the 40mM sample is comparable to that obtained by Shimon et al. in REF. [120]. They found the nuclear T_1 to be ∼63s at 6K and ∼10s at 50K.

Tempol Concentration Dependence

The non-monotonic behaviour of the temperature curves with respect to the concentration of Tempol is unexpected. In theory the addition of *any* concentration of paramagnetic centres should lead to a decrease in the nuclear T_1. Instead, the data show that below 15K, the 10mM & 20mM $\bar{T}_{1n}$ is in fact higher than for 0mM. Above 15K, the 20mM curve falls below 0mM, while the 0mM & 10mM samples become indistinguishable, and remain that way to 30K. This non-monotonic behaviour will be discussed in more detail shortly. The ratio of the 10mM & 50mM $\bar{T}_{1n}$ decreases from 2.8 at 3K to 2.2 at 30K, indicating that at even higher temperatures the relaxation time becomes concentration independent.

Variability

Before entering a discussion, it is reiterated that the statistics in FIG. 8-3 are from 4 or 8 data points only, and should therefore not be overinterpreted. Nonetheless, FIG. 8-3 has some interesting features: firstly, the variability seems to be neither particularly concentration nor temperature dependent, and secondly, the mean and median tend to be quite close. The latter suggests that the data is normally distributed, which is consistent with the assumption, corroborated by the former, that the nature of the variability is random. To further check this, the Shapiro-Wilk normality test [130] was applied to each box-and-whisker plot. This test was chosen because it is one of the few tests appropriate for sample sizes below 10 [131]. As expected, the normality test was successful in over 90% of cases.

8.3 Degassed Samples

In this section the effect of dissolved oxygen on the nuclear T_1 in a 50/50 water/glycerol sample is examined.

8.3.1 Sample Preparation

The degassed sample was prepared from the 0mM stock using a Schlenk line [132]. A small quantity of the stock was poured into a vial, which was then connected to the Schlenk apparatus via a flexible tube. The vial, vacuum manifold, nitrogen gas supply & vacuum pump must form a hermetically sealed system for the degassing to work. Once this was verified, the sample was placed in a bath of liquid nitrogen until fully frozen and then pumped on until a pressure 10^{-3}mTorr was achieved. The vacuum pump was then switched off and the sample allowed to defrost while being flushed with nitrogen gas. As the sample defrosts, oxygen comes out of solution to equilibrate with its new partial pressure in the oxygen-poor Schlenk line. The freeze-thaw process was repeated until there were no visible bubbles during thawing. To minimise re-oxygenation of the sample during transfer to the sample cup, the transfer was done under a constant flow of nitrogen gas. Once loaded, the NMR probe was

immediately inserted in the magnet.

8.3.2 Experiment Procedure

This set of experiments follows the procedure outlined in Section 8.2.2. The only differences are that longer τ_{d} were required (refer to Appendix B), and only one exeriment was performed at each temperature.

8.3.3 Results

The plots in FIG. 8-5 show the temperature dependence of $T_{1\mathrm{n}}$ in the degassed sample and the averaged 0mM sample. $T_{1\mathrm{n}}$, the temperature fit, and error were obtained in the same way as for FIG. 8-2.

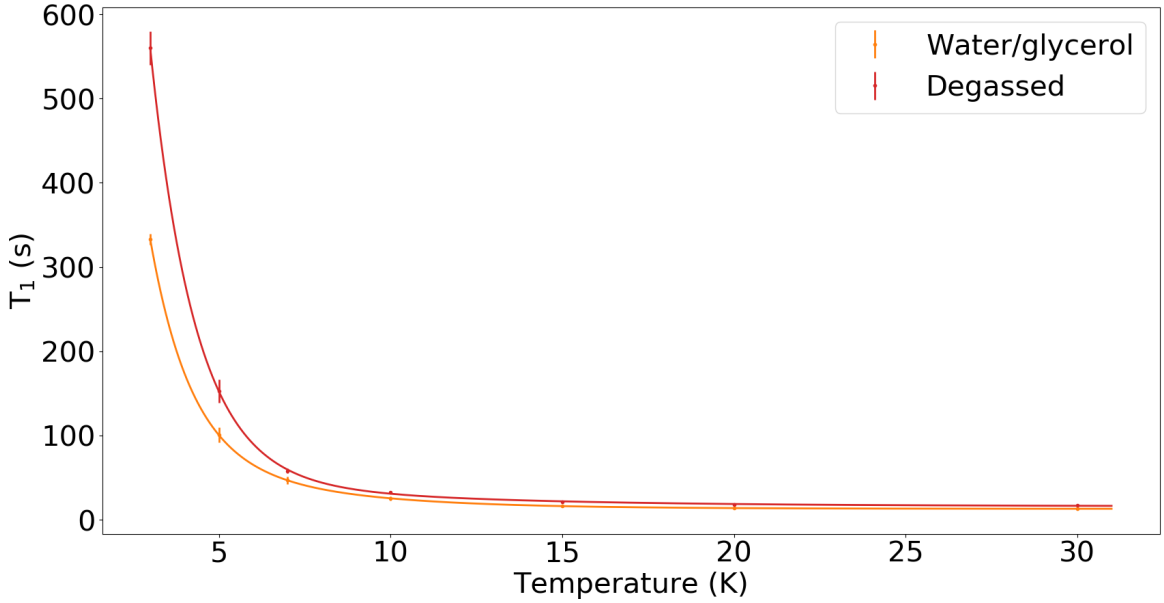


Figure 8-5: Temperature dependence of nuclear T_1 for 50/50 water/glycerol and a degassed sample from the same stock.

The fitting parameters for the biexponential fits (EQ. 8.1) are given in TAB. 8.2. The 0mM parameters are shown again for comparison.

Sample	**a**	**b**	**c**	**d**	**a**	$\mathbf{R^2}$
Degassed	5072.9	0.8	58.9	0.2	16.1	0.999
0mM	3307.9	0.9	165.2	0.3	13.1	0.999

Table 8.2: Fitting parameters for the biexponential fit to the temperature dependence of T_{1n} relaxation for a 50/50 water/glycerol mixture and a degassed sample of the same mixture.

8.3.4 Discussion

Despite the very low concentration of oxygen in solution (0.5mM or less, refer to Section 8.1.2), it has a significant effect on the relaxation of the 0mM sample, with the T_{1n} increasing by 230s at 3K when it is degassed. This suggests that the oxygen is able to efficiently relax the nuclei, even in very small concentrations. It also implies that the spin diffusion relaxation mechanism is highly effective, since with such a

low concentration of paramagnetic centres only a small fraction of the nuclei directly experience paramagnetic relaxation.

8.3.5 Non-monotonicity of Tempol Concentration Dependence

It was already mentioned in Section 8.2.4 that the non-monotonic concentration dependence of $\bar{T}_{1n}$ is unexpected. However, the drastic effect the removal of $<$ 1mM oxygen in solution has on the nuclear relaxation could be a key to understanding why. Although a hypothesis is provided in the paragraphs below, it is emphasised that the ensuing discussion is qualitative only, and requires experimental evidence to validate it.

Comparing FIGs. 8-2 & 8-5, it is observed that the increase in T_{1n} due to the removal of $<$ 1mM oxygen in solution ($\sim$ 230s) is greater than the decrease in $\bar{T}_{1n}$ due to the addition of 50mM Tempol ($\sim$ 180s), suggesting that oxygen is a better source of paramagnetic relaxation. The non-monotonic behaviour may therefore arise from Tempol (a weaker source of paramagnetic relaxation) kicking oxygen (a stronger source of paramagnetic relaxation) out of solution. Despite the concentration of Tempol being in the mM range, this could be plausible since the oxygen is only weakly attracted to the water molecules, and is present in small concentrations compared to Tempol. Assuming then that as Tempol is added to the sample, oxygen comes out of solution, the non-monotonic behaviour is expected, with monotonic behaviour only starting once the loss of oxygen has been compensated with (a much larger) concentration of Tempol. From FIG. 8-2, this appears to be somewhere bewteen 20mM and 30mM.

This hypothesis could corroborated by data collected by Shimon et al. for a non-degassed 40mM Tempol sample, and degassed 10mM and 40mM Tempol samples (FIG 8-6, FIG. 3(b) in REF. [120]). Data were collected in a similar magnetic field (3.38T), but using DMSO as a glassing agent rather than glycerol (DMSO/water 56/44 (w/w%)). At 20°C and atmospheric pressure, DMSO can dissolve 71mg/L [133], much more than either water or glycerol. If this persists to low temperatures,

it is therefore expected that degassing a DMSO solution has a much greater effect on the nuclear relaxation than degassing a glycerol solution.

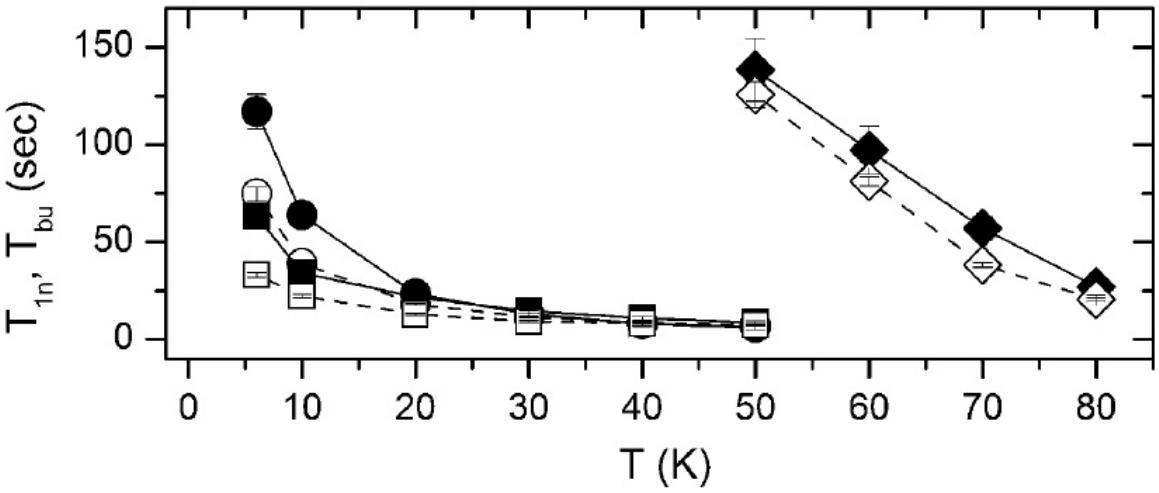


Figure 8-6: T_{1n} (filled symbols) relaxation times and the buildup times T_{bu} (open symbols) as a function of temperature of the degassed 40mM (circles), non-degassed 40mM (squares), and degassed 10mM (diamonds) samples. The buildup measurements were conducted at 94.952 GHz. Error bars represent the 95% confidence intervals of the time scale parameters resultant from the fitting procedure of the buildup and saturation recovery curves. Lines are to guide the eye only. This is FIG. 3b) from [120].

Assuming that a non-degassed 10mM Tempol sample in DMSO/water would follow a similar trend to the non-degassed 40mM sample in FIG. 8-6, or indeed the non-degassed data collected in this work (FIG. 8-2), then it is evident that degassing the 10mM sample (filled diamonds, FIG. 8-6) has a much more drastic effect on the nuclear T_1 than degassing the 40mM sample. This is expected in the framework of this hypothesis, since a 10mM sample still contains much more oxygen in solution than a 40mM sample. Furthermore, since a DMSO/water mixture can absorb much more oxygen than a glycerol/water mixture, degassing of DMSO mixtures is expected to have a greater effect on T_{1n} than degassing glycerol mixtures. A possible explanation for the molecular oxygen being more efficient at relaxing nuclei than Tempol is its smaller size. Tempol is a much larger molecule, which may cause its free electron to be shielded from the matrix such that nuclei are unable to approach it as closely as in O_2. Since paramagnetic relaxation requires interaction between the electrons and

nuclei, this could curb paramagnetic relaxation by Tempol.

Combined, the data collected here and that of Shimon et al. may suggest that the non-monotonic dependence of the nuclear longitudinal relaxation time on the Tempol concentration could be due to Tempol pushing oxygen out of solution. However, more detailed experiments are required to validate this hypothesis. It is for example possible that mM concentrations of Tempol are too small, and much larger concentrations of Tempol would be necessary to have a significant effect on the concentration of oxygen in solution.

8.4 Deuterated Experiments

In this section, focus is on the inherent nuclear relaxation. This is studied by examining the T_{1n} behaviour of 3 deuterated samples in which the proton concentration is halved with respect to the 0mM sample. Many MAS experiments are conducted with deuterated solutions to increase nuclear T_1, which is very fast at the temperatures typical of MAS DNP and therefore not conducive to good enhancement.

8.4.1 Sample Preparation

Three half-protonated samples were prepared by replacing some of either the water (H_2O), glycerol (Gly), or both with their deuterated counterpart (D_2O (Sigma Aldrich - Missouri, USA; 151882) and d8-Gly (Sigma Aldrich - Missouri, USA; 447498) respectively). The proton molarity of water is $111\text{Mol}_{\text{pr}}$ (since it has Molarity 55.5Mol and 2 protons) and that of glycerol is $109.6\text{Mol}_{\text{pr}}$ (since it has Molarity 13.7Mol and 8 protons). Because they have approximately equal Mol_{pr}, halving the proton concentration is easily achieved, since they provide protons in equal proportion. The sample compositions are given in TAB. 8.3.

Sample	D_2O	H_2O	d8-Gly	Gly
H_2O/Gly	-	50%	-	50%
D_2O/Gly	50%	-	-	50%
H_2O/d8-Gly	-	50%	50%	-
D_2O/H_2O/d8-Gly/Gly	25%	25%	25%	25%

Table 8.3: Composition of samples used to study the inherent nuclear relaxation.

Since the proton separation is calculated from the proton Molarity, the average separation of protons is ∼2.5Å in both water and glycerol. By halving the proton concentration, this is increased to ∼3.1Å. Consequently, the maximum dipolar coupling is decreased from ∼1220Hz to ∼640Hz. A decreased dipolar coupling leads to slower relaxation [37].

8.4.2 Experiment Procedure

Loading the Sample

The loading procedure was already described in Section 8.2.2, though for this set of experiments the sample cup was rinsed with acetone between samples instead of water since experiments were sensitive to residual water. Acetone was the solvent of choice because it evaporates quickly and is miscible with both water and glycerol [134].

Temperature Profile

Experiments in this section are significantly longer than in previous sections and therefore require better temperature stability. In an attempt to achieve this, the cooling rate was decreased and measurements started at 30K decreasing monotonically to 3K, giving the magnet more time to cool and equilibrate with the sample space. Experiments were also performed at 2.6K, but this was always done on a separate day due to their long duration. The magnet was allowed to cool for ∼2.5hrs to 3hrs before attempting 2.6K experiments.

T_1 Measurement

For these experiments the τ_d was increased significantly and was as long as 900s at low temperatures (refer to Appendix B).

T_{1n} was averaged over 10 experiments for temperatures 5K to 10K, 8 experiments at 3K and 2 to 3 experiments at 2.6K, depending on how stable the temperature could be kept.

8.4.3 Results

FIG. 8-7 shows the average temperature dependence of the nuclear T_1 for the 3 deuterated samples and the fully protonated 0mM sample. Results were obtained in the same way as FIGs. 8-2 & 8-5.

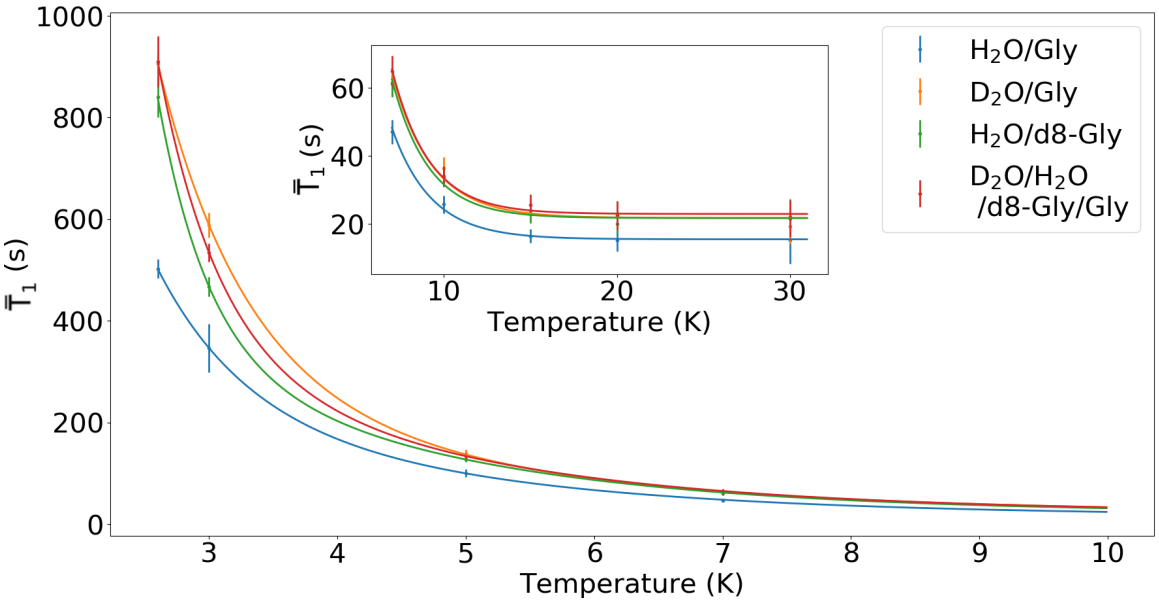


Figure 8-7: Averaged nuclear T_1 times for the 3 deuterated and 1 protonated samples. Note that the D_2O/Gly sample is present at 2.6K but is very similar to D_2O/H_2O/d8-Gly/Gly (906s and 910s respectively).

In FIG. 8-8 the nuclear longitudinal relaxation rate of each sample is plotted as a function of temperature along with a BPP model fit [66]. EQ. 2.45 was used as a fitting model, with fitting parameters $a - c$:

$$R_{1,\mathrm{BPP}} = \frac{d_0^2 \tau}{1+\omega_\mathrm{I}^2 \tau^2} = \frac{aeb/T}{1+ce2b/T}, \qquad \tau = \tau_0 \mathrm{e} T_0/T \tag{8.2}$$

where $a = d_0^2\tau_0$, $b = T_0$, and $c = \omega_\mathrm{I}^2\tau_0^2$. d_0 is proportional to the average dipolar coupling, τ_0 is the tumbling correlation time in the high temperature limit ($T \gg T_0$), and τ is the correlation time.

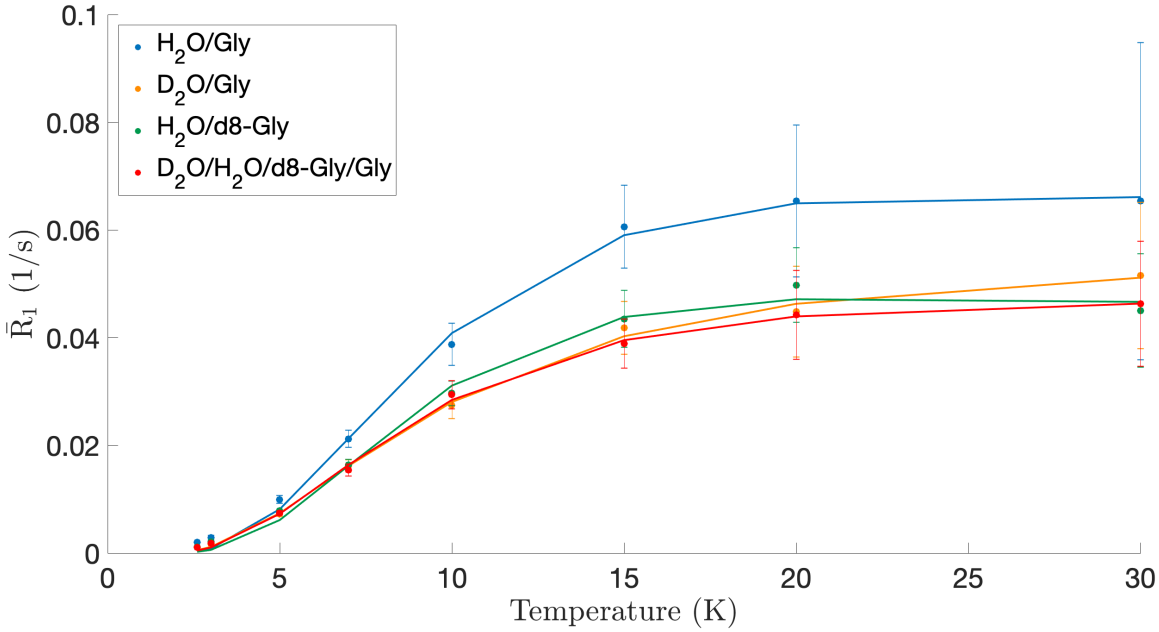


Figure 8-8: BPP fit of the nuclear longitudinal relaxation rates for the 3 deuterated and 1 fully protonated water/glycerol samples.

The fitting parameters and their physical interpretation are given in TAB. 8.4.

Sample	a	d_0 (Hz)	b (K)	c	τ_0 (ns)	R^2
H_2O/Gly	0.069	4382	17.2	0.270	3.59	0.997
D_2O/Gly	0.095	3959	14.0	0.777	6.08	0.998
H_2O/d8-Gly	0.044	3705	17.5	0.217	3.22	0.994
D_2O/H_2O/d8-Gly/Gly	0.063	3671	14.7	0.459	4.68	0.999

Table 8.4: Fitting parameters for the BPP model fit (EQ. 8.2) of deuterated and undeuterated water/glycerol samples. d_0 is proportional to the average dipolar coupling, τ_0 is the tumbling correlation time in the high temperature limit, and τ is the correlation time.

8.4.4 Discussion

Temperature Dependence

In the absence of paramagnetic centres, the nuclear relaxation is dominated by dipolar relaxation mechanisms (refer to Section 2.7.1). Since the samples were not degassed, oxygen in solution, which was shown to have a significant effect on the matrix relaxation in Section 8.3, is also present. Nonetheless, the dependence of T_{1n} on the proton concentration in FIG. 8-7 is clear. This suggests that as well as intra-molecular interactions, which are unaffected by the deuteration, inter-molecular interactions between the water and glycerol play a crucial role in the relaxation. This role is nuanced, with the removal of water protons having a greater effect on the relaxation time than the removal of glycerol protons.

At 2.6K the data is ambiguous because it is averaged over only 2 to 3 experiments and the temperature was difficult to keep stable over the long experimental duration. From 3K onward however, the ordering, from highest to lowest, of the relaxation times is clearly D_2O/Gly, D_2O/H_2O/d8-Gly/Gly, H_2O/Gly, H_2O/d8-Gly. Although the difference between the deuterated samples is small, it is present, corroborating the premise in Section 8.3.5 that different molecules have a different effect on the

relaxation time. Just as with the previous two sets of experiments, the temperature dependence is very strong for low temperatures, but becomes negligible at temperatures above 15K. The ordering however largely remains, with some scattering between the two D_2O samples. There is a slight decrease in the ratio between the D_2O/Gly and H_2O/Gly $\bar{T}_{1n}$ as the temperature rises, suggesting that at even higher temperatures the relaxation might become completely independent of proton concentration.

BPP model Fit

In FIG. 8-8, a BPP model fit to the nuclear relaxation rates is shown. Recall from Section 2.7.1 that the BPP model is best applied to relaxation that is dominated by a thermally activated process. Parameters can be found that yield a good BPP fit at temperatures above 7K. Below this however, the BPP model converges more than the data and underestimates the relaxation rate.

From the fitting parameters in TAB. 8.4 it appears that the activation temperature for the BPP-like relaxation is around 14K for samples containing H_2O and 17K for samples with D_2O. This is consistent with the general trend discussed in previous sections of the temperature dependence changing around 15K. It is beyond the scope of this work to discuss in detail what process is activated at T_0, however, at such low temperatures it is possible that it could be hopping on the water or glycerol molecule, a sort of quantum equivalent to molecular tumbling [135, 136, 137]. The two H_2O samples have higher τ_0, suggesting that they are more 'active'. However, this activity appears to be disturbed by the glycerol, as in both the H_2O and D_2O samples, the high temperature correlation time is shorter when the glycerol is deuterated. Finally, as expected, the removal of protons from the glycerol decreases d_0 more than the removal of protons from H_2O, simply because it is a larger molecule and therefore leaves larger gaps in the matrix.

The BPP-model fits to the data appear to be quite good, the R^2 values ranging from 0.994 to 0.999. However, with little information on physical values for parameters,

it is difficult to establish whether the fits work well because there are many fitting parameters, or if they have a genuine physical meaning. More focused experiments would be necessary to establish this. Assuming that the fits are physical, they imply that the dynamiccs are random and dominated by a single process fully characterisable by its correlation time τ. This process appears to become active at around 15K.

The presence of paramagnetic centres from the oxygen in solution has been ignored thus far. However, it appears from the quality of the fits that, at least above the activation temperature, it is not the dominant process in the nuclear relaxation. This is in agreement with the discussion in Section 8.2.4, where it was shown that the low temperature dependence is affected by some paramagnetic process (which becomes dominant for high Tempol concentrations) that becomes a background process at higher temperatures.

8.5 Fitting the Proton Relaxation Rate

In 1961 Bloembergen and Morgan showed that electron-proton dipole-dipole interactions, as formulated by Solomon, could be used to reasonably accurately describe the effect of T_{1e} on T_{1n} in dilute aqueous solutions of iron group ions [138]. This section seeks to find a solid state equivalent. Data from the previous sections and electron relaxation data gathered by R. Shakhovy will be used to fit the proposed model.
The observed relaxation rate (R_{1n}) can be separated into three contributing rates: matrix relaxation ($R_{0,1n}$), paramagnetic relaxation (R_{PM}), and spin diffusion (R_{SD})

$$R_{1n} = R_{0,1n} + R_{PM} + R_{SD}. \tag{8.3}$$

$R_{0,1n}$ is given by the 0mM Tempol data. R_{PM} and R_{SD} on the other hand are found by fitting the experimental data and are given explicitly by

$$R_{PM} = \frac{\langle B^2 \rangle}{4\omega_I^2}(1 - p_e^2)R_{1e},$$

and

$$R_{\mathrm{SD}} = \frac{\sigma}{N}$$

respectively. The paramagnetic relaxation rate is that proposed by Abragam and Goldman in REF. [38], where $\langle B^2 \rangle$ is the average squared pseudo-secular hyperfine interaction in the bulk, ω_{I} is the nuclear Larmor frequency and p_{e} is the electron thermal polarisation given by EQ. 2.3. $R_{1\mathrm{e}}$ is found experimentally.

The spin diffusion rate is derived by A. Karabanov. σ is the core-bulk exchange rate, which describes how well the core nuclei can exchange polarisation with the bulk. It is given by

$$\sigma = \frac{n d_0^2}{R_{\mathrm{c,2n}}}, \qquad R_{\mathrm{c,2n}} = A^2 \tau$$

where n is the number of spin pairs participating in the core-bulk exchange, d_0 is proportional to the nuclear interaction strength and is the same as d_0 obtained in Section 8.4, $R_{\mathrm{c,2n}}$ is the nuclear transverse relaxation rate of the core, A is the average secular hyperfine interaction in the core, and τ is the Arrhenius-type correlation time given in EQ. 8.2. It is assumed that the core protons interact much more strongly with the electron than with each other and therefore experience fast transverse relaxation. Finally, N is the number of bulk nuclei served by each electron. It is given by the ratio of the nuclear to electron concentrations $c_{\mathrm{n}}/c_{\mathrm{e}}$.

Both the paramagnetic and the spin diffusion rates increase with increasing electron concentration as this decreases the number of nuclei served by each electron. This in turn increases $\langle B^2 \rangle$ and decreases N. R_{PM} further favours fast electron relaxation and low thermal polarisation, both of which occur at high temperature. For the core-bulk exchange to be effective, there must be a strong dipolar matrix (large d_0) and the transverse relaxation should be minimised.

8.5.1 Electron Relaxation Rate

FIG. 8-9 shows the temperature dependence of R_{1e} for a 10mM Tempol sample at 94.895GHz. The data was collected by R. Shakhovy with the EPR magnet and pulse sequence described in Section 7.4. The data is not averaged.

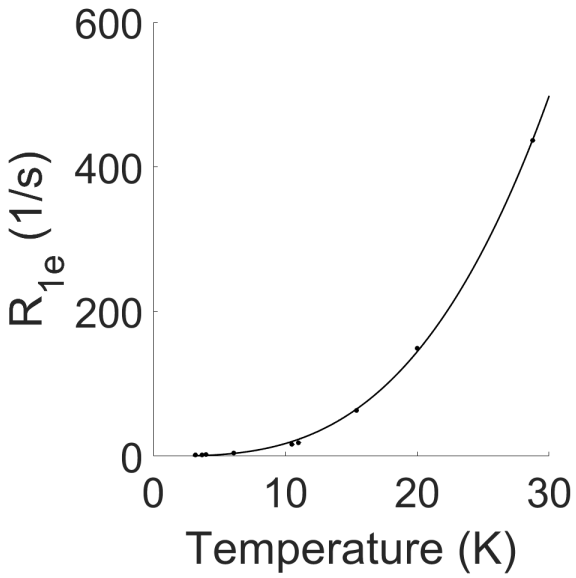


Figure 8-9: Relaxation rate for a 10mM Tempol sample measured at 94.895GHz. This data was collected by R. Shakhovy on the EPR magnet. The fit is a power law Raman fit ($A_{\mathrm{Ram}}T^{\lambda}$) with $A_{\mathrm{Ram}} = 0.015$ and $\lambda = 3.053$.

Of the electron relaxation processes described in Section 2.8, the best fit was found to be the two-phonon Raman process with a coefficient $A_{\mathrm{Ram}} = 0.015$ and power $\lambda = 3.053$ (refer to EQ. 2.48). The power is slightly higher than that found for DNP radicals in literature ($\sim$2.5) [139], although values of up to 5.5 have been reported for NMR-active molecules at low temperatures [140].

8.5.2 Nuclear Relaxation Rate

Using the 0mM Tempol data $R_{0,1n}$, the remaining Tempol data R_{1n}, parameters from the BPP fit to the protonated sample in Section 8.4, and the Raman fit of the electron relaxation, the nuclear relaxation rate can be fitted with

$$\delta R_{1n} = R_{1n} - R_{0,1n} = R_{PM} + R_{SD} = \frac{a_1}{4\omega_I^2}(1 - p_e^2)A_{Ram}T^{\lambda} + \frac{a_2 d_0^2}{\exp(a_3/T)}\frac{c_e}{c_n}. \quad (8.4)$$

$a_1 = \langle B^2 \rangle$, A_{Ram} and λ are given by fit to the electron relaxation rate, $a_2 = n/A^2\tau_0$, d_0 is taken from the BPP fit to the protonated sample (TAB. 8.4) since the dipolar interaction within the matrix is not expected to change between samples, $a_3 = T_0$, c_e is the Tempol concentration in Molar and c_n is 110M. The fit of EQ. 8.4 to the 30mM to 50mM samples is shown in FIG. 8-10. The 10mM & 20mM samples have been omitted since for some temperatures they relax slower than the 0mM sample and therefore, by EQ. 8.4, have unphysical negative relaxation rates.

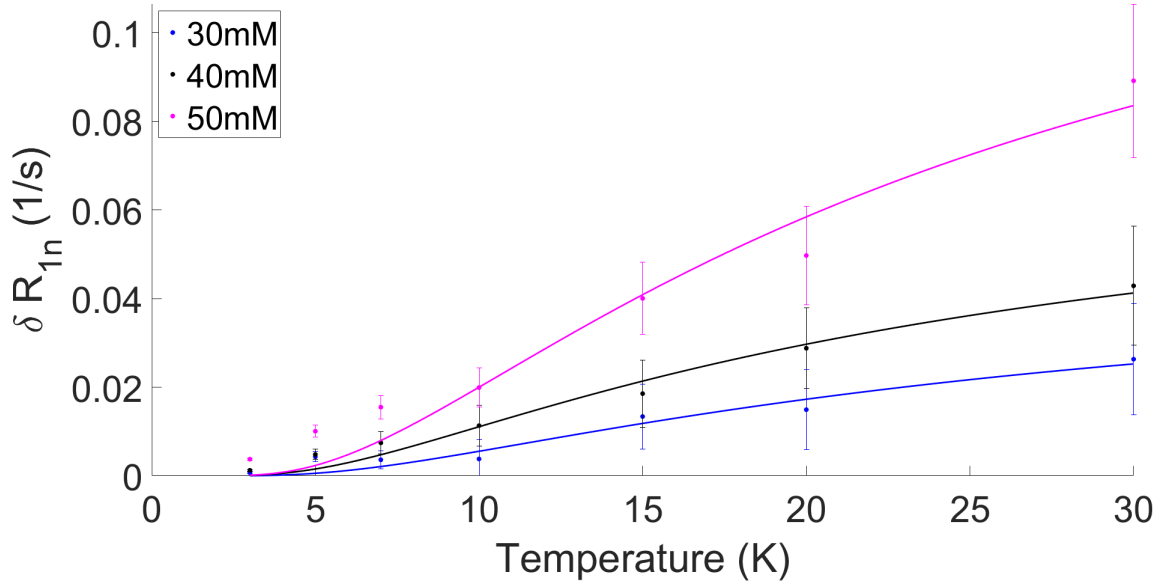


Figure 8-10: Fit of EQ. 8.4 to the experimentally measured relaxation rates for the 30mM to 50mM samples. The 10mM & 20mM samples have been omitted since for some temperatures they relax slower than the 0mM sample and therefore, by EQ. 8.4, have unphysical negative relaxation rates.

The fitting parameters are given in TAB. 8.5.

Sample	a_1	a_2	a_3
30mM	1e6	8.8e-6	22.8
40mM	1e6	9.7e-6	19.7
50mM	1e6	1.7e-5	21.5

Table 8.5: Fitting parameters a_1 through a_3 of EQ. 8.4 used to generate FIG. 8-10.

8.5.3 Discussion

Paramagnetic Relaxation Contribution

Although included in the fitting equation used for FIG. 8-10, the paramagnetic relaxation makes no contribution. The values for a_1 shown in TAB. 8.5 are simply the initial values given to the fitting algorithm. This is not entirely unexpected since at low temperatures the electron relaxation is long, and the thermal polarisation is high. Furthermore, the electron concentrations are relatively low, each electron in the 30mM and 50mM samples serving ∼3700 and ∼2200 nuclei respectively. With an average separation of 2.5Å between nuclei in the bulk, this leads to very small $\langle B^2 \rangle$. If the electron relaxation rate is also small, the $1/4\omega_{\mathrm{I}}^2$ term dominates and R_{PM} is on the order of $10^{-7}\mathrm{s}^{-1}$ at 30K and $10^{-12}\mathrm{s}^{-1}$ at 3K. It should be noted that $R_{1\mathrm{e}}$ is in fact concentration dependent and should increase with increasing electron concentration. However, a change in concentration of 40mM is not going to provide the orders-of-magnitude change in $R_{1\mathrm{e}}$ required for R_{PM} to become significant [72].

Spin Diffusion Relaxation Contribution

Below 10K, R_{SD} converges to zero much faster than $\delta R_{1\mathrm{n}}$ and does not capture the concentration dependence that persists down to 3K. This suggests that the model EQ. 8.4 is missing some mechanism that describes the low temperature behaviour of $\delta R_{1\mathrm{n}}$. Above 10K on the other hand, the spin diffusion rate seems to be a good fit for all concentrations. The activation temperature a_3 is similar for all three samples,

with an average of 21.3K. This is slightly higher than the activation temperatures calculated from the BPP fits to the H_2O samples in Section 8.4, which are around 17K. Again, it is not possible to say what exactly is activated by T_0 without further investigation. However, it is plausible that the electrons affect T_0 just like the removal of protons from water affects T_0, the effect of the latter being to decrease T_0 from 17K to 14K.

For the fit to be physical, it must be possible to recover a_2 using physical values for n, A and τ_0. An approximate value for n can be obtained from the chemical structure of Tempol (FIG. 8-1). Tempol has 13 structural protons whose proximity to the electron makes them all core protons. Letting the solvent protons form the bulk, and allowing each structural proton to interact strongly with just one solvent proton, the number of nuclei participating in the core-bulk exchange is $n = 26$. A can be found by assuming that the approximate distance between the electron and the four methyl groups is the same in both bTbk and Tempol. The structural bTbk data used in Section 6.1 can then also be used to calculate the average secular interaction in Tempol. With this approach, $A \sim 2$MHz for the 12 methyl group protons. Including the 13^{th} proton, which is located further from the electron and is not present in bTbk, does not change A significantly. With $n = 26$ and $A = 2$MHz, the high temperature correlation time is $\tau_0 = 6.5\mu$s. This is 3 orders of magnitude higher than τ_0 calculated for the deuterated samples, but still falls within the reported range of correlation times in water [135, 136, 137]. Nonetheless, experiments focused on studying the molecular dynamics should be performed before conclusive statements are made about the applicability of EQ. 8.4.

Of course, different values of n, A and τ_0 could be reasonably argued. For example, the core-bulk distinction made above could be too simplistic, as it neglects to take into account that some of the solvent protons are too strongly hyperfine shifted by A to be detectable experimentally, and should therefore be included in the core. The observable bandwidth in an experiment is given by the inverse of the tipping pulse

duration. In the experiments presented here, the pulse length was 4μs, and the bandwidth therefore 250kHz. The core can thus be defined as all protons hyperfine shifted from the reference frequency by more than $\pm$125kHz. Using the approach outlined in Section 5.4.3 to calculate the average A for each shell of solvent protons, the first shell must therefore also be included in the core [i], reducing the average secular hyperfine interaction of the core to $\sim$1MHz. Including the first shell of solvent protons in the core also increases its surface area, so n is expected to increase, though not by an order of magnitude. Therefore, even with these considerations, τ_0 remains on the order of μs.

The spin diffusion model appears to capture the temperature dependence of $\delta R_{1\mathrm{n}}$ at temperatures above 10K, but fails to give accurate results below 10K. This could be an indication that the model is missing a mechanism that describes the low temperature relaxation. Paramagnetic relaxation in the form used in EQ. 8.3 is shown to have no effect for the temperature and concentration regime studied, although it is known from the previous sections in this chapter that the presence of electrons strongly affects the nuclear relaxation. Furthermore, although the spin diffusion fit is good, further corroborating evidence is needed. Such proof could come for example from molecular dynamics studies or experiments that find τ_0 or T_0.

[i] $e-n \sim 2.8$Å, $n-n \sim 2.5$Å. Shell 1: $A \sim 270$kHz.

Chapter 9

Conclusion

The theory of DNP has recently undergone significant progress, particularly in its quantum mechanical description. This thesis aims to contribute to these developments by introducing two new, highly efficient simulation algorithms for CE DNP under static and MAS conditions, and by presenting a detailed relaxation study of the DNP radical Tempol. In this final chapter, results are summarised and avenues for further research explored.

9.1 Static Cross Effect DNP

The kinetic Monte Carlo algorithm developed for the static CE has unprecedented efficiency, and is thus uniquely placed for simulations of large spin systems. The algorithm was shown to be very accurate within the parameter regime applicable to adiabatic elimination, and was used to study the effect of solvent and radical geometries on the nuclear polarisation enhancement in a 125-spin system. Because the algorithm is based on classical rather than quantum dynamics, it scales favourably with system size and therefore lends itself to simulation of even larger systems. Such simulations could be used to generate parameter maps or to assist in system design for optimised DNP.

In Section 4.5, the effect of randomising the geometry of a solvent forming a cubic

lattice was examined. 5%, 10%, 15% & 20% linear randomisations were applied to the lattice to mimic the increasing disorder in the solvent as glassing agent is added. Optimal nuclear dynamics were obtained for moderate randomisations of 5% to 10%, for which the rearrangement of spins is enough to bridge the dipolar gap between unconnected planes in the lattice, but not enough to create pockets of spins that are poorly connected to the rest of the lattice. Spin diffusion is thus able to propagate nuclear polarisation to the extremes of the system effectively. These findings suggest that, while glassing agents are necessary to ensure an even distribution of radical in the sample, their effect on the lattice geometry may actually negatively impact DNP. For a more representative study, a hexagonal lattice should be used to more accurately represent the lattice formed by ice. Furthermore, the randomisations used here were arbitrary and not linked to proportions of glassing agent added. A more complete study should determine the percent randomisation in typical DNP solvents such as DNP juice.

Section 4.6 is a first attempt at using the kMC algorithm to assist in radical design. It was shown that the removal of certain nuclear spins in the immediate environment of the electrons can have a positive effect on the nuclear enhancement if they have high secular hyperfine interactions, and a negative effect if they have high pseudo-secular hyperfine interactions. In practice the removal of particular spins can be achieved by deuterating the radical, or building 'cages' around the electrons (such as the aromatic rings in Trityl). No particular radical geometry was used for the simulations in this section. However, there is no reason not to use exact radical geometries as was done in the MAS case. Simulations using exact geometries could then assist chemists in engineering radical molecules for specific applications

9.2 MAS Cross Effect DNP

In Chapters 5 & 6 a fast simulation algorithm for MAS CE DNP was outlined and applied. Provided the polarisation dynamics are accurately captured by incoherent

Landau-Zener transitions, the fast algorithm was shown to be in good agreement with simulations using the full master equation. Large-scale simulations of the 52 structural protons of bTbk radical and an additional 100 solvent protons, including 72 powder averages, took just a few days. This is remarkably fast considering that dynamics must be tracked within a rotor period as well as stroboscopically. Just like with the static case, the computational time-savings obtained by using the fast algorithm make it ideal for predictive simulations of the MAS CE DNP dynamics. Simulations in Chapter 6 however, are still more in the developmental stage.

In Section 6.4 the microwave offset, static field strength, and microwave irradiation amplitude were swept on the 52 structural protons of bTbk. These simulations demonstrate that the fast simulation algorithm is appropriate for generating parameter scans. They also suggest that at high magnetic fields, it is not necessary to average over the 9 possible nitrogen orientations in nitroxide radicals, thus significantly reducing simulation time.

Section 6.5 studies in more detail the interaction between the 52 structural protons of bTbk and 100 solvent protons. Results suggest that, under certain conditions, the bTbk and solvent protons evolve quite separately. It should therefore be possible to replace the large bTbk molecule in simulations with a single representative core nucleus, thus again greatly cutting back on computation time. Nonetheless, even in its current state, the fast algorithm could be used to study in detail the effects of radical and solvent geometry on the MAS DNP dynamics, as was done in the static case. Mentink-Vigier et al. [141] have already used their 3-spin model to help them engineer the radical AsymPol.

9.3 Tempol Experiments

The final part of this thesis steered away from theory, and explored the temperature & concentration dependence of nuclear T_1 relaxation in Tempol monoradical. Relax-

ation plays a critical role in DNP and must be well-understood in order to optimise the performance of DNP experiments. A new formalism relating the paramagnetic and spin diffusion contributions to the observed relaxation is presented.

The experiments performed are unique in that they extend from 30K to temperatures as low as 2.6K. Experiments down to such low temperatures are few and far between in the DNP literature, and thus give insight to new relaxation behaviours. Tempol is shown to become highly dependent on temperature and radical concentration for temperatures below 10K. Surprisingly however, the temperature dependence was shown to be much stronger for oxygen in solution, which is present in much smaller quantities than any of the Tempol concentrations studied. It is hypothesised that this may be because oxygen is a smaller molecule, and may therefore be more effective at relaxing a surrounding nuclear ensemble. To really test this hypothesis, more experiments should be carried out in which different concentrations of Tempol samples are degassed. If the hypothesis holds, degassing should have a decreasing effect as the Tempol concentration increases. 50% protonated experiments where either the water, glycerol, or both were deuterated demonstrate that the removal of water protons is not equivalent to the removal of glycerol protons. The data are well-fit by the BPP model, but it is unclear what mechanism is activated at $\sim$14K & 17K. This would require further experiments and possibly also simulations of molecular dynamics.

Finally, in the very last section, a relaxation theory was presented that attempted to relate the observed nuclear longitudinal relaxation to spin diffusion and paramagnetic relaxation. A reasonably good fit to the temperature and radical concentration data is obtained with the new model for temperatures above 15K and concentrations above 20mM. Below 15K the model converges to zero much faster than the data, suggesting that there is some low-temperature mechanism missing.

Even where the fit is good, derivations of parameters were mostly qualitative, and should be corroborated by specifically designed experiments. For example, although

the model is fit to radical concentrations of 30mM, 40mM & 50mM, EPR data for a 10mM sample was used to fit the data, when really the EPR data should match the NMR data.

Appendix A

Theory Toolbox Appendix

In the text EQ. 2.28 stated that

$$\int_0^\infty \int_0^t \mathrm{e}^{-\epsilon t} \hat{\hat{K}}(t-\tau)\hat{\rho}_{\mathrm{S}}(\tau)d\tau dt = l_{\hat{\rho}_{\mathrm{S}}}(\epsilon) \cdot l_{\hat{\hat{\mathrm{K}}}}(\epsilon), \tag{A.1}$$

where the $l_{\hat{\rho}_{\mathrm{S}}}(\epsilon)$ and $l_{\hat{\hat{\mathrm{K}}}}(\epsilon)$ are the Laplace transforms of $\hat{\rho}_{\mathrm{S}}(t)$ and the kernel function respectively. The derivation of this equality is not trivial, and makes use of the diagonal form of the memory kernel

$$\hat{\hat{K}}(t-\tau) = \sum_k \hat{\hat{K}}_k \mathrm{e}^{\epsilon_k(t-\tau)}, \tag{A.2}$$

where $\hat{\hat{K}}_k$ are its eigenfunctions and ϵ_k are its eigenvalues.

The first step is to substitute the diagonal form of the kernel function into the left hand side of EQ. A.1:

$$\sum_k \int_0^\infty \mathrm{e}^{(\epsilon_k-\epsilon)t}\left(\int_0^t \mathrm{e}^{-\epsilon_k\tau}\hat{\hat{K}}_k\hat{\rho}_{\mathrm{S}}(\tau)d\tau\right)dt. \tag{A.3}$$

This is then integrated by parts using

$$
\begin{aligned}
u' &= \mathrm{e}^{(\epsilon_k-\epsilon)t} \qquad u = \frac{\mathrm{e}^{(\epsilon_k-\epsilon)t}}{\epsilon_k-\epsilon} \\
v &= \sum_k \int_0^t \mathrm{e}^{-\epsilon_k\tau}\hat{\hat{K}}_k\hat{\rho}_{\mathrm{S}}(\tau)d\tau \qquad v' = \sum_k \left(\mathrm{e}^{-\epsilon_k t}\hat{\hat{K}}_k\hat{\rho}_{\mathrm{S}}(t)\right).
\end{aligned}
\tag{A.4}
$$

The derivative of v is obtained using the Leibniz rule [142]

$$
v' = \sum_k \left(\mathrm{e}^{-\epsilon_k t}\hat{\hat{K}}_k\hat{\rho}_{\mathrm{S}}(t)\cdot\frac{d}{dt}t - \mathrm{e}^{0}\hat{\hat{K}}_k\hat{\rho}_{\mathrm{S}}(0)\cdot\frac{d}{dt}0 + \int_0^t \frac{\partial}{\partial t}\mathrm{e}^{-\epsilon_k\tau}\hat{\hat{K}}_k\hat{\rho}_{\mathrm{S}}(\tau)d\tau\right), \tag{A.5}
$$

where the last two terms are trivially zero.

Starting the integration by parts,

$$
\begin{aligned}
uv &= \sum_k \frac{\mathrm{e}^{(\epsilon_k-\epsilon)t}}{\epsilon_k-\epsilon}\int_0^t \mathrm{e}^{-\epsilon_k\tau}\hat{\hat{K}}_k\hat{\rho}_{\mathrm{S}}(\tau)d\tau\Big|_{t=0}^{t=\infty} \\
&= \sum_k \frac{\mathrm{e}^{(\epsilon_k-\epsilon)\infty}}{\epsilon_k-\epsilon}\int_0^\infty \mathrm{e}^{-\epsilon_k\tau}\hat{\hat{K}}_k\hat{\rho}_{\mathrm{S}}(\tau)d\tau - \sum_k \frac{\mathrm{e}^{1}}{\epsilon_k-\epsilon}\int_0^0 \mathrm{e}^{-\epsilon_k\tau}\hat{\hat{K}}_k\hat{\rho}_{\mathrm{S}}(\tau)d\tau = 0,
\end{aligned}
\tag{A.6}
$$

where the first term is zero because the eigenvalues ϵ_k are assumed to be large and negative, and the second integration is trivial.

The second term of the integration by parts is

$$
-\int v'u = -\sum_k \int_0^\infty \frac{\mathrm{e}^{(\epsilon_k-\epsilon)t}}{\epsilon_k-\epsilon}\left(\mathrm{e}^{-\epsilon_k t}\hat{\hat{K}}_k\hat{\rho}_{\mathrm{S}}(t)\right)dt = -\sum_k \int_0^\infty \frac{\mathrm{e}^{-\epsilon t}}{\epsilon_k-\epsilon}\left(\hat{\hat{K}}_k\hat{\rho}_{\mathrm{S}}(t)\right)dt. \tag{A.7}
$$

Therefore,

$$
\begin{aligned}
\int_0^\infty\int_0^t \mathrm{e}^{-\epsilon t}\hat{\hat{K}}(t-\tau)\hat{\rho}_{\mathrm{S}}(\tau)d\tau dt &= \sum_k \frac{\hat{\hat{K}}_k}{\epsilon_k-\epsilon}\cdot\int_0^\infty \mathrm{e}^{-\epsilon t}\hat{\rho}_{\mathrm{S}}(t)dt \\
&= l_{\hat{\hat{\mathrm{K}}}}(\epsilon)\cdot l_{\hat{\rho}_{\mathrm{S}}}(\epsilon).
\end{aligned}
\tag{A.8}
$$

Appendix B

Acquisition Parameters

B.1 Delay Times & Other Parameters

Table B.1: Delay times (in seconds) for experiments in Section 8.2 testing the dependence of T_{1n} on temperature and concentration of Tempol.

Temperature (K)	**0mM**	**10mM**	**20mM**	**30mM**	**40mM**	**50mM**
3	120	135	111	90	60	60
5	35	20	28	23	23	18
7	20	15	13	12	8	8
10	10	10	9	7	5	5
15	7	6	5	4	3	3
20	5	5	4	3	3	3
30	5	5	4	3	2	2

Table B.2: Delay times (in seconds) for experiments in Section 8.3, where a degassed 0mM Tempol sample was used.

Temperature (K)	3	5	7	10	15	20	30
Delay Time (s)	250	120	30	15	10	7	5

Table B.3: Delay times (in seconds) for experiments in Section 8.4, where either the water, glycerol, or both were deuterated in a 50/50 water/glycerol sample.

Temperature (K)	2.6	3	5	7	10	15	20	30
D_2O/Gly	925	200	43	23	12	8	7	7
H_2O/d8-Gly	300	165	37	23	12	9	7	7
D_2O/d8-Gly	870	150	45	23	12	8	7	7

The spectral width is 1MHz, and there are 512 points in each FID.

B.2 Saturation Recovery Pulse Sequence

FIG. B-1 shows the saturation recovery pulse sequence used in the NMR experiments. The only parameter that changes between experiments is the delay time (D10 in the figure). The saturation pulse has a duration of 7μs and a power level of 10dB, the acquisition pulse has a duration of 4μs and a power level of 5dB.

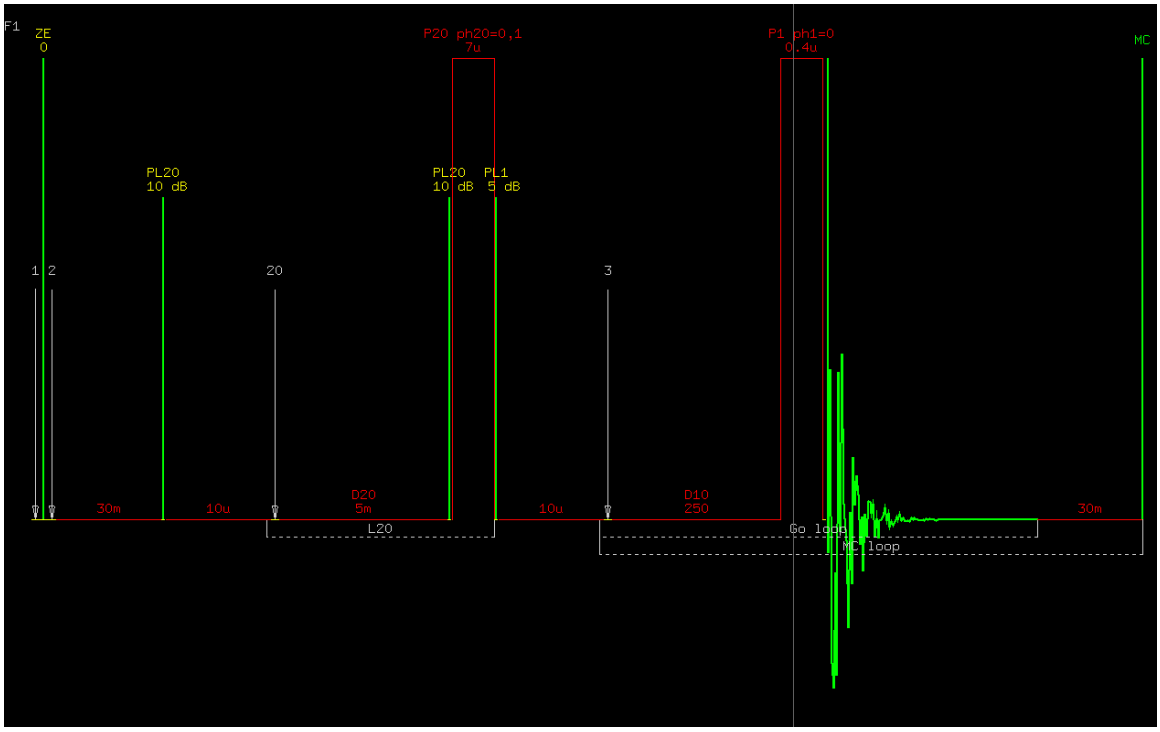


Figure B-1: Saturation recovery pulse sequence for NMR experiments.

Bibliography

[1] A. W. Overhauser. Polarization of nuclei in metals. *Phys. Rev.*, 92, 1953.

[2] W. Heitler and E. Teller. Time effects in the magnetic cooling method -I. *Proc. Roy. Soc. A*, 155, 1936.

[3] T. R. Carver and C. P. Slichter. Experimental verification of the Overhauser nuclear polarization effect. *Phys. Rev.*, 102, 1956.

[4] K. H. Hausser and D. Stehlik. Dynamic nuclear polarization in liquids. *Adv. Magn. Reson.*, 3, 1968.

[5] W. Mueller-Warmuth and K. Miese-Gresch. Molecular motions and interactions as studied by dynamic nuclear polarization in free radical solutions. *Adv. Magn. Reson.*, 11, 1983.

[6] A. Abragam and M. Goldman. *Nuclear magnetism: order and disorder*. Oxford; Clarendon Press, 198 Madison Avenue, New York, 10016, USA, 1982.

[7] R. A. Wind, M. J. Duijvestijn, C. van der Lugt, A. Manenschijn, and J. Vriend. Applications of dynamic nuclear polarisation in ^{13}C NMR in solids. *Nucl. Magn. Reson. Spectrosc.*, 17, 1985.

[8] L. C. Becerra, G. J. Gerfen, R. J. Temkin, D. J. Singel, and R. G. Griffin. Dynamic nuclear polarization with a cyclotron resonance maser at 5T. *Phys. Rev. Lett.*, 71, 1993.

[9] A. K. Geim and K. T. Novoselov. The rise of graphene. *Nat. Mat.*, 6, 2007.

[10] T. V. Can, Q. Z. Ni, and R. G. Griffin. Mechanisms of dynamics nuclear polarization in insulating solids. *J. Magn. Reson.*, 253, 2015.

[11] C. D. Jeffries. Polarization of nuclei by resonance saturation in crystals. *Phys. Rev.*, 106, 1957.

[12] A. Abragam and W. G. Proctor. Une nouvelle methode de polarisation dynamique des noyaux atomiques dans les solides. *C. R. Acad. Sci. Paris*, 246, 1958.

[13] A. V. Kessenikh, V. I. Lushchikov, A. A. Manenkov, and Y. V. Taran. Proton polarization in irradiated polyethylenes. *Sov. Phys. Solid State*, 5, 1963.

[14] A. V. Kessenikh, A. A. Manenkov, and G. I. Pyatnitskii. On explanation of experimental data on dynamic nuclear polarization of protons in irradiated polyethylenes. *Sov. Phys. Solid State*, 6, 1964.

[15] C. F. Hwang and D. A. Hill. New effect in dynamic polarization. *Phys. Rev. Lett.*, 18, 1967.

[16] C. F. Hwang and D. A. Hill. Phenomenological model for the new effect in dynamic polarization. *Phys. Rev. Lett.*, 19, 1967.

[17] A. S. L. Thankamony, J. J. Wittman, M. Kaushik, and B. Corzilius. Dynamic nuclear polarization for sensitivity enhancement in modern solid-state NMR. *Prog. Nucl. Magn. Reson. Spectroscop.*, 102, 2017.

[18] M. Goldman. *Spin temperature and nuclear magnetic resonance in solids.* Oxford; Clarendon Press, Great Clarendon St., Oxford, OX2 6DP, UK, 1970.

[19] A. Karabanov, A. van der Drift, L. J. Edwards, I. Kuprov, and W. Köckenberger. Quantum mechanical simulation of solid effect dynamic nuclear polarisation using Krylov-Bogolyubov time averaging and restricted state-space. *Phys. Chem. Chem. Phys.*, 14, 2012.

[20] G. Jeschke. A new mechanism for the chemically induced dynamic nuclear polarisation in the solid state. *J. Am. Chem. Soc.*, 120, 1998.

[21] C. T. Farrar, D. A. Hall, G. J. Gerfen, S. J. Inati, and R. G. Griffin. Mechanism of dynamic nuclear polarization in high magnetic fields. *J. Chem. Phys.*, 114, 2001.

[22] Y. Hovav, A. Feintuch, and S. Vega. Theoretical aspects of dynamic nuclear polarisation in the solid state - the solid effect. *J. Magn. Reson.*, 207, 2010.

[23] Y. Hovav, A. Feintuch, and S. Vega. Theoretical aspects of dynamic nuclear polarisation in the solid state - the cross effect. *J. Magn. Reson.*, 214, 2012.

[24] Y. Hovav, A. Feintuch, and S. Vega. Dynamic nuclear polarization assisted spin diffusion for the solid effect case. *J. Chem. Phys.*, 134, 2011.

[25] F. Mentink-Vigier, Ü. Akbey, Y. Hovav, S. Vega, H. Oshkinat, and A. Feintuch. Fast passage dynamic nuclear polarization on rotating solids. *J. Magn. Reson.*, 224, 2012.

[26] F. Mentink-Vigier, S. Vega, and G. De Paëpe. Fast and accurate MAS-DNP simuations of large spin ensembles. *Phys. Chem. Chem. Phys.*, 19, 2017.

[27] A. Karabanov, G. Kwiatkowski, and W. Köckenberger. Quantum mechanical simulation of cross effect DNP using Krylov-Bogolyubov averaging. *Appl. Magn. Reson.*, 43, 2012.

[28] D. Wiśniewski, A. Karabanov, I. Lesanovsky, and W. Köckenberger. Solid effect DNP polarization dynamics in a system of many spins. *J. Magn. Reson.*, 264, 2016.

[29] A. Karabanov, D. Wiśniewski, F. C. Raimondi, I. Lesanovsky, and W. Köckenberger. Many-body kinetics of dynamic nuclear polarization by the cross effect. *Phys. Rev. A*, 97, 2017.

[30] K-N Hu, G. T. Debelouchina, A. A. Smith, and R. G. Griffin. Quantum mechanical theory of dynamics nuclear polarisation in solid dielectrics. *J. Chem. Phys.*, 134, 2011.

[31] A. Karabanov, D. Wiśniewski, I. Lesanovsky, and W. Köckenberger. Dynamic nuclear polarisation as kinetically constrained diffusion. *Phys. Rev. Lett*, 115, 2015.

[32] B. Cowan. *Nuclear Magnetic Resonance and Relaxation.* Cambridge University Press, Edinburgh Building, Cambridge, CB2 2RU, UK, 2005.

[33] H-P. Breuer and F. Petruccione. *The Theory of Open Quantum Systems.* Oxford University Press, Great Clarendon Street, Oxford, OX2 6DP, UK, 2002.

[34] W. Gerlach and O. Stern. Das magnetische Moment des Silberatoms. *Z. Phys.*, 9, 1922.

[35] P. Zeeman. The effect of magnetisation on the nature of light emitted by a substance. *Nature*, 55, 1897.

[36] A. Abragam. *Principles of Nuclear Magnetism.* Oxford; Clarendon Press, Great Clarendon St., Oxford, OX2 6DP, UK, 1961.

[37] J. Keeler. *Understanding NMR spectroscopy.* John Wiley & Sons Ltd., The Atrium, Southern Gate, Chichester, PO19 8SQ, U.K., 2 edition, 2011.

[38] A. Abragam and M. Goldman. Principles of dynamic nuclear polarisation. *Rep. Prog. Phys.*, 41, 1978.

[39] F. Mentink-Vigier, S. Paul, D. Lee, A. Feintuch, S. Hediger, S. Vega, and G. de Paëpe. Nuclear depolarisation and absolute sensitivity in magic-angle spinning cross effect dynamic nuclear polarization. *Phys. Chem. Chem. Phys.*, 17, 2015.

[40] D. Browne. Lecture notes: Advanced quantum theory (PHASM/G426), Fall 2010/11.

[41] B. Falkenburg and M. Morrison, editors. *Why more is different.* Springer, 2015.

[42] H. D. Zeh. Decoherence: Basic concepts and their interpretation, 1995.

[43] W. H. Zurek. Decoherence and the transition from quantum to classical. *Phys. Today*, 44, 1991.

[44] M. H. Levitt. *Spin Dynamics*. John Wiley & Sons Ltd, The Atrium, Southern Gate, Chichester, PO19 8SQ, UK, 2 edition, 2015.

[45] I. Kuprov, N. Wagner-Rundell, and P. J. Hore. Polynomially scaling spin dynamics simulation algorithm based on adaptive state-space restriction. *J. Magn. Reson.*, 189, 2007.

[46] R. A. Horn and C. R. Johnson. *Topics in Matrix Analysis*. Cambridge University Press, The Pitt Building, Trumpington Street, Cambridge, UK, 1991.

[47] M. Am-Shallem, A. Lavy, I. Schaeffer, and R. Kosloff. Three approaches for representing lindblad dynamics by a matrix-vector notation. *arXiv: 1510.08634v2 [quant-ph]*, 2015.

[48] R. K. Harris. *Nuclear Magnetic Resonance Spectroscopy*. Longman Scientific & Technical, Longman House, Harlow, CM20 2JE, United Kingdom), 1986.

[49] M. Sanz, E. Solano, and I. L. Egusquiza. Beyond adiabatic elimination: Effective hamiltonians and singular perturbation. *arXiv: 1503.01369v1 [quant-ph]*, 2015.

[50] M. Born and V. Fock. Beweis des adiabatensatzes. *Z. Phys.*, 51, 1928.

[51] S. Nakajima. On the quantum theory of transport phenomena: Steady diffusion. *Prog. Theor. Phys.*, 20, 1958.

[52] R. Zwanzig. Ensemble method in the theory of irreversibility. *J. Chem. Phys.*, 33, 1960.

[53] N. M Krylov and N. N. Bogolyubov. *Introduction to non-linear mechanics*. Princeton University Press, 41 William St., Princeton, NJ 08540, USA, 1947. (Translated from Russian).

[54] M. B. Plenio and P. L. Knight. The quantum-jump approach to dissipative dynamics in quantum optics. *Rev. Mod. Phys.*, 70, 1998.

[55] A. Fichthorn and W. H. Weinberg. Theoretical foundations of dynamical Monte Carlo simuations. *J. Chem. Phys.*, 95, 1991.

[56] G. Hupin and D. Lacroix. Quantum Monte Carlo method applied to non-Markovian barrier transmission. *Phys. Rev. C*, 81, 2019.

[57] A. F. Voter. *Radiation Effects in Solids*, volume 235, chapter Introduction to the kinetic Monte Carlo method. Springer, 2007.

[58] MathWorks. rng: Control randon number generator. `https://www.mathworks.com/help/matlab/ref/rng.html`, 2020.

[59] P. Kratzer. Monte Carlo and kinetic Monte Carlo methods. *arXiv: 0904.2556v1 [cond-mat.mtrl-sci]*, 2009.

[60] L. Landau. Zur Theorie der Energieübertragung. II. *Physikalische Zeitschrift der Sowjetunion*, 2, 1932.

[61] C. Zener. Non-adiabatic crossing of energy levels. *Proceedings of the Royal Society of London A.*, 137, 1932.

[62] C. Cohen-Tannoudji, B. Diu, and F. Laloë. *Quantum Mechanics*. Wiley VCH, Boschstrasse 12, 69469, Weinheim, Germany, 2 edition, 1992.

[63] C. Wittig. The Landau-Zener formula. *J. Phys. Chem. B.*, 109, 2005.

[64] P. A. Beckmann. Spectral densities and nuclear spin relaxation in solids. *Physics Reports, Bryn Mawr College*, 171, 1988.

[65] I. Waller. Über die Magnetisierung von paramagnetischen Kristallen in Wechselfeldern. *Z. Phys.*, 79, 1932.

[66] N. Bloembergen, E. M. Purcell, and R. V. Pound. Nuclear magnetic relaxation. *Nature*, 160, 1947.

[67] B.V. Rollin and J. Hatton. Nuclear magnetic resonance at low temperatures. *Nature*, 159, 1947.

[68] M. Goldman. Formal theory of spin-lattice relaxation. *J. Magn. Reson.*, 149, 2001.

[69] N. Bloembergen. On the interaction of nuclear spins in a crystalline lattice. *Physica*, XV, 1949.

[70] K. N. Shrivastava. Theory of spin-lattice relaxation. *Phys. Stat. Sol. (b)*, 117, 1983.

[71] C. P. Scholes, R. Janakiraman, and H. Taylor. Temperature dependence of the electron spin-lattice relaxation rate from pulsed EPR of Cu_A and Heme a in cytochrome c oxidase. *Biophys. J.*, 45, 1984.

[72] Y. Zhou, B. E. Bowler, G. R. Eaton, and S. S. Eaton. Electron spin lattice relaxation rates for S=$\frac{1}{2}$ molecular species in glassy matrices or magnetically dilute solids at temperatures between 10 and 300K. *J. Magn. Reson.*, 139, 1999.

[73] S. K. Hoffmann, J. Goslar, and S. Lijewski. Suppression of Raman electron spin relaxation of radicals in crystals. Comparison of Cu^{2+} and free radical relaxation in triglycine sulfate and Tutton salt single crystals. *J. Phys. Condens. Matter*, 23, 2011.

[74] J.G. Jr. Castle and D. W. Feldman. Resonance modes at defects in crystalline quartz. *Phys. Rev. A*, 137, 1965.

[75] R. Orbach. Theory of spin-lattice relaxation in paramagnetic salts. *Proc. Phys. Soc.*, 77, 1961.

[76] V. A. Atsarkin, V. V. Demidov, and G. A. Vasneva. Metal-insulator transition in RbC_{60} polymer fulleride studied by ESR and electron-spin relaxation. *Phys. Rev. B*, 56, 1997.

[77] A. Lunghi, F. Totti, R. Sessoli, and S. Sanvito. The role of anharmonic phonons in under-barrier spin relaxation of single molecule magnets. *Nat. Commun.*, 8, 2017.

[78] J. R. Harbridge, G. R. Eaton, and S. S. Eaton. Electron spin-lattice relaxation processes of radicals in irradiated crystalline organic compounds. *J. Phys. Chem. A*, 107, 2003.

[79] S. K. Hoffmann and J. Goslar. Resonance local phonon mode and electron spin-lattice relaxation of formate-type free radicals studied by electron spin echo in $Cd(HCOO)_2.2H_2O$ crystal. *J. Phs. Condens. Matter*, 27, 2015.

[80] H. Sato, S. E. Bottle, J. P. Blinco, A. S. Micallef, G. R. Eaton, and S. S. Eaton. Electron spin-lattice relaxation of nitroxyl radicals in temperature ranges that span glassy solutions to low-viscosity liquids. *J. Magn. Reson.*, 191, 2008.

[81] E. Bouleau, P. Saint-Bonnet, F. Mentink-Vigier, H. Takahashi, J.-F. Jacquot, M. Bardet, F. Aussenac, A. Purea, F. Engelke, S. Hediger, D. Lee, and G. de Paëpe. Pushing NMR sensitivity limits using dynamic nuclear polarization with closed-loop cryogenic helium sample spinning. *Chem. Sci.*, 12, 2015.

[82] D. Wiśniewski. *Simulations of Dynamic Nuclear Polarisation pathways in large spin ensembles*. PhD thesis, The University of Nottingham, 2017.

[83] D. Shimon, A. Feintuch, D. Goldfarb, and S. Vega. Static 1H dynamic nuclear polarization with the biradical TOTAPOL: a transition between the solid effect and the cross effect. *Phys. Chem. Chem. Phys.*, 14, 2012.

[84] Y. Hovav, I. Kaminker, D. Shimon, A. Feintuch, and S. Vega. The electron depolarisation during dynamic nuclear polarization: measurements and simulations. *Phys. Chem. Chem. Phys.*, 17, 2015.

[85] F. A. Perras, R. R. Reinig, I. I. Slowing, A. D. Sadow, and M. Pruski. Effects of biradical deuteration on the performance of DNP: Towards better performing polarizing agents. *Phys. Chem. Chem. Phys.*, 18, 2016.

[86] Y. Matsuki, T. Maly, O. Ouari, H. Karoui, F. Le Moigne, E. Rizzato, S. Lyubenova, J. Herzfeld, T. Prisner, P. Tordo, and R. G. Griffin. Dynamic nuclear polarisation with a rigid biradical. *Angew. Chem. Int. Ed.*, 48, 2009.

[87] A. Mudalige and J. E. Pemberton. Raman spectroscopy of glycerol/D2O solutions. *Vib. Spectrosc.*, 45, 2007.

[88] J. J. Towey, A. K. Soper, and L. Dougan. Preference for isolated water molecules in a concentrated glycerol-water mixture. *J. Phys. Chem. B*, 115, 2011.

[89] J. Qvist, C. Mattea, E. P. Sunde, and B. Halle. Rotational dynamics in supercooled water from nuclear spin relaxation and molecular simulations. *J. Chem. Phys.*, 136, 2012.

[90] V. Agarwal, S. Penzel, K. Szekely, R. Cadalbert, E. Testori, A. Oss, J. Past, A. Samoson, M. Ernst, A. Böckmann, and B. H. Meier. 3D structure determination from sub-milligram protein samples by solid-state 100kHz MAS NMR spectroscopy. *Angew. Chem. Int. Ed. Eng.*, 53, 2014.

[91] L. B. Andreas, K. Jaudzems, J. Stanek, D. Lalli, A. Bertarello, R. Le Marchand, D. Cala-de Paëpe, S. Kotelovica, I. Akopjani, B. Knott, S. Wegner, F. Engelke, L. Emsley, K. Tars, T. Herrmann, and G. Pintacuda. Structure of fully protonated proteins by proton-detected magic-angle spinning NMR. *Proc. Natl. Acad. Sci. U.S.A.*, 113, 2016.

[92] S. Chaudhari, D. Wisser, A. Pinon, P. Berruyer, D. Gajan, P. Tordo, O. Ouari, C. Reiter, F. Engelke, C. Copéret, M. Lelli, A. Lesage, and L. Emsley. Dynamic nuclear polarisation efficiency increased by very fast magic angle spinning. *J. Am. Chem. Soc.*, 139, 2017.

[93] M. Afeworki, S. Vega, and J. Schaefer. Direct electron-to-carbon polarization transfer in homogeneously doped polycarbonates. *Macromolecules*, 25, 1992.

[94] M. Afeworki and J. Schaefer. Mechanism of DNP-enhanced polarization transfer across the interface of polycarbonate/polystyrene heterogeneous blends. *Macromolecules*, 25, 1992.

[95] M. Afeworki, R. A. McKay, and J. Schaefer. Selective observation of the interface of heterogeneous polycarbonate/hetergeneous blends by dynamic nuclear polarization carbon-13 NMR spectroscopy. *Macromolecules*, 25, 1992.

[96] D. A. Hall, D. C. Maus, G. J. Gerfen, S. J. Inati, L. R. Becerra, F. W. Dahlquist, and R. G. Griffin. Polarization-enhanced NMR spectroscopy of biomolecules in frozen solution. *Science*, 276, 1997.

[97] B. Corzilius, A. A. Smith, and R. G. Griffin. Solid effect in magic angle spinning dynamic nuclear polarization. *J. Chem. Phys.*, 137, 2012.

[98] A. A. Smith, B. Corzilius, A. B. Barnes, T. Maly, and R. G. Griffin. Solid effect dynamic nuclear polarization and polarization pathways. *J. Chem. Phys.*, 136, 2012.

[99] M. Abraham, M. A. H. McCausland, and F. N. H. Robinson. Dynamic Nuclear Polarization. *Phys. Rev. Lett.*, 2, 1959.

[100] K. R. Thurber and R. Tycko. Theory for cross effect dynamic nuclear polarization under magic-angle spinning in solid state nuclear magnetic resonance: the importance of level crossings. *J. Chem. Phys.*, 137, 2012.

[101] D. Mance, P. Gast, M. Huber, M. Baldus, and K. L. Ivanov. The magnetic field dependence of cross-effect dynamic nuclear polarization under magic angle spinning. *J. Chem. Phys.*, 142, 2015.

[102] K. R. Thurber and R. Tycko. Perturbation of nuclear spin polarizations in solid state NMR of nitroxide-doped samples by magic-angle spinning without microwaves. *J. Chem. Phys.*, 140, 2014.

[103] F. A. Perras and M. Pruski. Large-scale ab initio simulations of MAS DNP enhancements using a Monte Carlo optimization strategy. *J. Chem. Phys.*, 149, 2018.

[104] M. Bak and N. C. Nielsen. REPULSION, a novel approach to efficient powder averaging in solid-state NMR. *J. Magn. Reson.*, 125, 1997.

[105] E. B. Saff and A. B. J. Kuijlaars. Distributing many points on a sphere. *Math. Intell.*, 19, 1997.

[106] M. Edén. Computer simulations in solid-state NMR. II. Implementations for static and rotating samples. *Concept Magn. Reson. A.*, 18A, 2003.

[107] M. M. Haugland, E. A. Anderson, and J. E. Lovett. Tuning the properties of nitroxide spin labels for use in electron paramagnetic resonance spectroscopy through chemical modification of the nitroxide framework. *Electron Paramag. Reson.*, 25, 2017.

[108] R. Tycko and G. Dabbagh. Measurement of nuclear magnetic dipole-dipole couplings in magic angle spinning NMR. *Chem. Phys. Lett.*, 173, 1990.

[109] E. L. Dane, B. Corzilius, E. Rizzato, P. Stocker, T. Maly, A. A. Smith, R. G. Griffin, O. Ouari, P. Tordo, and T. M. Swager. Rigid orthogonal bis-Tempo biradicals with improved solubility for dynamic nuclear polarization. *J. Org. Chem.*, 77, 2012.

[110] F. Mentink-Vigier, Ü. Akbey, H. Oschkinat, S. Vega, and A. Feintuch. Theoretical aspects of magic angle spinning - dynamic nuclear polarization. *J. Magn. Reson.*, 258, 2015.

[111] S. K. Zaremba. Good lattice points, discrepancy, and numerical integration. *Ann. Mat. Pura. App. 4*, 73, 1966.

[112] H. Conroy. Molecular Schrödinger equation VIII: a new method for the evaluation of multidimensional integrals. *J. Chem. Phys.*, 47, 1967.

[113] V. B. Cheng, H. H. Suzukawa, and M. Wolfsberg. Investigation of a nonrandom numerical method for multidimensional integration. *J. Chem. Phys.*, 59, 1973.

[114] K. J. Åström and T. Hägglund. *PID Controllers: Theory, Design and Tuning.* Instrument Society of America, 67 Alexander Drive, Durham, NC 27709, USA, 2 edition, 1995.

[115] R. E. Hoffman and G. C. Levy. Modern methods of NMR data processing and data evaluation. *Prog. Nucl. Magn. Reson. Spectroscop.*, 23, 1991.

[116] D. I. Hoult and N. S. Ginsberg. The quantum origins of the free induction decay signal and spin noise. *J. Magn. Reson.*, 148, 2001.

[117] A. Haase, J. Frahm, and K. D. Matthaei. FLASH imaging: rapid NMR imaging using low flip angle pulses. *J. Magn. Reson.*, 67, 1986.

[118] P. Horowitz and W. Hill. *The Art of Electronics.* Cambridge University Press, 32 Avenue of the Americas, New York, NY 10013-2473, USA, 2 edition, 1989.

[119] J. R. Bolton and J. A. Weil. *Electron Paramagnetic Resonance: Elementary Theory and Practical Applications.* Wiley & Sons Inc., 111 River Street, Hoboken, NJ 07030, USA, 2 edition, 2007.

[120] D. Shimon, Y. Hovav, A. Feintuch, D. Goldfarb, and S. Vega. Dynamic nuclear polarisation in the solid state: a transition between the solid effect and the cross effect. *Phys. Chem. Chem. Phys.*, 14, 2012.

[121] H-Y. Chen and R. Tycko. Temperature-dependent nuclear spin relaxation due to paramagnetic dopants below 30K: relevance to DNP-enhanced magnetic resonance imaging. *J. Phys. Chem. B.*, 122, 2018.

[122] K.-A. Hansen and J. P. Blinco. Nitroxide radical polymers - a versatile material class for high-tech applications. *Polym. Chem.*, 9, 2018.

[123] G. Casano, H. Karoui, and O. Ouari. Polarising agents: evolution and outlook in free radical development for DNP. *eMagnRes*, 7, 2018.

[124] Tempol - cas 2226-96-2 - calbiochem. ONLINE: https://www.sigmaaldrich.com/catalog/product/mm/581500. Date Accessed: 3rd October 2019.

[125] A. J. Horne and C. R. Goldman. *Limnology.* New York; McGraw-Hill, 2 Pennsylvania Plaza, New York, 10121, USA, 2 edition, 1994.

[126] P. Atkins and J. de Paula. *Atkins' Physical Chemistry.* New York; W. H. Freeman and Company, 41 Madison Avenue, New York, 10010, USA, 8 edition, 2006.

[127] Water, water everywhere: Water quality factors reference unit. ONLINE: https://dep.wv.gov/WWE/getinvolved/sos/Documents/SOSKit/DOSaturation.pdf. Date Accessed: 27th September 2019.

[128] W. Xing, M. Yin, Q. Lv, Y. Hu, C. Liu, and J. Zhang. Oxygen solubility, diffusion coefficient, and solution viscosity. In *Rotating Electrode Methods and Oxygen Reduction Electrocatalysts*, pages 1 – 31. Amsterdam; Elsevier, Radarweg 29, Amsterdam, 1043NX, Netherlands, 2014.

[129] Oxygen. ONLINE: https://www.xylemanalytics.com/en/parameters/dissolved-oxygen-do. Date Accessed: 27th September 2019.

[130] S. S. Shapiro and M. B. Wilk. An analysis of variance test for normality (complete samples). *Biometrika*, 53, 1965.

[131] A. Ghasemi and S. Zahediasl. Normality tests for statistical analysis: a guide for non-statisticians. *Int. J. Endocrinol. Metab.*, 10, 2012.

[132] B. J. Burger and J. E. Bercaw. Vacuum techniques for handling air-sensitive organometallic compounds. *ACS Syposium Series*, 357, 1987.

[133] DMSO solubility data. ONLINE: CO_solubility_DMSO.pdf, 2007. Date Accessed: 14th April 2020.

[134] How to: Clean nmr tubes. ONLINE: https://s3.wp.wsu.edu/uploads/sites/33/2013/10/NMR-Tube-Cleaning.pdf, 2013. Date Accessed: 24th October 2019.

[135] Basics of relaxation. ONLINE: https://web.stanford.edu/class/rad226b/Lectures/Lecture4-2016-Relaxation-Basics.pdf. Date Accessed: 9th October 2019.

[136] F. Mallamace, C. Corsaro, D. Mallamace, S. Vasi, and H. E. Stanley. NMR spectroscopy study of local correlations in water. *J. Chem. Phys.*, 145, 2016.

[137] P.-O. Westlund. A proton T_1-nuclear magnetic resonance dispersion study of water motion in snowflakes and hexagonal ice. *Molecular Physics*, 117, 2019.

[138] N. Bloembergen and L. O. Morgan. Proton relaxation times in paramagnetic solutions. Effects of electron spin relaxation. *J. Chem. Phys.*, 34, 1961.

[139] L. Lumata, Z. Kovacs, A. D. Sherry, C. Malloy, S. Hill, J. van Toll, L. Yu, L. Song, and M. E. Merritt. Electron spin resonance studies of trityl OX063 at a concentration optimal for DNP. *Phys. Chem. Chem. Phys.*, 10, 2013.

[140] M. J. Giansiracusa, A. K. Kostopolous, D. Collison, R. E. P. Winpenny, and N. F. Chilton. Correlating blocking temperatures with relaxation mechanisms in monometallic single-molecule magnets with high energy barriers (U_{eff}>600K). *Chem. Comm.*, 55, 2019.

[141] F. Menkink-Vigier, I. Marin-Montesinos, A. P. Jagtap, J. van Tol, S. Hediger, D. Lee, S. T. Sigurdsson, and G. de Paëpe. Computationally assisted design of polarizing agents for dynamic nuclear polarization enhanced NMR: the AsymPol family. *J. Am. Chem. Soc.*, 140, 2015.

[142] H. Flanders. Differentiation under the integral sign. *Am. Math. Mon.*, 80, 1973.